Direct Observation of Magnetic Domain Structure by Field Emission Lorentz Microscopy

J.N. Chapman, L.J. Heyderman, S. McVitie and W.A.P. Nicholson
Department of Physics and Astronomy, University of Glasgow, Glasgow G12 8QQ, U.K.

Abstract

We describe how a high performance transmission electron microscope can be modified to make it better suited to the study of magnetic domain structures. The main additional features are two super mini-lenses (Lorentz lenses) located above and below the standard objective lens. Among the benefits to be derived from the modified instrument are new imaging modes and the ability to image magnetic structures in a magnetic field whose strength is chosen by the experimenter. Following a brief description of the coherent Foucault imaging mode, examples are given of how information can be derived on the magnetisation processes in small lithographically-defined magnetic elements, fine tips for magnetic force microscopy and Co/Pt multilayer films for magneto-optic recording.

Introduction

Transmission electron microscopy (TEM) plays a pivotal role in helping us understand and subsequently improve the properties of new materials. Its key attributes are very high spatial resolution (at or near the atomic level) and the wide range of interactions which take place between the impinging electrons and the specimen. Advantage can be taken of the latter to provide insight into the structural and electronic properties of the material under investigation. Unfortunately, in the standard microscope the specimen is located in a region of high magnetic field (~400 kA/m) which precludes or severely restricts information being obtained on the distribution of magnetic induction within a magnetic specimen. Such information is vital if we are to understand the role of growth and processing conditions on the magnetic properties of the many diverse magnetic materials in use today.

At Glasgow University we have undertaken an ambitious programme to extend the capability of the electron microscope for the study of magnetic materials. In this paper we describe the principal features of the new microscope and the instrumental modifications that have been required to realise them. In particular we highlight two important aspects of its performance. The first of these relates to the development of a new technique, coherent Foucault imaging, which can be regarded as an on-axis holographic mode capable of generating magnetic interferograms in real time. Thereafter we discuss how it is possible to image in a magnetic field chosen by the experimenter to suit the particular specimen under investigation. Examples are given of how these attributes yield information on the magnetisation process in small lithographically-defined magnetic elements, the magnetic state of fine tips used in magnetic force microscopy and domain nucleation in Co/Pt multilayers.

Instrumental Performance

The aims of our research have been (i) to develop new imaging configurations whereby a quantitative description of the spatial variation of magnetic induction can be determined, (ii) to improve the resolution in the magnetic images to significantly better than 10 nm so that fine structures associated with domain walls can be studied directly, (iii) to develop in-situ experimental methods so that changes in magnetic structure with magnetic field and temperature can be studied and (iv) to introduce compatibility between magnetic imaging and high spatial resolution microanalysis so that detailed correlations can be made between micromagnetic and microstructural features. To achieve these aims we have developed a unique electron microscope jointly with Philips Electron Optics [1]. The instrument is based on a Philips CM20 TEM/STEM equipped with a field emission gun. The entire specimen region has been redesigned to accommodate an extra pair of super mini-lenses (Lorentz lenses), necessary to allow suitable imaging conditions without the specimen being subjected to a field, and sufficient space for the immediate vicinity of the specimen to become a miniature micromagnetic laboratory. The disposition of the extra lenses relative to the specimen area and the standard objective lens is shown schematically in figure 1. It should be noted that the overall height of the instrument remains unchanged so that non-standard items are restricted to the region where they are most needed. In the modified instrument the specimen remains located at the centre of the gap of the objective lens although the lens gap itself has been extended to 20 mm to allow room for ancillary equipment and detectors.

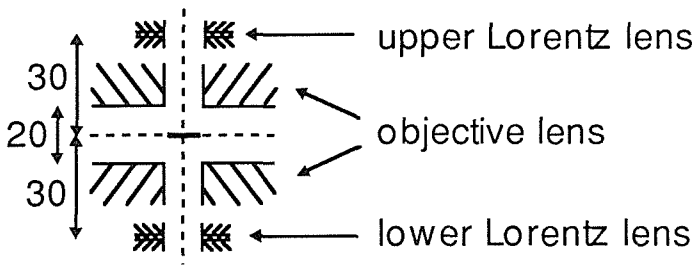

Figure 1 *The configuration of the lenses around the specimen region in the modified electron microscope.*

Using the modified objective lens in fixed-beam mode the 0.14 nm gold lattice fringes can still be resolved although the point resolution drops to 0.36 nm. In scanning modes, spot sizes <1 nm are available. For imaging magnetic microstructures, however, the objective lens normally remains unexcited and its role is replaced by one of the Lorentz lenses. In fixed-beam mode, with the lower Lorentz lens becoming the principal imaging lens, 1.3 nm lattice fringes have been resolved and the point resolution is calculated to be 2.1 nm. Using the upper Lorentz lens as a probe forming lens enables sub-5 nm spot sizes to be realised, the current in the probe being ≈0.5 nA. Furthermore, when both Lorentz lenses are used simultaneously it is possible to ensure that good imaging conditions can be achieved whilst the diffraction pattern is accurately located in an aperture plane, a prerequisite for the successful implementation of the coherent Foucault imaging mode described below. Thus the microscope offers extreme flexibility as far as imaging is concerned and we have successfully implemented the Fresnel, standard Foucault and differential phase contrast (DPC) modes [2] as well as the new coherent Foucault technique.

Although the standard objective lens is not needed directly for any of the magnetic imaging modes described above, its use as a source of (vertical) magnetic field greatly enhances the magnetic

information that can be collected. In the simplest operational mode it provides a means of changing the magnetic state of the specimen in-situ. Thus, by repeatedly switching it on and off through a series of pre-selected values, we have a convenient method of taking the specimen through an in-situ perpendicular remanence cycle. Images recorded between successive excitations provide a microscopic picture of the irreversible magnetic changes undergone by the specimen [3]. It should be noted that the field range available for this procedure is approximately 600 kA/m and that the direction of field can be reversed. A further possibility is to record images with the objective lens on at a pre-set excitation. Of course, as soon as the objective lens is excited the imaging conditions are affected by its focusing effect and this has to be compensated for by varying the current through one or both of the Lorentz lenses. In practice all the magnetic imaging modes remain available over part of the objective lens excitation range but only Fresnel imaging is possible as the highest excitation is approached.

A particularly convenient operational mode is one in which the objective lens is set at a suitable fixed value and the specimen is taken through a magnetisation cycle by simply tilting it. Under these conditions no change in the imaging conditions is experienced once they have been established initially so that the attention of the experimenter can be devoted to what is happening to the specimen. This operational mode is appropriate when the sample is susceptible to relatively small in-plane fields whilst remaining unaffected by the presence of somewhat larger fields perpendicular to its plane. The high demagnetising factor perpendicular to the plane of a thin film sample means that this condition is frequently fulfilled. A useful check on the importance or otherwise of the component of field perpendicular to the specimen plane is to note whether the domain structure of an untilted sample changes according to whether the objective lens is off or excited at the level to be used in a particular experiment. It is worth noting that, for the experiments under discussion, the specimen is mounted in a tilt/rotate holder so that the field can be applied in any direction deemed appropriate by the experimenter.

By subjecting the specimen to a tilting cycle, dynamical changes in the magnetisation process can be observed. For these purposes one of the fixed beam imaging modes is normally used. Observation of the magnetic structures then involves the use of a low-light-level TV camera coupled to a YAG scintillator situated below the viewing screen of the microscope. The TV signal is routed through a frame store equipped with an integrating facility which allows the signal to noise ratio in the image to be greatly improved at the expense of time resolution. Varied examples of how in-situ magnetising can be used to extend the range of micromagnetic information accessible are given following the description of the Foucault imaging technique.

Coherent Foucault Imaging

Coherent Foucault imaging is an on-axis holographic imaging technique and details of it have been given elsewhere [4,5]. It requires the high brightness of a field emission gun. It is applicable when the specimen does not extend across the entire field of view so that part of the electron beam passes through free space. This acts as a reference wave. In the diffraction pattern an opaque or, more usually, a phase-shifting aperture is used to modify a user-selected portion of the electron disturbance there. Under certain conditions, specified below, the resulting image is a magnetic interferogram in which a set of fringes are observed running parallel to the local induction direction. The spacing of the fringes depends on the component of induction perpendicular to the electron trajectory integrated along its length. Denoting this quantity by $\int B_{\perp} dz$ it is straightforward to show that the fringe spacing Δs is given by

$$\Delta s^{-1} = e\int B_{\perp} dz / h$$

Thus the technique gives not only an immediate picture of the distribution of flux throughout the specimen but provides quantitative information not readily accessible using the imaging techniques mentioned in the preceding section. The resulting magnetic interferograms closely resemble those obtained using the established off-axis helographic mode [6]. However, in coherent Foucault imaging, the interferogram is produced in real time on the microscope viewing screen or, by using the low-light-level TV camera, on a TV monitor. No processing whatsoever is required.

For successful coherent Foucault imaging the phase-shifting aperture should introduce a phase shift of approximately π radian and should contain a hole smaller in extent than the magnetic splitting of the central spot of the diffraction pattern. An amorphous silicon nitride film 50 nm thick introduces an appropriate phase shift for use with 200 keV electrons whilst electron beam lithography can be used to introduce micron-sized holes into the film. Thus a suitable aperture satisfying the size criterion in our instrument for the specimens described below is produced.

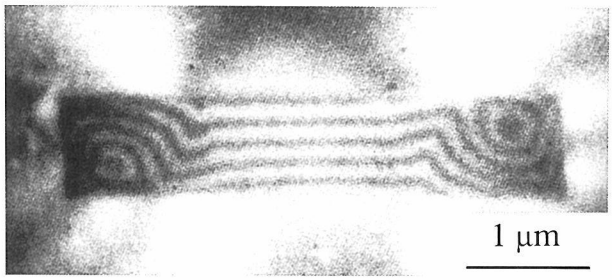

Figure 2 *Coherent Foucault image of a 30 nm thick element in zero applied field produced using a phase shifting aperture.*

Figure 2 illustrates the use of coherent Foucault imaging. It shows a 30 nm thick micron-sized rectangular permalloy element produced using electron beam lithography and lift-off techniques. It is immediately apparent that the magnetic structure is rather complex but that flux closure is incomplete. Whilst the magnetisation is fairly uniform over the central portion of the element it is more interesting to note what is happening towards the ends of the element. Here a continuation of near-uniform magnetisation would give rise to excessive magnetostatic energy whereas the element combats this through the introduction of small magnetisation vortices which can be seen clearly. The clarity with which the interferogram reveals the end structure is in marked distinction to what has been the case in the past using more conventional methods [7].

Imaging in a Magnetic Field

To explore further the magnetic properties of small elements, such as that shown in figure 2, the objective lens was excited so that the vertical field was 27 kA/m. No change to the induction distribution was seen with the specimen untilted. Figure 3 shows the effect of subsequently tilting the specimen. At a large positive tilt (figure 3a) a near uniform distribution of induction existed with only small deviations close to the ends of the element. As the tilt was reduced, changes were gradual although by $+5.5^{o}$ (figure 3b) the component of induction parallel to the shorter edge of the element had increased significantly. At a tilt of $+3.0^{o}$ (figure 3c) a sudden irreversibility occurred and a distorted form of the vortex structures of figure 2 reappeared. These structures persisted as the tilt

was reduced to zero and subsequently increased modestly in the opposite sense, corresponding to a reversal of field direction. However, by a tilt of –3.5° the complexity of the magnetisation distribution had increased as is apparent from figure 3d. The central region, which was uniformly magnetised, reduced in size and more rapid variations in magnetisation direction down the length of the element can be seen. Further increase in negative tilt resulted in a sudden switch of the magnetisation with the element once again assuming a slightly distorted version of the remanence state but with the magnetic moment of the element as a whole reversed. Although the actual switch itself was too rapid to observe, all other details of the way the induction distribution changed throughout the field cycle have been vividly revealed by coherent Foucault imaging.

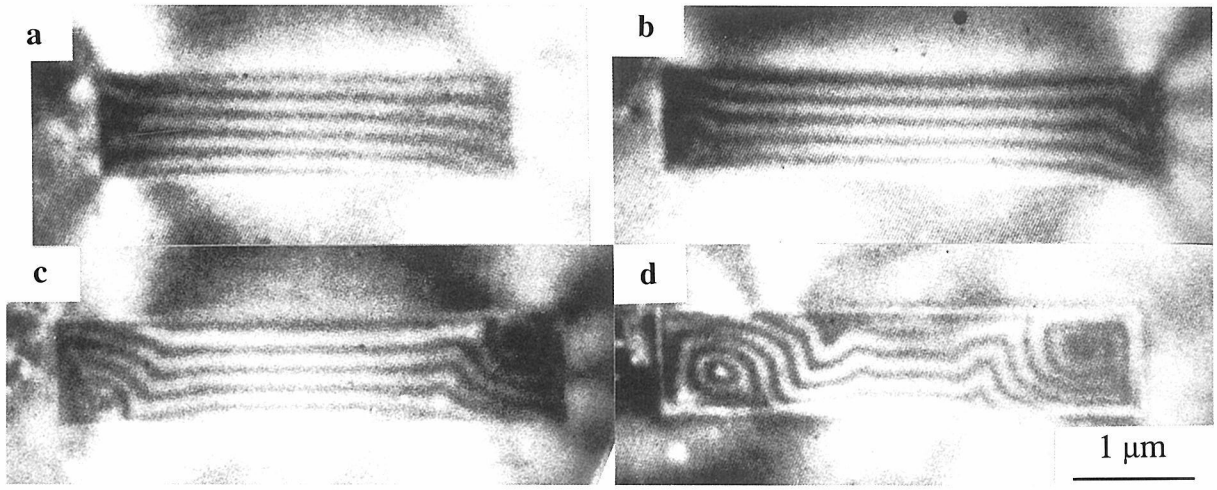

Figure 3 *Coherent Foucault images of the element in figure 2 with the objective lens excited to produce a vertical field of 27 kA/m. The images shown were taken with specimen tilt angles of (a) +33°, (b) +5.5°, (c)+3.0° and (d) -3.5°.*

A second example of where the ability to apply a magnetic field in-situ is important is in a recent study of tips for magnetic force microscopy (MFM). Here, a knowledge of the magnetic state of the tip and its response to an external field is imperative if quantitative information is to be extracted from MFM images. The tips investigated were grown by "contamination writing" using a focused electron probe in a scanning electron microscope and were subsequently coated with a thin Co-Ni alloy film. Figure 4 shows coherent Foucault images of two such tips which were grown adjacent to each other on a silicon substrate for investigation in the transmission electron microscope. This time a standard opaque TEM aperture was used throughout so figures 4a and b can be thought of as the images obtained using complementary opaque semi-infinite half-plane apertures. In figure 4a the orientation of the aperture is such that the magnetic contribution to the diffraction pattern is transmitted whilst in figure 4b all magnetic information is obstructed. Consequently fringes can be seen in figure 4a but not in figure 4b. The fact that the fringes run predominantly parallel to the length of the tip is indicative of the fact that the tip is approximately uniformly magnetised parallel to its length.

Figure 4c was obtained by retaining the aperture position used to record figure 4b but after the tip had been subjected to progressively larger reverse fields. As soon as fringes appeared it was clear that the magnetisation had switched thereby resulting in magnetic information being transmitted rather than obstructed by the aperture. In this way the switching field could be determined accurately and future work will relate switching fields to tip geometries. For now it is of interest to note that the

fringes are not of equal spacing across the tip in figures 4a and c but are more closely spaced towards the lower side of each tip in the former and towards the upper side in the latter. As well as providing conclusive proof that the tip magnetisations have indeed changed direction it is indicative of the fact that contrast effects in coherent Foucault imaging can arise from an electrostatic as well as a magnetic origin. Strictly, the coherent Foucault image provides information about the phase of the electron wave after transmission through the specimen. Thus in this case we must recognise that there is a contribution from the varying thickness of the tip itself as well as from the magnetisation distribution which is of primary interest. However, by combining information from pairs of images in which the only change is the direction of magnetisation, it should be possible to separate magnetic and electrostatic effects. Hence we have a realistic scheme for obtaining descriptions (in registration with each other) of both the magnetic structure and topography of specimens of this kind.

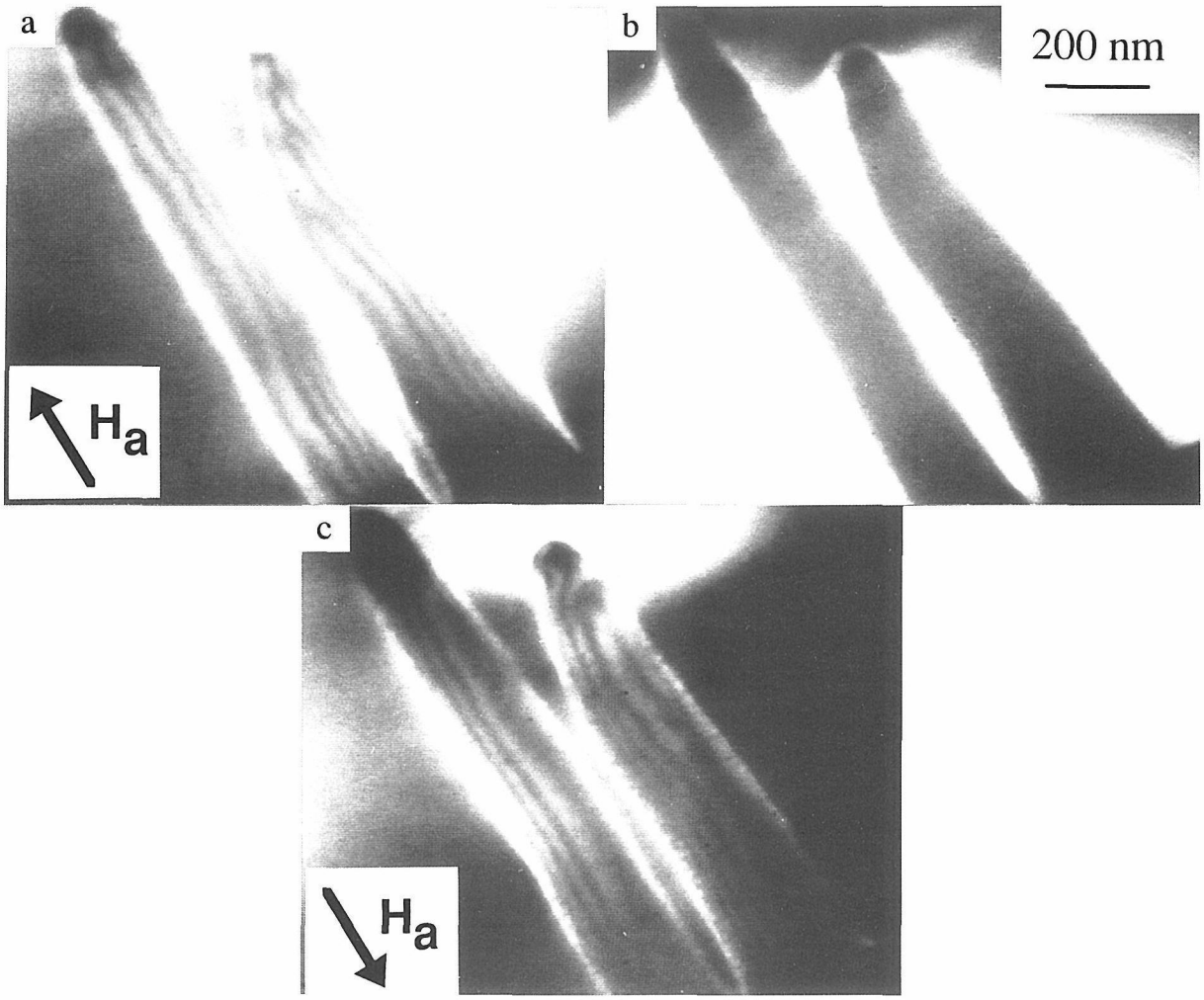

Figure 4 *Coherent Foucault images of two adjacent MFM tips using a standard opaque TEM aperture. (a) and (b) are taken following the application of a field whose direction is given by the arrow. The aperture is oriented so that the magnetic information is (a) transmitted and (b) obstructed. (c) is taken following the application of a reverse field, retaining the same aperture position as in (b). The magnetic information is now transmitted.*

Our third example of where new opportunities arise due to control over the field applied to the specimen during the imaging process relates to domain nucleation in Co/Pt multilayer films which are of interest as magneto-optic recording media [8]. Domain nucleation and time-dependent magnetic

effects have been studied for many years using optical microscopy [9,10] but difficulties arise when the scale of the domain structures of interest is significantly below the resolution limit of the optical microscope. This is the case with Co/Pt multilayers where nucleation and growth phenomena often require the higher resolution available in the transmission electron microscope. Previous work on samples of this nature where we did not have the ability to image whilst a field was applied have been reported elsewhere [3,11]. Here we began by applying a field of 76 kA/m, slightly lower than the coercive field, to the sample. Initially no nucleation was observed but after ≈60s domains nucleated and over the following few minutes spread across the field of view. The progressive spread of the domains is characteristic of a thermally-activated process and the whole sequence represents a microscopic example of the phenomenon alternatively known as magnetic after-effect or magnetic viscosity. Eventually, on a time scale of minutes, no further changes took place within the specimen and an increase in field was needed to show how the domain structure developed towards complete reversal relative to the initial state.

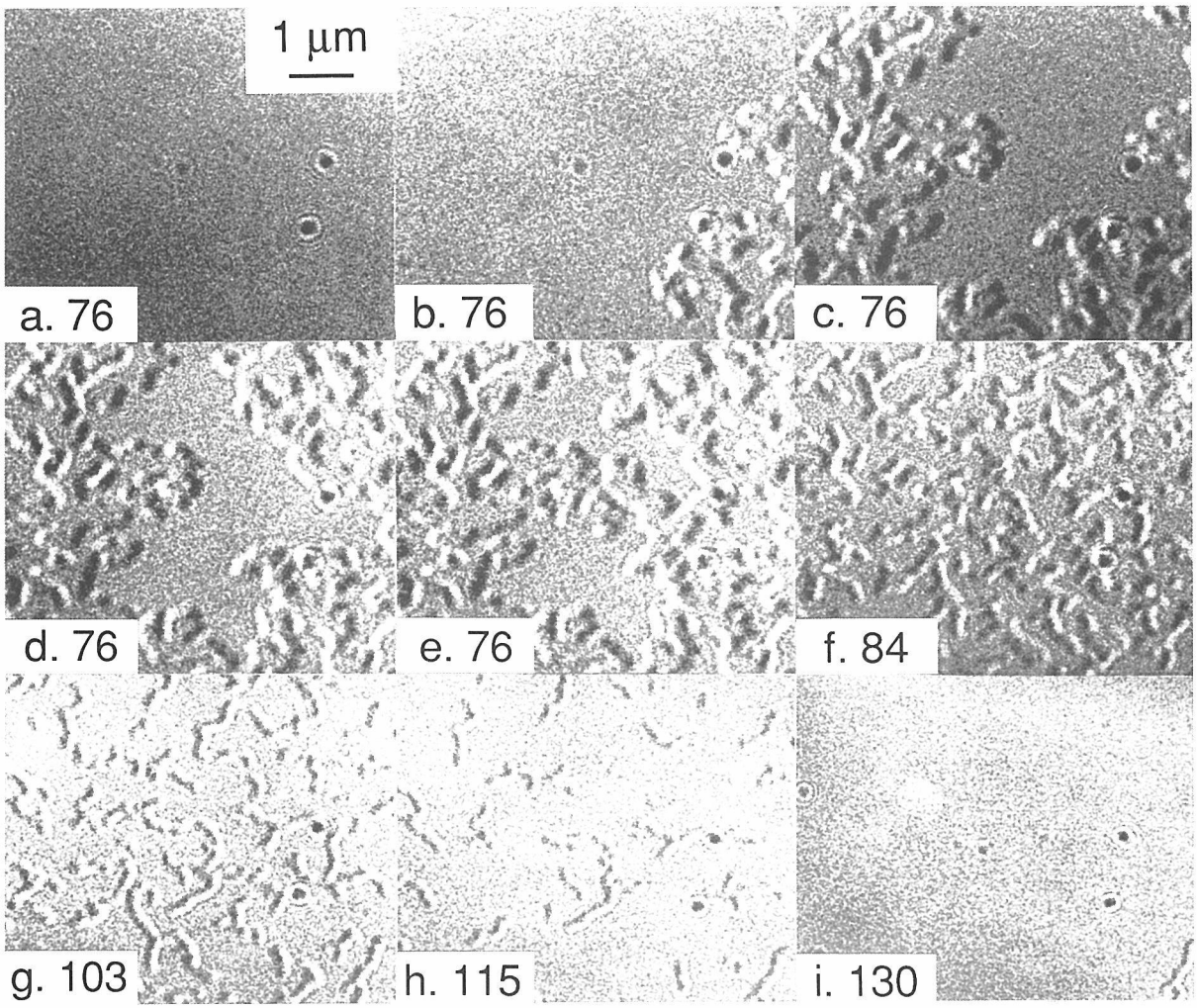

Figure 5 *Fresnel images of the magnetisation reversal in a Co/Pt multilayer film. Field values are given for each image in kA/m.*

Whilst the whole sequence described above has been recorded on video tape, individual images with a higher signal-to-noise ratio were obtained by simply removing the field at interesting stages in the process and recording the images directly on to film. Removal of the field has the effect of "freezing" the domain structure whilst its re-application at the same value allows its evolution to continue. This

was the method used for the images in figure 5. Figures 5a to e show how the domain structure spreads across the specimen with time without any need to increase the applied field. Later in the sequence (figures 5f onwards) higher fields were applied. It is worth noting that the very narrow domains seen in figures 5g and h persisted to very high fields and their study certainly required both the high sensitivity, because of the small Lorentz deflection from Co/Pt multilayers, and high spatial resolution of the new microscope.

Conclusions

Although the standard transmission electron microscope is ill-suited to the study of magnetic domain structures a modified instrument can provide a wealth of micromagnetic information without losing its ability to provide equally important microstructural detail. Here we have shown how a modified instrument with a field emission gun opens up the possibility of developing new quantitative imaging modes. Furthermore, by virtue of its flexible operational modes, imaging can be undertaken in a magnetic field which is selected by the experimenter as that most suitable for revealing insight into the magnetic processes of greatest interest. The results presented here are exemplary of where the experimenter needs to select the field and it is confidently anticipated that insight into a wide range of different magnetic processes will be gained by taking advantage of the additional versatility gained by the presence of the additional Lorentz lenses.

Acknowledgements

We would like to thank Alan Johnston, Lin Zhou and Chris Wilkinson (Glasgow University) for help with the coherent Foucault imaging and provision of the lithographic facilities, Cock Lodder and Manfred Ruhrig (Twente University) for the MFM tips and Hans van Kesteren (Philips Research Laboratories) for the Co/Pt multilayer films. We gratefully acknowledge financial support from the United Kingdom EPSRC and the European Union HCM Network scheme.

References

[1] J N Chapman, R P Ferrier, L J Heyderman, S McVitie, W A P Nicholson, B Bormans, Proc. EMAG 93 (IOP Conf. Ser. 138, IOPP Bristol) p1.
[2] J N Chapman, J. Phys. D: Appl. Phys. **17**, 1984, 623.
[3] D M Donnet, J N Chapman, H W van Kesteren, W B Zeper, J. Magn. Magn. Mat. **115**, 1992, 342.
[4] J N Chapman, A B Johnston, L J Heyderman, S McVitie, W A P Nicholson, IEEE Trans Mag. - in press.
[5] J N Chapman, A B Johnston, L J Heyderman, J. Appl. Phys. - in press.
[6] A Tonomura, Rev. Mod. Phys. **59**, 1987, 639.
[7] S J Hefferman, J N Chapman, S McVitie, J. Magn. Magn. Mat. **95**, 1991, 76.
[8] F J A M Greidanus, W B Zeper, B A J Jacobs, J H M Spruit, P F Carcia, Japan J. Appl. Phys. **28**, 1989, 37.
[9] M Labrune, S Andrieu, F Rio, P Bernstein, J. Magn. Magn. Mat. **80**, 1989, 211.
[10] J Pommier, P Meyer, G Penissard, J Ferre, P Bruno, D Renard, Phys. Rev. Lett., **65**, 1990, 2054.
[11] D M Donnet, V G Lewis, J N Chapman, K O'Grady, H W van Kesteren, J. Phys. D: Appl. Phys. **26**, 1993, 1741.

Plasma Etching Technique for TEM Observation of Grain Boundary Phase in Silicon Nitride

Hisayuki Suematsu, Yoshio Bando, Keiji Kurashima and Mamoru Mitomo
National Institute for Research in Inorganic Materials, 1-1 Namiki, Tsukuba, Ibaraki 305, Japan

ABSTRACT

Chemical composition of the grain boundary triple points is analyzed in Si_3N_4. A thin foil of Si_3N_4 is etched by CF_4+7.8%O_2 plasma and matrix Si_3N_4 grains are selectively removed for accurate analysis. The plasma etched sample is observed with an analytical transmission electron microscope with a beam size of 0.5nm in diameter. Concentration of Si is higher at the corner of the triple points than at the center.

INTRODUCTION

Silicon nitride(Si_3N_4) exhibits strength degradation above 1300°C because of the presence of glassy phase on the grain boundary[1]. To overcome this weak point, crystalization of the glassy phase has been studied[1,2] to raise the melting point of the grain boundary phases. Since the melting point depends on the chemical composition of the grain boundary phase, it is important to obtain precise composition of the grain boundary phase.

Transmission electron microscopes(TEM) with energy dispersive x-ray spectrometers(EDS) has better spatial resolution than other analysis methods. Even though in TEM with field emission guns, actual resolution is not good enough for chemical analysis in the grain boundaries. Electrons are scattered in the samples and it is practically impossible to eliminate x-ray signals of Si_3N_4 matrix from that of the grain boundary phase. Thus, it is required to remove Si_3N_4 matrix chemically for the precise analysis of the grain boundary phases.

In the present work, plasma etching was applied on Si_3N_4 ceramics to remove Si_3N_4 matrix grains. Chemical composition of remained grain boundary triple points was analyzed by an analytical TEM with an EDS.

EXPERIMENTAL PROCEDURE

Si_3N_4 powder was sintered with 1mol% of Y_2O_3 and Nd_2O_3 in each as sintering aids. TEM specimen was cut from a sintered body and was prepared by conventional Ar ion milling technique. Plasma etching was applied on the TEM specimen. The specimen was placed in between two electrodes in a chamber and CF_4 with 7.8% of O_2 gas was introduced at a pressure of 1mbar. 13.56MHz of radio frequency was applied on the electrodes for 30sec to 5min to produce plasma. After the plasma etching, the specimen was coated with a carbon film to prevent electron charge up during TEM observation. Detail of the plasma etching was described in elsewhere[3].

The plasma etched TEM specimen was observed with a field emission analytical electron microscope(JEM 3000F) operated at an accelerating voltage of 300kV. An EDS detector with a solid

angle of 0.2str was attached to the microscope. The chemical composition of the grain boundary triple points were analyzed by using an electron beam of about 0.5nm in diameter.

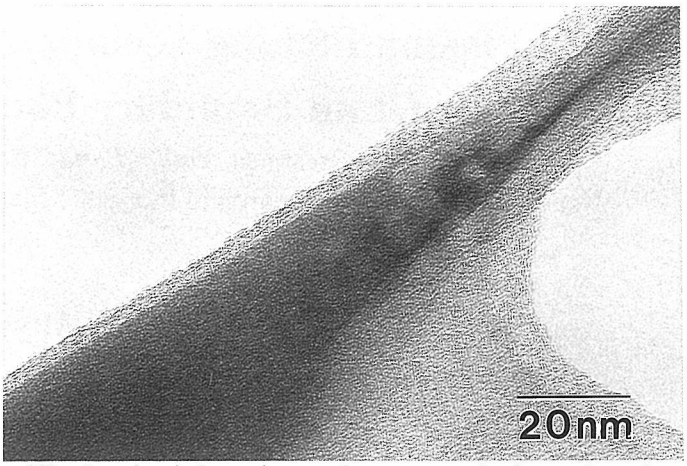

Fig.1 A triple point and a two-grain boundary in plasma etched Si_3N_4 with 1mol% Y_2O_3 and Nd_2O_3.

RESULTS AND DISCUSSION

Figure 1 shows a bright field image of Si_3N_4 ceramics after plasma etching. Dark thin area represents a grain boundary. Si_3N_4 matrix grains were present adjacent to the grain boundary before the etching. After the etching, Si_3N_4 is removed from the TEM sample and grain boundary phases remained as a honey-comb structure. The thicknesses of the grain boundary phases are about 1nm which is comparable to that before the plasma etching. It is clear that the plasma reacted with Si_3N_4 selectively and had little effect to the grain boundary phases. The etching rate of SiO_2 in CF_4+O_2 plasma is reported to be less than a tenth of that of Si_3N_4 [3,4]. Since the grain boundary phases in Si_3N_4 contain high amount of SiO_2, the grain boundary phases remained after the plasma etching.

Brighter area outside of the grain boundary phase is identified as pure carbon and concentration of nitrogen was smaller than the detection limit in this area. It confirms the fact that Si_3N_4 grains are completely removed from the grain boundary phase. Thus, X-ray intensity taken from this sample does not contain information from the Si_3N_4 matrix and reflects the chemical composition of the grain boundary triple points.

Figure 2 shows results of analysis in chemical composition in a grain boundary triple point. Content of Si shows maximum value of 57% at the corner of the triple point. Si content decreases gradually as the electron probe going into the center of the triple point. On the other hand, content of Nd increases from the corner to the center. The present experiment reveals that SiO_2 content is higher in the area where is close to the Si_3N_4. The condensation of SiO_2 is reflected by the fact that Si_3N_4 powder was originally covered by a thin layer of SiO_2 before sintering.

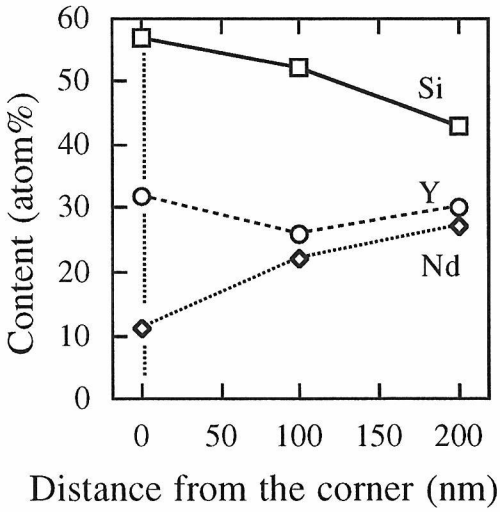

Fig.2 Change in chemical composition of grain boundary tripple point.

REFERENCES

1. M. Cinibulk, G. Thomas and S. M. Johnson, J. Am. Ceram. Soc., **73**, 1606-12 (1990)
2. D. A. Bonnell, T. Y. Tien and M. Ruhle, J. Am. Ceram. Soc., **70**, 460-65 (1987)
3. P. E. Riley and D. A. Hanson, J. Vac. Sci Technol., **B7**, 1352-56 (1989)
4. H. Suematsu, M. Mitomo and Y. Bando, J. Electron Microscopy, submitted.

Crystal Structures and Planar Defects of $LnBa_2Cu_4O_8$ Superconductors (Ln:Sm, Gd, Ho, Er) Examined by High-Resolution Electron Microscopy

Kasumi Yanagisawa, Fijio Izumi[a], Takayuki Miyatake and Yoshio Matsui[a]
Kobe Steel Ltd., 1-5-5 Takatsukadai, Nishi-ku, Kobe 651-22, Japan
[a]National Institute for Research in Inorganic Materials,1-1 Namiki, Tsukuba 305, Japan

Crystal structure of Ln-containing 1-2-4 type of superconductors, $LnBa_2Cu_4O_8$ in which Ln = Sm, Gd, Ho and Er, are examined by electron diffraction and high-resolution transmission electron microscope (HRTEM) measurements. Crystals containing Ln with large ionic radii, such as Sm and Gd, include planar defects due to intergrowth of 1-2-3 units. On the other hand, for Ho-and Er-specimens, no defects are observed in the 1-2-4 structure.

INTRODUCTION

Crystal structure of $YBa_2Cu_4O_8$ (1-2-4 phase) can be described as an alternate stacking of a $(CuO)_2$ double chain layer and a perovskite like component along the *c*-axis[1], as shown in Fig.1. Ln-containing 1-2-4 type of superconductors, $LnBa_2Cu_4O_8$, are isolated so far and it is reported that T_c's decrease as increasing of ionic radii for Ln[2-4]. In the present study, crystal structures of $LnBa_2Cu_4O_8$, where Ln = Sm, Gd, Ho and Er, are examined by means of electron diffraction and high-resolution transmission electron microscope measurements.

EXPERIMENTAL

Samples were prepared by solid state reactions under high oxygen pressure. Mixtures of Ln_2O_3, $BaCO_3$ and CuO with metal ratios Ln : Ba : Cu = 1 : 2 : 4, where Ln = Sm, Gd, Ho and Er, were calcined at 900 °C in flowing oxygen with intermediate grinding. After pressing into pellets, they are heated at 1000 to 1100 °C in a gas environment of argon with 20% oxygen by using an O_2-HIP apparatus. For TEM experiments, the obtained pellets were crushed in CCl_4 in an agate mortar. The crystal fragments are then mounted on carbon microgrids. Electron diffraction and high-resolution transmission electroscope measurements were made by a JEM 2000-EX machine operated at 200 kV.

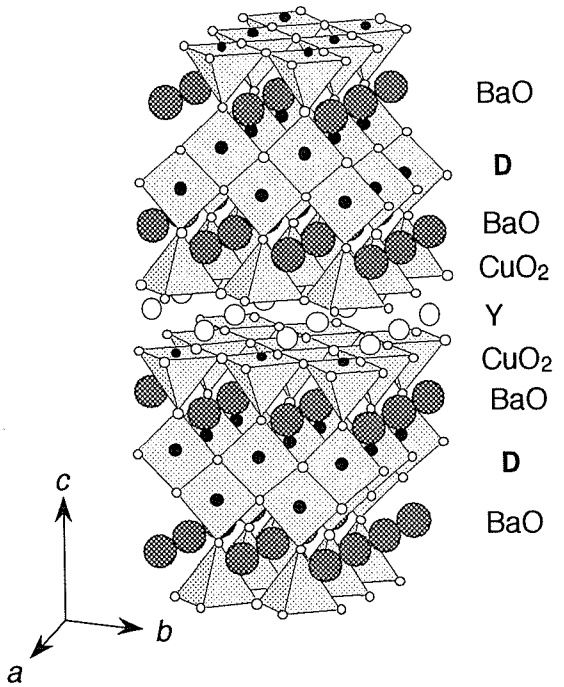

Figure 1. Crystal structure of 1-2-4 phase, after Karpinski *et al* [1]. The $(CuO)_2$ double chain layers are indicated with letter D.

RESULTS

A set of diffraction patterns of $LnBa_2Cu_4O_8$ is shown in Fig.2. Although electron diffraction spots of crystals containing Ln with large ionic radii, such as Sm and Gd, are indexed by the orthorhombic structure of 1-2-4 phase, weak streaks along the c^*-direction are observed in the patterns, suggesting an existence of defects stacking in the c-direction. A HRTEM image from a defective region of Sm-specimen is shown in Fig.3. The $(CuO)_2$ double chain layers projected along the b-direction are imaged as strong bright lines, as shown with letter D. Among the double chain layers, intergrowth of 1-2-3 units with single layers is observed, as indicated with letter S. On the other hand, for Ho- and Er-specimens, all of the reflections are indexed by the 1-2-4 structure and no streaks are observed in the diffraction patterns in Fig.2. Also in the corresponding HRTEM images, no defects are observed in the 1-2-4 structure.

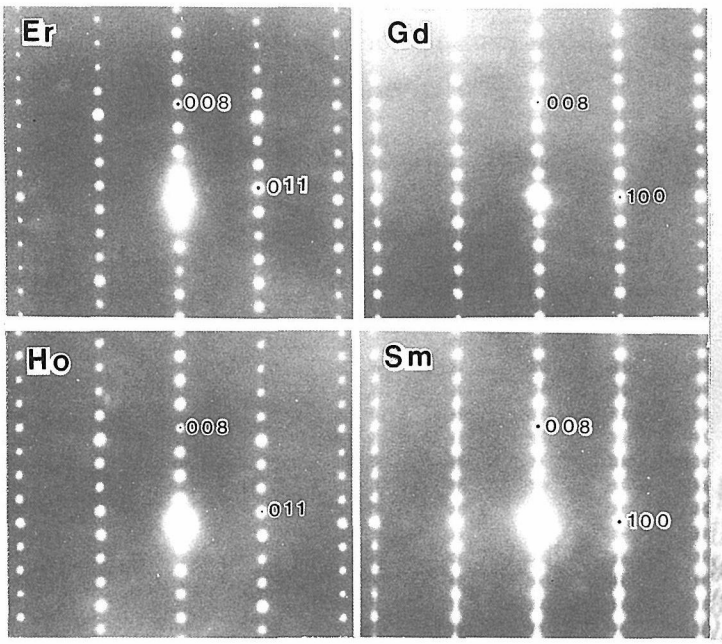

Figure 2. A set of electron diffraction patterns of $LnBa_2Cu_4O_8$: Ln = Sm, Gd, Ho, Er. Weak streaks in the c^*-direction are observed for Sm- and Gd-specimens.

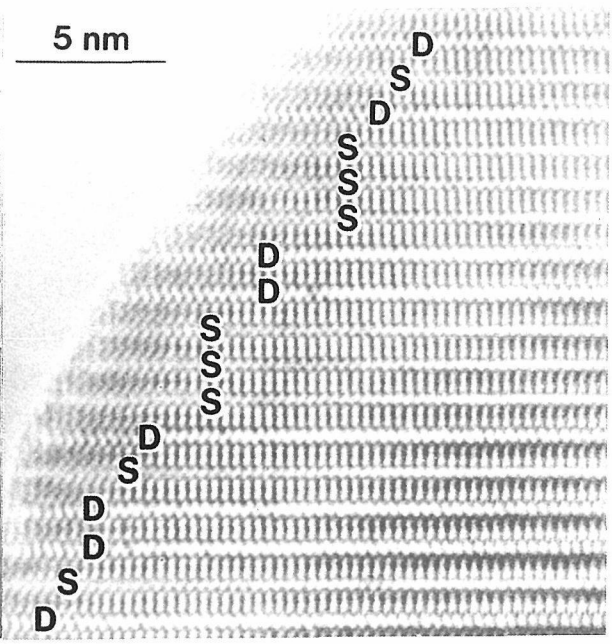

Figure 3. HRTEM image from a defective region of Sm-specimen. The symbol D stands for a $(CuO)_2$ double chain layer. CuO_X single layers are observed, as indicated with S.

Acknowledgment

The authors would like to thank Y. Kitami of NIRIM for his experimental supports.

REFERENCES

1. J. Karpinski, E. Kaldis, E. Jilek, S. Rusiecki and B. Bucher, Nature 336 (1988) 69.
2. D. E. Morris, J. H. Nickel, J. Y. T. Wei, N. G. Asmar, J. S. Scott, U. M. Scheven, C. T. Hultgren, A. G. Markelz, J. E. Post, P. J. Heaney, D. R. Veblen and R. M. Hazen, Phys. Rev. B 39 (1989) 7347.
3. T. Miyatake, M. Kosuge, T. Wada, Y. Yaegashi, H. Yamauchi and N. Koshizuka, Extended Abstract ISS '92 Kobe.
4. K. Mori, Y. Kawaguchi, T. Ishigaki, S. Katano, S. Funahashi and Y. Hamaguchi, Physica C 219 (1994) 176.

TEM Characterization of Ceramic Coatings Deposited by Spraying

K. Kuroda, T. Takeuchi and H. Saka
Department of Quantum Engineering and Department of Materials Science and Engineering, Nagoya University, Nagoya 464-01, Japan

Abstract

Microstructural and microchemical characterization has been carried out on plasma-sprayed oxide coatings by means of analytical transmission electron microscopy. Plasma-sprayed oxides exhibit characteristic microstructures formed by rapid solidification. Amorphous and/or metastable phases are freqently retained in the coatings. Thermal stability of the metastable phases has also been studied.

Introduction

Plasma spraying is a versatile coating technique which satisfies the demand of new materials needed to work in severe environments. Plasma-sprayed oxide coatings produce excellent properties of thermal barrier, wear resistance and corrosion resistance. Plasma spraying is well accepted technological process, however only a few careful studies [1-3] have been done on the microstrucrural characterization with transmission electron microscopy (TEM).

Physical and mechanical properties are influenced by the microstructure of sprayed oxides. Plasma spraying yields charastaristic microstructures obtained by rapid solidification. Thus metastable phases are often retained in the coatings. Thermal stability of the metastable phases is of interest both from metallographic and practical points of view. In this paper we present microstructural aspects of plasma-sprayed oxides of both as-sprayed and annealed at high temperatures.

Experimental

Commercially prepared mullite ($3Al_2O_3 \cdot 2SiO_2$), forsterite ($2MgO \cdot SiO_2$) and alumina-zirconia (71.6wt%Al_2O_3-25.7wt%ZrO_2-2.5wt%TiO_2) powders were used as the starting material for ceramic coatings. Plasma spraying was carried out by a Meteco 7MB type torch with spraying parameter reported previously [2]. Nitrogen gas was used as a plasma-forming gas. The ceramic coatings were deposited by plasma spraying onto SUS 304 stainless steel substrates and mechanically removed from the substrate. Some coatings were annealed at 1373K for 2h.

X-ray diffractometry was carried out to identify phases in coatngs. Thin foils for TEM studies were prepared from the coatings by cutting them into 3mm disks, mechanical polishing from the substrate side and argon ion milling to perforation. Analytical TEM was mostly done with a Hitachi H-800 equipped with a Kevex Delta 3 energy dispersive X-ray (EDX) analyzer.

Results and Discussion

a) Mullite

The as-sprayed mullite coatings consist mostly of crystalline and amorphous mullite phases. A typical microstructure is shown in Fig. 1(a). EDX spectra in Fig. 1(b) and (c) were taken from the regions A and B marked in Fig. 1(a), respectively. Both phases are identified as an alumina-rich mullite. Selected area diffraction patterns (SADP's) from crystalline mullite often show superlattice reflections due to ordering of oxygen vacancy,

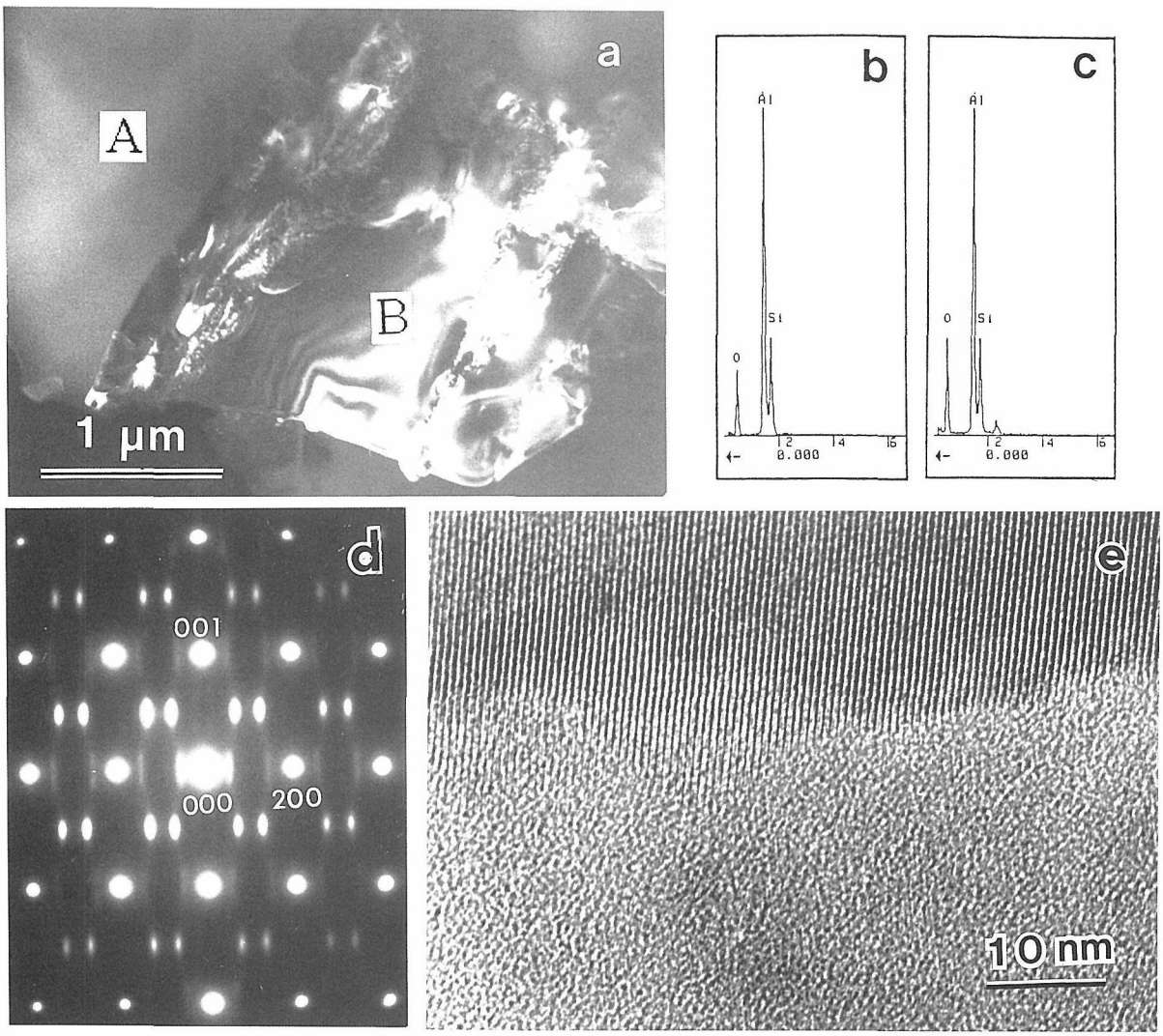

Fig. 1 Microstructure of mullite coating showing amorphous (A) and crystalline (B) phases (a). EDX spectra (b) and (c) taken from regions A and B in (a), respectively. SADP from crystalline mullite (d). High resolution image of amorphous–crystal interface (e).

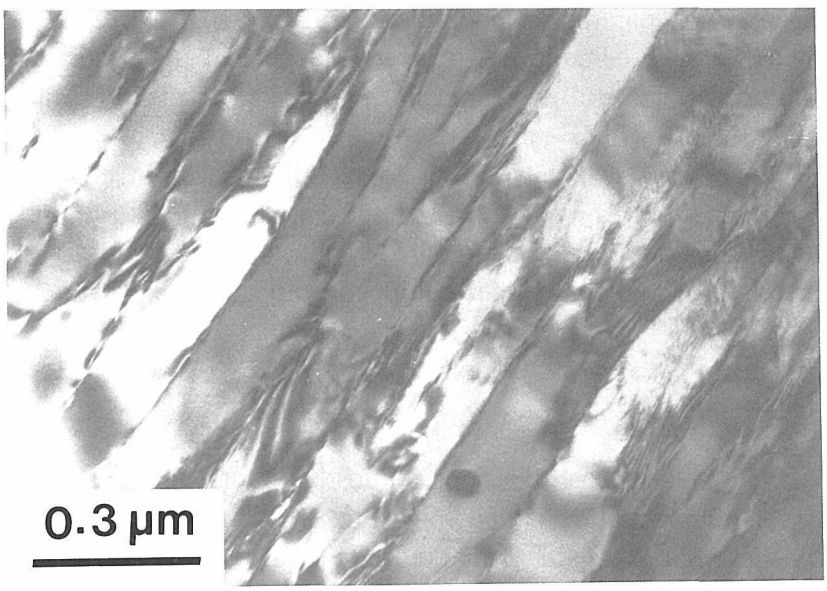

Fig. 2 Microstructure of mullite coating annealed at 1373K, showing many grain boundaries.

as shown in Fig. 1(d).

Mullite solid solution can be represented by the formula $Al_{4+2x}Si_{2-2x}O_{10-x}$, where x is the number of oxgen ions missing per unit cell. The splitting distance of superlattice reflections, s, was measured as a function of x by Cameron [4]. The value of s measured in Fig. 1(d) gives x=0.44 according to the Cameron's s-x diagram. This is in good agreement with x=0.43 determined by EDX analysis.

The high resolution image of an amorphous-crystal interface shown in Fig. 1(e) indicates that the interface is not faceted by the specific crystallographic plane. Faint lattice fringes are observed at some regions in the amorphous phase.

The crystallization of amorphous mullite takes place rapidly at 1243K. Fig. 2 shows the microstructure of the mullite coating annealed at 1373K for 2h. Fine domains devided by low angle grain boundaries seem to be twins. The X-ray diffraction pattern of this specimen indicated the lack of the 120/210 reflection pair. Pseudotetragonal symmetry of the phase is believed due to twinning and/or domain formation in orthorhombic mullite [5].

b) Forsterite

The as-sprayed forsterite coatings consist of clinoenstetite ($MgO \cdot SiO_2$) crystal and amorphous phases. The loss of MgO seems to take place during plasma spraying. The amorphous regions were generally observed to be larger than the crystalline phase. In crystalline phase, a twinning structure was observed.

The crystallization of the amorphous phase in the coatings occured at 1148K.

c) Alumina-zirconia

Fig. 3 shows a typical microstructure of the as-sprayed alumina-zirconia coatings. The coexistence of the amorphous and crystalline regions is again observed, but these two phases has different composition in contrast with mullite and forsterite coatings. The crystalline phase is idenfied as a γ -Al_2O_3 having a trace of Zr. Microchemical analysis indicates that the amorphous phase is the eutectic composition.

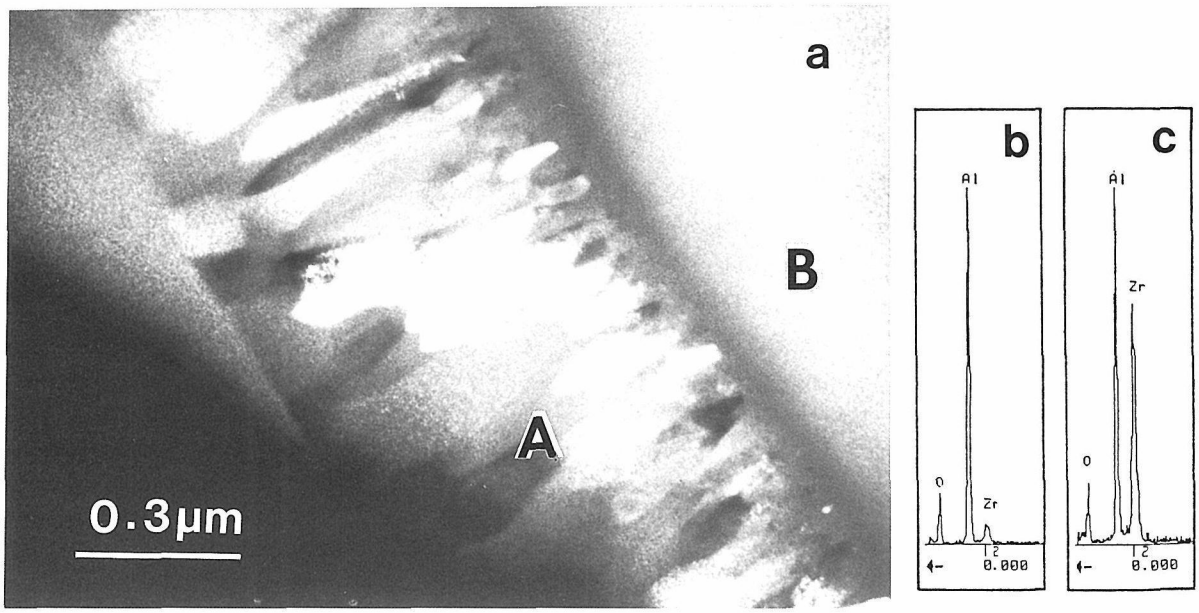

Fig. 3 Microstructure of alunina-zirconia coating showing crystalline (A) and amorphous (B) phases (a). EDX spectra (b) and (c) taken from regions A and and B in (a), respectively.

The amorphous phase in the coating crystallizes at 1213K. The microstructure of the alumina–zirconia coating annealed at 1373K for 2h, shown in Fig. 4, consists of small particles of tetragonal zirconia in the alumina matrix. It is possible to create a mesoscopic structure which has small zirconia particles disperced in the fine grained alumia by controlling the condition of heat treatment.

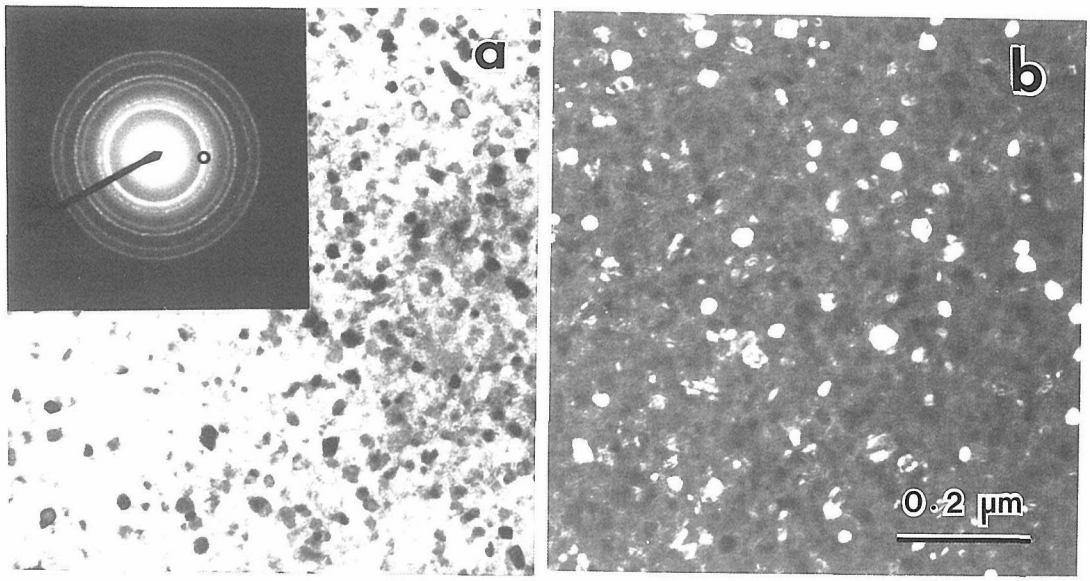

Fig. 4 Microstructure of alumina–zirconia coating annealed at 1373K for 2h. Bright field (a) and dark field micrograph (b) taken with zirconia reflection, showing fine grained zirconia and alumina.

Acknowledgements

The authors are grateful to Messrs Y. Kurisu and M. Amano of Nippon Steel Corporation for their cooperation. This work has partly been supported by a Grant–In–Aid for General Scientific Research No.02650516 from the Ministry of Education, Science and Culture.

References

[1]V. Wilms and H. Herman: Thin Solid Films, 39(1976), 251.
[2]K. Kuroda, S. Hanagiri, M. Suginoshita, H. Taira, S. Tamura, H. Saka and T. Imura: ISIJ International, 29(1989), 234.
[3]H. G. Wang, Y.M. Zhu and H. Herman: J. Mater. Sci., 24(1989), 4414.
[4]W. E. Cameron: Am. Mineral., 62(1977), 747.
[5]H. Schneider and T. Rymon–Lipinski: J. Am. Ceram. Soc., 71(1988), C162.

Characterization of Sol-Gel Derived Epitaxial $LiNbO_3$ Films

Kazuya Terabe, Yoshio Matsui, Nobuo Iyi, Kenji Kitamura and Shigeyuki Kimura
National Institute for Research in Inorganic Materials (NIRIM)
1-1 Namiki, Tsukuba-shi, Ibaraki 305, Japan

Abstract Sol-gel derived epitaxial $LiNbO_3$ films were obtained on sapphire, $LiTaO_3$ and 5% MgO doped $LiNbO_3$ substrates. When using the $LiTaO_3$ and 5% MgO doped $LiNbO_3$ substrates, with less lattice misfit, the crystallinity of the formed $LiNbO_3$ films approached that of the single crystal. Mismatch dislocations, twins and micro-pores were observed by high resolution transmission electron microscopy (HRTEM).

Introduction Lithium niobate ($LiNbO_3$) films have attracted considerable interest because of their usefulness as integrated electro-optical devices. Epitaxial films have been grown by liquid phase epitaxy (LPE), sputtering, molecular beam epitaxy (MBE) and metal-organic chemical vapor deposition (MOCVD). Recently, the sol-gel method, using metal alkoxides as raw materials, has become of major interest[1-3]. The many advantages of the sol-gel method include composition control at the molecular level, high productivity and low-temperature processing.

In the present study, epitaxial $LiNbO_3$ films were synthesized by the sol-gel method. The formed films were characterized, and the possibility of fabricating good quality epitaxial films was discussed.

Experimental Procedure Lithium ethoxide ($LiOC_2H_5$) and niobium pentaethoxide ($Nb(OC_2H_5)_5$) were used as raw materials. Equal molar amounts of the alkoxides were dissolved in absolute ethanol to give the 0.3M% mixed alkoxide solution. The solution was refluxed for 24 hrs under nitrogen atmosphere to synthesize a double metal alkoxide ($LiNb(OC_2H_5)_6$)[1,4]. The double metal alkoxide solution were spin coated on substrates at 2000 rpm under nitrogen atmosphere. Single crystals of (0001)-sapphire, (0001)-$LiTaO_3$ and (0001)-5% MgO doped $LiNbO_3$ were used as the substrates. These three substrates have crystal structures similar to that of $LiNbO_3$ films, but have a variety of lattice constants. The coated precursor films were heated to 250 or 500 °C for 30 min at the heating rate of 5 °C/min in an atmosphere of oxygen and water vapor. Then, the furnace was cooled to room temperature. The resulting films on these substrates were characterized by X-ray rocking curve measurement, atomic force microscopy (AFM) and HRTEM, etc.

Results and Discussion The smooth and dense textures of the prepared films, after heat-treatment at 500 °C, were observed on all substrates by SEM and AFM[3]. The AFM measurement indicated that the average roughness was 4.45 nm for the film on 5% MgO doped $LiNbO_3$. X-ray diffraction measurements revealed that the films on all substrates, after heat-treatment at 500 °C, showed a highly preferred orientation along the substrate orientation. The full-width values at half maximum of the x-ray rocking curve for the resulting films decrease with decreasing lattice mismatch. The value for the film on 5% MgO doped $LiNbO_3$, with the least lattice mismatch, approached that of a single crystal.

Figure 1 and 2 show HRTEM cross-sectional images of films on the sapphire substrate, with large lattice mismatch, after heat-treatment at 250 and 500 °C, respectively. The amorphous film, after heat-treatment at 250 °C, appeared to be firmly combined with the substrate. The crystallized film, after heat-treatment at 500 °C, showed the HRTEM image corresponding to lattice planes running continuously across the interface, it confirms that $LiNbO_3$ films grow epitaxialy on sapphire. However, twins, mismatch dislocations and Micro-pores of diameter about 0.5 nm were also observed. The pores seem to be formed by the removal of residual alkyls. On the other hand, the defects such as the twins and the dislocation were not observed for the films on 5% MgO doped $LiNbO_3$ with less lattice misfit.

In conclusion, our results suggest that better quality $LiNbO_3$ films can be prepared by the sol-gel method if substrates with a smaller lattice mismatch than sapphire, such as 5% MgO doped $LiNbO_3$ or $LiTaO_3$, are used.

Acknowledgement We would like to thank Dr. I. Sakaguchi for SIMS measurement and also Mr. Y. Kitami, Dr. H. Suematsu and Mr. K. Kurashima for TEM observation at National Institute for Research in Inorganic Materials.

Reference

(1) S. Hirano and K. Kato, Adv. Ceram. Mater., Vol. 3, p. 503, 1988
(2) K. Nashimoto and M. J. Chima, Mater. Lett., Vol. 10, p.348, 1991
(3) K. Terabe, N. Iyi, K. Kitamura and S. Kimura, J. Mater. Res., *submitted*
(4) K. Terabe, N. Iyi and S. Kimura, J. Mater. Sci., *in press*

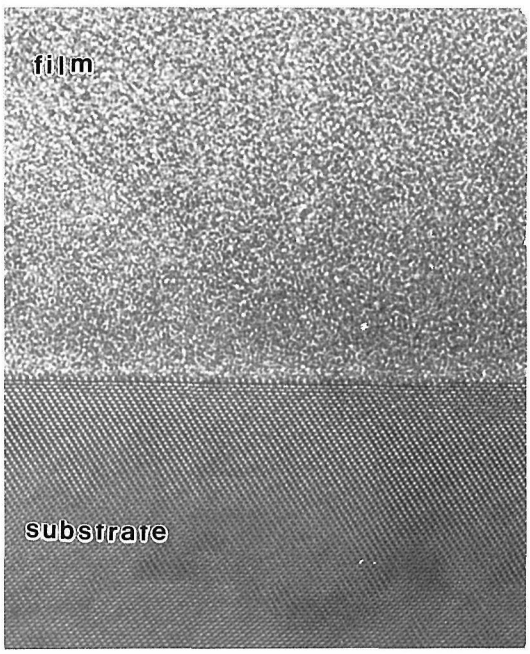

Fig.1 Cross-sectional images of films prepared at 250 °C on sapphire.

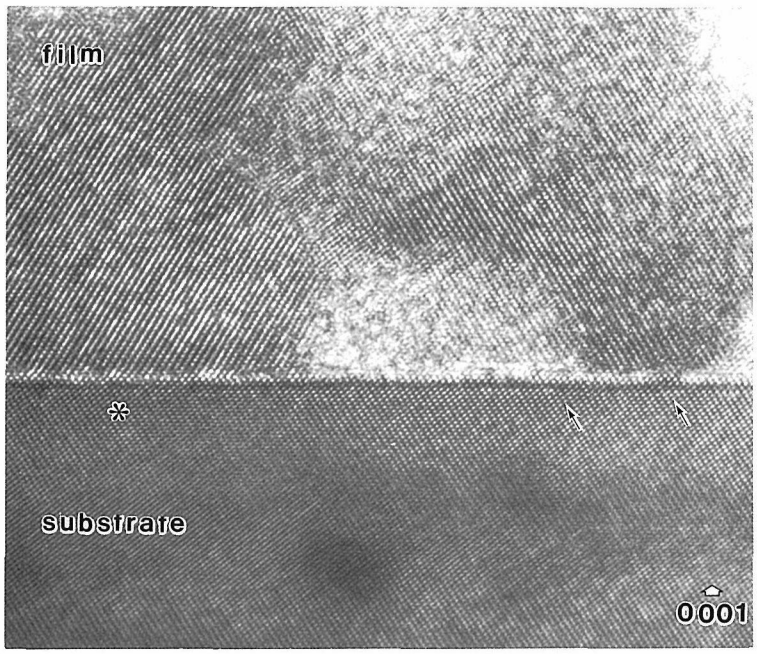

Fig.2 Cross-sectional images of films prepared at 500 °C on sapphire. Symbol (*) and arrows show the twins and mismatch dislocations, respectively.

HREM Study on the $Sr_{1-x}Ca_xCuO_2$ System

J. Ramírez[1,2], M. Vallet-Regí[3], S. Nicolopoulos[4], Y. Matsui[2] and J.M. González-Calbet[1]

[1)]Dpto. Q. Inorgánica, Facultad CC. Químicas, Universidad Complutense, 28040-Madrid, Spain

[2)]National Institute for Research in Inorganic Materials, Tsukuba, Ibaraki 305, Japan

[3)]Dpto. Q. Inorgánica y Bioinorgánica, Facultad de Farmacia, Universidad Complutense, 28040-Madrid, Spain

[4)]Centro de Microscopía Electrónica, Universidad Complutense, 28040-Madrid, Spain

ABSTRACTS

$Sr_{1-x}Ca_xCuO_2$ ($0 \leq x \leq 0.8$) phases with an oxygen-deficient perovskite-related structure were prepared by the nitrates decomposition method. We found that for $0 \leq x < 0.4$ compositional range, the *$SrCuO_2$-type* structure is conserved. On the other hand, for $0.4 \leq x \leq 0.5$ values a new double cell is observed by X-ray and electron diffraction and a possible structural model is proposed. For higher x values a phases mixture is formed. The physical properties were studied.

INTRODUCTION

Oxygen-deficient perovskite structural block seems to be responsible for the superconducting properties in many high T_c superconducting materials. For this reason, phases in the *M*-Cu-O system (*M*=Y, Ba, Sr, Ca, ...) are at the center of interest. Many researchers have synthetized phases in this system using diferent chemical compositions, preparation methods and atmospheres (1-9). However, superconducting phases in this system are only obtained using high-pressure methods (10-14).

In this work, we report the synthesis under ambient pressure, structural characterization and physical properties of $Sr_{1-x}Ca_xCuO_2$ phases.

EXPERIMENTAL

Samples with nominal compositions $Sr_{1-x}Ca_xCuO_2$ ($0 \leq x \leq 08$) were prepared dissolving stoichometric mixtures of starting materials ($SrCO_3$, $CaCO_3$ and CuO) in hot concentrated nitric acid. The resulting solution was slowly dried, until a blue-green solid appeared. The residue so obtained was decomposed increasing temperature from 400 °C until 800 °C, for 12 h. The resulting oxides mixture was treated, after grinding, at 950 °C for 96 h, in air.

The homogeneous black powders were characterized by X-ray diffraction (XRD) using a Siemens D-5000 diffractometer with a graphite monochromator and $Cu_{(k\alpha)}$ radiation. Selected area electron diffraction (SAED) and high resolution electron microscopy (HREM) were carried out on a JEOL 4000-EX.

The final composition of obtained materials was determined by inductive coupled plasma spectroscopy (ICP). In order to confirm these data a X-ray dispersive energy analysis (XEDS) was performed. The oxygen content was analyzed by volumetric analysis. DC electrical resistivity was measured by the standard four-probe technique and DC magnetic susceptibility was measured using a SQUID magnetometer with applied field of 10 Oe.

RESULTS AND DISCUSSION

ICP analysis show that the average cation ratio in the obtained samples are almost identical of those of the nominal compositions, as confirmed by XEDS showing a homogeneous Ca distribution in all crystals. The presence of Cu(III) was not detected by volumetric analysis.

Powder XRD patterns show that single phases are obtained in the $0 \leq x \leq 0.5$ compositional range. For $0 \leq x < 0.4$ samples, all diffraction maxima can be indexed on the basis of orthorrombic symmetry and space group Amam characteristic of the *$SrCuO_2$-type* structure (15). From these data, it can be seen that such unit cell parameters (listed in Table I) decrease as the amount of Ca increases. This may be attributed to the

smaller ionic size of Ca^{2+} with respect to Sr^{2+} ($^{VIII}r_{Sr(II)}$=1.26A, $^{VIII}r_{Ca(II)}$=1.12A) (16). On the other hand, in the $0.4 \leq x \leq 0.5$ compostional range a significant variation of the relative intensity of some XRD reflections, as well as a splitting of maxima at high 2θ values can be observed. For x values higher than 0.6 phase mixtures are obtained.

Table I. Unit cell parameters for $Sr_{1-x}Ca_xCuO_2$ samples ($0 \leq x < 0.4$).

Composition (x)	Reticular parameters a (A)	b (A)	c (A)	V (A^3)
0	3.906(2)	16.307(8)	3.564(1)	227.0(1)
0.1	3.898(1)	16.286(2)	3.552(1)	225.5(3)
0.2	3.893(1)	16.252(6)	3.521(1)	222.8(1)
0.3	3.886(2)	16.201(3)	3.493(1)	219.9(3)

A SAED and HREM study performed in this system indicates that Ca-doped samples in the $0 \leq x < 0.4$ range show the same situation as observed in $SrCuO_2$. However, for both x=0.4 and 0.5 samples a more complex microstructural situation was found, as expected from XRD patterns. Fig. 1a shows the SAED pattern along $[100]_o$ (o subindex is refered to the orthorrombic $SrCuO_2$ subcell) for x=0.5 sample. It can be observed that c* reciprocal direction of the basic cell is doubled. In a first aproximation, it can believed that this material has a unit cell with one doubled parameter, at least.

Fig. 1b shows the SAED pattern along $[10\bar{1}]_o$ obtained by tilting around b* axis. The $(1/2\ 1\ 1/2)_o$ and equivalent reflections show that both a* and c* are doubled.

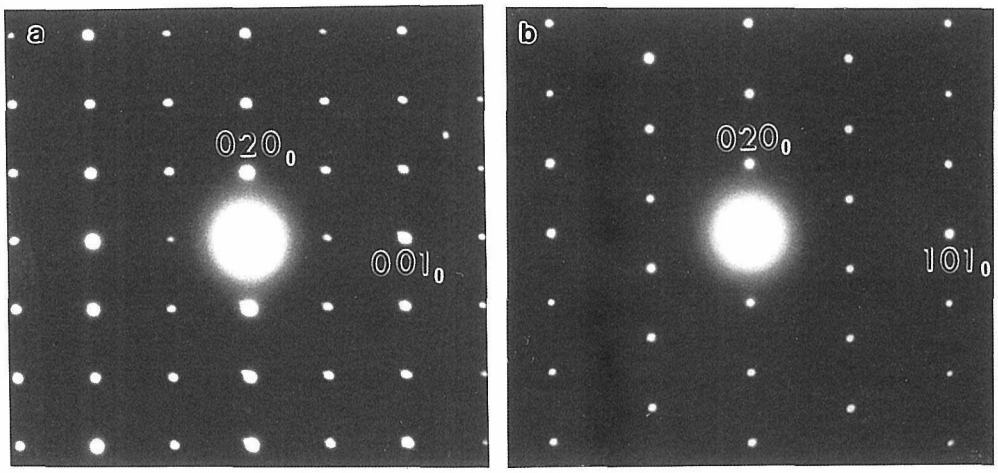

Fig. 1. SAED patterns corresponding to $Sr_{0.5}Ca_{0.5}CuO_2$ sample along (a) $[100]_o$ zone and (b) $[10\bar{1}]_o$ zone.

Fig. 2a shows the SAED pattern along $[10\bar{2}]_o$ confirms that c* is doubled. Fig. 2b shows the SAED pattern along $[10\bar{3}]_o$ direction, it can be observed that superstructure maxima appears at $(3/2\ 2\ 1/2)_o$, confirming that both a* and c* are doubled.

At this point, it is worth mentioning that chemical analysis confirmed the absence of Cu(III) indicating an average oxygen content per unit formula close to 2. Then, we can conlude that oxygen vacancies are not responsible for such as new cell.

On the basis of this information and taken into account the chemical composition, $Sr_{0.5}Ca_{0.5}CuO_2$, it seems that some kind of ordering between Ca and Sr atoms must exist in order to obtain a unit cell with $2a_o x b_o x 2c_o$ cell parameters.

Fig. 3a shows the HREM image of a well-ordered crystal corresponding to ED pattern along $[100]_o$ (shown in the inset). However, no different contrast can be observed in the Ca and Sr positions, as a result of the ordering of both cations.

In order to check this point, which means if it is possible to distinguish the contrast between both cations in the HREM image in this projection, an image calculation (fig. 3b) was performed using the multislice method (17), considering the 50% ordered +Sr-substitution by Ca in the Sr atomic positions in the basic unit cell, under the following conditions: sample thickness t=40 nm and focus Δf=-80 nm. On the other hand, this image calculation was also performed considering this substitution with any ordering between both cations.

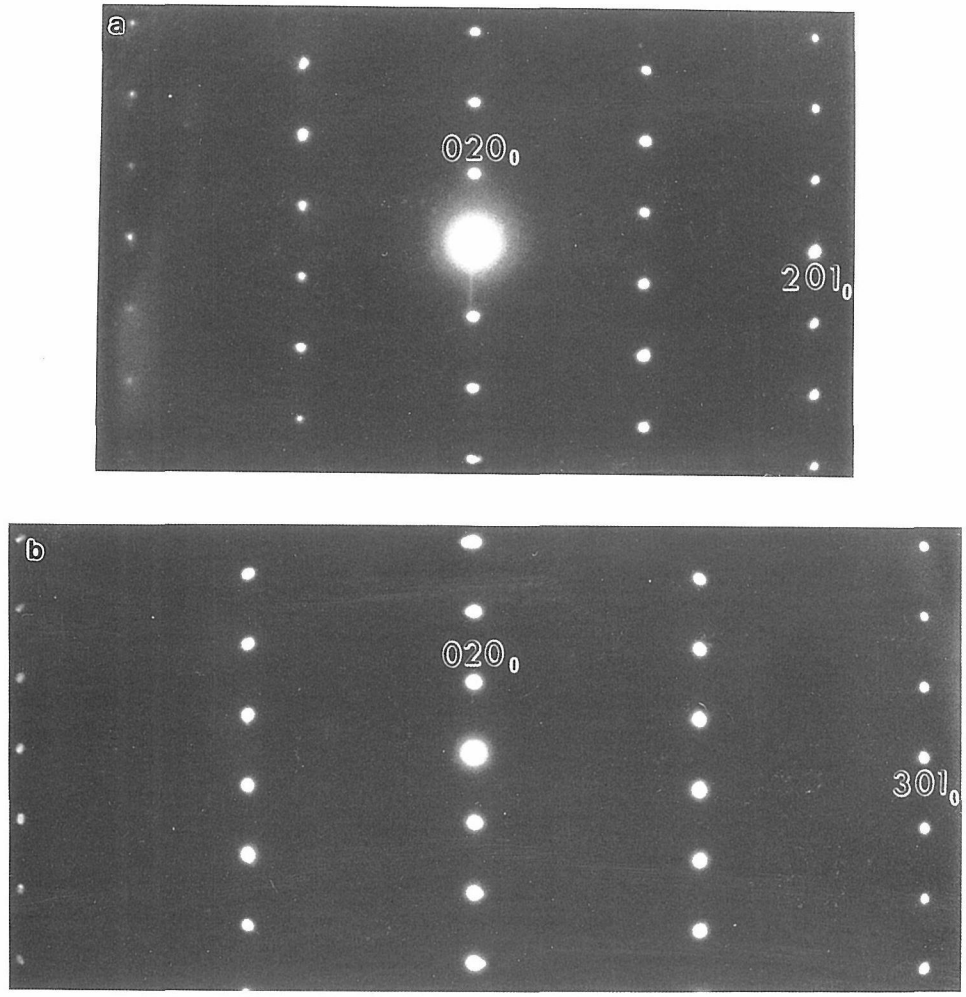

Fig. 2. SAED patterns of x=0.5 sample along (a) $[10\bar{2}]_0$ zone and (b) $[10\bar{3}]_0$ zone.

In both cases, identical calculated images were obtained and it was not possible to detect any variation in the contrast, in agreement with the experimental HREM image. This may be attributed to the very close scattering factors of both Sr and Ca cations. A study by means of *neutron diffraction* seems to be necessary in order to confirm this proposed structural model.

On the other hand, we have studied physical properties on these samples. The dc electrical resistivity measurements show a semiconductor-metal-semiconductor transition for $SrCuO_2$ material. However, for Ca-dopped samples a complex electrical behaviour is found, since between 300K and 150K the resistivity is slightly increased, after this temperature a small decreasing is observed, being abruptly increased at 120K. However, for x=0.5 sample the electrical resistance values are lower than those observed for the others samples. The dc magnetic susceptibility showed a similar paramagnetic behaviour for all samples. No diamagnetic evidence was found.

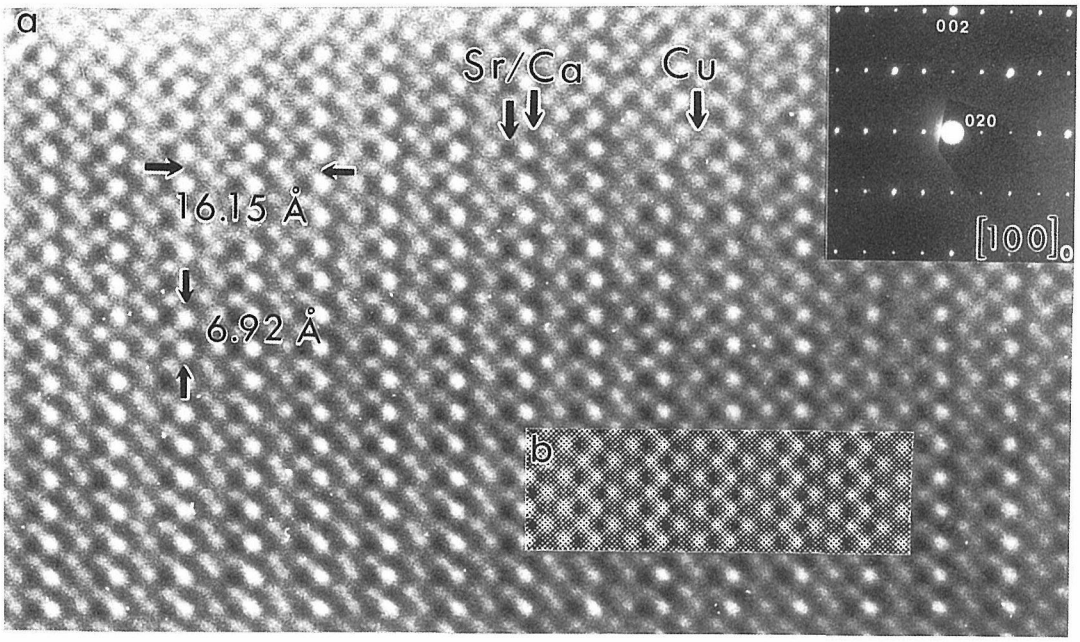

Figure 3. (a) HREM image corresponding to the SAED pattern along $[100]_o$ (shown in the inset). (b) Calculated image in the same projection.

From the above results, we can conclude that $Sr_{1-x}Ca_xCuO_2$ system conserves the *$SrCuO_2$-type* structure in the $0 \leq x < 0.4$ compositional range, with a lineal evolution of the reticular parameters. However, $0.4 \leq x \leq 0.5$ materials present a double unit cell, with related reticular parameters $\mathbf{a} \sim 2a_o$, $\mathbf{b} \sim b_o$ and $\mathbf{c} \sim 2c_o$, as a consequence of both Sr and Ca ordering in the structure. For higher x values a phases mixture is formed. On the other hand, a complex electrical behaviour is observed, however, the electrical resistivity is lower for x=0.5 sample, but zero electrical resistance and diamagnetic signal were not observed.

REFERENCES

(1) Siegrist, S.M.Zahurak, D.W.Murphy and R.S.Roth, Nature **334**, 231 (1988).
(2) R.S.Roth, C.J.Rawn, J.J.Ritter and B.P.Burton, J. Am. Ceram. Soc. **72**, 1545 (1989).
(3) H.Yamane, Y.Miyazaki and T.Hirai, J. Cer. Soc. Jpn. **97**, 143 (1989).
(4) T.Siegrist, Chem. Mat. **2**, 192 (1990).
(5) K.Kubo, M.Ichikawa, N.Sugii, K.Yamamoto and H.Yamauchi, Phys. Rev. **B49**, 6919 (1994).
(6) K.Kobayashi, Y.Ishihara, S.Matsushima and G.Okada, Jpn. J. Appl. Phys. **30**, L1931 (1991).
(7) K.Kobayashi, Y.Yshihara, S.Matsushima and G.Okada, Appl. Phys. Lett. **62**, 2868 (1992).
(8) X.Li, M.Kanai, T.Kawai and S.Kawai, Jpn. J. Appl. Phys. **31**, L217 (1992).
(9) K.Kobayashi, Y.Ishihara, S.Matsushima and G.Okada, J. Mat. Sci. **28**, 6699 (1993).
(10) A.Gupta, Physica C **231**, 389 (1994).
(11) M. Takano, Y.Takeda, H.Okada and K.Kusaka, Physica C **159**, 375 (1989).
(12) M.Takano, M.Azuma, Z.Hiroi, Y.Bando and Y.Takeda, Physica C **176**, 441 (1991).
(13) Z.Hiroi, M.Azuma, M.Takano and Y.Bando, J. Solid St. Chem. **95**, 230 (1991).
(14) Z.Hiroi, M.Takano, M.Azuma and Y.Takeda, Nature **356**, 775 (1992).
(15) C.L.Teske and H.Muller-Buschbaum, Z. Anorg. Allg. Chem. **379**, 234 (1970).
(16) R.D.Shannon, Acta Crystallogr. **A32**, 751 (1976).
(17) NCEMMS program, National Center for Electron Microscopy, Materials and Chemical Science Division, Lawrence Berkeley Laboratory, CA (1991).

Electrons from Intra- and Interatomic Auger Processes in Collisions of Slow Ions and Metastable Atoms with Surfaces

J. Günster, H. Müller, W. Maus-Friedrichs and V. Kempter
Physikalisches Institut der Technischen Universität Clausthal
Leibnizstr. 4, W 38678 Clausthal-Zellerfeld, Germany

ABSTRACT

In the Metastable and Ion Impact Electron Spectroscopies (MIES and IIES, respectively) the kinetic energies of the electrons ejected during the interactions of slow metastable atoms or slow ions with surfaces are analyzed. Both spectroscopies are only sensitive to the electronic structure of the outermost surface layer including species adsorbed on it.

A short introduction into the principles of both techniques is followed by specific examples dealing with (i) the growth on insulating adlayers (MIES), (ii) the charge transfer between C_{60} and Cs on Si(100) (MIES), (iii) the adsorption of polycyanurate films on Si(100) (MIES), and (iv) the dissociation of oxygen in O_2^+ - surface collisions (IIES).

1. Principle of the Ion and Metastable Impact Electron Spectroscopy (IIES and MIES)

Excited atoms (MIES) or slow ions (IIES) do strongly interact with surfaces when approaching them closer than about 10 a.u.. Depending in particular on the electronic structure, the surface density of states (SDOS) and the work function of the surface, resonant electron transfer between the projectile and the surface, either from (ions) or to (metastables) the surface can take place [1,2]. Besides this one-electron exchange process, various Auger processes can occur involving electrons from the surface [1,2]. As a consequence electrons can be ejected; their energy contains detailed information on the electronic structure of the surface as well as on the dynamics of the projectile-surface interaction. Common to both techniques is their extreme surface sensitivity: the projectiles do only interact with the tails of the wavefunctions of the surface atoms or with those of surface-adsorbed atomic and molecular species.

Metastable Impact Electron Spectroscopy (MIES):

On clean metals the excited electron (2s in the case of He^*) tunnels into an empty state of the surface by resonance ionization. The resulting He^+ ion is then neutralized by Auger capture: in this interatomic Auger process the neutralization energy is shared by two surface electrons, one of them eventually being ejected. The resulting energy spectrum of the emitted electrons is essentially a self-convolution of the SDOS. Consequently, deconvolution procedures are required to obtain information on the electronic structure of the surface.
For insulators and many adsorbate covered metal surfaces as well the resonance ionization of the metastable atom is inhibited; the atom is deexcited by Auger deexcitation (Surface Penning ionization). As in UPS only one surface electron is involved in this inter-atomic Auger process: the energy spectrum of the ejected electrons essentially images the SDOS.

Low-work function surfaces such as alkali-covered surfaces represent a special case. Here the work function of the alkalated surface becomes sufficiently low to allow for the resonant capture of an additional electron by the metastable. In the case of $He^*(1s2s)$ metastables this leads to the formation of the temporary negative ion $He^{-*}(1s2s\ ^2S)$ (Feshbach resonance) which decays via the intra-atomic Auger process, autodetachment, within about 10^{-14} s [3,4]. Electrons of about 19eV are ejected by the projectile producing a comparatively narrow (0.6eV wide) feature in the electron spectra. It was shown that for work functions below about 2.2eV this process greatly dominates over Auger deexcitation.

Ion Impact Electron Spectroscopy (IIES):

The same processes, resonant one-electron transfer and inter- and intra -atomic Auger processes occur between ions and surfaces. In the following we confine ourselves to low-energy collisions (<300eV) of singly charged ions under grazing incidence (<5degs) with respect to the surface. Other situations have been discussed in [5,6]. Under most conditions, in particular for metals, the ions are neutralized by Auger capture, and, as described above, the resulting spectrum is a self-convolution of the SDOS [1]. Binding energies of excited electrons in atoms are typically between 4.5 and 3eV. Therefore resonant capture of surface electrons by the ionic projectile occurs only at surfaces whose work function is below about 3.3eV. Once the formation of an excited atom has taken place in this way, the electron energy spectra, resulting from Auger deexcitation and autodetachment, will be rather similar to those produced by metastable atoms. The great advantage of IIES lies in the fact that a large variety of ions with widely differing ionization potentials can be employed. Also, when using molecular ions, the competition between Auger and dissociation processes can be studied (see section 2).

The interpretation of both IIES and MIES spectra has become considerably facilitated by the feasibility to simulate them in a semi-quantitative manner [7,8]. Briefly, a reaction scheme describing the sequence of processes during the interaction of the He^* with the adlayer must be selected. A set of coupled rate equations, one for the occupation number of each intermediate state involved in the collision process, must be solved during the projectile's path in the vicinity of the surface. Reasonable choices must be made for the rates describing the transitions between the involved states and their energies as a function of the projectile-surface distance. Energy spectra of the ejected electrons are obtained by correlating the transition rates calculated as a function of the distance from the surface with the transition energies at these distances [7,8].

The apparatus for IIES and MIES is the same as for UPS with the exception of different excitation sources:

- In MIES this is normally a source for the production of thermal metastable inert gas atoms [9,10] which, at the same time, is capable to produce a photon beam sufficiently intense for UPS [9].
- For IIES a slow, monoenergetic and mass analyzed ion beam must be used [11,12]. In order to avoid penetration of the ions into the surface as well as to avoid kinetic emission of electrons, the beam interacts with the surface under grazing incidence.

Both in IIES and MIES the electrons, ejected under normal emission, are energy analyzed in order to get information on the surface structure and on the dynamics of the collision process. The low-energy cutoff of the spectra gives direct information on the surface work function, in particular its change during the exposure to adsorbate atoms.

Summarizing, we can state that MIES appears to be ideally suited to study (i) the electronic structure of adsorbed molecules [10], (ii) layer growth on surfaces [13], (iii) cluster formation on surfaces, and (iv) catalytic reactions on surfaces [14]. On the other hand, IIES is well suited to study dynamic

processes at surfaces, such as electron exchange and its consequences (Auger processes) eventually in competition with collision induced dissociation [12,15].

2. Case Studies

2.1 The Growth of Insulating Layers (MIES)

The combination of MIES and UPS (HeI) was applied during the simultaneous supply of Al and O_2 to W(110) held at 725K (**Fig.1 (a)** and **(b)**) [13]. The bottom spectra are for the clean W(110) substrate:

- The UPS spectrum near the Fermi level E_F is dominated by W(5d) emission,
- The MIES spectrum is due to Auger capture involving He^+ formed in front of the surface by resonance ionization of the He^* metastable atoms.

Both the MIES and UPS spectra display a 7.5 eV wide structure whose maximum is located between E_B=6.5 and 7.5 eV depending on the exposure time. This structure is located in the region where the

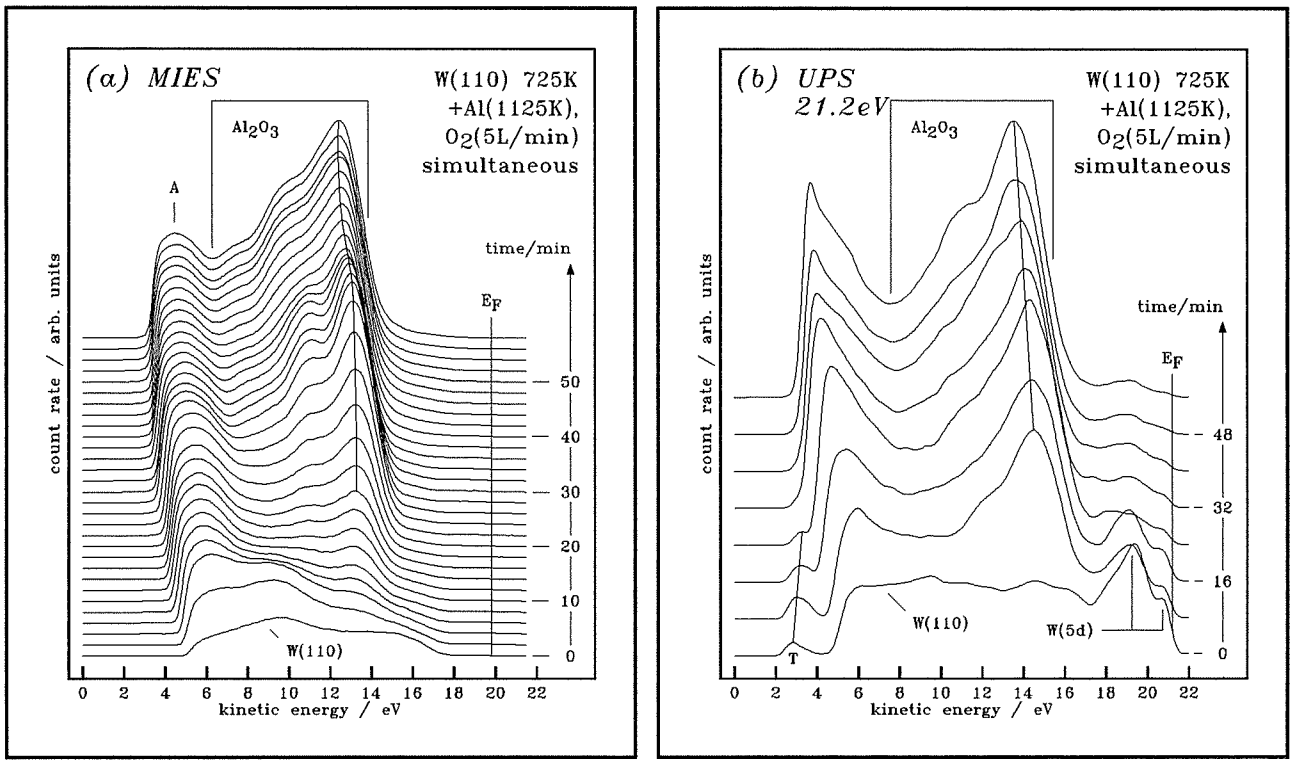

Fig.1: MIES (a) and UPS (b) spectra obtained during the coadsorption of Al (evaporation temperature 1150 K) and oxygen (5 L/min) onto W(110) held at 725 K [13]

O(2p) derived emission was observed during the sorption of oxygen on an Al adlayer. From the general similarity of the MIES and UPS spectra we conclude that in MIES this structure (Fig. 1(a)) is caused by the Auger Deexcitation process involving states from the selvedge of the adlayer. The UPS spectra of these films look rather similar to those characteristic for bulk alumina (for more details see ref.[13]).

There is very little emission between E_F and about 15 eV; this is compatible with the formation of an insulator surface having a bandgap of about 8.5 eV width (estimated under the assumption that E_F is located in the middle of the bandgap). There is in particular no indication for metallic Al in the toplayer (see also the AES results of ref.[13]): this would lead to emission in the MIES spectra similar to what is observed for Al adlayers and for the initial stage of oxygen sorption [13]. We conclude that the coadsorption of Al and oxygen on W(110) indeed leads to the formation of Al oxide layers.

We have confirmed above statements by simulating the top MIES spectrum of fig.1(a) in the way sketched in section 1. The SDOS of ref.[16] was employed. The comparison with the experimental results indeed indicates that the MIES emission between 10 and 15eV is caused mainly by the O(2p) orbital density. This does not necessarily mean that the surface is oxygen-terminated, but solely that the O(2p) wavefunction protrudes the farthest into the vacuum.

In a similar manner we have studied the growth of alkali halide layers on W(110) [17,18,19]. Our studies of the coadsorption of Cs and I atoms on W(110) [20] reveal that in the initial stage of the adsorption a mixed adlayer is formed where both Cs and I atoms are in direct contact with the substrate. The Cs bonds ionically to the metallic substrate while I forms a covalent bond with it. Only after the completion of the first passivating adlayer molecular growth of the adlayer id found. By using D^+ ion scattering Souda et al. [21] have arrived at the same conclusion for many other alkali halogen combinations

2.2 Electronic Structure of Clusters on Surfaces: C_{60}/Si(100) + Cs (MIES)

Fig.2 shows MIES and UPS spectra obtained during the deposition of C_{60} on Si(100) (bottom spectra). Several sharp C_{60} induced features are seen in the UPS spectra. They are due to the

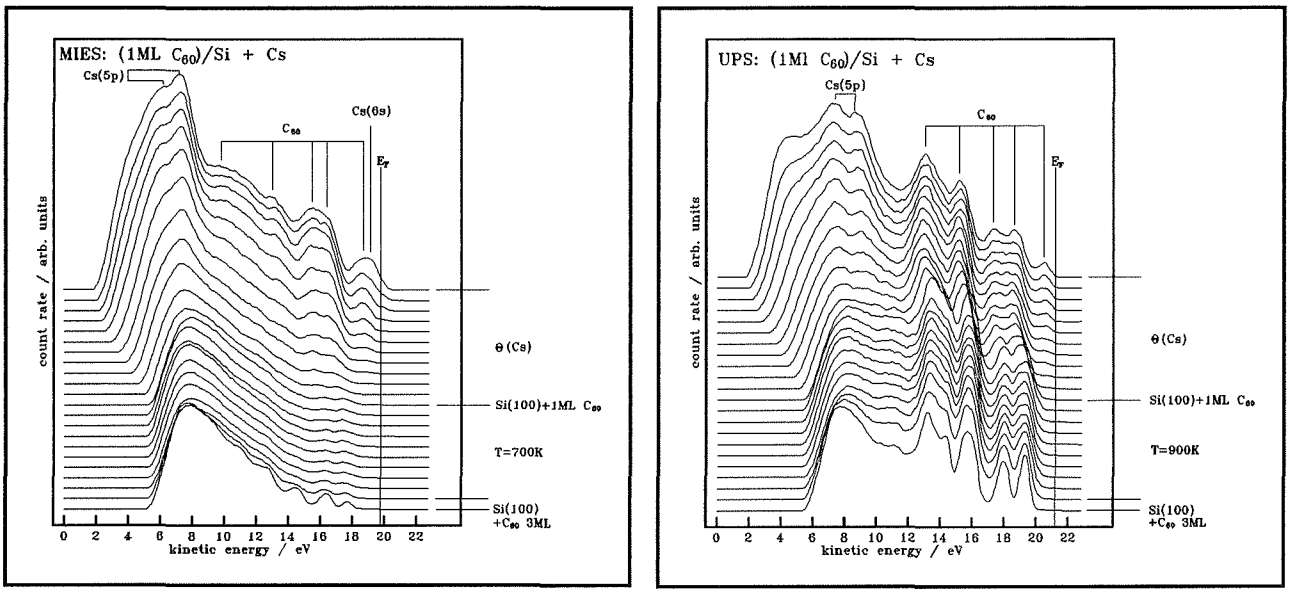

Fig.2: MIES (a) and UPS (b) spectra recorded during the exposure of a C_{60} film on Si(100) to cesium at room temperature. Bottom curve is for a C_{60} film on Si(100); the film is heated to 600 K (curve 10). Exposure to Cs starts with curve 11 [20].

photoionization of the highest occupied π-and σ-type MO's. Position and relative intensities of the

photoionization features agree well with those reported in ref. [22] for UPS (HeI) from C_{60} films (for a summary on photoemission studies on fullerenes see ref. [23]). The fullerite film is heated up to 600K. Only one adlayer remains on the substrate at this temperature (11th spectrum from the bottom) [24]. This C_{60} monolayer was exposed to Cs atoms. During the exposure the surface work function decreases from 5.5 to about 1.7eV (see change in the low-energy cutoff of the spectra).

During the exposure the two fine structure components from Cs5p ionization appear in the UPS spectra of **Fig.2 (b)**. Simultaneously with the work function decrease the C_{60} induced features shift by about 0.6 eV to larger binding energies, and t_{1u} (the former LUMO of C_{60} / binding energy 0.8 eV with respect to E_F) becomes gradually occupied starting at a work function of about 4.2 eV.

The following interpretation of the MIES spectra is based on simulations of spectra for C_{60}/Si(100) [24] along the lines given in section 1. The same sharp fullerite-induced features as in UPS are seen in the bottom spectrum for the C_{60} film on Si(100). These are attributed to Auger deexcitation involving one electron from surface-adsorbed C_{60} molecules. The underlying broad continuum is due to Auger capture involving two electrons from the C_{60} film. As in UPS emission from the ionization of Cs5p and the fullerene t_{1u} appears during the exposure to cesium. The population of t_{1u} is due to the transition of the Cs6s valence electron into the t_{1u} LUMO. Only after the saturation population of t_{1u} is reached, emission involving the Cs6s electron (labeled Cs(6s) in fig.2(a)) appears. This emission signals the presence of the 6s electron at the Cs core. Further exposure to cesium leads to a strong increase of the Cs(6s) feature (mainly due to autodetachment of He^{-*} involving the 6s electrons) similar to what is seen from s adsorption on Si(100) [25].

2.3 Adsorption of Polycyanurate films on Si(100) (MIES)

The fundamental understanding of the chemical and physical phenomena of the adhesion at substrate/polymer interfaces is of great importance to the control of adhesion problems. We have investigated thin films of the trimer of p-CPC on Si(100) with MIES [26]. The chemical structure of the trimer molecules is given in **Fig.3**. XPS studies [27] suggested that the adsorption of the first layer is governed by the interaction of the triazine rings with the substrate. **Fig.4** shows the comparison of MIES spectra of the p-CPC film with those of benzene condensed on graphite [10]. As discussed in detail in ref. [10], the sharp features are due to Auger deexcitation involving the highest occupied σ- and π-MO's of the benzene molecules. The p-CPC induced spectra in fig.4 show essentially the same sharp structures. Therefore, they must be caused by

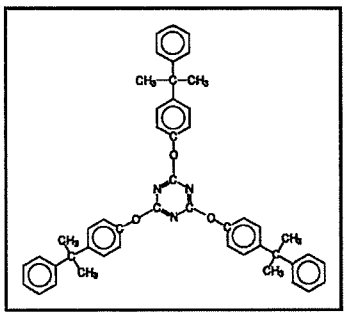

Fig.3: Chemical structure of the p-CPC trimer

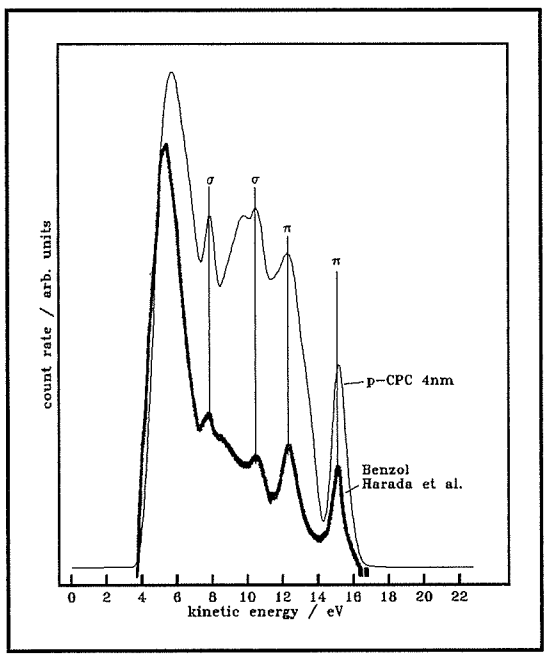

Fig.4: MIES spectra of a p-CPC trimer film on silicon [26] and benzene adsorbed on graphite [10]

Auger deexcitation involving the aromatic rings of the trimer molecule. This is strong evidence to state that the adsorption of the first layer is due to the interaction of the triazine rings with the substrate while the benzene containing branches point away from the substrate and are therefore accessible to MIES.

2.4 Electronic Transitions and Dissociation in Low-Energy Collisions of O_2^+ with W(110) Partially Covered by Alkali Atoms (IIES)

Fig.5 shows the spectra of the electrons emitted in slow collisions (50eV) of O_2^+ with W(110) surfaces partially covered by Cs atoms [15]. The following interpretation of the spectra is based on (i) corresponding results obtained for slow O^+ collisions [11], and (ii) simulations of the electron spectra for both O^+ and O_2^+ collisions along the lines described in section 1 [28].

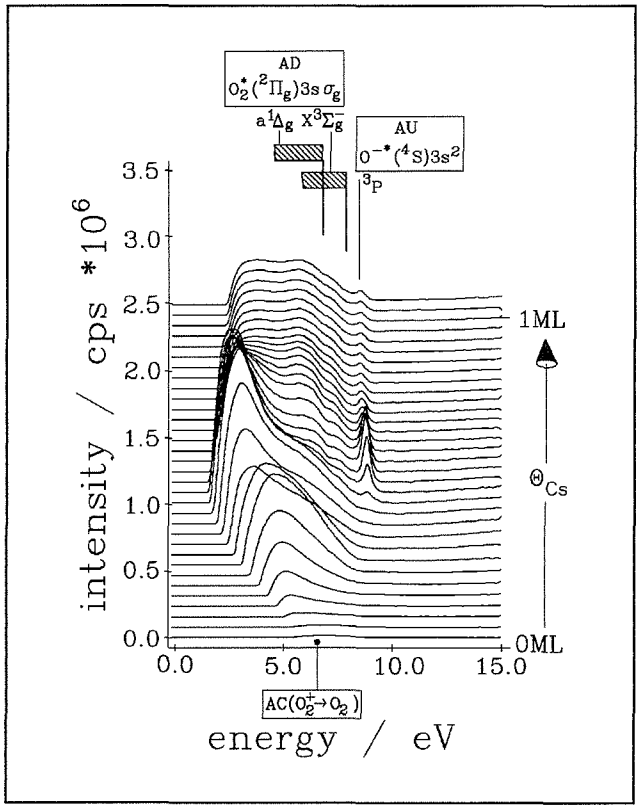

Fig.5: Energy spectra of electrons emitted in 50 eV collisions of O_2^+ ions with W(110) partially covered by Cs atoms. Coverage increases by 0.3 monolayers between each two spectra. Bottom curve is for clean W(110)

For large work functions the emission is caused by O_2^+ neutralization in the Auger capture process: the O_2 ionization potential (12.2eV) modified by image force effects (estimated as 1.5eV) is barely sufficient to cause electron ejection into the vacuum; most of the electrons involved in the Auger process are simply lifted into empty states above the Fermi level.

The relatively flat contribution seen for work functions below about 3eV that extends up to about 8eV is due to Auger deexcitation of core excited O_2^* molecules ($O_2^*(^2\Pi)3s\ \sigma_g$). The comparison with the O^+ results shows that the narrow peak near 9eV is due to autodetachment of the $O^{-*}(^4S)3s^2$ temporary ion. These ions are formed as follows: $O^*(^4S)3s$ core excited atoms are formed by the dissociation of core excited O_2^* molecules. They capture an additional surface electron thus forming the $O^{-*}(^4S)3s^2$ ions. We attribute the broad feature (below about 4eV) seen around the work function minimum to Auger deexcitation of the repulsive valence excited $O_2^*(^{1,3}\Pi_u)$ states formed by dissociative neutralization of the O_2^+ ions. Auger deexcitation of the dissociating molecule gives rise to a broad spectrum confined below 8eV and peaking at the lowest energies [28].

Slow CO_2^+ collisions with partially alkalated surfaces under grazing incidence offer another example for the feasibility to get information on collision-induced dissociation from the spectra of the emitted electrons [29]: core excited CO_2^* molecules are formed with large probability at low work functions. Most of them do dissociate into core excited CO^* fragments rather than being deexcited by Auger

deexcitation to the CO_2 ground state. The CO^* fragments on the other hand manifest themselves in the electron spectra by their Auger deexcitation.

3. Concluding Remarks

In this contribution we have presented the basic ideas of the Ion and Metastable Impact Electron Spectroscopies (IIES and MIES). Examples for their application where chosen from the fields of (i) layer growth on surfaces, (ii) electronic structure of clusters (C_{60}) on silicon, (iii) adhesion properties of polycyanurate films, and (iv) molecular dissociation in slow ion-surface collisions. There are numerous other areas where these techniques were also successfully applied, such as the determination of the orientation of surface adsorbed organic molecules [10], the study of the properties of liquid surfaces [30], the study of magnetic properties of surfaces using spinpolarized He metastables [31], the surface spectroscopy with spatial resolution [32] and the production and characterization of unusual atomic species such as short-living negative ion (Feshbach) resonances [11,33,34]

4. Acknowledgements

Financial support of the Deutsche Forschungsgemeinschaft and of the Deutsche Volkswagen-Stiftung is gratefully acknowledged.

5. References

[1] H.D. Hagstrum, Springer Series Surf. Sci. **10** (1988) 341
[2] G. Ertl, J. Küppers, "Low Energy Electrons and Surface Chemistry", VCH Weinheim 1985, and J. Küppers, "Physics and Chemistry of Alkali Metal Adsorption", Elsevier Amsterdam 1989
[3] R. Hemmen, H. Conrad, Phys. Rev. Lett. **67** (1991) 1314
[4] H. Brenten, H. Müller, V. Kempter, Z. Phys. D**22** (1992) 563
[5] R. Baragiola, in: "Low Energy Ion Surface Interactions", ed. J.W. Rabalais, ch.4, Wiley New York 1993
[6] A. Niehaus, in: "Ionization of Solids by Heavy Particles", ed. R. Baragiola, Plenum Press New York 1993
[7] P.A. Zeijlmans van Emmichhoven, P.A.A.F. Wouters, A. Niehaus, Surf. Sci. **195** (1988) 115
[8] P. Eeken, J.M. Fluit, A. Niehaus, I, Urazgil'din, Surf. Sci. **273** (1992) 160
[9] W. Maus-Friedrichs, S. Dieckhoff, V. Kempter, Surf. Sci. **253** (1991) 137
[10] Y. Harada, H. Ozaki, Jap. J. Appl. Phys. **26** (1987) 1201
[11] H. Müller, D. Gador, H. Brenten, V. Kempter, Surf. Sci. **313** (1994) 188
[12] H. Müller, R. Hausmann, H. Brenten, V. Kempter, Nucl. Instr. Meth. Phys. Res. B**78** (1993) 239
[13] A. Hitzke, J. Günster, J. Kolaczkiewics, V. Kempter, Surf. Sci. **318** (1994) 139
[14] W. Maus-Friedrichs, S. Dieckhoff, M. Wehrhahn, S. Pülm, V. Kempter, Surf. Sci. **271** (1992) 113, and

W. Maus-Friedrichs, S. Dieckhoff, V. Kempter, Surf. Sci. **273** (1992) 311
[15] H. Müller, D. Gador, V. Kempter, Surf. Sci. **318** (1994) 403
[16] S. Ciraci, I.P. Batra, Phys. Rev. B**28** (1983) 982
[17] S. Dieckhoff, H. Müller, W. Maus-Friedrichs, H. Brenten, V. Kempter, Surf. Sci. **279** (1992) 233
[18] A. Hitzke, S. Pülm, H. Müller, R. Hausmann, J. Günster, S. Dieckhoff, W. Maus-Friedrichs, V. Kempter, Surf. Sci. **291** (1993) 67
[19] S. Pülm, A. Hitzke, J. Günster, H. Müller, V. Kempter, Rad. Eff. Def. in Solids **128** (1994) 151
[20] S. Pülm, A. Hitzke, J. Günster, W. Maus-Friedrichs, V. Kempter, Surf. Sci. **xxx** (1994) in press
[21] R. Souda, Int. J. Mod. Phys. B**8** (1994) 679
[22] M. Merkel, M. Knupfer, M.S. Golden, J. Fink, R. Seemann, R.L. Johnson, Phys. Rev. B**47** (1993) 11470
[23] J.H. Weaver, Phys. Chem. Sol. **53** (1992) 1433
[24] J. Günster, Th. Mayer, A. Brause, W. Maus-Friedrichs, H.G. Busmann, V. Kempter, Surf. Sci. **xxx** (1994) to be published
[25] S. Nishigaki, T. Sasaki, S. Matsuda, N. Kawanishi, H. Takeda, Y. Yamada, Surf. Sci. **242** (1991) 358
[26] J. Günster, S. Dieckhoff, V. Kempter, Surf. Int. Analysis **xxx** (1995) to be published
[27] S.Dieckhoff, V. Schlett, W. Possart, O.-D. Hennemnann, Proc. AOFA 8 (1994) Kaiserslautern Germany, to appear in Fresenius J. Analyt. Chem.
[28] H. Müller, D. Gador, V. Kempter, Surf. Sci. **xxx** (1994) to be published
[29] H. Müller, D. Gador, V. Kempter, Surf. Sci. **xxx** (1994) to be published
[30] H. Morgner, J. Overbrodhage, K. Richter, K. Roth, J. Phys. Cond. Matt. **3** (1991) 5639
[31] M.S. Hammond, F.B. Dunning, G.K. Walters, Phys. Rev. B**45** (1992) 3674
[32] Y. Harada, S. Yamamoto, M. Aoki, S. Masuda, T. Ichinokawa, M. Kato, Y. Sakai, Nature **372** (1994) 657
[33] H. Müller, R. Hausmann, V. Kempter, Surf. Sci. **291** (1993) 78
[34] H. Müller, R. Hausmann, V. Kempter, Surf. Sci. **303** (1994) 56

Charge Exchange between Low-Energy Ions and Solid Surfaces and Its Application to Surface Chemical Analysis

R. Souda
National Insitute for Research in Inorganic Materials
1-1 Namiki, Tsukuba, Ibaraki 305, Japan

In this paper, a review is presented concerning alkali-metal adsorption on well-defined transition-metal and semiconductor surfaces, with particular emphasis on the bond-nature analysis using low-energy D^+ scattering. The analysis based on resonance neutralization of the D^+ ions associated with the 1s hole diffusion into the valence band reveals that Na, K, and Cs adatoms have significant covalency on the transition-metal surfaces while those except for Na are ionically adsorbed on the semiconductor surfaces in a small coverage regime ($<1.7\times10^{14}$ adatoms/cm^2). The charge state of Na is rather critical because of the larger ionization energy than the others.

I. INTRODUCTION

We have been systematically investigating the mechanism of the electronic transition in low energy D^+ scattering from a large number of surfaces [1-3]. As a consequence, we have recently proposed a novel experimental approach to the analysis of a surface chemical bond [2]. The use of D^+ scattering for this end rests on the fact that resonance neutralization associated with the D 1s hole diffusion into the valence band has intimate relevance to the bond nature of individual target atoms. In addition to this aspect, the information about the bond nature can be obtained from the inelastic energy loss of scattered ions due to electron-hole pair excitation [1,2].

The adsorption of alkali metals (AMs) on metal and semiconductor surfaces has attracted considerable attention with respect to a variety of technological applications together with basic physics. However, the nature of the AM-surface bond still continues to be a subject of considerable controversy [4-18]. The weakly-bound AM s electron is intuitively considered to be donated to the conduction band of substrates, the resulting AM ions being responsible for the formation of the dipole layer or the lowering of the work function [4]. In more recent work by Ishida and Terakura [10], it is concluded that the adatom is neutral at any coverage. In all these studies, it is evident that the definition of ionicity or neutrality on which various authors are based is certainly correct within the framework of their methods. Unfortunately, however, there is no unified way to rationalize this kind of issues without confusion [20,21].

In this paper, a review is presented concerning the analysis of AM-surface bonds on the basis of D^+ scattering [2]. It is demonstrated that the bonding of AMs on the metal surface [Pt(111), W(110)] sharply differ from those on covalent [Si(100), Ge(100)] and ionic [TiO_2(110), SiO_2] semiconductor surfaces. The Na, K, and Cs adatoms are essentially neutral on the Pt(111) and W(110) surfaces, whereas K and Cs are ionically adsorbed on the semiconductor surfaces. The Na adsorption on the semiconductor surfaces is somewhat specific and large ionicity of Na is concluded only on the TiO_2(110) surface. The specificity of the Na charge state on the semiconductor surfaces can qualitatively be ascribed to the larger ionization energy of Na than the others.

II. EXPERIMENTAL

The experimental setup has been described elsewhere [1] and only the features important to this experiment are briefly summarized here. The sample chamber was evacuated down to an ultrahigh vacuum (UHV) condition (1×10^{-8} Pa) and equipped with facilities for low-energy ion scattering (ISS), low-energy electron diffraction (LEED), and ultraviolet photoelectron spectroscopy (UPS). The D^+ ions were generated in a discharge-type ion source and were mass analyzed by a Wien filter.

The D^+ beam of E_0=100 eV was commonly used in the measurements. The D^+ ions were incident upon a surface with a glancing angle of 80° and the positive ions reflected with a scattering angle of 160° were analyzed by a hemispherical electrostatic energy analyzer with a constant energy resolution of 1 eV.

III. NEUTRALIZATION OF D^+

In this chapter, the proposed mechanism [1-3] of the charge-exchange interaction between D^+ and a surface is briefly summarized. The uniqueness of H^+ or D^+ scattering was reported earlier by Smith [22] and Eckstein and coworkers [23] in comparison with the results of He^+ scattering. Ions scattered from the outermost surface atoms are more likely to survive neutralization than those scattered from the bulk, and form so-called surface peaks in their energy distribution. This is in fact the case for He^+ scattering but the surface peak is in most cases completely absent in H^+ scattering and the spectrum is composed mostly of an extended background. It is well established that electron capture occurs via one-electron resonance (RN) and two-electron Auger (AN) processes and that the relative role of these processes depends sensitively upon the energy position of the vacant ionic level relative to that of the valence band. Uniqueness comes about for the D^+ ions since the 1s level is located just around the bottom of the valence band as shown in Fig. 1. In such an electronic level configuration, RN takes place because the 1s level can be promoted in the vicinity of a surface due to

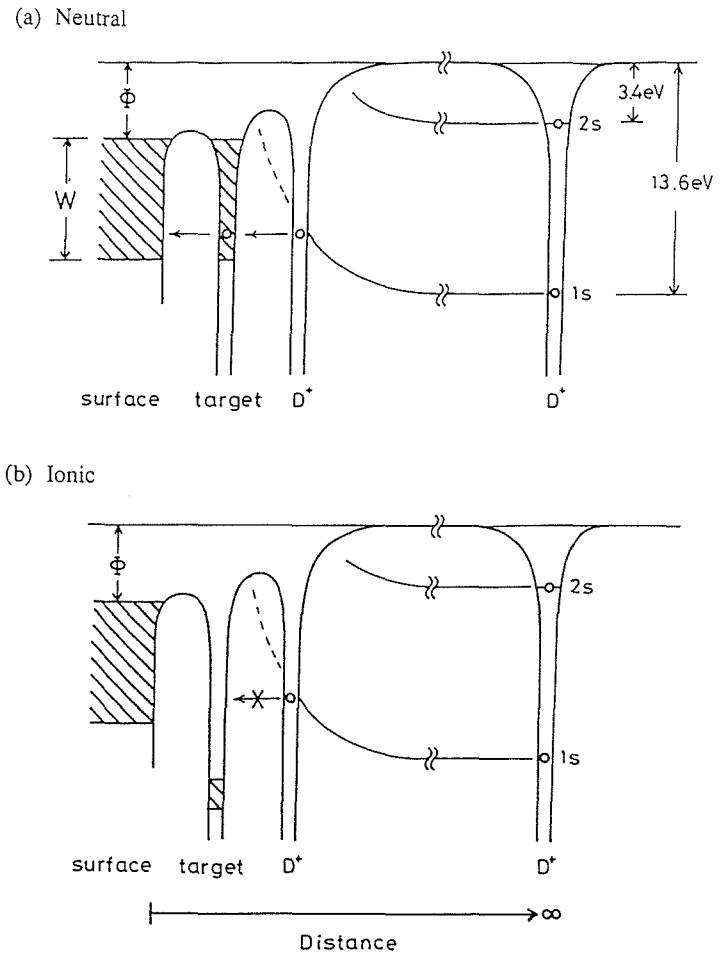

Fig. 1. Energy-level diagram for resonance neutralization of D^+ associated with a promotion of the ionic levels and subsequent hole diffusion into the band. (a) The hole diffuses immediately via the target-hole state if the target has covalent or metallic orbital hybridization, while (b) diffusion is suppressed if the target is perfectly ionized.

the image charge effect and/or the antibonding interaction with a target core orbital in the collisional regime [1,2,24,25]. The occurrence of RN has recently been confirmed from the molecular-orbital-energy calculations as well [3]. In this picture, the 1s orbital hybridizes the valence band except for very close encounters with the target atom. Here we denote this kind of RN process as $D^+ \rightarrow D^0$. The neutralization probability of D^+, therefore, is determined by the competition between the duration of the D^+-surface interaction ($\sim 10^{-15}$ s) and the lifetime τ of the hole given by

$$\tau = \hbar / W, \qquad (1)$$

where W indicates the valence band width.

As far as surface scattering is concerned, D^+ interacts mainly with the electronic states around the specific target atom and its surroundings because of the localized nature of the D 1s orbital (~0.5 Å). Hence, the above-mentioned band picture can alternatively be stated as follows (see Fig. 1): The D 1s hole diffuses irreversibly if target atoms bond to coordinating atoms via metallic or covalent orbital hybridization but hole diffusion is suppressed if the bonding is ionic. Especially in scattering from cations of simple ionic compounds, the hole is highly localized in deuterium and hence D^+ survives neutralization considerably. Inversely, complete neutralization ($D^+ \rightarrow D^0$) occurs in scattering from metals and covalent semiconductors. We have confirmed this issue in a large number of D^+ scattering experiments [1], in which intense surface peaks are observed for ionic compounds [NaCl, NaI, KF, KCl, KI, RbCl, CsF, CsCl, $SrCl_2$, CaF_2, SrF_2, BaF_2, $CdCl_2$, Sb_2O_3] while no appreciable surface peak appears for simple, transition, and noble metals [Ba, Ag, Mo(111), Ta(111), W(110), Pt(111)] and materials with significant covalency [diamond(100), Si(100), Si(111), Ge(100), SiO_2, $MnCl_2$, $CoCl_2$]. It should be mentioned that RN ($D^+ \rightarrow D^0$) provides a real experimental definition of ionicity, which has not been achieved by most of the alternative approaches.

In the case of AM adsorption, the work function is reduced considerably so that RN to the excited 2s level ($D^+ \rightarrow D^*$) makes significant contribution in a high coverage regime [2]. Indeed, the D^+ yield is found to be decreased rapidly if the work function is reduced below about 3-3.5 eV which agrees approximately with the binding energy of the D 2s level. This additional RN channel is independent of the local adatom-substrate bonding due to the extended nature of the D 2s orbital. In order to avoid complexity occurring from RN ($D^+ \rightarrow D^*$), we focus on the low AM coverage (<0.25 ML).

IV. RESULTS AND DISCUSSION

A. Si(100)

Fig. 2 shows representative energy spectra of D^+ (E_0=100 eV) scattered from the Si(100) surface covered with (a) Na, (b) K and (c) Cs adatoms. The D^+ ions scattered from the Si(100) substrate is almost completely neutralized, so that all of the D^+ ions in Fig. 2 are concerned with the AM adatoms. The AM coverage was estimated to be 0.25, 0.21, and 0.18 monolayer (ML), respectively, for Na, K and Cs adsorption. All of the spectra explicitly shown in this paper are taken under these AM coverages and the intensities are normalized relative to the Cs surface peak intensity shown in Fig. 2(c). Also shown by broken lines are the spectral changes due to successive 2 L (1 L=1.0×10^{-6} Torr s) O_2 exposure. Each spectrum except for Na adsorption exhibits the clear surface peak without oxygenation. Besides elastic peak A, there exist at least two energy loss structures labeled as B and C, together with an extended background appearing in the energy region below 75 eV.

The absence of the Na surface peak shows occurrence of nearly perfect neutralization in D^+-Na collision. There are alternative possibilities to explain this result; one is that the Na-Si bond has covalency to some extent and the other is that the metallic Na-Na bond is locally formed. The latter might be the case for the high coverage regime (>1/3 ML) but may not hold for coverage as small as below 0.25 ML where the Na layer breaks up into a set of individual adatoms. The features observed in Fig. 2 should be ascribed to the ion neutralization effect associated with ionicity of the local AM-Si bond.

In order to evaluate the degree of ionicity of the AM adatoms, the effect of oxygenation has been examined since, if AMs are ionized only in part or neutral species coexist on the surface, oxygenation

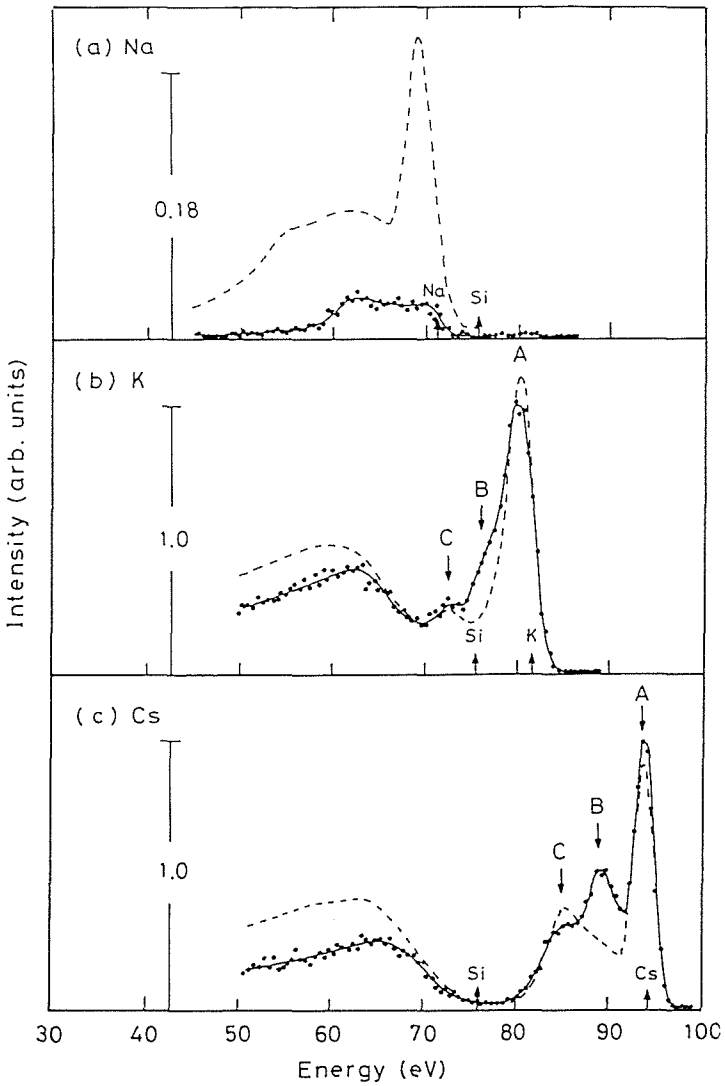

Fig. 2. Energy spectra of E_0=100 eV D^+ ions scattered from (a) Na-, (b) K-, and (c) Cs-adsorbed Si(100) surfaces with coverage of 0.25, 0.21, and 0.18 ML, respectively. The broken lines show the D^+ spectra obtained after subsequent exposure to 2-L O_2 gas. The energy for elastic binary collision with each surface atom is indicated by arrows on the abscissa. The spectral intensities are normalized relative to the Cs surface peak.

may lead to ionization of such adatoms due to formation of more ionic AM-O bonds. This is the case for Na adsorption. However, oxygenation induces only a small change in the intensity of peak A for K and Cs, indicating that the K-Si and Cs-Si bonds are essentially ionic in nature. This tendency is assignable to the smaller ionization energy of K and Cs (4.3 eV and 3.9 eV, respectively) than that of Na (5.1 eV). The Na 3s level may be overlapped in part with the Si valence state.

The ionic nature of the AM adatoms on Si(100) is substantially consistent with the theoretical predictions by Ciraci and Batra [17]. They have claimed that the K adatom is highly ionized because the K 4s electron is preferentially accommodated by the active dangling bond states. The specificity of the Na-Si bond, however, has not been revealed neither by theoretical calculations nor by other conventional experimental techniques. It should be noted here that the Na peak in Fig. 2(a), though increased in intensity upon oxygenation, is not so pronounced in intensity relative to the surface peaks of the other AMs. This result suggests that Na is ionized only in part even after oxygenation and a considerable portion of the Na adatoms retains covalency with the Si substrate.

As regards inelastic scattering, there exist at least two kinds of electronic excitation; reionization

($D^+ \rightarrow D^0 \rightarrow D^+$) and e-h pair excitation [1-3]. Both channels are thought to occur in the course of binary collision due to antibonding interaction between the D 1s orbital and a target core orbital. Since the binding energy of an AM core level becomes closer to the D 1s level in order of Na (2p: 31 eV), K (3p: 18 eV) and Cs (5p: 13 eV), the degree of the D 1s orbital promotion increases in the same order [3]. Consequently, the contribution of inelastic scattering relative to elastic scattering is target specific and increases in going from Na to Cs as can be seen in Fig. 2. Peak C is essentially assignable to reionization ($D^+ \rightarrow D^0 \rightarrow D^+$) while peak B is due to e-h pair excitation. Indeed, peak B is attributable to excitation of a Si valence electron to an empty state of AMs. Oxygenation decreases the intensity of peak B and shifts the peak position to the lower energy side, leading to overlapping with peak C. This is because excitation of the O 2p electron, as a result of a more preferable AM-O bond formation, results in a larger loss energy. In this respect, it should be mentioned that the energy loss value of peak B is smaller for K (2.5 eV) than Cs (4.5 eV). This is presumably because the empty K 4s state is located close to the Fermi level compared to the Cs 6s state. In the case of Na adsorption, the 3s level is in part overlapped with the Fermi level. These results are well correlated with the ionization energy of AMs.

Another conspicuous feature of the energy spectra in Fig. 2 is the broad spectral background appearing in the energy range below 75 eV. We have assigned the background to reionization ($D^+ \rightarrow D^0 \rightarrow D^+$) on the basis of the experiment using both D^+ and D^0 beams [1]. The background cannot be ascribed to surface scattering but is due to multiple scattering involving deeper layers. For these ions, duration of the interaction with the surface is much longer than in single scattering and, hence, perfect neutralization should occur. The fact that the background is almost absent at the clean Si(100) surface and increases in intensity with the amount of the adsorbates indicates that reionization

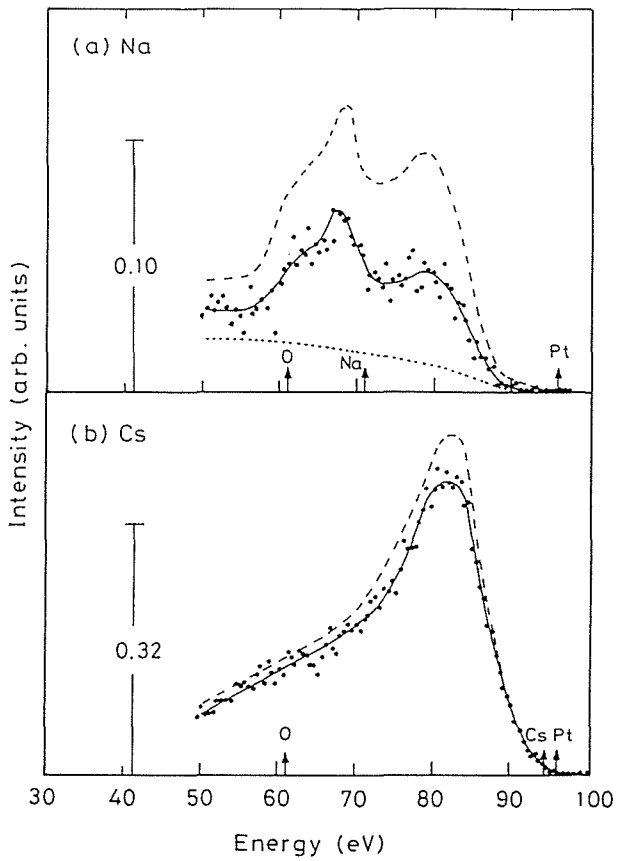

Fig. 3. Energy spectra of E_0=100 eV D^+ ions scattered from (a) Na- and (b) Cs-adsorbed Pt(111) surfaces. The spectral change due to subsequent exposure to 2-L O_2 gas is displayed by broken lines. A dotted line in (a) shows the spectrum from the clean Pt(111) surface.

($D^+ \rightarrow D^0 \rightarrow D^+$) takes place in the course of small-angle scattering by the adatoms just before leaving the surface. The high energy cutoff of the background is located at an energy position smaller than the exact binary collision energy for the substrate Si atoms because reionization involves excitation of the D 1s electron to an empty surface electronic state.

B. Pt(111)

Shown in Figs. 3 (a) and (b) are the D^+ spectra (E_0=100 eV) obtained at the Na- and Cs-adsorbed Pt(111) surfaces, respectively, the AM coverage being the same as that shown in Fig. 2. The spectrum for the clean Pt(111) surface, displayed in Fig. 3(a) by a dotted line, is fairly small in intensity with no surface peaks. The adsorption of Na induces a small change in the spectrum and the surface peak of Na is very little recognized. Cesiation, on the other hand, markedly increases the background intensity but no appreciable Cs peak emerges. The spectrum in Fig. 3(b) is almost identical to that obtained for the O- and CO-adsorbed Pt(111) surfaces, representing that the existence of the impurities other than AMs has similar effects on reionization of D^0. The intensity of the Cs (Na) surface peak for the Cs/Pt(111) surface [the Na/Pt(111) surface] is at most 2% (3%) of the Cs peak for the reference Cs/Si(100) surface. These surfaces are subsequently exposed to 2 L O_2 gas and the results are indicated by broken lines in Fig. 3. The surface peak is almost unchanged in intensity by oxygenation. It is thus concluded that the AM adatoms are not ionized on the Pt(111) surface and the interplay of AMs with coadsorbed oxygen is so weak that the covalent AM-Pt bond is substantially intact. This is one of the strongest pieces of evidence in support of the calculation by Ishida and Terakura [10]. The AM adatoms can directly bond to oxygen on the Pt(111) surface provided that the AM coverage exceeds about 1/3 ML and the metallic patches of AM are formed, which can be confirmed from the fact that oxygenation dramatically increases the AM surface peak relative to the background.

V. SUMMARY AND CONCLUSIONS

There is an intimate relevance between the bond nature of target atoms and the neutralization probability of the D^+ ions. This is because D^+ is neutralized by the resonant tunneling of the D 1s hole to the target electronic state and subsequent hole diffusion from the target into the ligand via

	Na	K	Rb	Cs
W(100)		×		×
Pt(111)	×	×		×
Si(100)	×	○	○	○
Ge(100)	×	○		○
SiO_2	△	○		○
TiO_2(110)	○	○		○

Table 1. The ionicity of AM adatoms on various surfaces estimated from the appearance of the AM surface peaks. A circle shows that the surface peak intensities normalized through AM coverages and ion beam intensities are comparable to the reference [the Cs surface peak at Cs/Si(100) shown in Fig. 2(c)] while an X indicates that the intensities are below 5% of the reference.

metallic or covalent orbital hybridization. By contrast, the ionic bond suppresses the hole diffusion so that the D^+ ion survives neutralization considerably. Of significance in this process is the spatially localized nature of the D 1s orbital, which allow one to obtain information about local bonding of specific target atoms with ligands. The results of D^+ scattering are summarized in Table 1, where a circle indicates that the AM peak intensity, normalized through the AM coverage and the ion beam intensity, is comparable to that of the reference surface [Cs/Si(100) shown in Fig. 2(c)] and an X shows that the intensity is less than 5% of the reference. The AM adatoms are essentially neutral on the transition-metal surfaces. On the other hand, K and Cs adatoms are ionized on the semiconductor surfaces such as Si(100), Ge(100), TiO_2(110), and SiO_2. The Na adsorption is rather critical, and the ionization is concluded only on the TiO_2(110) surface, on which Na may interact preferentially with the protruded ridges of surface oxygen atoms and the Na_2O-like bond can be formed [26].

Acknowledgements

The experiments described in this review were carried out in collaboration with W. Hayami, T. Aizawa, S. Otani, and Y. Ishizawa. The author is deeply indebted to K. Terakura, Y. Murata, S. Tsuneyuki, K. Kobayashi, Y. Morikawa, M. Nakamura, A. Namiki, and T. Koshikawa for fruitful conversations. This work was supported in part by the Special Coordination Funds Promoting for Science and Technology.

References

[1] R. Souda, T. Aizawa, W. Hayami, S. Otani, and Y. Ishizawa, Phys. Rev. B **42**, 7761 (1990); **43**, 10062 (1991); **45**, 14358 (1992); Surface Sci. **241**, 190 (1991); Phys. Rev. B **50**, 1934 (1994); R. Souda, K. Yamamoto, W. Hayami, T. Aizawa, and Y. Ishizawa, Phys. Rev. B **50** 4733 (1994).

[2] R. Souda, W. Hayami, T. Aizawa, S. Otani, and Y. Ishizawa, Phys. Rev. Lett. **69**, 192 (1992); Phys. Rev. B **47**, 6651 (1993); 9917 (1993); Surf. Sci. **285**, 265 (1993); **290**, 245 (1993); Phys. Rev. B **48**, 17255 (1993); R. Souda, Int. J. Mod. Phys. B **8**, 679 (1994).

[3] R. Souda, K. Yamamoto, B. Tilley, W. Hayami, T. Aizawa, and Y. Ishizawa, Phys. Rev. B, in press; R. Souda, K. Yamamoto, B. Tilley, W. Hayami, T. Aizawa, and Y. Ishizawa, Surf. Sci., in press.

[4] R. W. Gurney, Phys. Rev. **47**, 479 (1935).

[5] B. Boratschek, W. Sesselman, J. Kuppers, G. Ertl, and H. Haberland, Phys. Rev. Lett. **55**, 1231 (1985).

[6] K. Horn, A. Hohlfeld, J. Somers, Th. Lindner, P. Hollins, and A. W. Bradshaw, Phys. Rev. Lett. **61**, 2488 (1988).

[7] Y. Enta, T. Kinoshita, S. Suzuki, and S. Kono, Phys. Rev. B **39**, 1125 (1989).

[8] L. S. O. Johansson and B. Reihl, Phys. Rev. Lett. **67**, 2191 (1991).

[9] E. Wimmer, C. L. Fu, and A. J. Freeman, Phys. Rev. Lett. **55**, 2618 (1985).

[10] H. Ishida and K. Terakura, Phys. Rev. B **38**, 5752 (1988).

[11] D. M. Riffe, G. K. Wertheim, and P. H. Citrin, Phys. Rev. Lett. **64**, 571 (1990).

[12] A. Schmalz, S. Aminpirooz, L. Becker, J. Haase, J. Neugebauer, M. Scheffler, D. R. Batchelor, D. L. Adams, and E. Bogh, Phys. Rev. Lett. **67**, 2163 (1991).

[13] J. N. Andersen, M. Qvarford, R. Nyholm, J. F. van Acker, and E. Lundgren, Phys. Rev. Lett. **68**, 94 (1992).

[14] M. Kerkar, D. Fisher, D. P. Woodruff, R. G. Jones, R. D. Diehl, and B. Cowie, Phys. Rev. Lett. **68**, 3204 (1992).

[15] C. Stampfl, M. Scheffler, H. Over, J. Burchhardt, M. Nielsen, and D. L. Adams, Phys. Rev. Lett. **69**, 1532 (1992).

[16]. T. Aruga, H. Tochihara, and Y. Murata, Phys. Rev. Lett. **53**, 372 (1984); M. Tsukada, H. Ishida, and N. Shima, *ibid*, **53**, 376 (1984).

[17] S. Ciraci and I. P. Batra, Phys. Rev. Lett. **56**, 877 (1986).
[18] I. P. Batra and P. S. Bagus, J. Vac. Sci. Technol. A **6**, 600 (1988).
[19] Y. Ling, A. J. Freeman, and B. Belley, Phys. Rev. B **39**, 10144 (1989).
[20] H. Ishida and K. Terakura, Phys. Rev. B **40**, 11519 (1989).
[21]. I. P. Batra, Phys. Rev. B **43**, 12322 (1991).
[22] D. P. Smith, Surf. Sci. **25**, 171 (1971).
[23] R. Bhattacharya, W. Eckstein, and H. Verbeek, Surf. Sci. **93**, 563 (1980); P. J. Schneider, W. Eckstein, and H. Verbeek, J. Nucl. Mater. **111&112**, 795 (1982).
[24] S. Tsuneyuki and M. Tsukada, Phys. Rev. B **34**, 5758 (1986).
[25] S. Tsuneyuki, N. Shima, and M. Tsukada, Surf. Sci. **186**, 26 (1987).
[26] H. Onishi, T. Aruga, C. Egawa, and Y. Iwasawa, Surf. Sci. **199**, 54 (1988).

Non-Destructive XPS Analysis of Surface Nano - Structures

Sven Tougaard
Department of Physics, Odense University, DK-5230 Odense M, Denmark

Abstract.

A new formalism for non-destructive analysis of surface nano-structures by XPS is discussed. The formalism relies on analysis of the peak shape of the measured spectrum over a wide energy range. Examples on the practical application, in the form of a commercially available software packet QUASES™, is given.

1. Introduction.

X-ray Photoelectron Spectroscopy (XPS) has become one of the most popular techniques for chemical analysis of the outermost surface region of solids [1]. Combined with surface erosion as a result of inert ion bombardment of the surface, XPS can be used as an alternative to AES to study also the composition of deeper layers. This is the subject of another paper in these conference proceedings by Hofmann [2].

Determination of the quantitative surface chemical composition by XPS relies on several assumptions of which the most important may be knowledge of photoionization cross sections and inelastic electron mean free paths [3]. For a meaningful quantification, assumptions on the in-depth distribution of atoms must be made since the measured peak intensity depends critically on that. Now, in practice the in-depth atomic distribution is never known when sample is analyzed, because if it were, it would be a waste of time and money to perform the analysis. It is then usually assumed that the surface region is homogeneous up to a depth of a few nano meters [1]. This assumption may result in incredibly large errors in quantification [4,5].

In recent years, much effort has therefore been devoted to the development of an improved formalism for quantitative surface analysis. The fact that the shape of the energy spectrum depends characteristically on the depth of origin of the x-ray excited electrons has led to the formulation, by Tougaard et al, of a new technique for quantitative XPS which also provides quantitative information on the in-depth nano structure of the surface region of the solid. This formalism, which is based on the analysis of the XPS-peak shape in a wide energy region is the subject of the present paper.

2. Elements of Inelastic Peak Shape Analysis.

2.1 Basic Idea.

The fundamental idea behind the new formalism is illustrated in Fig.1. After being photon excited, the energetic core electrons move in the sample. Some of them escape through the solid surface and enter the electron energy analyzer. During this transport, the electrons may undergo elastic and inelastic scattering events. This will lead to a change in the peak shape, the peak height, and the intensity on the low energy side of the peak. The extent to which the energy spectrum is thus distorted depends on the distribution of path lengths that the electrons have travelled before reaching the solid surface. Thus the XPS peak shape depends critically on the in-depth distribution of electron emitting atoms (see Fig.1). This phenomenon has led to the development of a new formalism for quantitative analysis of surface nano structures.

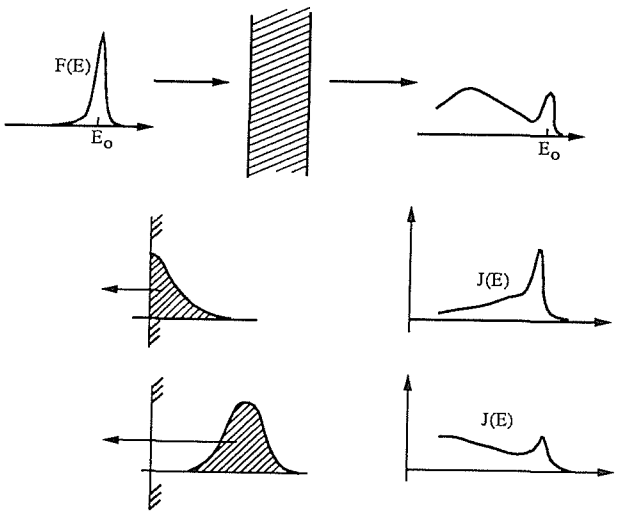

Figure 1. Transport of the photoelectrons cause a change in the energy distribution. The spectral peak shape depends therefore in a characteristic way on the in-depth concentration profile.

2.2 Theory.

The basic algorithms for quantitative surface analysis have been developed over the past several years [4-8]. Here we briefly summarize the basic principle. Denote by F(E) the energy distribution of x-ray excited core electrons from a single atom and by J(E) the measured spectrum. The distortion of the energy spectrum depends on the in-depth concentration profile f(x) and the differential inelastic electron scattering cross section K(T). The relationship is given in Fig. 2.

2.3 Practical Application.

The extent to which the peak intensity and peak shape depends on the in-depth concentration profile may be illustrated by the spectra in Fig.3. Here a thin (~1 nm thick) gold layer was evaporated onto a nickel substrate [10]. The Au4d core electrons excited by Al-Kα radiation were

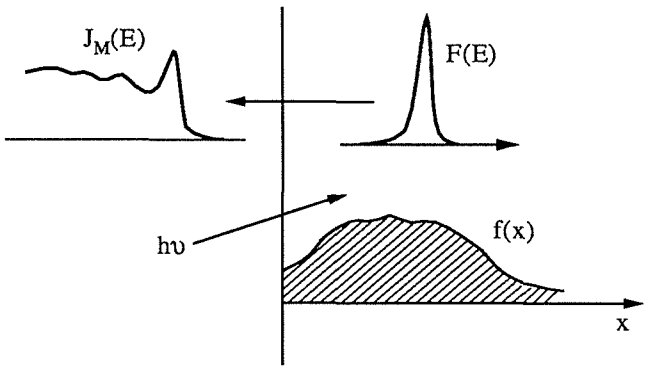

F(E): atomic spectrum

$J_M(E)$: measured spectrum

K(T): inelastic scattering cross section

f(x): in-depth concentration profile

Method I:

Calculation of atomic spectrum

$$F(E) = \frac{1}{2\pi}\int dE' J_M(E') \int ds' e^{is'(E'-E)} \left[\int_{x=0}^{\infty} f(x) e^{-x\int_0^{\infty} K(T)(1-e^{-isT})dT}\, dx\right]^{-1}$$

Adjust f(x) until $F(E) = \underbrace{F_{Reference}(E)}_{\text{From pure elemental sample}}$.

Method II:

Simulation of spectrum

$$J_s(E) = \int dE_0 F(E_0) \int dx f(x) G(E_0, x/\cos\theta; E)$$

$$G(E_0, x/\cos\theta; E) = \frac{1}{2\pi}\int_{-\infty}^{\infty} e^{is(E_0-E)} - e^{-\frac{x}{\cos\theta}\cdot\int_0^{\infty} K(E_0,T)(1-e^{-isT})dT}\, ds$$

Adjust f(x) until $J_s(E) = J_M(E)$

Figure 2. The basic procedures in quantitative surface nano-structure determination by peak shape analysis.

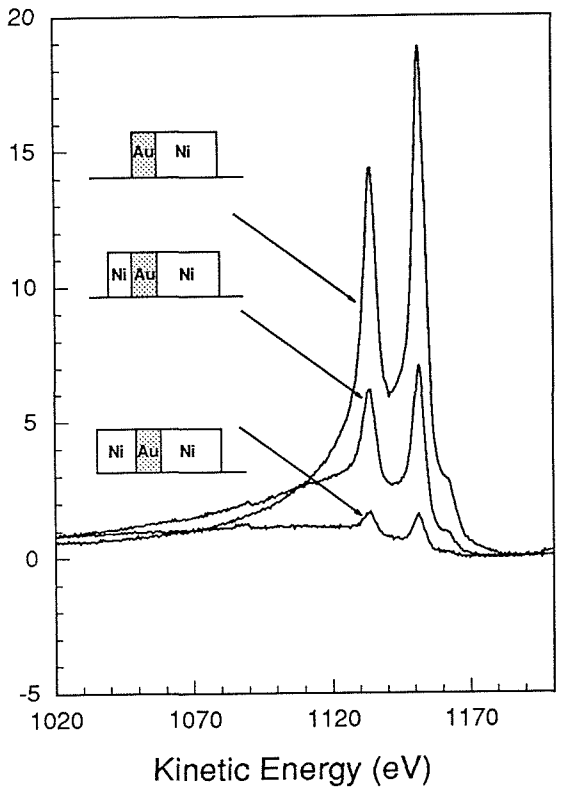

Figure 3. Spectra in the Au4d energy region from a sample produced by evaporating layers of gold and nickel on top of a nickel substrate [10].

measured. The spectra show the development of the peak intensity and peak shape as various amounts of nickel (on the order of ~1 - 5 nm) were evaporated on top of the gold-nickel structure. From this example, it is evident that the error in quantification may easily reach several hundred percent, when as has been usual practice, the sample composition is assumed to be homogeneous within the surface region of the solid.

In practice, there are fundamentally two different approaches to the application of the new formalism for quantitative surface analysis.

2.3.1 Method I.

Here the atomic excitation spectrum F(E) is determined and the in-depth concentration profile f(x) is adjusted until F(E) is as close as possible to a reference spectrum $F_{Reference}$ (E). After this procedure, the composition of the surface of the sample on the nano-scale has been determined. The reference F(E) spectrum may conveniently be determined by analysis of the measured spectrum from a sample with known structure, for instance the spectrum from a pure elemental sample.

2.3.2 Method II.

Here the spectrum of emitted electrons is simulated by assuming a composition profile f(x). When the best agreement with the measured spectrum is found, the in-depth composition profile f(x) has been determined. With this procedure it is necessary to know the atomic spectrum F(E). This is conveniently determined from the spectrum of a pure elemental sample as described above.

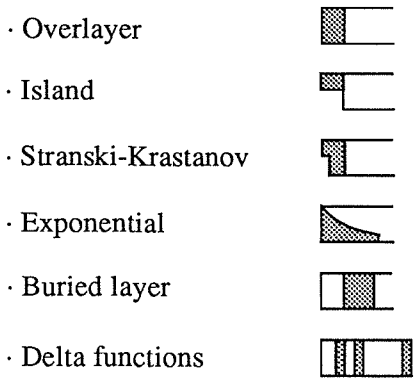

Figure 4. The surface morphologies that can be treated by the software QUASES™ [8].

3. Software to Implement the Ideas in Practice.

The ideas presented in Section 2 have been implemented in the form of a commercially available software packet QUASES™ [8]. It is a menu-oriented software which runs under DOS on any IBM or compatible PC (386 or higher) with a mathematical co-processor. All necessary data handling can be performed within the program. The software allows for using either Method I or II described above. The assumed surface morphology can be changed within the types shown in Fig.4. The parameters characterizing the structure can be changed interactively. Analysis of a single spectrum takes ~ 1 sec and as a result, several structures can quickly be tried for determination of the actual in-depth concentration profile f(x).

4. Example.

As an example, in Fig.5, the lower spectrum in Fig. 3 has been analyzed. The figure shows the appearance of the interactive graphical user interface of the software QUASES™ . In the menu in the left part of the screen, the surface structure can be changed and the chosen structure is also shown graphically in the lower left part. The result of the spectral analysis is shown in the right part of the picture. The three examples shown in Fig.5 correspond to the assumption of a buried layer of gold of 8 Å width centered at depths 50 Å, 36 Å, and 22 Å in the nickel matrix. It is not possible to get an acceptable analysis of the same spectrum when assuming the alternative surface morphologies (see Fig.4). From the analysis it is then clear that the gold is present as a ~ 8 Å thick layer situated roughly at a depth of 36 Å.

The method described in this paper has been applied in the study of many different systems [5-26] including surface nano-structures of metal/metal - [9-10], metal/silicon - [11,12], and polymer/metal - systems [13] as well as metal-oxide growth [14].

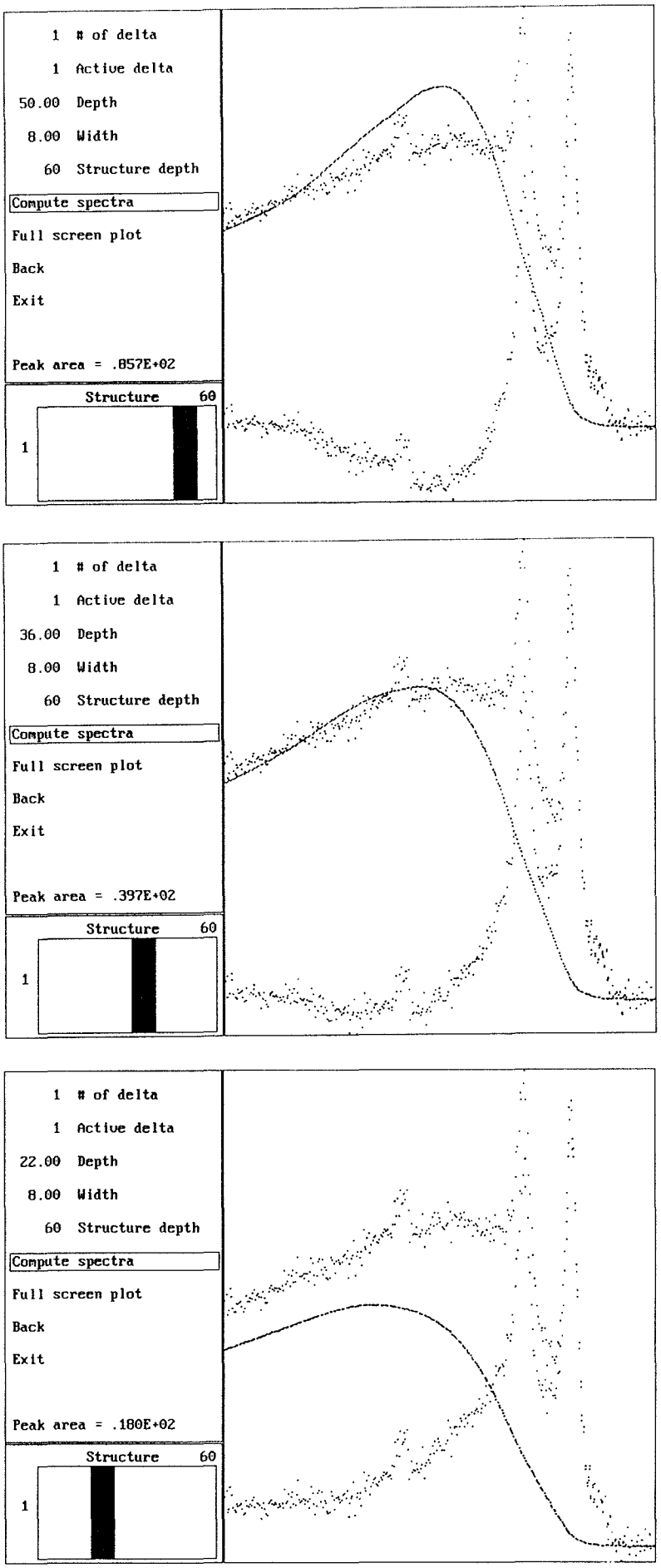

Figure 5. The lower spectrum in figure 3 analyzed by the software QUASES™.

References

[1] D.Briggs and M.Seah (Eds), Practical Surface Analysis, 2nd Edn. Wiley, Chinchester (1990).

[2] S. Hofman, These Proceedings.

[3] S.Tanuma, C.J.Powell and D.R.Penn, Surf. Interface Anal. 11, 577 (1988).

[4] S. Tougaard, Surf. Interf. Anal. 11, 453 (1988)

[5] S.Tougaard, J.Electron Spectrosc. Relat. Phenom. 52, 243 (1990).

[6] S.Tougaard and H.Hansen, Surf. Interface Anal. 15, 730 (1989).

[7] S. Tougaard and C. Jansson, Surface Interf. Analysis **20**, 1013 (1993)

[8] S. Tougaard, "QUASES: Software Packet for Quantitative XPS/AES of Surface Nano-Structures by Inelastic Peak Shape Analysis", 1994. (Contact S. Tougaard for more information).

[9] S. Tougaard and H. S. Hansen, Surf. Sci. **236**, 271 (1990)

[10] S.Tougaard, H.S.Hansen and M.Neumann, Surf. Sci. 244, 125 (1991).

[11] H. S. Hansen, C. Jansson, and S. Tougaard, J. Vac. Sci. Technol. **A10**, 2938 (1992)

[12] M. Schleberger, D. Fujita, C. Scharfschwerdt, and S. Tougaard, Surf. Sci. (1995) In press.

[13] H.S.Hansen, S. Tougaard, and H. Biebuyck, J. Electr. Spectr., 58, 141 (1992)

[14] S. Tougaard, W. Hetterich, A. H. Nielsen, and H.S. Hansen, Vacuum, 41, 1583 (1990)

[15] B.S. Norgren, M.A.J. Somers and J.H. de Wit, Surf. Interf. Anal. In press.

[16] H. Bender, Surf. Interf. Anal. 15, 767 (1990)

[17] M. Sastry, D.V. Paranjape, and P. Ganguly, J. Electr. Spectr., 59, 243 (1992)

[18] T. Ogama and T. Horikawa, J. Vac. Sci. Technol. A8, 2204 (1990)

[19] M. Repoux, Surf. Interf. Anal., 18, 567 (1992)

[20] S. Zeggane and M. Delamar, Appl. Surf. Sci., 29, 411 (1987)

[21] H. Tokutaka, N. Ishihara, K. Nishimori, S. Kishida, and K. Isomoto, Surf. Interf. Anal.,18, 697 (1992)

[22] L-S. Johansson and T. Losoi, Surf. Interf. Anal., 17, 230 (1991)

[23] J. Végh, Surf. Interf. Anal., 18, 545 (1992)

[24] K.H. Richter, J. Electr. Spectr., 60, 127 (1992)

[25] A. Jouaiti, A. Mosser, M. Romeo, and S. Shindo, J. Electr. Spectr., 59, 327 (1992)

[26] M. Sastry and S.R. Sainkar, J. Appl. Phys., 73, 767 (1993)

XPS Analysis of Si-Oxide/Si Interface Formed by Ozone Oxidation

A. Kurokawa and S. Ichimura
Electrotechnical Laboratory, 1-1-4, Umezono, Tsukuba 305, Japan

Abstract

The Si-oxide/Si interface formed with high purity ozone jet was investigated by X-ray Photoelectron Spectroscopy (XPS) with special attention to suboxide structure at the interface. High purity ozone jet (ozone concentration; over 80 % at the sample surface) was used for the initial oxidation of Si (111) surface. The suboxide structure at the interface was estimated from the shape of the Si 2p spectra. Comparing the interface structure formed by ozone oxidation with that formed by conventional thermal oxidation process (with oxygen molecules), it became clear that ozone forms less suboxide structure at the interface than oxygen. It was also revealed from the energy shift of the Si 2p peak that ozone oxidizes the pure surface about 10^4 times faster than oxygen. The energy shift of Si 2p peak, which was caused by oxidation with ozone at room temperature, was equivalent to the shift caused by oxidation with oxygen at about 700 C. It was also confirmed that ozone can oxidize the Si surface terminated with hydrogen at monohydride condition in spite that oxygen can hardly react with the surface.

1. Introduction

The importance of the uniformity of Si-oxide layer is increasing more and more in accordance with the continuous scaling down of semiconductor device dimensions. The control of the Si-oxide/Si interface is one of the most important subjects to be investigated for such fine device processing. It is already known that different suboxide states are formed at the Si-oxide/Si interface by conventional thermal oxidation process. Such suboxide states can be studied by XPS since Si 2p spectra appears at different binding energies depending on chemical states. For example, chemical shifts of 0.97 eV, 1.80 eV, 2.60 eV, and 3.82 eV have been observed for chemical states of Si^+, Si^{+2}, Si^{+3}, and Si^{+4}, respectively[1]. Such chemical states corresponds to chemical bonding of Si_2O (Si^+), SiO (Si^{+2}), Si_2O_3 (Si^{+3}), and SiO_2 (Si^{+4}).

Oxidation mechanism on Si with oxygen (O_2) is considered as follows: An oxygen molecule chemisorbs at two neighboring empty sites (dangling bonds) on clean Si surface and then dissociates. Dissociated oxygen breaks backbond of Si atoms and forms Si-O-Si bridge configuration. Therefore, the existence of the chemisorption sites is inevitable for the progress of the oxidation, and the surface density of the sites controls the oxidation. On the contrary, ozone (O_3) does not need any chemisorption sites, since it easily dissociates on the surface resulting in the generation of atomic oxygen. This atomic oxygen reacts as an active specie for oxidation so that ozone will have a different mechanism for oxidation. It is possible, therefore, that ozone can make a better SiO_2/Si interface with less suboxide states at low temperature, which is one of the important points to be considered for advanced device processing.

The aim of the present paper is to show how the interface of the Si-oxide/Si could be finely controlled by ozone, and how the interface condition could be estimated by XPS. Clean Si(111) surface showing 7x7 structure was chosen as the substrate for the oxidation. The Si-oxide/Si interface formed by ozone oxidation on clean and hydrogen terminated Si surface was compared with

that formed by thermal oxidation with oxygen molecules.

2. Experimental

Fig.1 shows the experimental set up. The same vacuum chamber was used both for the oxidation of Si and the analysis of it by XPS. The chamber, which was evacuated with two turbomolecular pumps connected in series (tandem type), had a base pressure of about 3 x 10^{-8} Pa.

P-doped Si (111) surface having the resistivity of 1 Ωcm was used as a sample. After setting the sample in the chamber, the sample was first irradiated with ozone jet to decompose hydrocarbon contamination, and then thermally flashed. Clean Si surface appeared by the procedures, which was confirmed by the appearance of 7x7 LEED pattern and the disappearance of contamination (mainly carbon) peak in XPS spectra. A reverse-view LEED apparatus was used for the observation of the surface structure. The XPS analysis of the sample was performed using the combination of an conventional Al Kα X-ray source and a double pass type CMA. The pass energy of photoelectrons through the CMA was set at 150eV for survey spectra and at 50eV for O1s and Si2p observations.

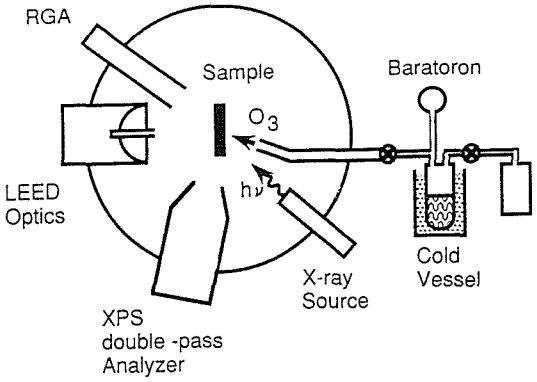

Fig.1 Schematic view of the experimental setup

The ozone jet was supplied to the sample through small aluminum pipe. Although the construction of the ozone jet supply has already been described elsewhere[2, 3], we briefly describe here the operational principle and characteristics of the supply to help understanding of the present experiment.

Figure 2 shows schematic diagram of the construction of the ozone jet supply. The ozone-oxygen mixture gas with an ozone concentration of about 5 mol.% was generated by flowing pure (99.95%) oxygen through an ozonizer. Ozone in the mixture gas was liquefied and accumulated in the ozone vessel, since the saturation vapor pressure of ozone and oxygen differ by several orders in magnitude in the temperature range below 100 K. After collecting a certain amount of liquid ozone (less than 0.5 cc), the gas flow was stopped and the ozone vessel was kept at a desired temperature to evaporate ozone. The vessel temperature was controlled within an accuracy of 0.1 K using the combination of cryocooler and heater. Such accurate control of the vessel temperature is essential to get stable flux of ozone (fluctuation; less than 2.5 %) and to avoid possible ozone explosion by heat invasion.

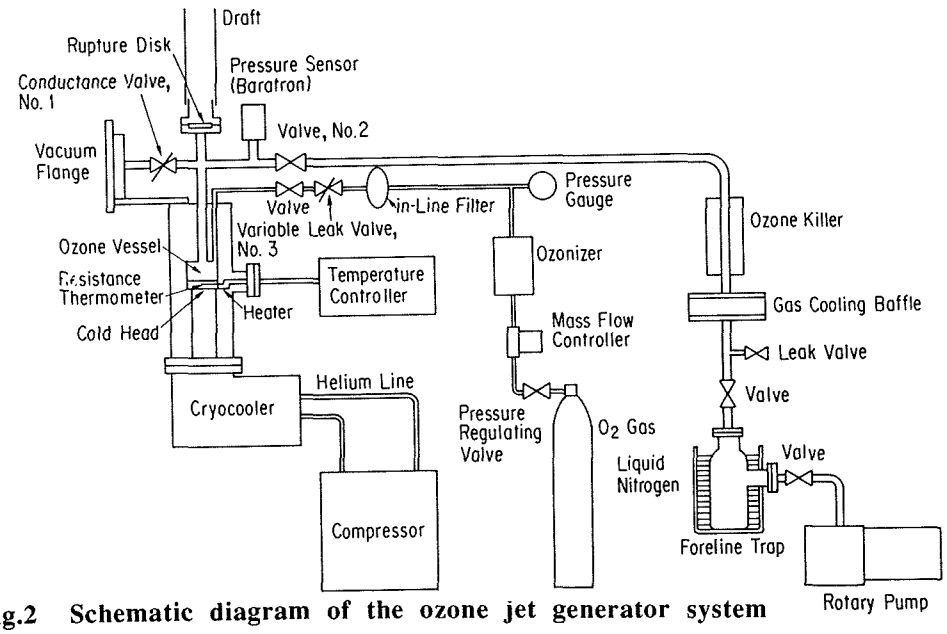

Fig.2 Schematic diagram of the ozone jet generator system

The purity of liquid ozone was more than 98 mol.%, judging from the vapor pressure vs. temperature of the accumulated ozone. The concentration of ozone in the ozone jet was over 80 at.% at sample position. Other gas component in the ozone jet was only oxygen, which was generated by the decomposition of ozone through aluminum pipe. The concentration of ozone and other gas components were investigated by mass analysis of the jet with a quadrupole mass spectrometer.

For the oxidation of H-terminated Si surface, the passivated surface was made by in-situ method as follows: Following the thermal flushing, the sample was exposed to hydrogen gas (purity: 99.995%). To generate atomic hydrogen from hydrogen gas, a hot filament heated at 1700C was placed in front of the sample during the exposure. The sample temperature was set at 380C during the exposure, because it is reported that monohydride adsorption occurs at the temperature[4]. After sufficient exposure of hydrogen gas to the clean Si surface, we found tne disappearance of 7x7 structure and the appearance of 1x1 structure by LEED.

3. Results and discussion

Fig. 3 shows a typical XPS spectrum of the Si-oxide/Si surface. We measured the energy position and the intensity of O1s peak, and estimated binding condition and total amount of oxygen at surface region. The intensity was measured from the area of the peak after subtracting the background with Shirley method.

First we compared the O1s intensity for different exposure of ozone and oxygen at 70 C and 400 C. In the case of oxygen exposure, the exposed amount in unit of Langumuire (1L=1.33x10^{-4} Pa s) was estimated from the exposure time and the chamber pressure measured with an ionization gauge. The pressure was kept at 3x10^{-5} Pa below 10L exposure, while it was kept at 3x10^{-4} Pa above 10L exposure. However, we could not estimate the exposure of ozone in the same manner, since the sensitivity factor of the ionization gauge for ozone was not given. So we estimated the exposure of ozone from the pressure at the ozone vessel with a capacitance manometer. Since the indication of the capacitance manometer does not depend on gas species, we could supply the same number of ozone and oxygen molecules by monitoring the pressure.The mass dependence of the conductance of the aluminum pipe was also taken into account in the estimation. The results is shown in Fig. 4.

Open marks in Fig. 4 represent the results for the oxygen exposure at the sample temperatures of 70 C (open square) and 400 C (open triangle). Solid square marks represent those for ozone exposure at 70 C.

At low oxygen exposure (less than 10L), the O1s intensity is higher for the lower substrate temperature. It probably reflects the difference of the sticking probability of oxygen on Si substrate. It

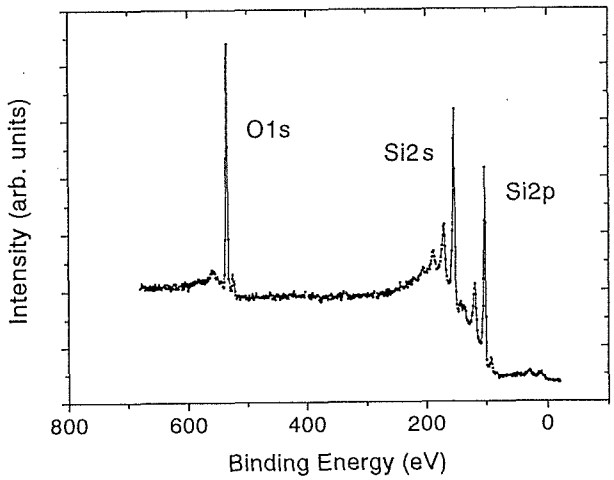

Fig.3 A typical XPS spectrum of the Si-oxide/Si surface.

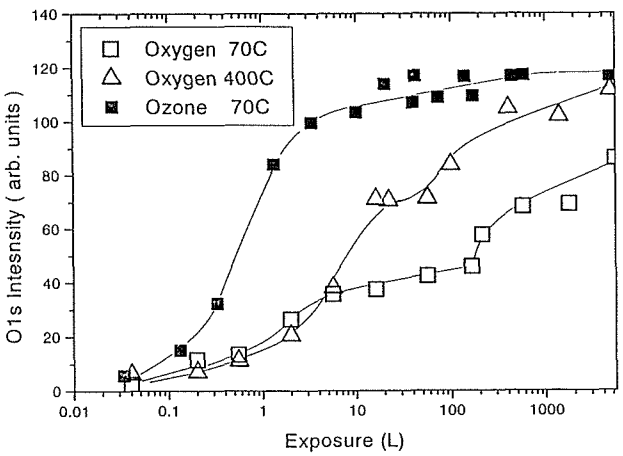

Fig.4 O1s peak area intensity for different ozone/oxygen exposure to the clean Si surface.

is known that the sticking probability of oxygen is about 0.13 at 300K, and it is about 0.06 at 600K[4]. In accordance with the increase of oxygen exposure, two step-like increase in intensity was observed; for the exposure at 70 C, the first step appeared at at a few L and the second one at about 200L, while the first and second step appeared closely at about several tens L for the exposure at 400 C. Between the two steps, a plateau like structure appears for both cases.

We consider that these step-like change arises from different mechanisms in the oxidation. That is, the first step appeared in accordance with the change from physisorbed or chemisorbed oxygen to stable oxide. The second step appeared due to the enhancement of oxidation by electric-field assisted growth, which is known as the Mott-Cabrera mechanism[5]. A strong electric field across the oxide enhances diffusion of ions and ionic defects, leading to enhancement of oxygen transport.

In the case of ozone exposure, on the other hand, only one step-like increase of O1s intensity was observed. We think this fact can be explained by the disappearance of the first step increase. That is, we think that absorbed ozone on the substrate quickly forms Si-oxide without passing the chemisorbed or physisorbed state, since the chemical reaction of ozone with Si substrate is so strong. The steep increase of O1s intensity shown in Fig.4 will support our thought. O1s intensity for about 1L exposure of ozone (at 70 C) corresponds to the intensity for 100L exposure of oxygen molecules at 400 C, and to the intensity for 5,000L exposure of oxygen molecules at 70 C.

The O1s intensity at the second stage is higher for ozone exposure than oxygen exposure. As is mentioned above, the adsorption of oxygen forms various oxidation states like SiOx (x=0.5,1,1.5). Usually various oxidation states coexists on the surface, and the change of SiOx states density may change the sticking probability of oxygen, resulting in a different plateau coverage. Therefore, higher O1s intensity may indicate that the ratio of the higher oxidation state is larger.

The shift of O1s peak position, which is shown in Fig. 5 as a function of sample temperature, also indicates the existence of higher oxidation state in the case of ozone exposure. At the exposure of $1x10^{18}$ oxygen molecules, peak shift to higher binding energy side was observed only at high sample temperature (>400C). For ozone exposure, however, the peak shift was observed even at room temperature for both exposures of $1x10^{18}$ and $1x10^{19}$ molecules. The shift at room temperature corresponded to the shift caused by the oxygen at 700C. it is known that when the temperature increased, the population of suboxide states decreases and the SiO2 state increases[7]. So the above result suggests that the oxidation by ozone forms SiO_2 with high population even at room temperature.

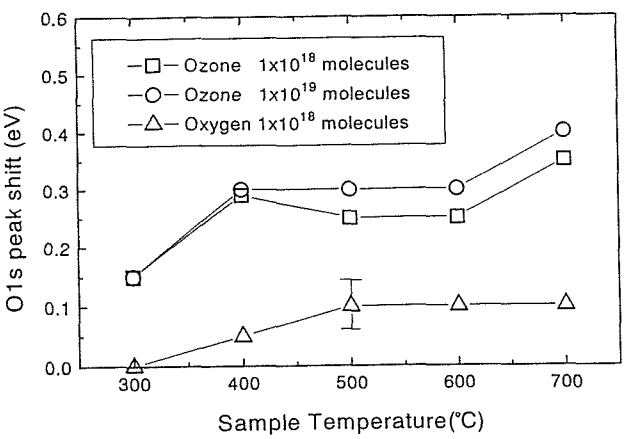

Fig.5 O1s energy shifts for exposures of ozone and oxygen at different temperature.

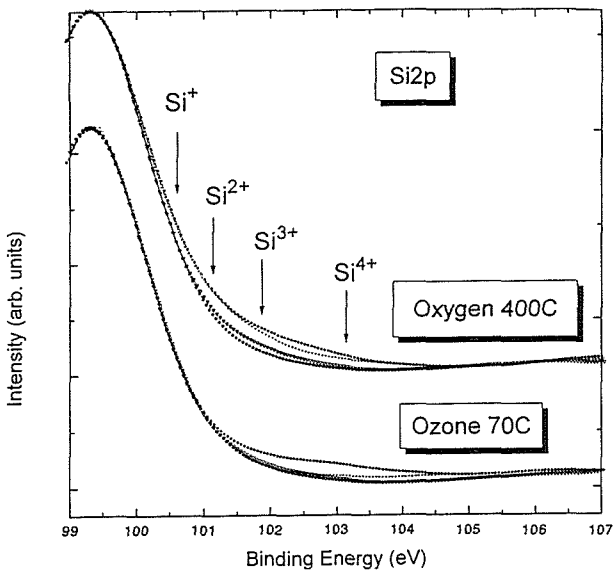

Fig.6 Si2p spectra taken at four different exposure of ozone jet and oxygen. .

In order to investigate the change of the suboxide states clearly, we measured the Si2p peak. As is already mentioned, Si 2p photoemission spectra exhibits several peaks corresponding to the suboxide states of SiOx (x=0.5,1,1.5,2). However, the energy resolution was not enough to separate different suboxide states by our conventional XPS system. Instead, theses peaks appeared at the shoulder of the Si bulk peak. So we estimated the suboxide condition from the overall peak shape.

Fig. 6 shows the Si2p spectra taken at four different conditions of ozone and oxygen exposure at 70C (ozone) and 400C (oxygen). The exposures conditions were 0 L (before exposure), 0.3 L, 1.3 L, and 73 L for ozone, and 0 L, 5.6 L, 99 L, and 400 L for oxygen. Although the exposure levels are different between ozone and oxygen, they were chosen so that almost same O 1s intensity was observed at the exposure. For example, as is seen in Fig.4, the O1s intensity level at 0.3 L exposure of ozone almost corresponds to that at 5.6 L exposure of oxygen. Similarly, the O 1s intensity levels are same for 1.3 L exposure of ozone and 99 L exposure of oxygen, and for 73 L exposure of ozone and 400 L exposure of oxygen.

The peak positions correspond to suboxide states such as Si^{+}, Si^{2+}, and Si^{3+} are shown by arrows in Fig. 6 together with the positions of Si^{4+}. By increasing the ozone and oxygen exposure, the peak shape changed. Especially intensities at the position of Si^{2+}, Si^{3+} and Si^{4+} increased in accordance with the increase of exposure for both ozone and oxygen. However, the intensity change at these suboxide peak positions was different between oxygen and ozone exposure. For ozone exposure the intensity around the Si^{4+} position increased mainly, and slight increase in intensity was observed around the position corresponds to Si^{3+} peak. For oxygen exposure, on the other hand, the intensity increased more at the Si^{3+} peak position than at the Si^{4+} position. Intensity increase around the positions of Si^{+} and Si^{2+} peak were also noticed for oxygen exposure.

Spectra taken after the same amount (50L) of exposure for ozone and for oxygen are compared in Fig.7, both for full spectra (Fig.7(a)) and expanded spectra around the suboxide state region (Fig. 7(b)). As can be seen, the intensity around the Si^{4+} peaks are nearly same, while the intensity around the suboxide peak positions are largely reduced for ozone exposure. These results suggest that Si-oxide with stoichiometric structure of SiO_2 was formed by ozone oxidation.

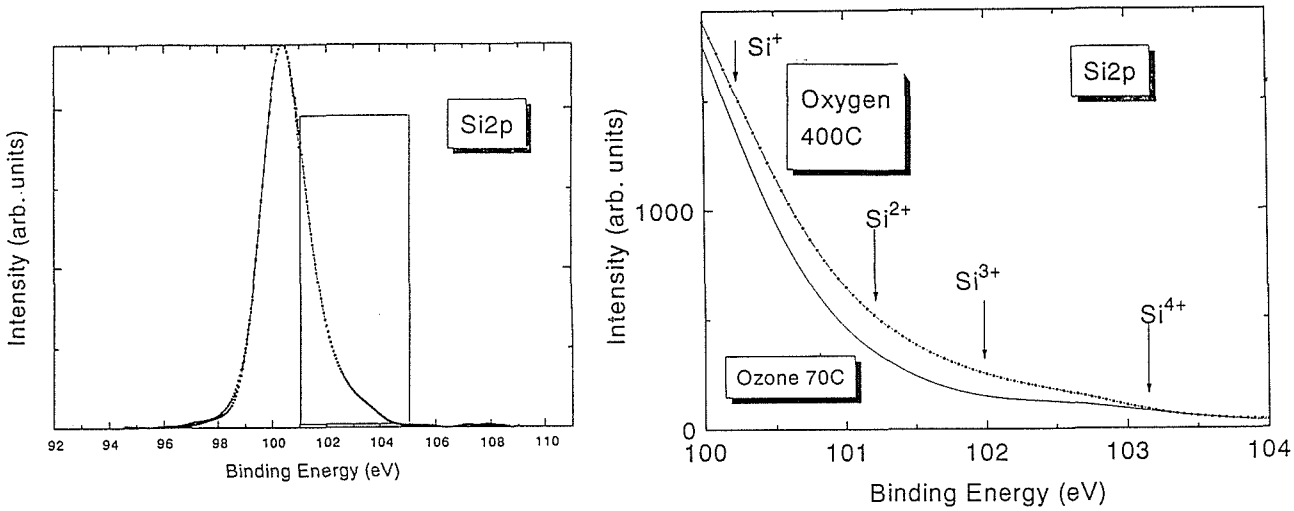

Fig.7 Si 2p spectra taken after the 50L ozone (at 70C) and oxygen (at 400C) exposure: (a) Full spectra, (b) Expanded spectra near the shoulder of (a).

Finally, the increase of O 1s intensity by the exposure of ozone and oxygen was investigated after the termination of Si (111) surface with hydrogen. The results is shown in Fig.8. This figure shows the change of O1s intensity by the ozone/oxygen exposure to the Si surface which was exposed to 2000 L of hydrogen. Clear 1x1 LEED pattern was observed after the 2000L exposure of hydrogen to the clean Si surface, which indicating the formation of monohydride on the Si surface.

It is known that the hydrogen termination reduces the oxidation with oxygen by a factor of 10^{12} for Si(111) or Si(100) surface[8]. In fact, oxidation with oxygen was reduced largely by the termination as compared with the oxidation for clean surface (compare Fig.8 with Fig. 4). With ozone, on the contrary, the oxidation was reduced only by one third. The difference between ozone and oxygen in the oxidation of H-terminated surface was much more prominent when we enhanced hydrogen exposure to the Si surface before ozone/oxygen exposure.

Fig. 9 shows the O 1s intensity after the 4L exposure of ozone/oxygen to the Si-substrate which was exposed beforehand to different amount of hydrogen. No O1s intensity was observed for the oxygen exposure when the exposure to hydrogen was more than about 3,000 L. However, O 1s intensity was noticed for ozone exposure even when the pre-exposure of hydrogen was over 10,000 L.

These results suggest that ozone has different mechanisms in the oxidation. Ozone can easily dissociate to atomic oxygen and oxygen molecules at the surface. The atomic oxygen may attack the H-terminated Si surface, which has one Si-H bond oriented normal to the surface and three Si-Si backbonds, will atack both Si-H bond and and the backbonds to form Si-O bonding.

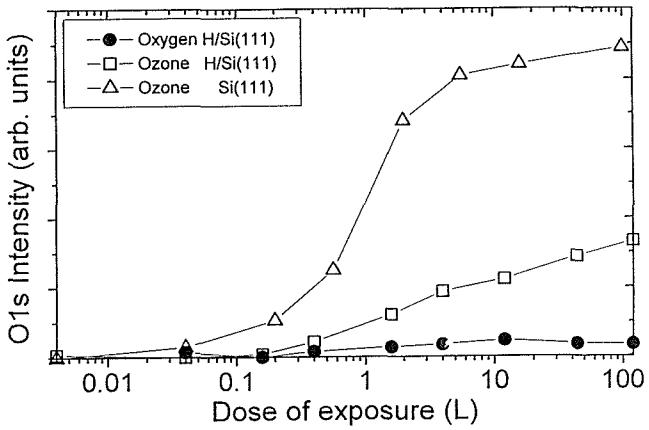

Fig.8 O1s intensity change as a function of ozone/oxygen exposure to hydrogen terminated Si surface.

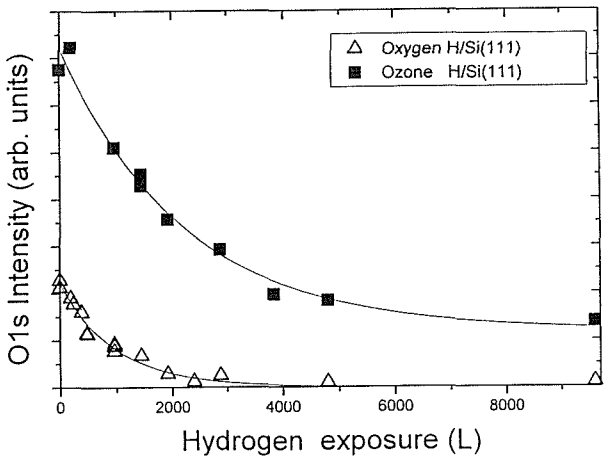

Fig.9 Dependence of O1s intensity after 4L ozone/oxygen exposure to the Si surface covered with hydrogen.

4. Conclusion

The initial stage of oxidation with ozone at clean and hydrogen preadsorbed (monohydride) Si (111) surface was investigated using XPS. We found that ozone can oxidize the Si-surface quite actively than oxygen, even at low (70 C) temperature. The Si-oxide formed by ozone has less suboxide states, which was confirmed from the shape of Si 2p peak. It was also confirmed that ozone can oxidize H-terminated Si surface.

References

(1) Z. Lu, M. Graham, D, Jiang and K. Tan: Appl Phy. Lett. 63(1993)2941
(2) S. Hosokawa and S. Ichimura: Rev. Sci. Instrum. 62 (1991) 1614
(3) S. Ichimura, S. Hosokawa, H. Nonaka and K. Arai: J. Vac. Sci. Technol. A9(1991)2369.
(4) F. Owman, P. Martensson: Surf. Sci. Lett. 303(1994)L367.
(5) P. Gupta, C. H. Mak, P. A. Coon and S. M. George: Phy. Rev B40(1989)7739.
(6) N. Cabrera and N.F. Mott, Rep. Prog. Phys. 12 (1949) 163
(7) Y. Ono, M. Tabe and H. Kageshima: Phy. Rev. B48(1993)14291.
(8) J. Westermann, H. Nienhaus and W. Monch: Surf. Sci. 311(1994)101.

High Resolution Analysis of Interfaces by AES Depth Profiling

S. Hofmann
Max-Planck-Institut für Metallforschung, Institut für Werkstoffwissenschaft
Seestr. 92, D-70174 Stuttgart, Germany

Abstract

Depth profiling by ion sputtering in combination with a surface analysis method such as AES has become a powerful tool for the chemical characterization of thin film interfaces with high resolution. The limiting factors for the attainment of high depth resolution have been disclosed by numerous experiments with model bilayer and multilayer systems. Examples of recent progress in reducing the degradation of depth resolution caused by sputtering induced changes of surface topography and composition show that the physical limits of depth resolution of the order of a few atomic monolayers can be approached. Comparison of theoretical modeling of depth profiles with experimental data, taking into account atomic mixing, surface roughness and information depth (i. e. Auger electron escape depth for AES), allows the determination of the resolution function. This enables deconvolution of the measured profiles with high precision in the monolayer regime.

1. Introduction

Advanced materials science and technology is increasingly based on thin film structures with connecting interfaces, the properties of which often are decisive for the whole system. Therefore, analysis and control of the chemical composition at the atomic monolayer level is essential and can be provided by sputtering in combination with a surface analysis technique such as Auger electron spectroscopy (AES) /1/. Today, this universally applicable method of compositional sputter depth profiling has become the most frequently used method for the chemical analysis of thin films. By bombardment of the surface with energetic ions, generally Ar^+ ions, the sample surface is eroded and deeper layers are laid free for AES analysis. Ideal microsectioning should proceed layer-by-layer in order to measure the true, original in depth distribution of composition. In practice, however, the measured profiles often are considerably broadened by various effects usually categorized as instrumental factors, sample characteristics and ion beam induced surface distortions (see e. g. reviews in refs. /2/ - /4/). Thus, only careful optimization of the experimental conditions enables a detailed analysis of interfacial layers, as shown in Fig. 1 /5/. The 7 nm thick Ti interface layer between the Si substrate and the TiN layer is only disclosed when sputtering with 1 keV ion energy and glancing incidence angle lead to improved depth resolution. The aim of this paper is to summarize the important progress in the achievement of high depth resolution particularly for AES depth profiling.

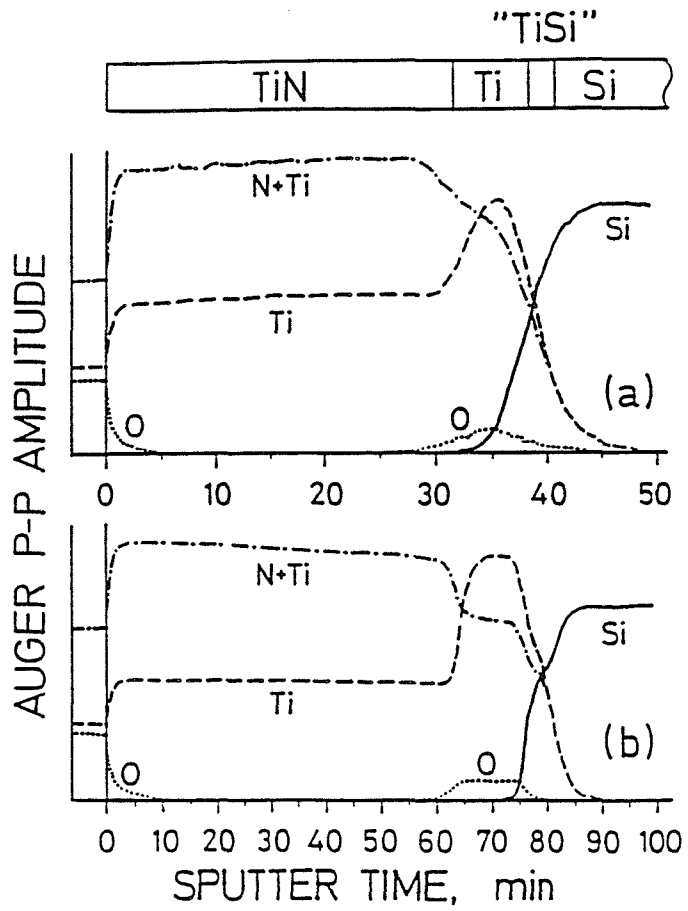

Fig. 1: Depth profiles of aTiN layer on top of Si with a Ti interlayer, sputter profiled with two different conditions:
(a) 3 keV Ar^+, $\Theta = 50$ °; (b) 1 keV Ar^+, $\Theta = 80$ °;
From Pamler et al. /5/. (With permission of John Wiley & Sons, Ltd.).

2. Different Contributions to Profile Broadening

Depth resolution in sputter profiling is defined by a certain broadening of the relation signal intensity versus depth when sputtering through a sharp interface between two media /6/. By convention, the depth resolution Δz is defined by the distance within which the intensity decreases from 84 % to 16 % (or increases from 16 % to 84 %) of its maximum value /2, 3, 6/. Assuming the shape of the interface profile to be an error function, this definition means $\Delta z = 2\sigma$ where σ is the standard deviation of the Gaussian resolution function /2, 3/.

There is a large number of effects which cause interface broadening in sputter profiling and thus a deterioration of the depth resolution. Many researchers have contributed to establish general guidelines for minimizing these effects and therefore obtaining high resolution depth profiles, as summarized in Table 1.

Table 1
Guidelines for optimized sputter depth profiling conditions and methods

Sample ambient	Low residual reactive gas pressure ($< 10^{-8}$ Pa); "free" sample mount to prevent redeposition
Ion beam	Constant uniform intensity (scanning); low beam energy (≤ 1 keV); high mass ion species (or reactive species); large incidence angle for smooth sample ($> 60°$)
Analyzing conditions	Analyzed area centered in and small against sputtered area; sample rotation; minimized information depth
Sample characteristics	Smooth, polished surface; non-crystalline, no 2nd phases; oxides, semiconductors; components with similar sputtering yields; negligible diffusion and segregation and good electrical and thermal conductivities

The measured Δz is composed of different contributions. Assuming approximatively Gaussian shape resolution functions and mutual independence, they add up in quadrature as given by /2 - 4, 7/:

$$\Delta z = \left[\Delta z_0^2 + \Delta z_s^2 + \Delta z_k^2 + \Delta z_\lambda^2 + \Delta z_r^2 + \Delta z_i^2 + \ldots\right]^{1/2} \qquad (1)$$

$$= \left[\sum_j \left(\Delta z_j\right)^2\right]^{1/2}$$

Equation (1) explicitly contains the original interface width Δz_0 (which should be zero for optimum test samples), surface roughening by sputtering statistics Δz_s, atomic mixing Δz_k, information depth Δz_λ, ion beam induced roughening Δz_r, inhomogenous ion beam intensity Δz_i. Whereas Δz_s, Δz_k and Δz_λ are typically constant (after the first few nanometers), Δz_r and Δz_i generally increase with sputtered depth /2 - 4/. Therefore, eq. (1) can be used to extract the different contributions to the measured Δz, as recently shown by Vajo et al. /7/.

3. Approaching the Limits of Depth Resolution

A prerequisite to obtain high resolution depth profiles is an optimum set up of the instrumental parameters (see Table 1), e. g. sufficiently low reactive gas pressure ($< 10^{-8}$ Pa), and homogeneous ion beam current density in the analysed area (to be small against the ion beam rastered area). Usually, a test of appropriate experimental conditions is performed with certified reference material Ta_2O_5/Ta, for which $\Delta z \leq 2$ nm should be attained when sputtering with 1 - 3 keV Ar^+ ions /8, 9/.

The next step in optimizing depth profiling conditions is the reduction of ion beam induced changes of the surface topography, i. e. roughening (Δz_r in eq. (1)). It originates from variations of the local sputtering rate across the surface, owing to either inhomogeneous ion beam density or inhomogeneities in the sample. Whereas the first effect can be avoided by a careful set up and rastering of the primary ion beam, the latter one occurs - even for a compositionally homogeneous sample - for polycrystalline samples characterized by variations of crystal lattice orientation within the analysed area. In this case, sputtering with an ion beam from one direction leads to considerable roughening caused by the crystalline orientation dependence of the sputtering yield /10/. Both the above effects can be drastically reduced by glancing incidence of the ion beam and by multidirectional ion bombardment as achieved by sample rotation during sputtering /11/.

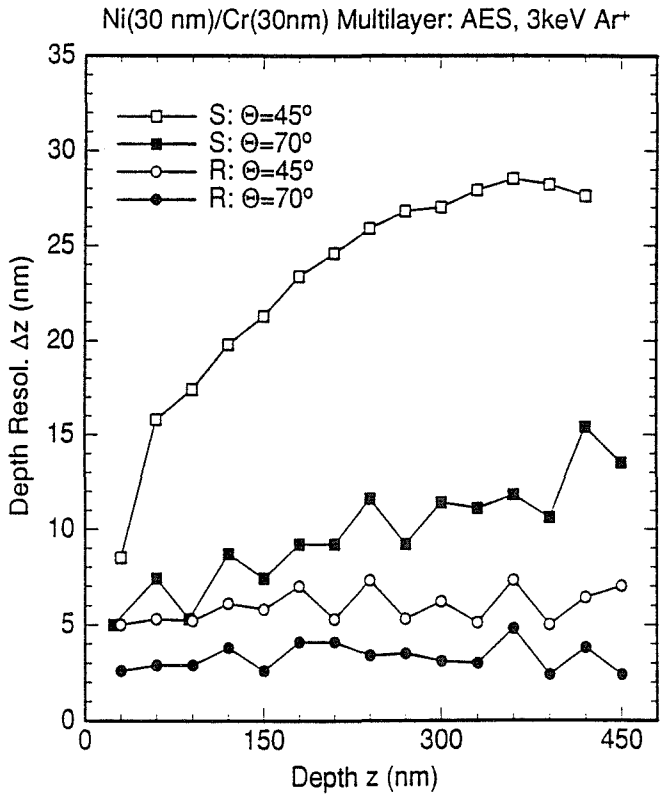

Fig. 2: Depth resolution Δz as a function of the sputtered depth for AES profiling of Ni(30 nm)/Cr(30 nm) multilayer samples with 3 keV Ar^+ ion without (S) and with (R) sample rotation (1 rpm) for the ion incidence angles Θ = 45 ° and 70 °. Adapted from ref. /13/.

A typical example of the above improvements of depth resolution are the results, shown in Fig. 2 for depth profiling of Ni/Cr multilayes /12/, where $\Delta z \approx 3$ nm is obtained for Θ = 70 ° ion incidence angle and sample rotation, being near the limit of Δz for 3 keV Ar^+ ions /13/. It is obvious that amorphous targets do not need sample

rotation to obtain high depth resolution. This is also valid for Ar^+ ion bombarded semiconductor samples which amorphize under the ion beam. Even metal/semiconductor multilayer systems with metal layer thicknesses in the nanometer range are not prone to ion beam induced roughening. The latter is easily recognized in multilayer samples by increasing Δz width depth /2 - 4/.

Besides ion beam induced changes of the surface topography, changes in surface composition are detrimental to high depth resolution. Provided that preferential sputtering, radiation enhanced diffusion and segregation are negligible /2 - 4/ the remaining fundamental effect is atomic mixing caused by the energy deposition of the primary ion beam incollisional cascades and inevitably coupled with sputtering /14/. It is most efficient within the projected ion range and should therefore vary with ion species, energy and incidence angle. An example is shown in Fig. 3

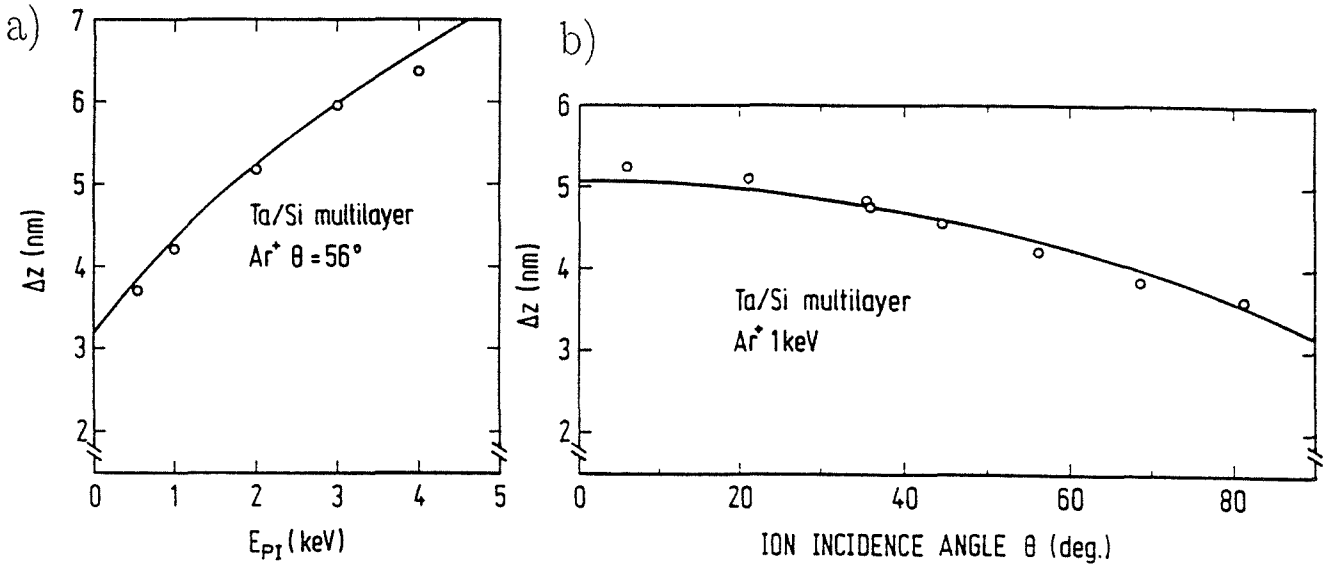

Fig. 3: Depth resolution Δz determined from Ta/Si multilayer AES depth profiles
(a) as a function of the Ar^+ ion energy at $\Theta = 56$ °,
(b) as a function of the ion incidence angle Θ for 1 keV Ar^+ ions.
After ref. /4/.

for Δz obtained in AES depth profiling with Ar^+ ion sputtering of Ta/Si multilayers (3/7 nm thickness, 20 layers), as a function of the ion energy E_{PI} (Fig. 3a) and of the incidence angle Θ (Fig. 3b) /4/. It is recognized that $\Theta > 80$ ° and $E_{PI} < 1$ keV give optimum Δz. The extrapolated values of about $\Delta z \approx 3$ nm show that there are probably additional contributions to Δz, like Δz_0, Δz_s and Δz_λ in eq. (1). Besides the theoretical limit of sputtering threshold energy, in practice the approach to low ion energy and high incidence angle is impeded by extremely low sputtering rates and therefore too long profiling times, and a useful compromise has to be found.

Last but not least, the information depth has to be optimized (i. e. Δz_λ in eq. (1)). In AES, this means to use low energy Auger electrons for elemental analysis and/or a

high emission angle to minimize the escape depth as determined by the characteristic attenuation length /15/. Depth profiling studies on a GaAs/AlAs superlattice structure demonstrated the magnitude of the depth resolution that can be obtained under different conditions in these high quality samples (with $\Delta z_0 \rightarrow 0$, see eq. (1)) /16, 17/. An example of recent results is shown in Fig. 4 /17/.

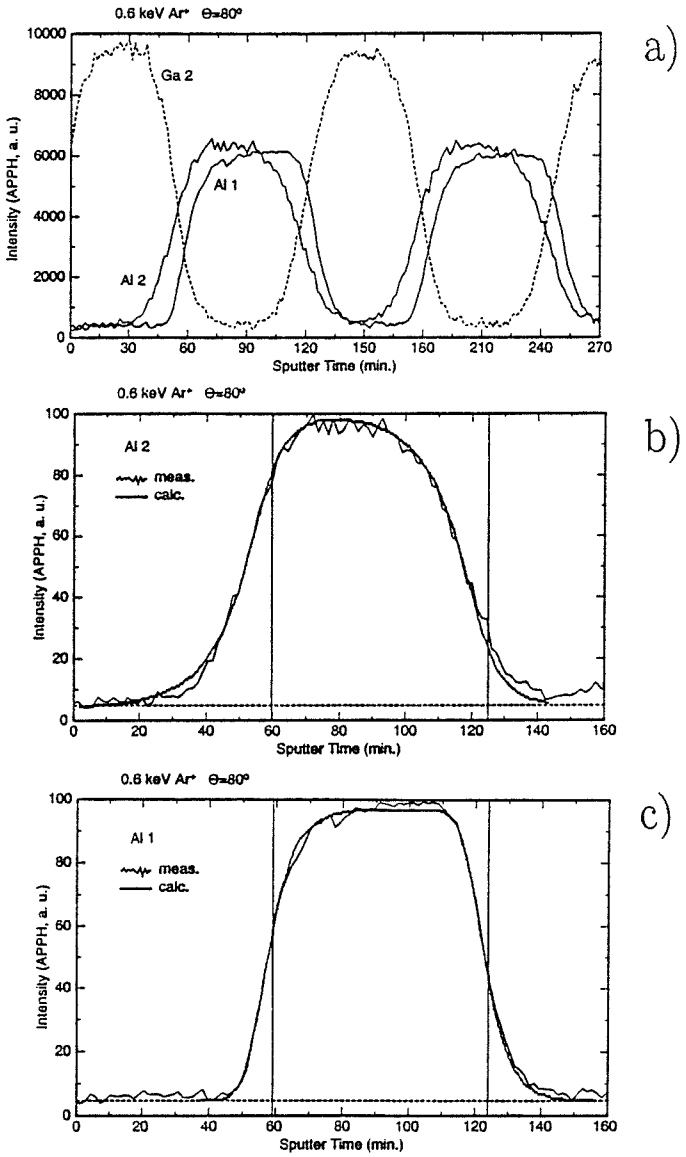

Fig. 4: AES depth profiles of a GaAs/AlAs superlattice structure sputtered with 0.6 keV Ar^+ ions at $\Theta = 80$ °:
(a) Measured Ga and Al intensities (Al 1: 68 eV, Al 2: 1396 eV) as a function of the sputtering time;
(b) Fit of the MRI profile calculation to the measured profile of Al 2 (λ = 1.7 nm) from Fig. 4a;
(c) Fit of the MRI calculation to the measured profile of Al 1 (λ = 0.4 nm) from Fig. 4a.
After ref. /17/.

To obtain optimum depth resolution, according to Fig. 3 the sputtering conditions where chosen to E_{PI} = 0.6 keV primary ion energy and Θ = 80 ° incidence angle. The measured profile of the first four layers is depicted in Fig. 4a. Note that the 9.9 nm thick AlAs layers are profiled using simultaneously the low energy Al peak (Al 1, 68 eV) and the high energy Al peak (Al 2, 1396 eV), giving $\Delta z \approx 1.9$ nm and $\Delta z \approx 3.1$ nm, respectively.
By application of a simple model calculation to reproduce interfacial profiles in term of the three fundamental effects atomic mixing (M), surface roughness (R) and information depth (I) (the so called MRI model) it was possible to quantitatively simulate the measured profiles for Al 2 and Al 1 as shown in Fig. 4b and 4c, respectively /17/. The corresponding values of the atomic mixing length w = 1.0 nm, the roughness parameter σ = 0.6 nm, and the information depth, given by the Auger electrons escape depth λ(Al 1) = 0.4 nm, λ(Al 2) = 1.7 nm are in agreement with literature values of ion ranges and electron attenuation lengths /15/. By reducing the ion energy to 0.2 keV, Δz can be lowered to about 1.5 nm /18/, which is close to the limit of Δz in sputter depth profiling.

4. Conclusions

High resolution interface analysis by AES depth profiling requires careful optimization of the experimental profiling conditions. It is based on understanding the detrimental effects of instrumental factors, ion beam - sample interaction and specific sample characteristics derived from studies with well defined reference materials. In particular for metallic samples, sample rotation during profiling yields optimum depth resolution, which is generally achieved with low energy primary ions (< 1 keV) and high incidence angle (> 70 °). Provided that preferential sputtering, radiation enhanced diffusion and segregation are negligible, the remaining fundamental effects in profile broadening are atomic mixing in the collisional cascade, surface roughening in the monolayer regime due to the statistical nature of sputter erosion and the information depth given by the mean escape depth of the Auger electrons. Recent results on high quality GaAs/AlAs superlattice structures demonstrated that a depth resolution below 2 nm can be obtained and the profile shape can be fitted by calculations (MRI-model) which clearly disclose the influence of atomic mixing, surface roughness and information depth.

References:

/1/ D. Briggs and M.P. Seah, eds, Practical Surface Analysis Vol. 1: AES and XPS, 2nd ed. (Wiley, Chichester, 1990).
/2/ S. Hofmann, Depth Profiling by AES and XPS, chap. 4, p 148 in ref. /1/.
/3/ S. Hofmann, J. Vac. Soc. Japan 33 (1990) 721
/4/ S. Hofmann, Progr. Surf. Sci. 36 (1991) 35
/5/ W. Pamler, E. Wildenauer and A. Mitwalsky, Surf. Interface Anal. 15 (1990) 621
/6/ ASTM E-42 Doc. Nr. 673 (1991)
/7/ J.J. Vajo, E.-H. Cirlin, R.C. Wilson and T.C. Hasenberg, in: SIMS 8, eds: A. Benninghoven, K.T.F. Janssen, J. Tümpner and H.W. Werner (Wiley, Chichester 1992) p.355
/8/ Certified Reference Material, BCR No. 261 (NPL No. 87B83)
/9/ C.P. Hunt and M.P. Seah, Surf. Interface Anal. 5 (1983) 199
/10/ W. Pamler, K. Wangemann, S. Kampermann and W. Hösler, Nucl. Inst. Meth. Phys. Res. B 51 (1990) 34
/11/ S. Hofmann and A. Zalar, Surf. Interface Anal. 21 (1994) 304
/12/ S. Hofmann, A. Zalar, E.-H. Cirlin, J.J. Vajo, H.J. Mathieu and P. Panjan, Surf. Interface Anal. 20 (1993) 621
/13/ S. Hofmann, Appl. Surf. Sci. 70/71 (1993) 19
/14/ U. Littmark and W.O. Hofer, Nucl. Instr. Meth. 168 (1980) 329
/15/ S. Tanuma, C.J. Powell and D.R: Penn, Surf. Interface Anal. 17 (1991) 927
/16/ K. Yoshihara, D.W. Moon, D. Fujita, K.J. Kim and K. Kajiwara, Surf. Interface Anal. 20 (1993) 673
/17/ S. Hofmann, Surf. Interface Anal. 21 (1994) 673
/18/ K. Kajiwara and H. Kawai, Surf. Interface Anal. 15 (1990) 433

Three-Dimensional Three-Atom Model for Computer Simulation of Impact-Collision Ion Scattering Spectroscopy

Wataru Hayami, Ryutaro Souda, Takashi Aizawa and Yoshio Ishizawa
National Institute for Research in Inorganic Materials
1-1 Namiki, Tsukuba, Ibaraki 305, Japan

A new model for computer simulation of impact-collision ion scattering spectroscopy (ICISS) has been developed. Using this model, the scattering cross section of the three target atoms arbitrary placed in the three-dimensional space can be calculated. The ICISS data of the NbC(111) surface has been analysed within sufficiently short time.

1.Introduction

Impact-collision ion scattering spectroscopy is one of powerful techniques for analyses of surface structure [1]. In the case that the structure is complicated due to reconstruction or adsorption etc. or a quantitative result is required from ICISS data, computer simulations are inevitable. To calculate the differential scattering cross section of the target atoms in an arbitrary configuration, approximations are usually adopted to simplify the scattering process and make the computational time reasonably short.

Among models reported so far [2-9], Williams, Kato, Daley and Aono (WKDA) proposed a algorithm which utilize an analytical solution to the trajectory calculation to reduce the computational time considerably [9].

In this paper, extending WKDA algorithm, we will describe the new model to calculate the three-dimensional(3D) scattering cross section of the three target atoms arbitrary placed in the 3D space [10]. Compared with the two dimensional case, the computational time does not increase so much. This is the merit of our algorithm.

2.Theory

2.1.General formula of scattering cross section.

Variables concerning the 3D scattering process is illustrated in fig.1. Let us define N as the number of ions scattered into the direction of the solid angle element, $d\Omega_L = \sin\theta_L \, d\theta_L \, d\phi_{out}$, and I_0 as the incident beam flux. From the conservation of the number of particles,

$$N = I_0 \, s_1 \, ds_1 \, d\phi_1 = I(\theta_L, \phi_{out}) \sin\theta_L \, d\theta_L \, d\phi_{out} \qquad (1)$$

Then the differential cross section σ is expressed as

$$\sigma(\theta_L, \phi_{out}) = I(\theta_L, \phi_{out}) / I_0 = (s_1 / \sin\theta_L) |D|^{-1} , \qquad (2)$$

where D is the Jacobian determinant,

$$D = \frac{\partial(\theta_L, \phi_{out})}{\partial(s_1, \phi_1)} = \frac{\partial\theta_L}{\partial s_1}\frac{\partial\phi_{out}}{\partial\phi_1} - \frac{\partial\theta_L}{\partial\phi_1}\frac{\partial\phi_{out}}{\partial s_1} \qquad (3)$$

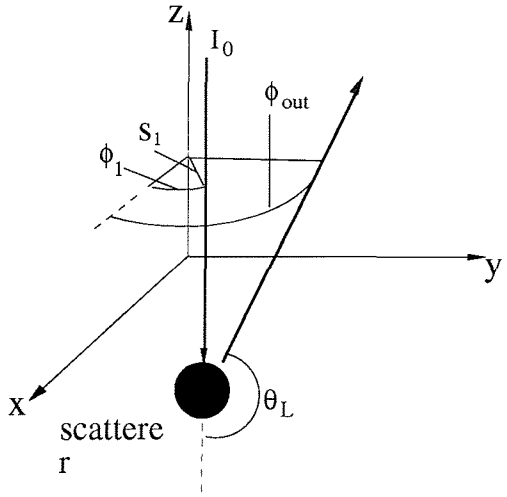

Fig. 1

The ion beam with intensity I_0 is set parallel to the z axis. θ_L is the scattering angle in the laboratory coordinate system.

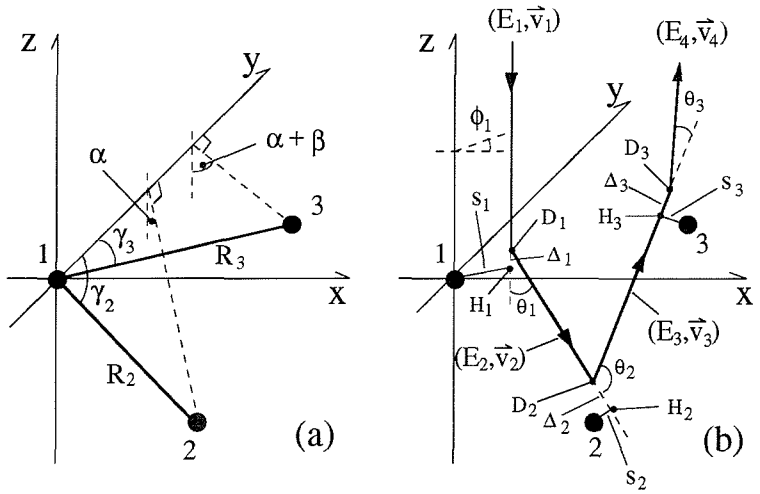

Fig. 2.

Variables in the model. Atom 1 is at the origin. $\overrightarrow{R_2}=(R_{2x}, R_{2y}, R_{2z})$: vector from atom 1 to 2. $R_2 \equiv |\overrightarrow{R_2}|$. γ_2 : angle between $\overrightarrow{R_2}$ and the y axis. α : angle between the yz plane and $\overrightarrow{R_2}$ y plane.E_1: energy of the ion. $\vec{v_1}$: unit vector of the direction. s_1: impact parameter. θ_1: scattering angle. D_1: turning point. $\Delta_1 \equiv |\overrightarrow{D_1H_1}|$. The same with atom 2 and 3.

2.2 Model

The configuration of three target atoms and the trajectory of an ion are illustrated in fig.2 (a),(b). Atom 1 is placed at the origin. The ion is supposed to collide sequentially with the three atoms (i.e. in the order of atom 1-2-3) and to proceed straightforward between atoms. The atom 3 works as a blocking atom.

Let us look at the parameters and equations required for the calculation. Suppose the beam-detector plane is parallel to xz plane in fig.2 (b).

As to the first scattering,

$$D_{1x}=s_1 \cos\phi_1 \quad (4)$$

$$D_{1y}=s_1 \sin\phi_1 \quad (5)$$

$$v_{2x}=\sin\theta_1 \cos\phi_1 \quad (6)$$

$$v_{2y}=\sin\theta_1 \sin\phi_1 \quad (7)$$

where θ_1 is known from s_1 and E_1.

About the position of the second atom,

$$R_{2x}=R_2 \sin\gamma_2 \sin\alpha \quad (8)$$

$$R_{2z}= - R_2 \sin\gamma_2 \cos\alpha \quad (9)$$

Since line D_1D_2 is expressed as $\overrightarrow{D_1} + t\,\vec{v_2}$, where t is a parameter,

$$s_2= | \overrightarrow{D_1} - \overrightarrow{R_2} + \{ (\overrightarrow{R_2} - \overrightarrow{D_1}) \vec{v_2} \} \vec{v_2} | \quad (10),$$

and

$$D_{2x}=D_{1x} + \{ (\overrightarrow{R_2} - \overrightarrow{D_1}) \vec{v_2} - D_2 \} v_{2x} \quad (11)$$

$$D_{2y}=D_{1y} + \{ (\vec{R_2} - \vec{D_1}) \vec{v_2} - D_2 \} v_{2y} \quad (12)$$

$$D_{2z}=D_{1z} + \{ (\vec{R_2} - \vec{D_1}) \vec{v_2} - D_2 \} v_{2z} \quad (13)$$

θ_2 and D_2 are obtained from the table previously calculated. So,

$$\theta_2 = \theta_2 (E_2, s_2) \quad (14)$$

$$D_2 = D_2 (E_2, s_2) \quad (15)$$

where E_2 is known from E_1 and θ_1.

The direction after the second scattering is described as

$$v_{3x} = v_{2x} \cos \theta_2 + \sin \theta_2 / s_2 [D_{1x} - R_{2x} + \{ (\vec{R_2} - \vec{D_1}) \vec{v_2} \} v_{2x}] \quad (16)$$

$$v_{3y} = v_{2y} \cos \theta_2 + \sin \theta_2 / s_2 [D_{1y} - R_{2y} + \{ (\vec{R_2} - \vec{D_1}) \vec{v_2} \} v_{2y}] \quad (17)$$

$$v_{3z} = v_{2z} \cos \theta_2 + \sin \theta_2 / s_2 [D_{1z} - R_{2z} + \{ (\vec{R_2} - \vec{D_1}) \vec{v_2} \} v_{2z}] \quad (18)$$

About the position of the third atom,

$$R_{3x}=R_3 \sin \gamma_3 \sin (\alpha + \beta) \quad (19)$$

$$R_{3z}= - R_3 \sin \gamma_3 \cos (\alpha + \beta) \quad (20)$$

Just like the second scattering,

$$s_3 = | \vec{D_2} - \vec{R_3} + \{ (\vec{R_3} - \vec{D_2}) \vec{v_3} \} \vec{v_3} | \quad (21)$$

$$\theta_3 = \theta_3(E_3, s_3) \quad (22)$$

$$E_3 = E_3(E_2, \theta_2) \quad (23)$$

Under the condition that $\phi_{out} = 0$ and $v_{4z} = \cos(\pi - \theta_L)$,

$$v_{4y} = v_{3y} \cos \theta_3 + \sin \theta_3 / s_3 [D_{2y} - R_{3y} + \{ (\vec{R_3} - \vec{D_2}) \vec{v_3} \} v_{3y}] = 0 \quad (24)$$

$$v_{4z} = v_{3z} \cos \theta_3 + \sin \theta_3 / s_3 [D_{2z} - R_{3z} + \{ (\vec{R_3} - \vec{D_2}) \vec{v_3} \} v_{3z}] = \cos(\pi - \theta_L) \quad (25)$$

E_1, $\vec{v_1}$ and θ_L are fixed in a calculation. R_2, R_3, γ_2, γ_3, and β are given from the configuration. When s_1 is given, the undetermined variables are ϕ_1, α, D_{1x}, D_{1y}, v_{2x}, v_{2y}, R_{2x}, R_{2z}, s_2, θ_2, D_2, D_{2x}, D_{2y}, D_{2z}, v_{3x}, v_{3y}, v_{3z}, E_3, R_{3x}, R_{2z}, s_3 and θ_3. They are 22 in all. Since the number of the equations is also 22, ϕ_1 and other variables are definitely determined for given s_1.

In order to solve these simultaneous equations, Newton's (Newton - Raphson) method is adopted. The cross section is calculated at once from α and ϕ_1 using eq. (2) and (3). The calculated spectrum is convoluted with the Gaussian function to take in the effect of thermal vibration.

3.Comparison with experiments

As an example, let us take an ICISS data of the NbC(111) surface. NbC has an NaCl type structure and its (111) clean surface is terminated by a 1×1 Nb-atom layer (fig. 3). When the incident beam is along [$\bar{1}$10] direction, an Nb-Nb pair of the first layer (arrow 1) lies on the beam-detector plane. But, considering shadowing of the first-layer Nb over the third-layer Nb (arrow 3) and blocking by the first-layer Nb, this three-atom configuration does not lie on the beam-detector plane.

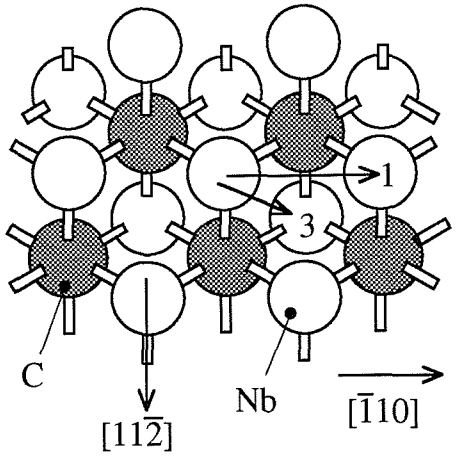

Fig. 3
Top view of the NbC(111) surface. Arrow 1 and 2 indicate the shadowing of the first-layer Nb over the first-layer Nb and over the third-layer Nb, respectively.

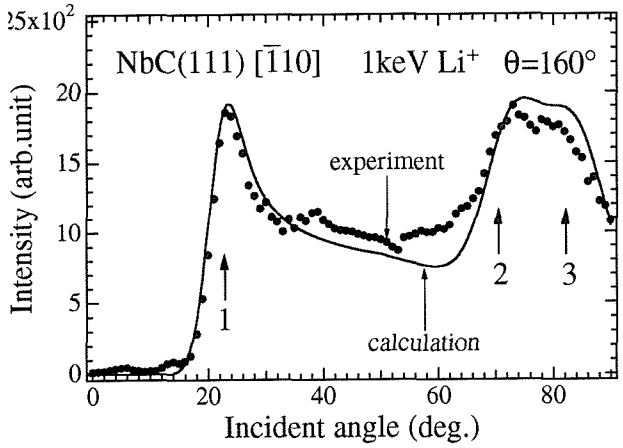

Fig. 4
ICISS data of the NbC(111) surface along [$\bar{1}$10] azimuth. The abscissa is the incident angle of the beam and the ordinate is the intensity of Li ions backscattered by Nb atoms. Numbered arrows correspond to those in fig. 3.

Fig. 4 shows the ICISS data of this surface. In the experimental data, the peak around 20° comes from the shadowing effect of the first-layer Nb-Nb pair. The broad peak around 70° - 90° is the superposition of the shadowing and blocking effects due to the three-atom configuration mentioned above. The configuration has already been determined from the ICISS data along [11$\bar{2}$] and [$\bar{1}$ $\bar{1}$ 2] directions, which indicates that the first-layer Nb atom sift inward by 0.2 Å [11].

Using this configuration, a computer simulation by our model has been performed and the result is shown in the fig. 4. It is convoluted with the Gaussian function and corrected by multiplying $1/\sin\alpha$. It seems in a good agreement with the experiment. The two-atom potential used here is Thomas-Fermi-Moriér potential and the Firsov factor for the screening length is 0.85. The CPU time required for the calculation with our computer (3.5 MIPS) was about 30 seconds.

References

[1] M.Aono, C.Oshima, S.Zaima, S.Otani and Y.Ishizawa, Jpn. J. Appl. Phys. 20 (1981) L829
[2] O.S.Oen, Phys Lett. 19 (1965) 358
[3] R.M.Tromp and J.F.van der Veen, Surf. Sci. 133 (1983) 159
[4] R.S.Daley, J.H.Huang and R.S. Williams, Surf. Sci. 215 (1989) 281
[5] K.Sato, S.Kono, T.Teruyama, K.Higashiyama and T.Sagawa, Surf. Sci. 158 (1985) 644
[6] J.A.Yarmoff, D.M.Cry, J.H.Huang, S.Kim and R.S.Williams, Phys. Rev. B 33 (1986) 3856
[7] Y.Yamamura and W.Takeuchi, Radiat. Eff. 82 (1984) 73
[8] W.Takeuchi and Y.Yamamura, Surf. Sci. 277 (1992) 351
[9] R.S.Williams, M.Kato, R.S.Daley and M.Aono, Surf. Sci. 225 (1990) 355
[10] W.Hayami, R.Souda, T.Aizawa and Y.Ishizawa, Surf. Sci. 303 (1994) 247
[11] W.Hayami, R.Souda, T.Aizawa, S.Otani and Y.Ishizawa, Phys. Rev. B 47 (1993) 13752

Surface Segregation in TiC Studied by Low-Energy Ion Scattering and Auger Electron Spectroscopy

R. Souda, W. Hayami, T. Aizawa, S. Otani and Y. Ishizawa
National Institute for Research in Inorganic Materials
1-1 Namiki, Tsukuba, Ibaraki 305, Japan

The segregation of W impurities at the TiC(001) surface has been investigated by using impact collision ion scattering spectroscopy and Auger electron spectroscopy. The topmost layer of TiC(001) is strongly enriched with W accompanied by carbon vacancies (20-25%) in their nearest neighbors. The oxygen is incorporated by the (001) surface irrespective of the existence of W segregants, but its uptake rate is moderately enhanced by W, due probably to oxygen diffusion into the bulk mediated by the carbon vacancies.

1. Introduction

Interest in transition-metal carbides (TMCs) has been promoted by their unique properties. Most exhibit high melting points and great hardness, characteristic of strong metal-carbon covalent-like bonding, together with the metallic properties similar to those of the parent transition metals [1]. Recently, surface properties of TMCs have attracted considerable attention with respect to various technological applications such as a catalyst [2] and a new stable electron emitter with high brightness [3]. We have been investigating surface segregation of dilute transition-metal impurities in titanium carbide (TiC) by using impact collision ion scattering spectroscopy (ICISS) [4]. Impurity segregation should largely influence the surface properties, and a knowledge of interactions of each surface component with impinging gases such as oxygen, hydrogen, and carbon monoxide is crucial in surface chemistry [5-8]. In this paper, attention will be paid mainly to the segregation of W to the TiC(001) surface.

2. Experimental

The experiments were performed in an ultrahigh vacuum (UHV) system (base pressure of $1x10^{-10}$ Torr), consisting of a main scattering chamber equipped with Li^+ and He^+ ion sources, low-energy electron diffraction (LEED) optics, and a built-in rotatable hemispherical electrostatic energy analyzer. A beam of Li^+ was generated by a thermionic-type ion source while the He^+ ion was produced in a discharge-type ion source. The ions were incident upon a surface by changing glancing angles, α, and ions scattered through a fixed scattering angle of 160° were detected by means of the electrostatic analyzer.

A single-crystal rod of TiC including 0.6 wt% bulk W impurities was grown with a floating zone method [9]. The TiC(001) surface was cleaned by several flash heatings up to 1600°C in UHV. The surface thus prepared showed a sharp, well-defined 1x1 pattern in LEED and no visible oxygen contamination in He^+ ion scattering. The sample was then flash heated at 1700°C to segregate the W impurities to the surface. This treatment did not change the LEED pattern.

3. Results and discussion

The polar angle scans of the surface peak intensities (at E=555 eV for Ti and E=855 eV for

W) along the [110] azimuth are shown in Fig. 1. Also indicated in the inset is a schematic of the ion trajectories together with the shadow cones for Ti (open circles) and C (solid circles) atoms calculated using the Thomas-Fermi potential. The cutoff of the Ti peak intensity at around α=20° is due to the shadowing effect occurring on the Ti chain in the topmost layer. The W segregants are substituted for Ti at the topmost layer. Indeed, the occurrence of the shadowing effect at the same angles for both Ti and W intensities indicates that W sits in the same plane formed by Ti within an experimental accuracy of ±0.5 Å. The marked enhancement in intensity at around α=50° arises from the focusing of the incident ion beam onto the second-layer Ti atoms by the first-layer C atoms. However, such a structure is not recognized in the W intensity. Thus, W is highly concentrated at the topmost layer and its distribution in the second layer is negligible. From the comparison of the surface peak intensities with and without the W segregants, the sensitivity factor for W is estimated to be 2.1 relative to Ti. The first layer composition of the surface shown in Fig. 1 is determined as 27% Ti and 73% W.

The polar-angle scans in the [100] azimuth are shown in Fig. 2. The intensity drop at around α=20° is due to the shadowing effect of the Ti or W atom by the adjacent C atom. The W peak exhibits a marked shoulder around α=15° which is not present for Ti. The shoulder is attributable to the carbon vacancies and its concentration is estimated to be 20-25 % from the intensity ratio of the shoulder to the focusing peak at α=25°. It is notable that the C atoms surrounding the W segregants are selectively absent.

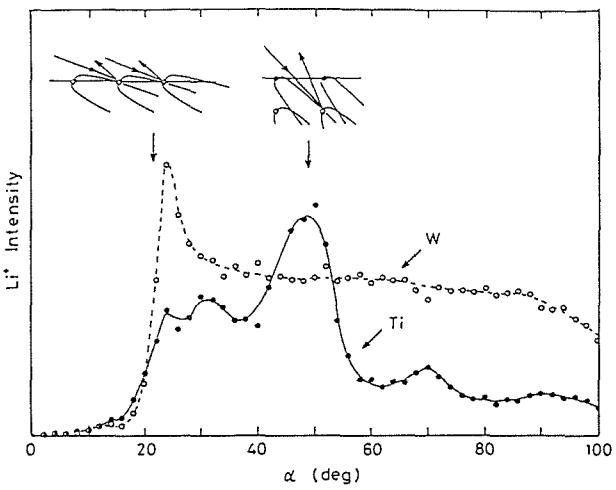

Fig. 1. The ICISS polar-angle scans at the W-segregated TiC(001) surface. The Li^+ intensities corresponding to Ti (555 eV) and W (855 eV) surface-peak positions are plotted against α in the [110] azimuth.

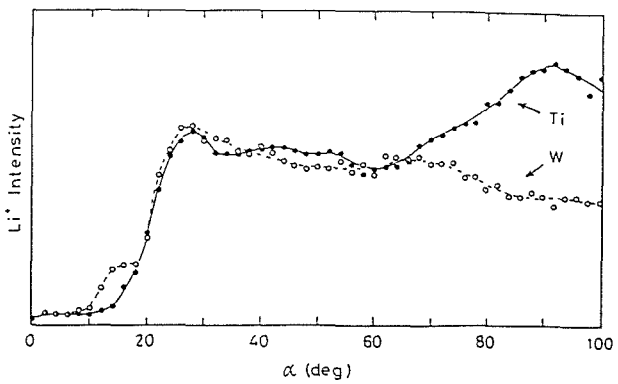

Fig. 2. Same as in Fig. 2 but along the [100] azimuth.

The surface oxidation is investigated by He^+ ICISS combined with AES. The surface peak intensities in He^+ scattering (E_0=1 keV) are taken as a function of the O_2 exposure. In Fig. 3 are shown the results for (a) the W-free TiC(001) surface and (b) the TiC(001) surface. At the initial stage, the Ti (O) peak intensity decreases (increases) with O_2 exposure and becomes constant above 10L ($1L$=1 langumuir=1x10^{-6} Torr·s). The results are almost independent of the segregation of W except for a more dramatic change of the W peak intensity compared to the Ti peak intensity.

The results for AES of the W-free and W-segregated TiC(001) surfaces are shown in Fig. 4,

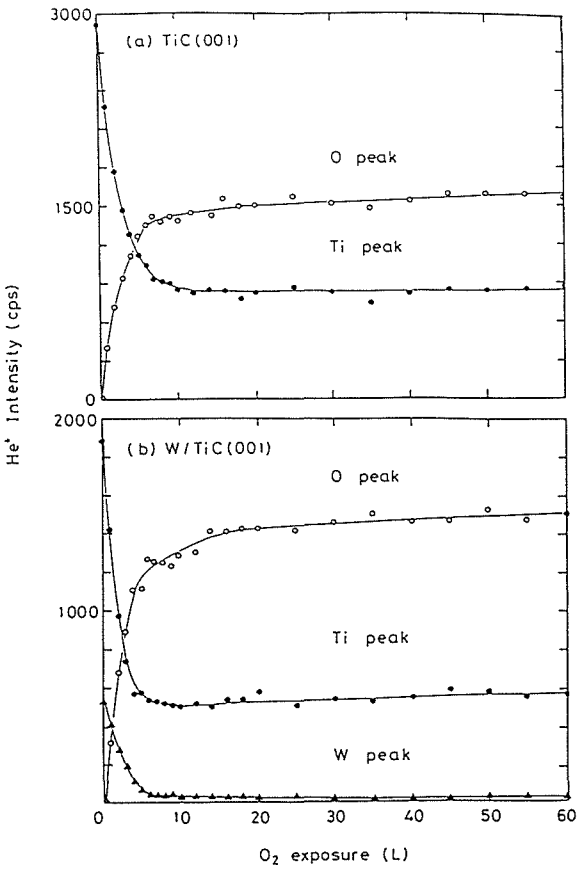

Fig. 3. Changes of the ICISS He^+ peak intensities upon oxygenation of (a) the W-free TiC(001) surface and (b) 35 at% W-segregated TiC(001) surface. The measurements were made at α=80° under the 160°-ICISS condition.

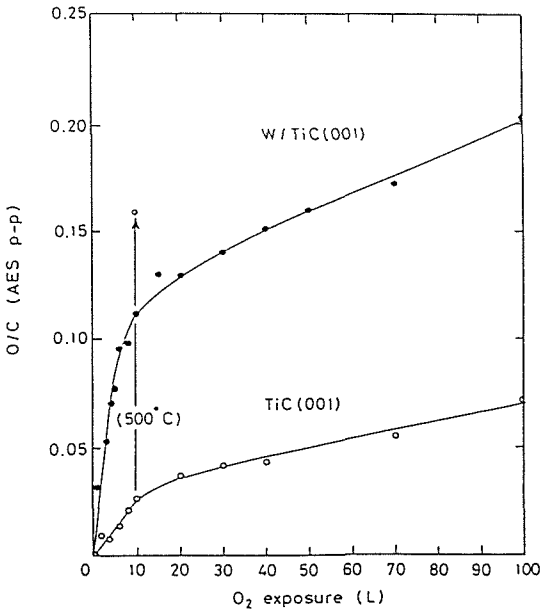

Fig. 4. Changes of the Auger peak ratio, O (513 eV)/C (272 eV), as a function of the O_2-gas exposure.

where the KVV Auger lines for oxygen (513 eV) are plotted relative to those for carbon (272 eV) as a function of the O_2 exposure. In contrast to ICISS, the AES results show no saturation behavior. This has been attributable to the difference in the sampling depth between ICISS and AES: ICISS can detect only the topmost layer if one uses He^+ ions because of the strong ion neutralization effect, while AES may sample the depth of about 5-10 Å which corresponds to the first few layers of TiC. The absence of saturation behavior in Fig. 4 thus indicates that the oxidation proceeds to deeper layers after the surface is covered with chemisorbed oxygen. Interestingly, the AES peak-ratio curve at the W-segregated surface increases rapidly compared to the W-free surface especially at the initial stage, though the ICISS O-peak intensity, corresponding only to the chemisorbed oxygen, shows no such difference between these two surfaces. These behaviors are best understood as the occurrence of the W-induced promotion of oxygen uptake at the TiC(001) surface.

4. Conclusion

Impact collision ion scattering spectroscopy and Auger electron spectroscopy are employed for determination of the structure and the composition of the oxygenated TiC(001) surface with and without the W impurities. The W atoms segregate at the topmost layer with concentrations up to 75

at% but no marked enrichment of W occurs in the deeper layers. The W atoms at the surface are accompanied by 20-25% carbon vacancies in their nearest neighbors. The oxidation of the TiC(001) surface proceeds into the deeper layers and oxygen uptake is moderately enhanced by the existence of W. The promotion effect of the surface oxidation induced by W may be mediated by the carbon vacancies through which oxygen chemisorbed at the W sites can diffuse into the deeper layers.

Acknowledgements

This work was supported in part by the Special Coordination Funds Promoting for Science and Technology.

References

[1] L. E. Toth, Transition Metal Carbides and Nitrides, Vol. 7 (Academic Press, New York, 1971).
[2] I. Kojima, E. Miyazaki, Y. Inoue and I. Yasumori, J. Catal. 59 (1979) 472.
[3] Y. Ishizawa, T. Aizawa and S. Otani, Appl. Surf. Sci. 67 (1993) 36.
[4] R. Souda, W. Hayami, T. Aizawa, S. Otani and Y. Ishizawa, Surf. Sci. 303 (1994) 179; 315 (1994) 93.
[5] C. Oshima, M. Aono, T. Tanaka, S. Kawai, S. Zaima and Y. Shibata, Surf. Sci. 102 (1981) 312.
[6] S. Zaima, Y. Shibata, H. Adachi, C. Oshima, S. Otani, M. Aono and Y. Ishizawa, Surf. Sci. 157 (1985) 380.
[7] I. Kojima, M. Orita, E. Miyazaki and S. Otani, Surf. Sci. 160 (1985) 153.
[8] M. Orita, I. Kojima and E. Miyazaki, J. Chem. Phys. 87 (1987) 4162.
[9] S. Otani, T. Tanaka and Y. Ishizawa, J. Cryst. Growth 92 (1988) 359.

Theoretical Study of Ion Neutralization at Alloy Surfaces

M. Kato, D.J. O'Connor and R.J. MacDonald*
School of Engineering, Nagoya University, Aichi 464-01, Japan
*Department of Physics, The University of Newcastle, NSW 2308, Australia

ABSTRACT: Charge exchange between ions and impurity atoms embedded in metals has been studied. There are two charge exchange processes to be considered; one is that between the ion and the impurity, and the other is that between the ion and the host metal surface. The neutral fraction increases or decreases, depending on the creative or destructive interference between the two processes. Consequently, the neutral fraction strongly depends on the local electronic states and their environment. The effect of interference may be experimentally observed in low energy ion scattering spectroscopy(LEIS).

1. Introduction

When ions are scattered by compound surfaces, the energy of the scattered particles is different depending on the mass of the surface atoms. Thus, LEIS enables the surface compositional and structural analyses. Moreover, if the charge fraction of scattered particles is measured, it is also possible to study the local electronic states. In fact, several experimental evidences that ion beams can probe a local electronic structure have been reported[1-3].

In order to extract a quantitative information from these observations, we need a theory which links the local electronic properties to the neutralization probability. However, available theoretical descriptions appears incomplete for this purpose as most theories assume simple metals, for which band structure and local electronic structure are disregarded[4]. In this paper, therefore, we provide a theoretical study about how the charge exchange collision is related to the local electronic structure, and report remarkable dynamical aspects.

2. Model

We use atomic units, where $\hbar=e=m$(the mass of the electron)=1. Our assumption is that impurity atoms are embedded in a host metal at a very low concentration and primary ions are scattered by an impurity and the valence electron level of the primary ion is energetically situated within the conduction band of the host metal. For this system, there are two resonant-charge-transfer (RCT) processes; one is RCT between the ion and the impurity, and the other is RCT between the ion and the host metal. The local electronic states of the impurity atom are considered by the Anderson-type Hamiltonian. Therefore, the model Hamiltonian takes the form:

$$H(t) = E_a(t)\, C_a^{+}C_a + E_b\, C_b^{+}C_b + \sum_k E_k C_k^{+}C_k + \left[V_{ab}(t)\, C_a^{+}\, C_b + \text{h.c.} \right] + \sum_k \left[W_{bk}(t)\, C_b^{+}\, C_k + \text{h.c.} \right] + \sum_k \left[V_{ak}(t)\, C_a^{+}\, C_k + \text{h.c.} \right] , \quad (1)$$

where the subscript a and b refer to the ion and the impurity atom, respectively. The subscript k refers to the kth conduction electron of the host metal. The energy of the ion's valence level, E_a, is, in general, a function of time because of the image interaction. $V_{ab}(t)$ is the matrix element for RCT process between the ion and the impurity atom, and $V_{ak}(t)$ is that between the ion and the host metal, and W_{bk} is the interaction between the impurity and the host metal. The time dependence of $V_{ab}(t)$ and $V_{ak}(t)$ arises from the classical trajectory of the ion. In contrast, W_{bk} is stationary. These matrix elements can be determined by theories. The processes described by eq.(1) is schematically depicted in fig.1.

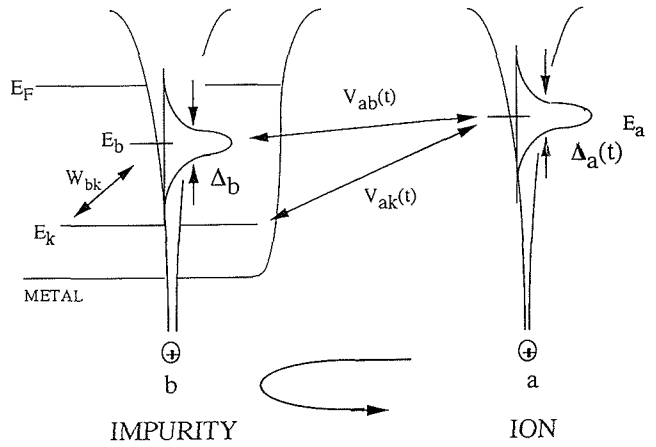

Fig.1 A schematic figure of the processes described by eq.(1) and energy parameters.

3. Numerical Results

The Heisenberg equations derived from eq.(1) are

$$i\dot{C}_a(t) = E_a(t)\,C_a(t) + V_{ab}(t)\,C_b(t) + \sum_k V_{ak}(t)\,C_k(t) \quad , \tag{2a}$$

$$i\dot{C}_b(t) = E_b(t)\,C_b(t) + V_{ab}^*(t)\,C_a(t) + \sum_k W_{bk}(t)\,C_k(t) \quad , \tag{2b}$$

$$i\dot{C}_k(t) = E_k\,C_k(t) + V_{ak}^*(t)\,C_a(t) + W_{bk}^*(t)\,C_b(t) \quad . \tag{2c}$$

We define three energy parameters(see fig.1). First,

$$\Delta_a(t) = 2\pi \sum_k |V_{ak}(t)|^2\,\delta(E - E_k) \quad , \tag{3a}$$

$\Delta_a(t)$ is the energy-width of ion's valence level. Second,

$$\Delta_b(E) = 2\pi \sum_k |W_{bk}|^2\,\delta(E - E_k) \quad , \tag{3b}$$

$\Delta_b(E)$ is the energy width of the impurity level. The third energy parameter is

$$\Theta(t) = 2\pi \sum_k V_{ak}(t)\,W_{bk}^*\,\delta(E - E_k) \quad . \tag{3c}$$

$\Theta(t)$ is named the interference energy.

For numerical integration of eq.(2), the parameter values are assumed as follows. The band width of the host metal is 10 eV and the conduction electrons occupy a half of this band, and E_a=-0.25 eV which is assumed to be time-independent, and E_b=-2 eV. These energies are measured from the Fermi energy E_F(i.e., E_F=0 eV). The time dependence of the interactions is characterized by the collision time t_c, such as $V_{ab}(t)=V_{ab}\exp\{-|t|/t_c\}$ and $V_{ak}(t)=V_{ak}\exp\{-|t|/t_c\}$. V_{ab}=2 eV. The k-dependence of V_{ak} and W_{bk} is neglected. $V_{ak}=\pm W_{bk}$, in which the sign $\pm$ is unfixed as the sign depends on the symmetry of the wavefunctions of the states a, b and k. The value of W_{bk} is that which gives the value Δ_b=5 eV. Thus, Θ=+5 or -5 eV corresponding to $V_{ak}=+W_{bk}$ or $-W_{bk}$, respectively. The number of states of the conduction band is 100.

Fig.2 shows the neutral fraction, $n_a(t)=\langle C_a^+(t)C_a(t)\rangle$, and the electron occupation number of the impurity level, $n_b(t)=\langle C_b^+(t)C_b(t)\rangle$ as a function of time. The initial charge state of the particle is ion. The parameter values used are indicated in the inset. Fig.2(a) is the result for the assumption that $V_{ak}=W_{bk}$, while fig.2(b) is that for the assumption $V_{ak}=-W_{bk}$. Surprisingly, a difference in the relative phase of the matrix elements results in a drastic change of the neutralization process. The solid circles, triangles and crosses in fig.3 are the final neutral fraction(at the limit $t\to\infty$) as a function of collision time t_c. The triangles in fig.3 are the results for the case of Θ=0(i.e., random phase case). The lines of fig.3 are analytical results(sec.4).

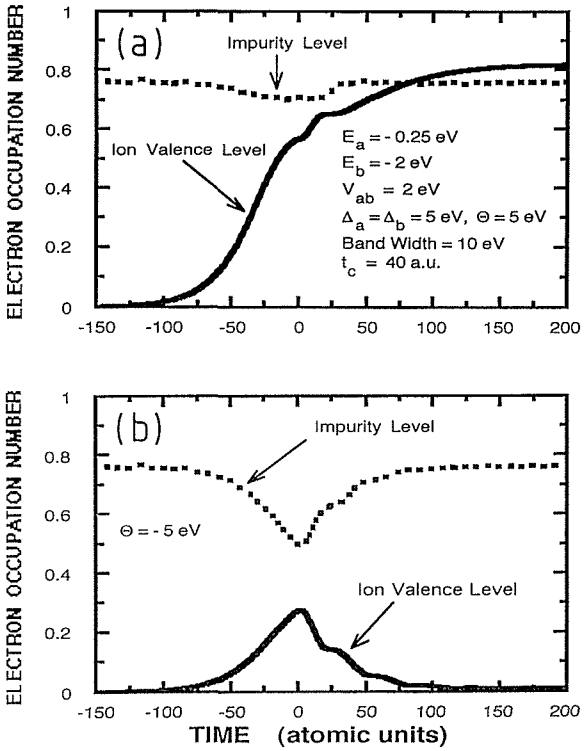

Fig.2 The electron occupation number of the impurity level(dashed line) and ion valence level(full) as a function of time. (a) for Θ=+5 eV and (b) for Θ= -5 eV.

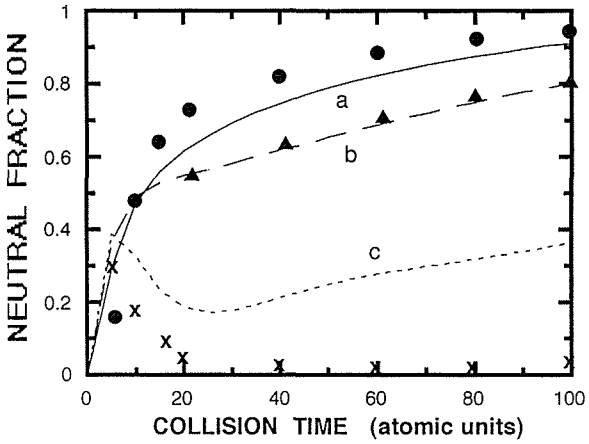

Fig.3 The neutral fraction as a function of the collision time. 1 a.u. = 2.42×10^{-17} sec. Energy parameters used are the same as fig.2. See text for further information.

4 Discussion

It has been accepted that the neutralization probability is large when E_a is energetically situated below the Fermi level[5]. However, the present numerical study clearly elucidates that this simple rule is not applicable generally. We briefly discuss the physical origin of the dramatic change of neutralization probability.

Since it is difficult to solve eq.(2) exactly, we transform eq.(1) to the effective Hamiltonian. The operator C_b can be approximately eliminated by means of a standard manipulation for the Anderson Hamiltonian. After this elimination of C_b, eq.(1) reduces to

$$H(t) = E_a C_a^{+} C_a + \sum_k E_k C_k^{+} C_k + \sum_k \left[\Gamma_{ak}(t)\, C_a^{+} C_k + \text{h.c.} \right] , \qquad (3)$$

with the effective matrix element,

$$\Gamma_{ak}(t) = \underbrace{V_{ak}(t) \exp\{2i\delta(E_k)\}}_{\text{term A}} + \underbrace{\frac{V_{ab}(t) W_{bk}}{E_k - E_b + i\Delta_b/2}}_{\text{term B}} , \qquad (3')$$

where $\delta(E_k)$ is the phase shift of the kth electron because of impurity scattering. The term A of eq.(3') describes the *direct* RCT between the ion and the host metal, and the term B dose the *indirect* RCT between the ion and the host metal via the impurity level. Thus, RCT between the ion and the impurity is modified to the term B. Since the neutralization rate is proportional to $|A+B|^2$, the interference between the terms, A and B, would occur. The destructive or creative interference depends on the sing of two terms, or the relative phase difference between the interactions[6]. The strength of the interference can be quantified by Θ.

When the time evolution of the system is predominantly determined by Δ_b^{-1}(i.e., a large Δ_b in comparison to other energy parameters), it is allowed to employ the local-time-approximation[7]. After this approximation, the neutralization probability n_a is found to be

$$n_a = n_a^0 \exp\left[-\int^{\infty} dt'\ \mathrm{Re}\{\Phi(t')\}\right]$$

$$+ \sum_k f(E_k)\left[-\int^{\infty} dt'\ \Gamma_{ak}(t')e^{-i(E_k - E_a)t'}\ \exp\left\{\frac{1}{2}\int^{t'} dt''\ \Phi(t'')\right\}\right] \quad , \qquad (4)$$

where

$$\Phi(t) = \Delta_a(t) - i\,\frac{2|V_{ab}(t)|^2}{E_b - E_a - i\Delta_b/2} - \frac{2V_{ab}^*(t)\Theta(t)}{E_b - E_a - i\Delta_b/2} \quad ,$$

and n_a^0 is the initial charge state, 1 or 0 for the neutral or ion, respectively. f(E) is the Fermi distribution function. Three lines in fig.3 are the neutral fraction, eq.(4).

It should be noted that the quantity $\mathrm{Im}\{\Phi(t)\}$ is equivalent with the energy shift of the ion valence level. This equivalence is easily confirmed by comparison between eq.(4) and eq.(16) of ref.[5]. The interference effect can be understood in terms of this energy shift. Depending on the sign of Θ, the energy level of the ion shifts downward or upward. When this energy level rises above the Fermi level, the neutral fraction decreases significantly. The detailed discussion about this point is provided elsewhere[8]. As shown in fig.3, the interference effect is very large[9]. Since the sign of Θ is determined by a nature of chemical bonds between the host atoms and the impurity, LEIS experiments using different host metals would manifest the interference effect.

5. Conclusion

Depending on the relative phase difference between interactions, the neutral fraction increases or decreases significantly. This is a consequence of the interference between two neutralization processes(ion-impurity and ion-host metal). Analytical investigation shows that the effect can be discussed by the effective energy shift of ion's valence level. Since the relative phase difference is determined by a spatial symmetry of the wavefunctions(a nature of chemical bonds), LEIS will be useful to probe not only the local electronic states but also their environmental electronic states.

References

[1] R. Souda, W. Hayami, T. Aizawa and Y. Ishizawa; Phys.Rev. **B48** (1993) 17255.
[2] K.A.H. German, C.B. Weare, P.R. Varekamp, J.N. Andersen and J.A. Yarmoff; Phys.Rev.Lett. **70** (1993) 3510.
[3] K.A.H. German, C.B. Weare and J.A. Yarmoff; Phys.Rev.Lett **72** (1994) 3899.
[4] J. Los and J.J.C. Geerlings; Physics Reports **190** (1990) 133.
[5] R. Brako and D.M. Newns; Surf. Sci. **108** (1981) 253.
[6] Without loss of generality, V_{ab} can be defined as a positive quantity.
[7] M. Kato, D.J. O'Connor; and R.J. MacDonald; Nucl. Instrum and Meth. **B78** (1993) 77.
[8] M. Kato; in preparation.
[9] According to numerical calculations using various sets of the parameter values, the strong interference effect was seen for most cases.

Low Energy Ion Scattering Apparatus for the Analysis of Sub-Surface and Interface and Structures

Kiyoshi Kawamoto, Kei Inari, Tatsuo Mori, Michio Watamori and Kenjiro Oura
Department of Electronic Engineering, Faculty of Engineering
Osaka University, Suita, Osaka 565, Japan

A new type of time-of-flight impact collision ion scattering spectroscopy apparatus which can change ion beam energy in a range of 2~20 keV is presented. The system mainly consists of a 20 kV PIG ion source, a beam chopper and an annular-type micro channel plate. We show that this apparatus enables us to observe rather deep layers of 10 layers below the topmost layer, and not to receive focusing effect outer few layers in the low indexes direction.

1. Introduction

Low energy ion-scattering spectroscopy (LEIS) and its specialized techniques such as impact collision ion scattering spectroscopy (ICISS) [1,2], co-axial ICISS (CAICISS) [3], and time-of-flight ICISS (TOF-ICISS) [4] are powerful techniques for the determination of the atomic structure of single crystal surfaces [5]. The basic experimental technique of LEIS is to monitor the intensity and the energy of the scattered particle as a function of the incident ion beam direction with respect to the sample orientation. The interpretation of these LEIS data is relatively straightforward since ion trajectories are determined by classical mechanics. Thus, it becomes possible to know configurational and compositional structures of atoms nearby surface as well as in the topmost layer.

As for many LEIS apparatuses, the acceleration voltage of primary ions are usually selected in a range of 1~5 keV because it is enough to observe the structure and composition of outer layers of surfaces. Shadow cones formed behind surface atoms by ions in this energy range have radii comparable to lattice constants of target materials. Since the probing depth in this energy range is limited to less than several layers of specimens, higher energy ions are necessary to study subsurfaces or buried regions, such as materials interface, superlattice, or thin film layered materials. Our purpose is to investigate a shallow interface structure during thin film growth process.

2. Experimental

The detail of the TOF-LEIS apparatus with a UHV system has been already described elsewhere [6]. An ion accelerator consists of a differential pumped ion source, an E×B Wien filter and an electrostatic deflector. The beam energy is in the range of 2~20 keV. Scattered particles from the sample were detected with a micro channel plate that was mounted on coaxially along the primary ion beam at a flight length about 45 cm from the sample. Energy analysis of backscattered particles is made by measuring the flight time between the chopping plate and the detector. The following, the experimental result of Si(001) surface with $^4He^+$ ion beam are described.

3. Results and discussion

The LEIS polar scan of the Si(001) along the (010) planes were collected for 10 keV $^4He^+$. The [100] azimuth consists of two equivalent (010)

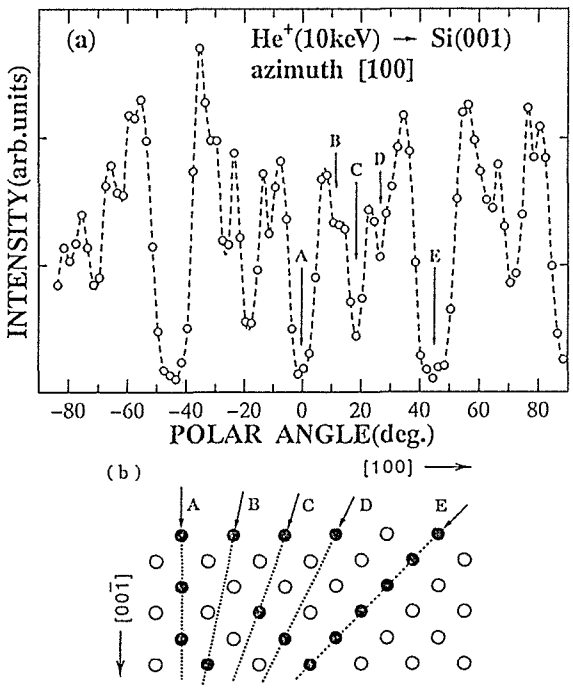

Fig. 1. (a) Polar angular scan along the [100] azimuth for Si(001) surface by 10 keV $^4He^+$ ion beam. The dashed line is only guide for the eyes. (b) Schematic drawing of side view along the [100] azimuth of the (001) terminated Si surface. Allows correspond to the directions shown in (a).

planes apart from a quarter of the lattice constant of Si. The 10 keV scan shown in fig. 1, has the features involving several intensity maxima in the range of 0° ~90°. The dip marked by A in fig. 1 originates from the shadowing effect aligned with the [00$\bar{1}$] direction, corresponding to the [00$\bar{1}$] channeling axis, so that atoms from above the fourth layer hide more deeper layer atoms. Similarly, the dip C corresponds to the [$\bar{1}0\bar{3}$] direction and layers deeper than the fourth layer atoms are hidden from near surface atoms. The dip E corresponds to the [$\bar{1}0\bar{1}$] directions, and only the first and second layers are observed. Whereas the dips B and D correspond to the [$\bar{1}0\bar{5}$] and the [$\bar{1}0\bar{2}$], respectively. These indexes are higher than those mentioned above. The ridges on the side of dips B and D can be considered to originate from particles scattered by 9th or 11th and more deeper layer atoms. These results clearly show that our present apparatus can be well used to investigate subsurfaces or buried regions of materials.

Fig. 2 shows normalized polar angular scan in fig. 1(a) of Si(001) along the [100] azimuth by 10 keV He^+ ions. This intensity is multiplied cosine of polar angle in order to compensate area exposed ion beam [7] and is normalized by absolute value of intensity of <101> direction. Number of observed atoms of the [00$\bar{1}$] direction is twice as much as that of the [$\bar{1}0\bar{1}$]. In fig. 2, normalized intensity of the [00$\bar{1}$] is twice of the [$\bar{1}0\bar{1}$], so that third and fourth layer atoms suffer no-focusing effect of first and second layers in the [00$\bar{1}$] channeling axis. Moreover, that indicates no-focusing effect from first to second layer atoms in the [$\bar{1}0\bar{1}$] incidence. These quantitative relations are derived the following equations.

$$I_E = \eta_0 (1+\eta_1) x,$$

$$I_A = \eta_0 (1+\eta_1 (1+\eta_2 (1+\eta_3))) x,$$

where I_A and I_E represent the signal intensities for the [00$\bar{1}$] and the [$\bar{1}0\bar{1}$] incidence, respectively. The x means signal intensity from single layer and η_i the ratio of the flux distribution at the first layer atoms with respect to the position of ith layer deeper from the first layer; the degree of the focusing effect was assumed to be equal for atom pairs which have equivalence in geometrical arrangement, e.g., η_1 was defined focusing factor from first to second layer, from second to third, and so on. The η_i were assumed to be larger than 1 because near surface atoms are not hidden from ions flux in these direction, especially iso-plane focusing factor η_0 was regarded as 1. To take into consideration that the situation for the η_1 focusing are not along the [100] azimuth, η_1 was regard as

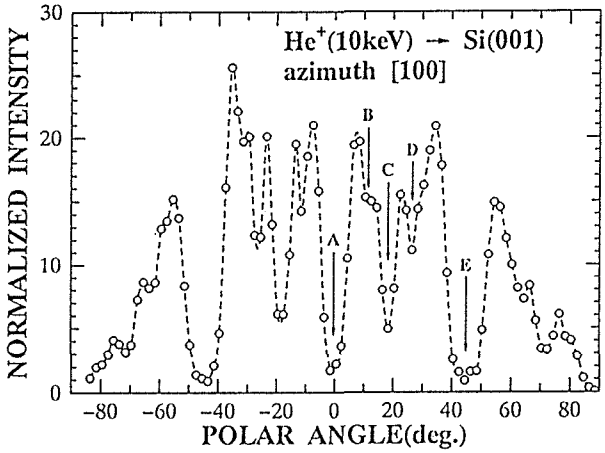

Fig. 2. Normalized polar angular scan of fig.1 (a).

static value except glancing incidence. Then, the ratio of the scattering yield for the [00$\bar{1}$] with respect to the [$\bar{1}0\bar{1}$], R, was derived

$$I_A / I_E = R = \xi+1,$$

where

$$\xi = \eta_1\eta_2 (1+\eta_3) / (1+\eta_1).$$

If ξ=1 then η_i=1, therefore outer four layers don't suffer focusing enhancement caused by other atoms. In fig. 2, R is equal to 2, then we are enable to know quantitative information in low indexes channelling axis.

Authors would like to thank Mr. S. Kujime for his assistive work.

References

[1] M. Aono, Y. Hou, R. Souda, C. Oshima, S. Otani, Y. Ishizawa, K. Matsuda and R. Shimizu, Jpn J. Appl. Phys. 21 (1982) L670.
[2] H. Niehus and G. Comsa, Nucl. Instrm. Methods B 15 (1986) 122.
[3] M.Katayama, E.Nomura, N.Kanekama, H.Soejima and M.Aono, Nucl. Instrum. Methods B 33 (1988) 857.
[4] K.Sumitomo, K.Oura, I.Katayama, F.Shoji and T.Hanawa, Nucl. Instrum. Methods B 33 (1988) 871.
[5] For example, see H. Niehus, W. Heiland and E. Taglauer, Surf. Sci. Rep. 17 (1993) 213.
[6] K. Kawamoto, K. Inari, T. Mori, M. Watamori and K. Oura, The proceeding of the 13th international conference on the application of accelerators in research and industry (Nov. 8, 1994), submitted.
[7] K. Kawamoto and S. Nakanishi, J. Vac. Soc. Jpn. 34 (1991) 827 (in Japanese).

Structure Analysis of Cu/Si(111)"5x5" with MEIS and STM

T. Yasue, T. Koshikawa, H. Tanaka, I. Sumita* and Y. Kido ***
Department of Applied Electronics and Fundamental Electronics Research Institute, Osaka Electro-Communication University, 18-8 Hatsu-cho, Neyagawa, Osaka 572, Japan
*Matsushita Research Institute of Tokyo, Inc., Higashimita, Tama-ku, Kawasaki 214, Japan
**Department of Physics, Ritsumeikan University, Noji-cho, Kusatsu, Shiga 525, Japan

Abstract

The surface structure of the Cu/Si(111)"5x5" which is the high temperature phase formed between 130 and 600°C is analyzed with using the medium energy ion scattering (MEIS) and the scanning tunneling microscope (STM). The top-most layer of the substrate is determined to be the double layer structure in which the inward relaxation of the 1st layer of 0.01nm is observed. In the incommensurate layer, the Cu layer locates above the Si layer by 0.05nm, which is observed under a ultra-high depth resolution condition with MEIS. The atomic density of Si atoms in the incommensurate layer is also determined to be about 1ML with STM.

1. Introduction

The formation of the metal-semiconductor interface is one of the most important subject on the physical and the industrial problem. In general, the several surface structure phases are observed in the metal/semiconductor system by varying the substrate temperature and the metal coverage. When Cu is deposited onto the Si(111)7x7 surface, the "5x5" structure is formed on the hot substrate (130-600°C). The "5x5" structure is the incommensurate phase, so it is difficult to determine the surface structure fully. Several surface analysis techniques, for example the reflection electron microscope (REM)[1], the X-ray standing wave method (XSW)[2], the scanning tunneling microscope (STM)[3] *etc.*, have been employed to analyze the "5x5" structure. However the details of the "5x5" structure is not understood so far.

In the present paper, we show the study on the substrate structure and the height difference between the Cu and the Si layer in the incommensurate layer with the medium energy ion scattering(MEIS). The Si atom density in the incommensurate layer is also determined with STM.

2. Experimental

A specimen was a B-doped p-type Si(111) for the MEIS experiment and P-doped n-type ones for the STM study. Cu was evaporated from a Cu bead (99.9999%) prepared on the

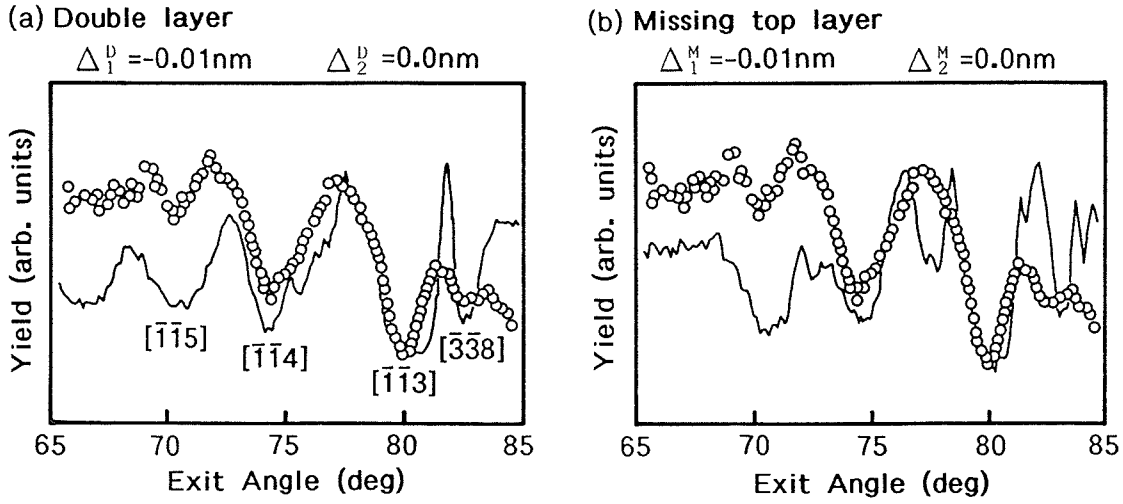

Fig.1 Comparison of the blocking profiles obtained by the experiment (circles) and the calculation (line). The double layer structure is assumed in (a) and the missing top layer is assumed in (b).

W filament. The Cu/Si(111)"5x5" surface was prepared by two ways. One was the deposition of Cu onto the hot Si(111) substrate (about 600°C). This sample was used in the MEIS measurements. The other was the annealing of the Cu/Si(111) prepared at room temperature. Annealing temperature was below 300°C. This was for the STM observation. In the MEIS measurement, He^+ ion beam whose accelerating voltage was 175 kV was used. The incident angle was 35.3° and 60.5° from the surface normal when the blocking profiles were measured to determine the substrate structure. These two directions are along channeling axes. The incident ion beam can see up to the 2nd layer atoms for 35.3° and up to the 4th layer atoms for 60.5°. A Monte Carlo simulation of the blocking profiles was carried out to explain the experimental blocking profiles. One can obtain the higher depth resolution when the take-off angle of the scattered ions is smaller. The height relationship between the Cu and the Si layers in the incommensurate layer is observed under the ultra-high depth resolution condition. The incident angle is 70° which is nearly a random condition and the take-off angle was less than 5°. The depth resolution for the take-off angle of 4.4° is about 0.16nm for the Si surface. In the STM experiment, the constant current topographic mode was employed, where the tunneling current was 50 Pa. The observation of the STM images was carried out at room temperature.

3. Results and Discussion

Since the relative atomic position between the substrate atoms and the atoms in the incommensurate layer is not unique, we can neglect the blocking effect of the scattered ions from the substrate atoms caused by the atoms in the incommensurate layer. Therefore the atomic arrangement of the top-most layer of the substrate is discussed firstly. Fig. 1 shows the blocking profiles which was taken for the incident angle of 60.5°. Circles shows the experimental profile and the solid line is the simulated ones. In fig. 1(a) the double layer structure is assumed and fig. 1(b) is obtained for the missing top layer structures, in which the

inward relaxation of the 1st layer by 0.01nm is assumed for both structure models. For the missing top layer structure, the discrepancy of the blocking profile between the experimental and the calculated profiles is seen at around 77°. This blocking dip is caused by the scattered ions at the 4th layer. Since the 4th layer in the missing top layer structure corresponds to the 5th layer for the double layer structure, the clear blocking dip is not expected for the double layer structure in the present scattering geometry. This is the reason of the difference of the blocking profiles at around 77° between the double and the missing top layer structure. When the take-off angle of the scattered ions is very small, the depth resolution becomes better. Fig. 2 shows the energy spectrum obtained for the take-off angle of 4.4° from the surface. In the Si spectrum, several small peaks are seen. The energy spacing for these peaks corresponds to the distance between the double layers of the bulk Si. This means that the ultra-high depth resolution is realized in the present condition. In the figure K^2 indicates the scattered energy which is expected by the elastic binary collision at the surface. For the Cu spectrum, the peak position coincides with K^2, while the energy shift toward the lower energy is observed for the Si spectrum. This indicates that the Cu layer locates above the Si layer. With using the Ziegler's stopping power[4] the height difference between the Cu and the Si layers is estimated to be about 0.05nm in the incommensurate layer.

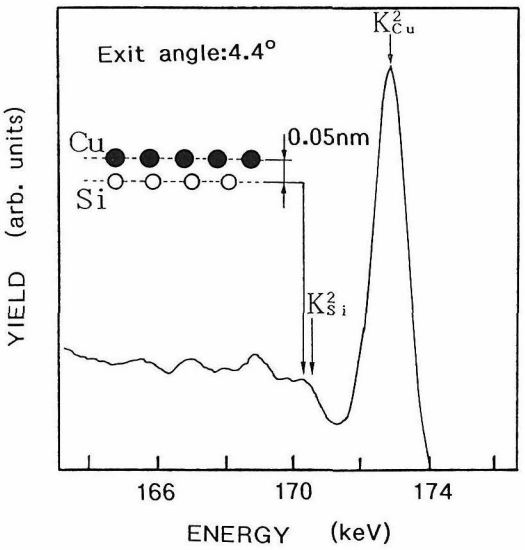

Fig.2 The high resolution MEIS spectrum taken at the take-off angle of 4.4°.

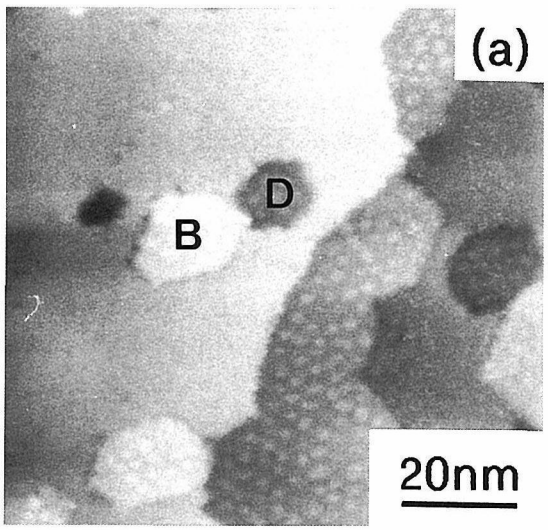

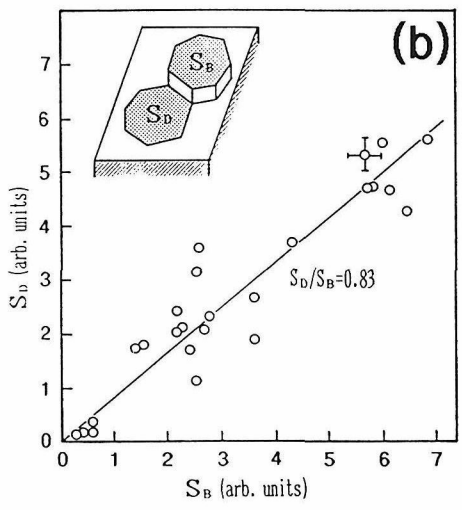

Fig.3 (a) The STM image of the growth of the "5x5" structure on the terrace. (b) The area relationship between the area of the B-region (S_B) and that of the D-region (S_D).

Fig. 3(a) shows the STM image of the growth of the pair of the "5x5" structure (marked by "B" and "D") on the terrace. The growth of the pair of the island and hole has been observed in the case of the Au/ and Ag/Si(111) $\sqrt{3}$x $\sqrt{3}$ structure[5]. When the reconstruction from the Cu/Si(111) at room temperature to the "5x5" structure takes place, the number density of Si atoms must be conserved. Therefore the atomic density of Si atoms in the incommensurate layer is deduced by the area ratio of the D–region to the B–region. The area ratio S_D/S_B is about 0.83, which is obtained from fig. 3(b). Since the incommensurate layer is formed on the double layer substrate, which is confirmed by the results of MEIS as shown before, the structure model of the "5x5" structure shown in fig. 4 is plausible. From the structure model, the atomic density of Si atoms in the incommensurate layer N_i can be calculated by the following equation:

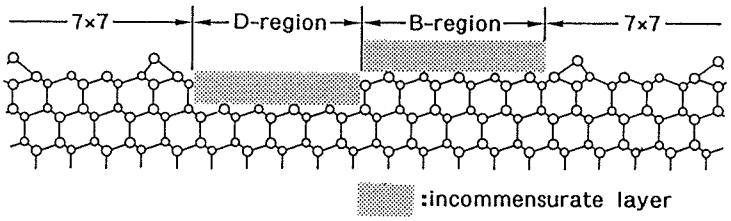

Fig.4 The structure model of the "5x5" structure formed on the terrace.

$$N_i(S_D+S_B)=(N_{7x7}-N_{double})S_B+N_{7x7}S_D,$$

where N_{7x7} is the atomic density for the Si(111) 7x7 structure (102 atoms per 7x7 unit) and N_{double} the atomic density for the normal double layer (98 atoms per 7x7 unit). From the equation the atomic density of Si atoms in the incommensurate layer is calculated to be about 1ML (1ML is $7.83x10^{14}$ atoms/cm^2). This value is consistent with the density obtained by the REM by Takayanagi *et al.*[1]. The structure model which was proposed by Takayanagi *et al.*, however, is the missing top layer structure for the substrate. As shown before the substrate structure is the double layer structure.

4. Conclusion

The Cu/Si(111) "5x5" structure is analyzed with MEIS and STM. The structure of the top most layer of the substrate is the double layer structure with the inward relaxation by 0.01nm. In the incommensurate layer, about 1ML Si atoms are included, and the Cu layer locates above the Si layer by 0.05nm.

References

[1] K.Takayanagi, Y.Tanishiro, T.Ishitsuka and K.Akiyama, Appl. Surface Sci. **41/42** (1989) 337.
[2] J.Zegenhagen, E.Fontes, F.Grey and J.R.Patel, Phys. Rev. **B46** (1992) 1860.
[3] K.Mortensen, Phys. Rev. Letters **66** (1991) 461.
[4] J.F.Ziegler, *He Stopping Powers and Ranges in All Elements* (Pergamon, New York, 1977).
[5] A.Shibata and K.Takayanagi, Jpn. J. Appl. Phys. **32** (1993) 1385.

Interaction of Oxygen and Alkali Metals with Si(100) or Ge(100) Surfaces Studied with a Helium Metastable-Atom Beam

Satoshi Nishigaki, Hisao Iga, Kenji Yamada and Masamichi Naitoh*
Kyushu Institute of Technology, 1-1 Sensui-cho, Tobata, Kitakyushu, 804 Japan
*Ishikawa National College of Technology, Kitachujyo, Tsubata, Ishikawa 929-03, Japan

Abstract
The electronic structure of Cs plus oxygen co-adsorbed layers on the Ge(100) or the Si(100) surface has been studied by metastable deexcitation spectroscopy (MDS) mainly concerning Cs 6s̃, O 2p̃ and $\Delta\Phi$. It is shown that the degree of electron transfer from Cs 6s̃ to incoming oxygen at the Ge(100) surface remains incomplete in strong contrast to a complete charge outflow from the Cs 6s̃ orbitals at the Si(100) surface.

The role of alkali metals as an electron donor is played at surfaces to incoming molecules promoting their dissociative adsorption. Thus, alkali-promoted oxygenation or nitrogenation has been intensively investigated at various semiconductor surfaces.[1] Schirm *et al.*[2] recently found, however, that K does not act as a catalyst for oxidation at Ge surfaces in contrast to the well-known promotion role at Si surfaces. Question has been aroused on what brings such a difference: Can it be attributed to a difference between Ge-O and Si-O bondings ?[3] Should one pay attention, unlike this, to any differences in electronic structure of alkali plus oxygen systems at Ge or Si surfaces ? From the latter point of view, we have attempted extracting local density of states of Cs + oxygen co-adsorbed layers on Ge(100) and Si(100) substrates by metastable deexcitation spectroscopy (MDS).

A beam of excited helium atoms mainly at the 2^3S state (the excitation energy 19.8 eV) is produced by a pulsed hot-cathode discharge. Influences of UV photons and other particles have been removed by a time-of-flight technique. A p-type Ge(100) or a p-type Si(100) specimen was cleaned in vacuum by direct resistive heating. Cs was deposited upto a saturation coverage monitored by the MDS Cs 6s̃ peak height.

Figs.1 and 2 show series of MDS spectra from Cs-saturated Ge(100) and Si(100) surfaces, respectively, subjected to oxygen exposure. A Cs 6s̃ state appears in spectra *a* and *a'* at energies around 14 eV above the vacuum level of the clean surface. Its intensity decrease upon oxygen exposure is a clear indication of the electron outflow from the Cs 6s̃ orbitals to oxygen. We notice here, however, that it remains still incomplete at Ge(100) in Fig.1 even with more than 0.5 L of oxygen exposure. This point is in strong contrast to the fact shown in Fig.2 that all states above 12 eV at the Cs/Si(100) surface have completely been swept away with the same amount of oxygen exposure.

As long as judged from O 2p̃ intensities in the MDS spectra, the oxygen uptake process at the Cs/Ge(100) or the Cs/Si(100) surface exhibits a similar trend, namely, an initial fast process of adsorption followed, at 0.2-0.3 L, by a very slow one. The O 2p̃ peak at the end of the initial fast step at Cs/Ge(100) was about 35 % as high as the initial Cs 6s̃ peak, which by no means inferior to that at Cs/Si(100).

We measured the work function change $\Delta\Phi$ induced by the oxygen uptake, monitoring the low-energy threshold of MDS spectra, in order to get a corroboration for electron transfer from Cs to oxygen. An initial decrease in $\Delta\Phi$ was found to be limited to about -0.3 eV for

O/Cs/Ge(100) while it amounted to about -0.9 eV for O/Cs/Si(100). This result coincides with the fact of incomplete charge transfer at the Ge(100) surface.

Our MDS results show that the basic electronic process driving oxygen uptake by preadsorbed Cs is local electron transfer from the Cs 6s̃ states to oxygen, but that it need be modified for the process at the Ge(100) surface. We only suggest that if one assumes oxygen-Cs bonds at the Ge(100) surface being partly covalent, the explanation of incompleteness of electron outflow and a little work function change may be straightforward.

A further MDS test has been undertaken to the charge states of Cs adsorbed at a partially-oxidized GeO_x or SiO_x surface. A striking difference between the two surfaces appeared in a result that Cs 6s̃ and O 2p̃ peaks co-existed in a spectrum from the GeO_x surface while, from the SiO_x surface, an MDS spectrum contained a large Cs 6s̃ peak alone. This infers that oxygen atoms coordinating with Ge is pulled towards newcome Cs atoms, which corresponds to the findings of Schirm et al. that Cs at the Ge(100) surface acts rather as an oxygen acceptor.[2)]

In conclusion, the catalytic role of Cs on the oxygenation of the Ge(100) or Si(100) surface via local electron transfer from Cs 6s̃ to oxygen was well evidenced by MDS. Moreover, it is revealed that the electron outflow from the Cs layers to oxygen at the Ge(100) surface remains incomplete even at the end of the first adsorption step, though it is characterized by complete charge transfer at the Si(100) surface.

This work was supported in part by a Grant-in-Aid for Scientific Research from the Ministry of Education, Science and Culture of Japan.

1) As a review, see: "Physics and Chemistry of Alkali Metal Adsorption," eds. H. P. Bonzel, A. M. Bradshaw and G. Ertl (Elsevier, Amsterdam, 1989).
2) K. M. Schirm *et al.*, Appl. Surf. Sci. 68(1993)433.
3) L. Surnev and M. Tikhov, Surf. Sci. 123(1982)519.

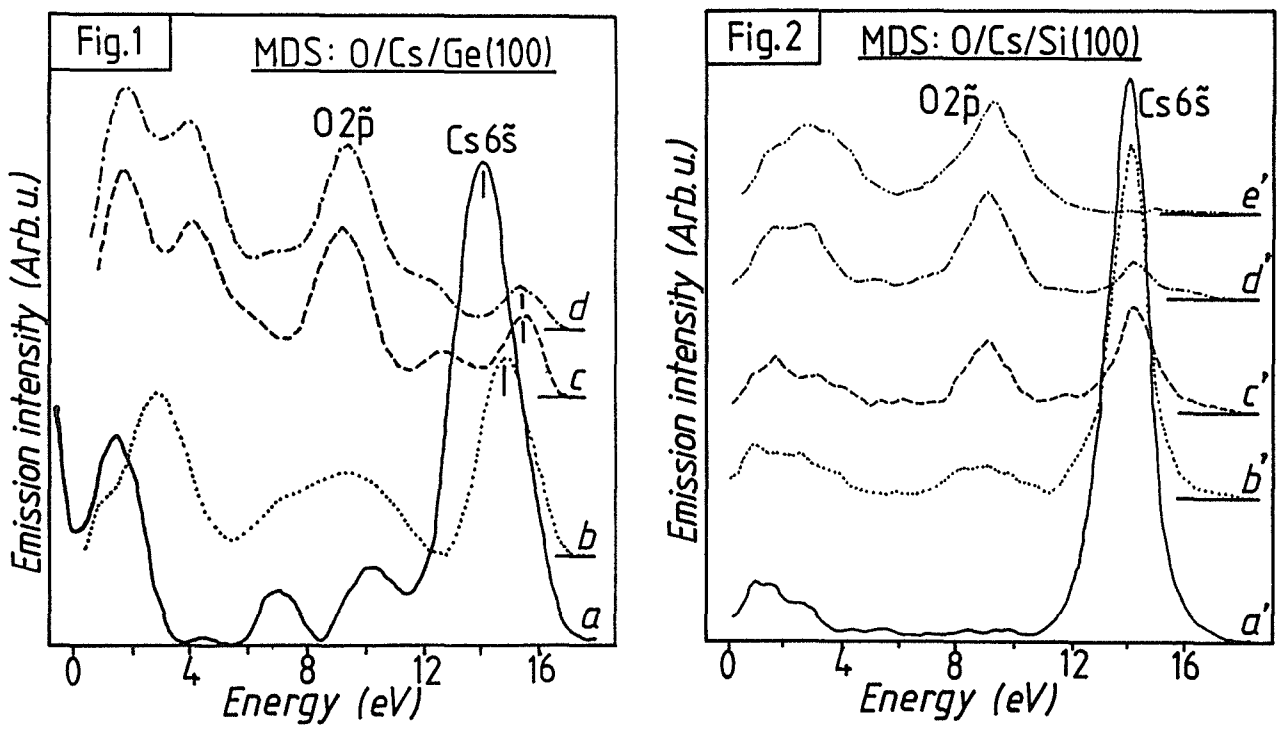

Fig.1. MDS spectra from O/Cs/Ge(100) surfaces: curve (*a*) from the Cs-saturated Ge(100) surface, (*b*) oxygen exposure 0.08 L, (*c*) 0.19 L, (*d*) 0.45 L.
Fig.2. MDS spectra from O/Cs/Si(100) surfaces: curve (*a'*) from the Cs-saturated Si(100) surface, (*b'*) oxygen exposure 0.11 L, (*c'*) 0.16 L, (*d'*) 0.27 L, (*e'*) 0.65 L.

CAICISS Study of $SrTiO_3$(100) Surface Structure: Experiment vs. Simulation

M. Shinohara[1], O. Ishiyama[1], T. Nishihara[1], F. Ohtani[1], M. Yoshimoto[2], T. Maeda[2] and H. Koinuma[2]

[1]Keihannna Research Laboratory, Shimadzu Corporation, Hikaridai 3-9, Seikacho, Sorakugun, Kyoto 619-02, Japan, [2]Research Laboratory of Engineering Materials, Tokyo Institute of Technology, Nagatsuta 4259, Midoriku, Yokohama 227, Japan

ABSTRACT

The surface structure of SrTiO3(100) was studied by means of coaxial impact-collision ion scattering spectroscopy (CAICISS). High-temperature annealed STO substrates of which surface were predominantly terminated with TiO2 atomic plane were applied to the study of the surface structure. We developed a three dimensional simulation program for CAICISS and employed this program to interpret the observed data . As a result of that, it is found that the distance between the 1st TiO2 plane and 2nd SrO one is reduced by 0.05 ±0.005 nm toward [001] direction.

Among oxide single crystals, the perovskite SrTiO3(STO) with a cubic structure (a=0.39nm) is well known as a lattice-matched substrate suitable for the epitaxial growth of high Tc cuprate films. In order to control the epitaxial growth of oxide layers on an atomic scale, it is important to study the atomic species and their alignments in the surface of STO substrate [1]. However, it is difficult to determine the topmost atomic plane by using RHEED, STM, and XPS. RHEED and STM cannot identify atom species directly. XPS is impossible to determine the topmost atomic plane, because the escape depth of photoelectron is more than several nanometers. Therefore, we employed Coaxial Impact Collision Ion Scattering Spectroscopy (CAICISS). An STO sample cleaned by supersonic-rinsing in acetone & ethanol and dried was introduced to the analysis chamber (background pressure of $1x10^{-7}$ Pa) equipped with a RHEED system, and was mounted on a two-axis goniometer for polar and azimuth rotations with respect to the primary He^+ ion beam of 3 keV.

As STO crystals has a structure stacked alternately by two kinds of non polar atomic planes, i.e. SrO and TiO2, along c-axis, different surface terminations with either SrO or TiO2 at the (001) top layer are possible. We already presented that the topmost-layer of as-purchased STO is terminated by both TiO2 plane and SrO one [2]. On the other hand, in the case of the annealed substrate which is treated at 1000 °C for 10 h in 1 atom O2 atmosphere, the top layer is predominantly terminated as shown in Fig. 1 by TiO2 plane. The well-defined terminating surface should be essential not only for the fabrication of high-quality high Tc superconducting films but also for the artificial layer-by-layer construction of oxide superlattices. Hence, we studied surface structure of this annealed STO substrate by CAICISS. Figure 2 shows the azimuth angle dependence of Sr signal intensity at the incident angle of 45 °.

In order to interpret the result of Fig. 2, we developed the program of computer simulation of CAICISS. This is based on the three dimensional two-atom model extending the algorithm which is developed by Williams et al. [3]. The algorithm of this simulation method is as follows. (1) Extract the unit cell for ion scattering at arbitrary polar and azimuth angle. (2) Select a target atom for the binary collision in the extracted unit cell. (3) Evaluate the elements, length and angle of the all atom-pairs contained the selected target atom in 3 dimensional space within the extracted unit cell . (4) Divide binary collision in each atom-pair into kinds of scattering region which are no-scattering (within shadow cone), triple scattering and quasi-single scattering. (5) Solve the nonlinear system of equation (Fig. 3) in only the case of triple scattering at the fixed polar and azimuth angle. At this time, isotropic thermal vibration is considered. (6) Calculate the total cross section.

We applied this method to the CAICISS simulation of the STO surface terminated by TiO2 plane

completely. As a result of that, it is found that the distance between the 1st TiO2 plane and 2nd SrO one is reduced by 0.05±0.005 nm toward [001] direction. Because, the shape of the observed data in Fig.2 does not agree with the data in the case of ideal STO structure but almost agree with one in the case of distorted STO structure, as shown in Fig. 4.

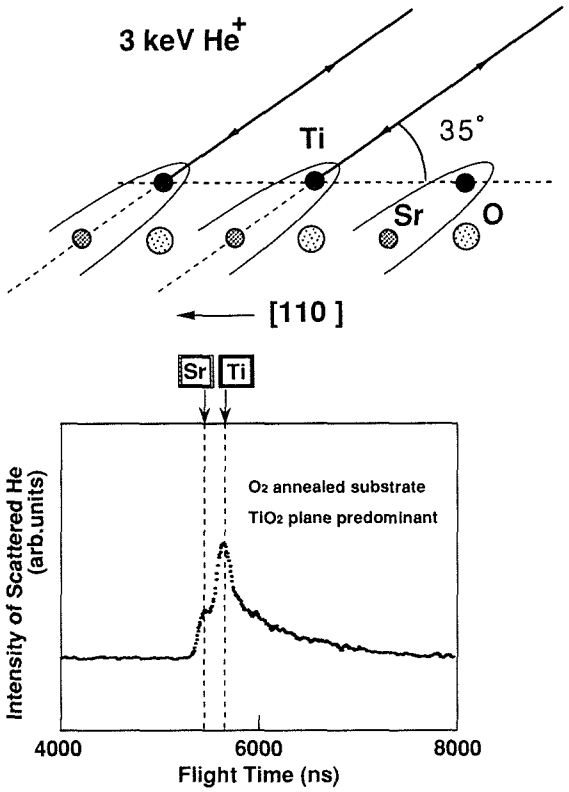

Fig.1 TOF Spectrum measured in [111] direction

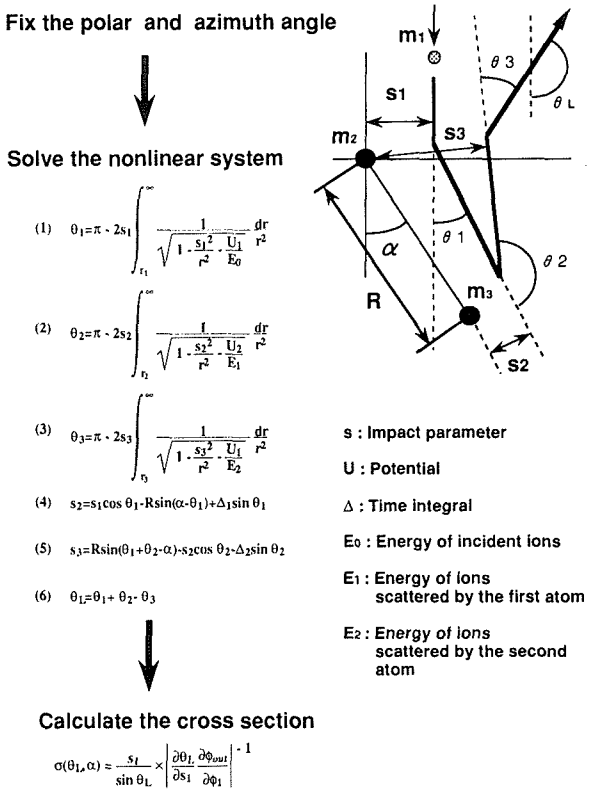

Fig3. Nonlinear system of equation for the two-atom model

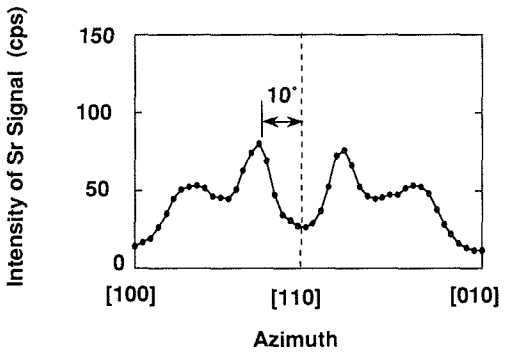

Fig.2 Azimuth angle dependence of Sr signal intensity in the case of the high-temperature annealed substrate

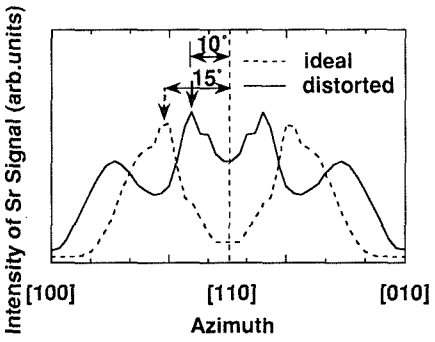

Fig.4 Simulation results

references

1. M.Kawai, Z.Liu, R.Sekine, H.Koinuma , Jpn.J.Appl.Phys. 32(1993)L1208.
2. M.Yoshimoto, T.Maeda, K.Shimozono, H.Koinuma,M.Shinohara, O.Ishiyama, and F.Ohtani, Appl.Phys.Lett.65(1994)3197.
3. R.S.Williams, M.Kato, R.S.Daley and M.Aono, Surf.Sci.225(1990)355.

Comparison of Depth Profiling of GaAs/AlAs Multilayers by AES and SNMS

S. Suginuma, H.-S. Im and S. Ichimura*
Electrotechnical Laboratory, 1-1-4, Umezono, Tsukuba 305, Japan

Abstract

Depth profile of GaAs/AlAs multilayer sample having interface abruptness of atomic order was investigated by AES and SNMS. In AES, not only the intensities of Al- and Ga-Auger signals, but the intensity of As-Auger signal periodically changed depending on the layer, probably due to the matrix effect of AES signals. The interface width estimated from Al and Ga signals at 84%-16% intensity level was about 5 to 6 nm. The As intensity measured by SNMS showed almost constant values during depth profiling, suggesting the possibility of reliable depth profiling with SNMS method. However, the depth resolution of SNMS was deteriorated due to the contribution of neutrals sputtered from the ion beam edge. The improvement of the depth resolution in SNMS was discussed.

1. Introduction

Depth profiling of multilayer samples has been performed mainly in two ways. The first one is AES/XPS depth profiling, which measures Auger or photoelectron signal intensity as a function of sputtering time. Since quantitative corrections for AES and XPS has been investigated intensibly, the result of AES/XPS depth profiling is accepted to be reliable. Problem of AES/XPS depth profiling is low detection sensitivity for minor elements, which is usually considered as % order. The second one is depth profiling by SIMS, which has high detection sensitivity in the order of ppb (parts per billion). The SIMS depth profiling, however, is not so reliable as AES/XPS depth profiling, since the matrix effects often modifies the signal intensity.

Sputtered Neutral Mass Spectrometry (SNMS) is expected to solve the problem of the matrix effects keeping high detection sensitivity for minor elements; it is already confirmed that 100% ionization (i.e., the saturation of the ionization) of neutral atoms/molecules is possible when laser beam is used for the ionization[1]. It is afraid, however, that depth profiling by SNMS may be deteriorated since all neutrals which reach post-ionization region are analyzed. That is, the analyzing area is as large as the diameter of the primary ion beam in spite that the sputtering speed is different between the center and the edge of the ion beam.

The aim of the present paper is to compare the depth profiling by AES and SNMS using the same AlAs/GaAs multi-layer sample, and to discuss the possibility and current problems of SNMS depth profiling.

2. Experimental

The sample used for the present experiment is a GaAs/AlAs multi-layer sample, which was fabricated by depositing 20 nm AlAs layer and 20nm GaAs layer alternatively on GaAs substrate. The top layer is GaAs, and the number of GaAs and AlAs layers is 3, respectively. It was confirmed by TEM analysis that each GaAs and AlAs interface is very steep with almost one atomic layer roughness.

AES depth profiling was done with a microprobe scanning Auger equipment (PHI; SAM 660). Measured Auger spectra are Al-LVV, Ga-LMM, and As-LMM. Since the ionization energy of

* Permanent Address; Korean Research Institute for Standards and Science, P.O. Box 3, Taeduck Science Town, Taejeon, Korea

Ga and As L-shell is more than 1 keV, primary electron energy was set at 10 keV. The angle of electron beam incidence was normal to the surface. The primary beam current and the beam size were 2 μA and 3 μm in diameter, respectively. The sample surface was sputtered with 3 keV Ar^+ ions for depth profiling. The angle of ion incidence was 60 deg. from the surface normal. The ion beam current and the diameter were 0.3 μA and 0.5 mm in diameter. Since the ion incidence was not normal to the surface, the surface had an elliptic crater after the sputtering.

Figure 1 shows a schema for the SNMS experiment. Almost the same ion beam condition was adopted in SNMS depth profiling. That is, Ar^+ ion beam energy was set at 3 keV, and the angle of ion incidence was 60 deg. from the surface normal. The ion beam current was 0.1μA with the beam size of about 1 mm in diameter.

ArF excimer laser with wavelength of 193 nm (photon energy; 6.04 eV) was used for post ionization of sputtered neutrals. The laser beam was focused with a spherical lens (focal length; 400 mm) at a point about 8 mm apart from the ion bombarded surface. The ionization potentials of Al, Ga, and As are 5.97eV, 6.00 eV, and 9.81 eV, respectively. So Al and Ga atoms were ionized by single photon process, while As atoms were ionized by two photon process.

The ionized neutral particles were mass separated with a time-of-flight (ToF) mass analyzer having a reflectron at one edge of the analyzer. The total flight length of the ToF analyzer was about 2 m, and the mass resolution was about 600 $(=m/\Delta m)$[2]. The angle between the central axis of the ToF analyzer and the sample surface normal was 30 deg. Photoions were detected with a microchannel plate (MCP) intensifier, and analyzed with a waveform digitizer (LeCroy; 9400)[3].

3. Results and discussion

Fig.2 shows the result of depth profiling by AES. Open circles show intensity of Ga Auger peak appeared at the energy of about 1070 eV, while solid circles show intensity of Al Auger peak appeared at about 68 eV. The depth resolution of each interface was estimated from the figure at the 84%-16% level of the averaged intensity which is shown with bold lines for Al and Ga signals. Possible errors at the maximum and minimum intensity level are also shown with fine lines. The estimated interface width are summarized in Table. 1.

Two points are clear from the results of Ga depth resolution shown in Table 1: Firstly, the width at the 1st, 3rd, and 5th interfaces which correspond to GaAs/AlAs (GaAs on AlAs) interface is narrower than that at the 2nd, 4th, and 6th interface (AlAs/GaAs interface). The second point is that the interface width is wider when the interface locates deeper from the surface. This becomes clear by comparing separately the results for GaAs/AlAs interface or those for AlAs/GaAs interface. It should be stressed here that the depth resolution of the third (GaAs/AlAs) interface is smaller than the resolution of the second (AlAs/GaAs) interface in spite that the third layer locates deeper from the surface. So the indication of the second point dose not interfere with the suggestion of the first one.

As to the dependence of depth resolution on interface depth, it is often pointed out that the resolution often increase proportionally with the sputtered depth[4]. Surface roughness caused by sputtering is considered as a main origin for the proportional increase of the depth resolution. However, the dependence of the depth resolution on the type of interface is not well known. The similar tendency is not clearly observable for the results estimated using Al Auger signals. Further experiments is necessary to understand the tendency.

The As signal intensity in GaAs layer and that in Al layer are different in spite that As content in each layer is same. The intensity is about 1.4 times larger in AlAs layer than GaAs layer. Such intensity change is due to the AES matrix effect. Usually atomic number density, backscattering correction factor, and escape depth (inelastic mean free path; IMFP) of Auger electrons contribute largely to the AES matrix effects.

The backscattering correction factor of As-LMM Auger peaks excited by 10 keV primary

electrons of normal incidence is calculated using the results of Monte Carlo simulation[5]. The values are obtained only for AlAs substrate and GaAs substrate (not for the multilayer samples), and they are 1.6 for the AlAs substrate and 1.7 for the GaAs substrate. Apparently the backscattering effect should result in the opposite intensity change from that shown in Fig.2. Even if we calculate the backscattering factor accurately for the multilayer structure, it is impossible to explain the observed intensity change since the As intensity at the GaAs substrate is smaller than that at the AlAs layer on the GaAs substrate.

The IMFP of As-LMM Auger electrons appeared at the energy about 1230 eV can be calculated using the TPP-2M equation[6]. The results were 2.9 nm in AlAs layer and as 2.8 nm in GaAs layer. The atomic density of GaAs and AlAs is 7.87×10^{14} and 7.95×10^{14}, respectively. The difference between the values for GaAs and AlAs is apparently too small to explain the observed intensity difference. So another factor of the AES matrix effect has to be considered to explain the results. This work is also left for further study.

The sputtering time necessary to etch each layer was also estimated using Fig.2. The results are shown in Table 2. It is clear that the time necessary to sputter GaAs layer is almost same with the time necessary to sputter AlAs layer. Since the layer thickness is 20 nm for both AlAs and GaAs layers, this results suggest that the sputtering yield the two layers is comparable. This fact explains the result of SNMS experiments, which is shown in Fig.3.

Open circles in Fig. 3 show measured Ga intensity, and solid circles show those of measured Al intensity. The intensity of Ga signal shows maximum at sputtering times around 60, 280, and 480, while the intensity of Al signal shows maximum at around 200, 380, and 600 sec. The time interval between two maximum points is nearly equivalent, especially at time regions after 280sec. We think, therefore, the former three maximum appeared at GaAs layer, and the latter three maximum appeared at AlAs layer. However, the observed intensity change of Ga and Al signals with sputtering time is very weak compared with the change observed in AES depth profiling (Fig.2).

The weak change is attributable to the contribution of edge part within the sputtered area. Fig.4 describes schematically how the ion beam sputters the sample surface. It is easily imagined that when the center of the ion beam bombards a deeper layer, the edge of the ion beam still sputters upper layers. Therefore, the observed signal of SNMS includes the information of the neutrals sputtered from the ion beam edge as well as those from the ion beam center. This fact makes the depth resolution of SNMS worse than that of AES. Moreover, even when central ion beam reaches the GaAs substrate, the edge ion beam still bombard the multilayers. This is the reason for the continuous appearance of Al signal intensity, even though the ion beam center reached the GaAs substrate at about 600 sec of sputtering time.

As mentioned above, the sputter yields of GaAs and AlAs layer are almost the same. This means the quantity of sputtered As doesn't change during sputtering of the multilayer samples. This fact clearly appears in Fig. 3, where As signal intensity is almost constant while sputtering. Therefore, SNMS has the possibility of precise qualification without suffering from the matrix effect The affect of ion beam edge resulting in the deterioration of the depth resolution in SNMS was intensified by the glancing incidence of the primary ion beam, which was used to have the same condition with AES depth profiling. We expect, therefore, that the resolution of the SNMS depth profiling will be improved by adopting the normal incidence of the primary ion beam, and moreover rastered ion beam to sputter the sample uniformly. If we can ionize only those neutrals which come from the central area of the primary ion beam, reliable quantitative depth profiling by SNMS will be possible. The improvement of the experimental set-up for the purpose is on progress.

4. Conclusion

(1) In AES depth profiling, a tendency that the interface width estimated using Ga Auger signal at the GaAl/AlAs interfaces is smaller than that at AlGa/GaAs interfaces was observed. The As Auger

signal intensity changed depending on the type of the layer due to the matrix effect.

(2) In SNMS depth profile, the depth resolution is worse than AES due to the contribution of neutrals sputtered from the ion beam edge. Only the weak intensity change with sputtering time was observed for both Al and Ga signals. However, the As intensity showed almost constant intensity throughout the sputtering time, suggesting the possibility of quantitative depth profiling without suffering the matrix effect.

Acknowledgement

We wish to thank Drs. Tanuma and Ogiwara of Japan Energy Co. for providing the samples.

Reference

1) S. Ichimura, S. Sekine, K. Kokubun, and H. Shimizu, J. Vac. Sci. Technol. 12, 1734 (1994)
2) M. Kato, A. Mogami, M. Naito, S. Ichimura, and H. Shimizu, Rev. Sci. Instrum. 59, 1947 (1988)
3) H. Shimizu, H. Hashizume, S. Ichimura, and K. Kokubun, Japan. J. Appl. Phys. 27, L502 (1988)
4) S. Hofmann, Shinku 33, 721 (1990)
5) S. Ichimura,Ding Ze-Jun,and R.Shimizu:Surf. Interface Anal.13(1988)149
6) S.Tanuma,C.J.Powell,D.R.Penn:Surf.Interface Anal.21(1994)165

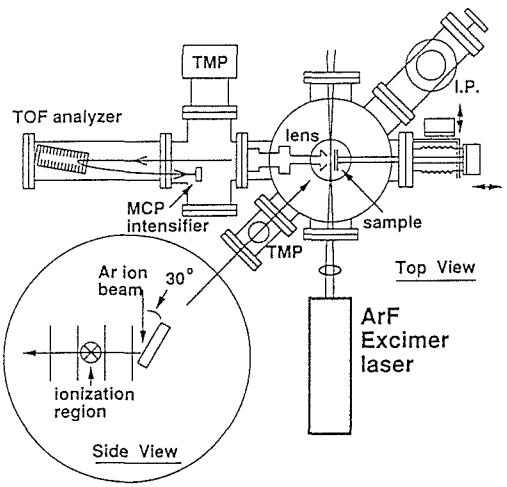

Fig. 1 Scheme of the SNMS experimental apparatus

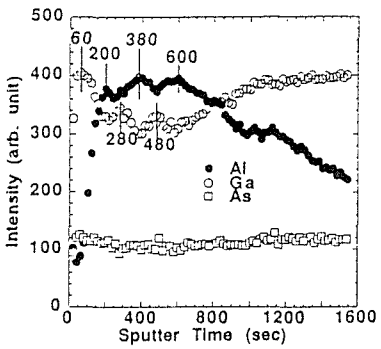

Fig. 3 SNMS depth profiling of GaAs/AlAs multilayer sample

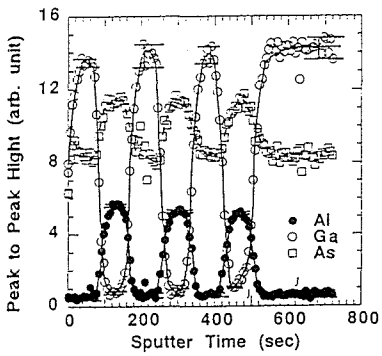

Fig.2 AES depth profiling of GaAs/AlAs multilayer sample

Table. 1 Depth resolution of the interfaces of GaAs/AlAs multilayer sample by AES

	layer1-2 GaAs/AlAs	layer2-3 AlAs/GaAs	layer3-4 GaAs/AlAs	layer4-5 AlAs/GaAs	layer5-6 GaAs/AlAs	layer6-substrate AlAs/GaAs
Al	5.8 ±0.2nm	4.6 ±0.3nm	5.9 ±0.5nm	5.3 ±0.3nm	5.6 ±0.3nm	5.7 ±0.5nm
Ga	4.4 ±0.2nm	6.2 ±0.6nm	4.7 ±0.4nm	6.7 ±0.5nm	6.0 ±0.5nm	7.1 ±0.5nm

Table. 2 Thickness of each layer of GaAs and AlAs represented by sputter time

	layer1 GaAs	layer2 AlAs	layer3 GaAs	layer4 AlAs	layer5 GaAs	layer6 AlAs
Sputter Time	83.2 ±0.5s	83.5 ±1.3s	87.3 ±2.1s	83.3 ±1.3s	83.2 ±1.2s	85.3 ±1.7s

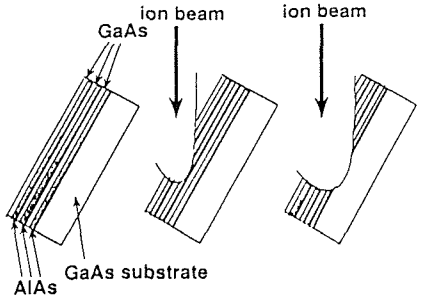

Fig.4 Drawing of the Ion Beam Sputtering on the Surface during SNMS Analysis

Scanning Tunneling Spectroscopy of Hydrogen-Terminated Homoepitaxial Diamond Surfaces

Atsuhiro Sato[1], Hiroshi Kawarada[1] and Satoshi Yamashita[2]
[1]School of Science & Engineering, Waseda University, Ohkubo 3-4-1, Shinjuku-ku, Tokyo 169, Japan
[2]Tokyo Gas Co., Ltd., 7-7, Suehiro-cho, 1-chome, Tsurumi-ku, Yokohama 230, Japan

Abstract

STM combined with STS has been employed to acquire the information on the electronic structure of H-terminated homoepitaxial diamond (001) and (111) surfaces. The STS spectra for (001) and (111) surfaces reveal the existence of surface state near the top of valence-band. We speculate that this surface state is responsible for the formation of p-type surface semiconductive layers.

1. Introduction

P-type semiconductive layers exist on H-terminated diamond surfaces, even if the diamonds are "undoped"[1,2,3]. The layers are used as active regions for high-performance diamond field effect transistors[4]. However, the origin of this surface conductivity has not been reported clearly. Therefore it is very important to acquire the information on the electronic structure of H-terminated diamond surface.

Scanning tunneling microscopy (STM) combined with scanning tunneling spectroscopy (STS) is powerful and unique technique for studying the surface geometric and electronic structure in atomic scale. It has been used to reveal the energy levels and microscopic location of surface electronic states[5].

In this report, we have performed the STM/STS of H-terminated homoepitaxial diamond (001) and (111) surfaces, and discussed the origin of the surface conductivity.

2. Experimental

Diamond homoepitaxial films were grown by means of a conventional microwave plasma-assisted CVD method on high-pressure synthetic type Ib diamond (001) and (111) substrates. During the deposition, the flow rates of CO and H2 were 10 and 190 sccm, respectively, the total pressure was 35 Torr, the microwave power was 300W and the substrate temperatures were 890℃ on (001) surface and 850℃ on (111) surface, respectively. STM/STS observations have been carried out on the as-grown samples in air.

3. Results and Discussion

Figure 1(a) is the STM image of the as-grown homoepitaxial diamond (001) surface. This image shows parallel lines at equal distance(5Å) along two perpendicular directions. This lines

corresponds to the dimer rows of diamond (2x1) monohydride structure shown in Fig.1(b).

Figure 2(a) is an STM image of the as-grown homoepitaxial diamond (111) surface. Atom-like dots exist with threefold symmetry and the separation among dots measures 2.5 Å. This can be interpreted as H-terminated diamond (1x1) structure shown in Fig.2(b). These two images are consistent with the STM images of the previous studies[6,7,8].

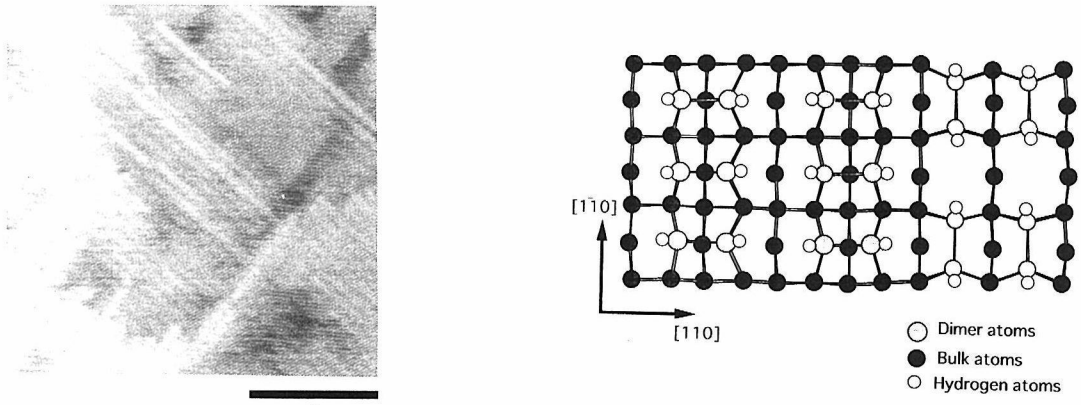

(a) (b)

Fig.1 (a) STM image of the as-grown homoepitaxial diamond (001) surface. Sample voltage and tunneling current were -0.1V and 1.0nA, respectively. (b) Atomic structural model for diamond (2x1) monohydride structure.

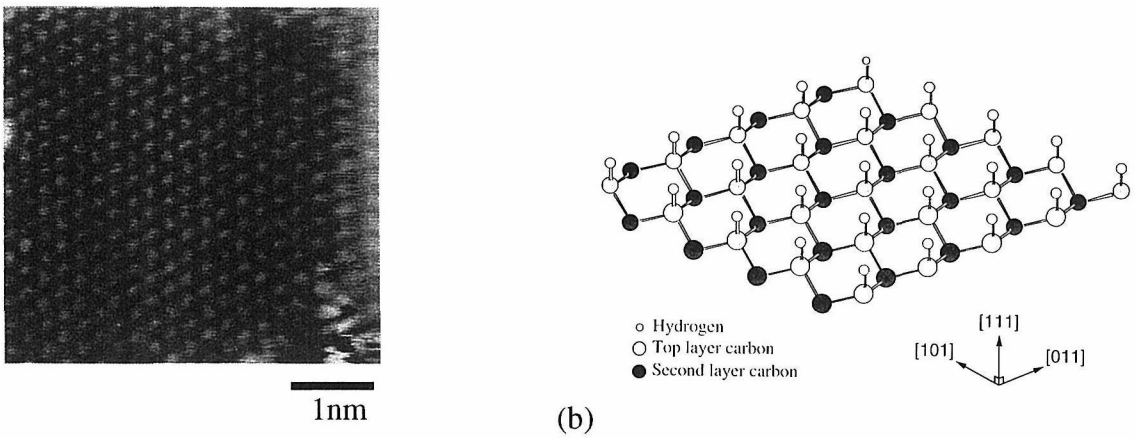

(a) (b)

Fig.2 (a) STM image of the as-grown homoepitaxial diamond (111) surface. Sample voltage and tunneling current were 0.05V and 1.0nA, respectively. (b) Atomic structural model for H-terminated diamond (1x1) structure.

In order to study the density of states(DOS) of H-terminated diamond (001) and (111) surface, we have measured the tunneling I-V characteristics on them (Fig.3(a) and 4(a)). Figure 3(b) and 4(b) show the normalized conductance (dI/dV)/(I/V) which is approximately proportional to the surface DOS[9]. For both the (001) and (111) surfaces, the broad states exist below the Fermi level. The existence of p-type semiconductive layers leads us to associate these states with valence-band states.

In Fig.3(b) and Fig.4(b), a pronounced state also exists near the top of valence-band states. In the (2x1) monohydride phase of (001) surface, the same type of surface state has been observed by ultraviolet photoemission spectroscopy (UPS)[10]. In order to elucidate the location of this state, STM observations of (001) surface have been performed at 0.5V bias (Fig.5). Figure 5 shows the dots with their separation of 2.2 Å. These dots correspond to the hydrogen atoms of (2x1) monohydride structure(Fig.1(b)). This result indicates that the pronounced state in Fig.4(b) is H-

related state. The electronegativity difference between H atoms and C atoms result in the empty states (the antibonding states) localized mainly around the H atoms. We speculate that the origin of the state in Fig.4(b) is ascribed to the C-H antibonding state.

In surface-molecule picture, the antibonding states are described as adsorbate-induced surface states of acceptor type. For H-terminated diamond surface, a surface state of acceptor type exists near the top of valence-band maximum. If the bands remain flat up to the surface as shown in Fig.6(a),

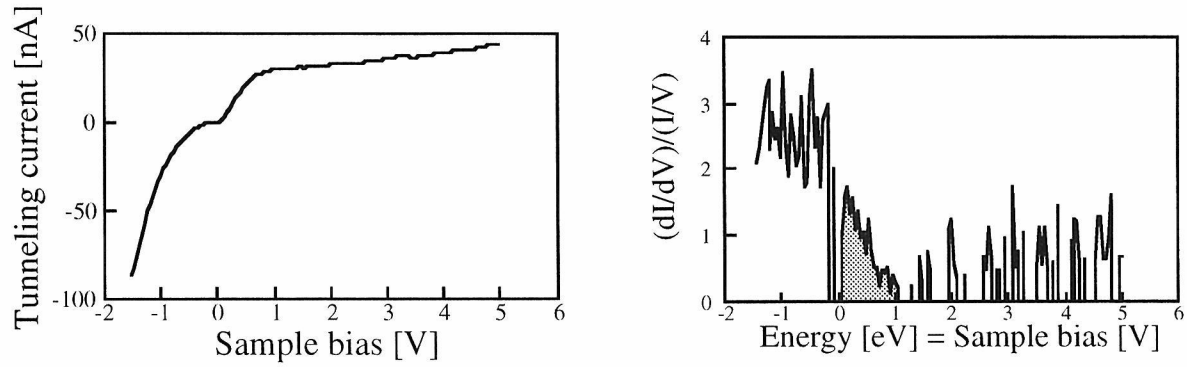

(a) (b)

Fig.3 (a) Tunneling current vs sample bias characteristics of H-terminated homoepitaxial diamond (001) surface and (b) the quantity (dI/dV)/(I/V).

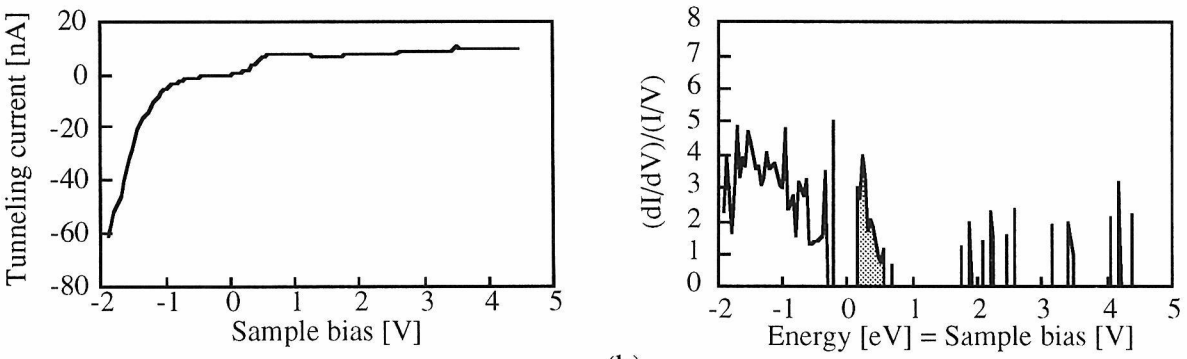

(a) (b)

Fig.4 (a) Tunneling current us sample bias characteristics of H-terminated homoepitaxial diamond (111) surface and (b) the quantity (dI/dV)/(I/V).

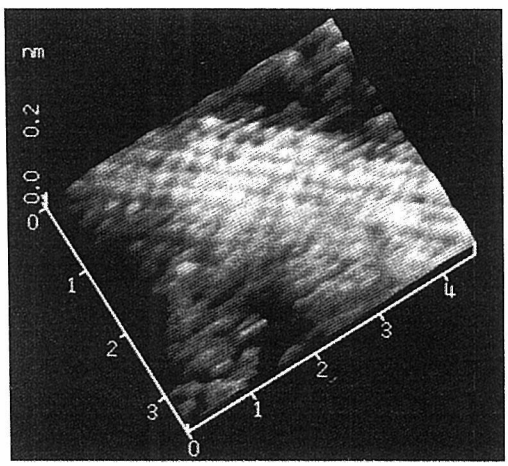

Fig.5 STM image of H-terminated (2x1) monohydride structure shown in Fig.1(b) with 0.5V applied to the sample. Tunneling current was 1.0nA.

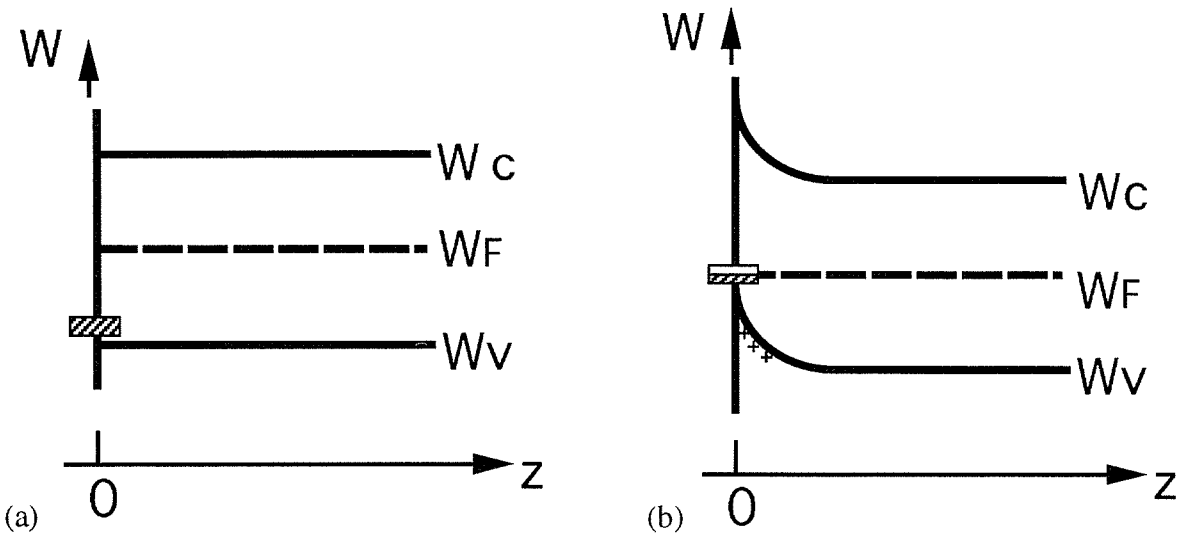

Fig.6 Band diagrams showing (a) flat bands and (b) accumulation of holes at H-terminated diamond surface.

surface acceptor is below the Fermi level and charged negatively. Thus the condition of surface charge neutrality is not satisfied. To satisfy the condition of surface charge neutrality, an accumulation of holes is needed at the surface. The bands are bend upward as shown in Fig.6(b) as a result.. This is one of the possible mechanisms of the formation of p-type semiconductive layers.

Acknowledgments

Special thanks to Mr.H.Sasaki and Mr.T.Imai of the Department of Electronics and Communication, Waseda University for their cooperation. The authors express their appreciation to Mr.N.Fujimori of Sumitomo Electric Industries, Ltd. and Mr.K.Nishimura of Osaka Diamond for providing the synthetic diamonds used in this work.

References

[1] M.L.Landstrass and K.V.Ravi, Appl. Phys. Lett., **55**(1989)975
[2] S.A.Grot, G.Sh.Gildenblat, C.W.Hatfield, C.R.Wronski, A.R.Badzian, T.Badzian and R.Messier, IEEE Electron Device Lett., **11**(1991)100
[3] T.Maki, S.Shikama, M.Komori, Y.Saguchi, K.Sakuta and T.Kobayashi, Jpn. J. Appl. Phys., **31**(1992)L1446
[4] H.Kawarada, M.Aoki and M.Ito, Appl. Phys. Lett., **65**(1994)1563
[5] for example, R.J.Hamers, R.M.Tromp and J.E.Demuth, Phys. Rev. Lett., **56**(1986)1972
[6] T.Tsuno, T.Imai, Y.Nishibayashi, K.Hanada and N.Fujimori, Jpn. J. Appl. Phys., **30**(1990)1063
[7] H.-G.Busmann, W.Zimmermann -Edling, H.Sprang, H.-J.Güntherodt and I.V.Hertel, Diamond and Related Materials, **1**(1992)979
[8] H.Sasaki and H.Kawarada, Jpn. J. Appl. Phys., **32**(1993)L1771
[9] R.M.Feenstra, J.A.Stroscio and A.P.Fein, Surf. Sci., **181**(1987)295
[10] A.V.Hamza, G.D.Kubiak and R.H.Stulen, Surf. Sci., **237**(1990)35

SNMS Techniques and Its Applications

Shigeki Kato
KEK (National Laboratory for High Energy Physics), Japan

ABSTRACT

Both postionization of sputtered neutrals and decoupling from secondary ions allow us improvements in sensitivity, tremendous reduction of matrix effects (higher quantificability) and simple analysis (unnecessity of detection of both positive and negative ions in two independent runs, for instance). A type of SNMS, SNART (Sputtered Neutral Analysis - Riken Type) has been developed to provide a means for semi-quantitative analysis of bulk or surface composition of both insulating and conducting materials. In SNART, material sputtering and postionization of sputtered neutrals are achieved using an electron-beam-excited, E.B.E. plasma which runs purely in a D.C. mode gives the potential for high sputter-etch rates (few nm/s) at low bombarding energy (100eV) with the added advantage that it may be operated over a wide range in discharge conditions. The applicability of this method to achieve analytical measurements is shown practically. As another technique of postionization, it is great of interest that synchrotron radiation from a storage ring accelerator which brings us a larger energy of photons compared with laser is capable to postionize sputtered neutrals in a scheme single photon ionization.

1. INTRODUCTION

Detecting sputtered atoms and molecules in a charged state using magnetic and/or electric fields became popular as SIMS, i.e., a technique to get information about chemical composition of surface and bulk of materials, because of its simplicity in principle to analyze ions emitted from a surface. Many application studies over years, however, revealed some difficulties in SIMS technique. Secondary yields even from elemental targets under the same sputtering condition range over 5 to 6 orders of magnitude [1]. The selection of primary ion species is strongly dependent on which charge state of ions should be detected for better secondary ion yields, positive or negative. It is also a general finding that sensitivity to chemical composition in SIMS analysis again strongly depends on the matrix of a target sample. In addition it is a problematic item that sputtered neutrals are the dominant fraction of all total sputtered particles, compared with sputtered ions which are in a fraction of 10^{-6} to 10^{-2}. On the other hand, SNMS allows us separation of sputtering and ionization processes, different from SIMS. Many techniques to postionize sputtered neutrals in surface and bulk analysis were proposed and developed [2-33], showing the results of great improvements in quantitative or quick semi-quantitative analysis owing to the decoupling.

Table 1 shows phenomena used for postionization and practical power sources to cause postionization. One might utilize those techniques mixed to get higher sensitivity and quantificability.

In this paper, focusing is made on that development and applications of SNART are reviewed and applicability of synchrotrons radiation to SNMS using a photon beam line of TRISTAN AR accelerator is considered.

Phenomena in Use for Postionization

1. Thermalization
2. Photon, Electron, Ion) Impact
3. Penning Effect
4. Electron Tunneling

Power Sources for Postionization

1. Thermalization ; Hot Furnace
2. Photon ; Laser Beam or Synchrotron Radiation
3. Electron ; Electron Beam, Plasma
4. Ion ; Sputtering Ion Beam
5. Penning Effect ; Plasma
6. Tunneling ; High Electric Field

Table 1 Phenomena and techniques used for postionization.

2. SNART AND ITS APPLICATIONS

In SNART [15,18,30-34], material sputtering and postionization of sputtered neutrals are achieved using an electron-beam-excited, E.B.E. plasma. A schematic of SNART is shown in Fig. 1. Electrons produced in the glow discharge plasma (region 1) are accelerated to energy V_a (typically 100 eV) in region 2 and subsequently flow into region 3 in the form of an electron beam guided by an axial magnetic field (typically, several hundred Gauss). In region 3 where Ar gas is introduced, a dense plasma is formed as a result of impact ionization of Ar atoms by the beam. Charged particle diffusion losses to the walls are reduced in this region by the magnetic field, which counteracts the plasma expansion and results in the formation of a dense narrow plasma column. Some of the ions created in region 3 are accelerated back into region 2, thus reducing the electron space charge in the accelerating region. Hence, the electron beam is steadily maintained without a current limit.

The distribution of electron energies in the E.B.E. plasma shows a distinct high-energy tail superimposed on a collisionally relaxed thermal background of typically several eV temperature. It is a characteristic of this source that deep sheath potentials are generated to sample surfaces perpendicular to the beam flow, resulting in sample sputtering by plasma ions. Therefore SNART has the capability to analyze insulating samples without a neutralizer for charge compensation at the target. Also, the probability of postionization of sputtered atoms is high. Calculations based on Langmuir probe measurements have shown a postionization probability of over 20 %. Both these effects are directly due to the presence of the electron beam component. Both bombarding ion energy and flux are controlled by the ion sheath established between the plasma and the surface. The nature of the sheath itself

is critically dependent on the plasma conditions. In this system we can independently control the sputtering energy and bombarding ion flux by simply varying the plasma discharge conditions. Despite the low sputtering energy (100 eV), high ion current densities of several tens of mA/cm^2 at the target position can be achieved, giving sputtering rates of a few tens of nm/s.

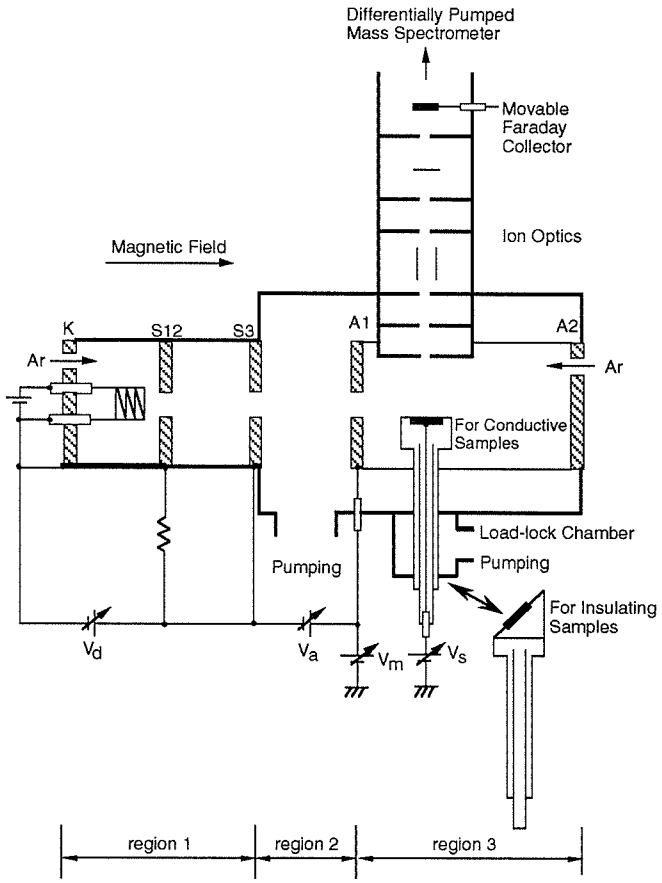

Fig. 1 A schematic of SNART System

The design of SNART allows for analysis of both insulating and conducting samples. In the latter case, the sample is placed with its surface normal to the beam direction and usually positioned about 10mm from the beam axis. The sample surface potential (up to 600 V) is regulated independently of the plasma using a voltage power supply. For insulator analysis the sample is oriented at an angle of 45 degrees to the beam direction and situated at the beam centre. In both cases the sample and housing are cooled by liquid nitrogen. An electrically floating ion extractor plate which forms the first electrode in the extraction lens system is located directly across the beam axis. Postionized sputtered particles are accelerated through the extractor sheath normal to the beam and are focused though a set of lenses to a quadrupole mass spectrometer. The extracted beam flux (up to 500 μA) and ion energy (typically 20 eV) are a function of the edge plasma parameters. Recent improvements in the ion optics design (lens positioning and dimensions) have increased the transmission to the quadrupole orifice from 10^{-4} % to 0.03 %. The target holder is equipped with a shield apparatus which floats electrically in the plasma. With the present operating conditions it is unavoidable that the holder is sputtered during analysis of the insulators. The opening diameter can be chosen so as to restrict the sputtered area.

Fig. 2 shows an example of depth profiles of the multilayered Cr-Ni target obtained by SIMS and SNART. Each layer of Cr-Ni on Si (100) has 3 nm thickness was prepared by ion beam sputter deposition method in 8 layers. SIMS analysis was performed under bombarding energy of 2.5 keV 0_2^+, ion current of 5 nA, and electronically gated area of 8μmϕ in rastered area of125x125μm^2. The primary ion energy was a lower limit to resolve

the multilayered structure under tolerable signal to noise ratio. One clearly finds five peaks in the profile of Cr. The third and fourth Cr layers as well as Ni layers could be observed in a large difference of ion counting rates while the fourth Ni layer was enhanced at the interface of the Si substrate. These are obviously due to its matrix effect. Sputter rate by SIMS in this case was estimated 0.004 nm/s which leads to relatively time- consuming analysis. Depth profiles of the same sample by SNART with measuring time of 30s are shown in Fig. 2(b). Alternative Cr and Ni layers were obviously observed in the same range of ion intensity although signal to noise ratio was relatively low because of the troubled secondary electron multiplier in the mass spectrometer. One can see Cr modulation ratio defined by peak-height to valley-height ratio remarkably increases as to compensate decrease of Ni modulation ratio in addition to a fact of slight difference of film thickness in each layer. This is explainable on the basis of both slight difference of deposition rate or deposition time on each layer during the film formation and the concerned interface diffusion. Reproducibility of the depth profiles in the same lot of samples was confirmed. Depth profile of Ni in the other lot of samples analyzed under the same sputtering condition as in Fig. 2(b) gave interface width of 16 to 84 % level was estimated 1.4 nm using relatively improved secondary electron multiplier of the mass spectrometer. Lateral homogeneity of sputtering over the target surface was investigated by AES line analyses across the surface after stopping sputtering

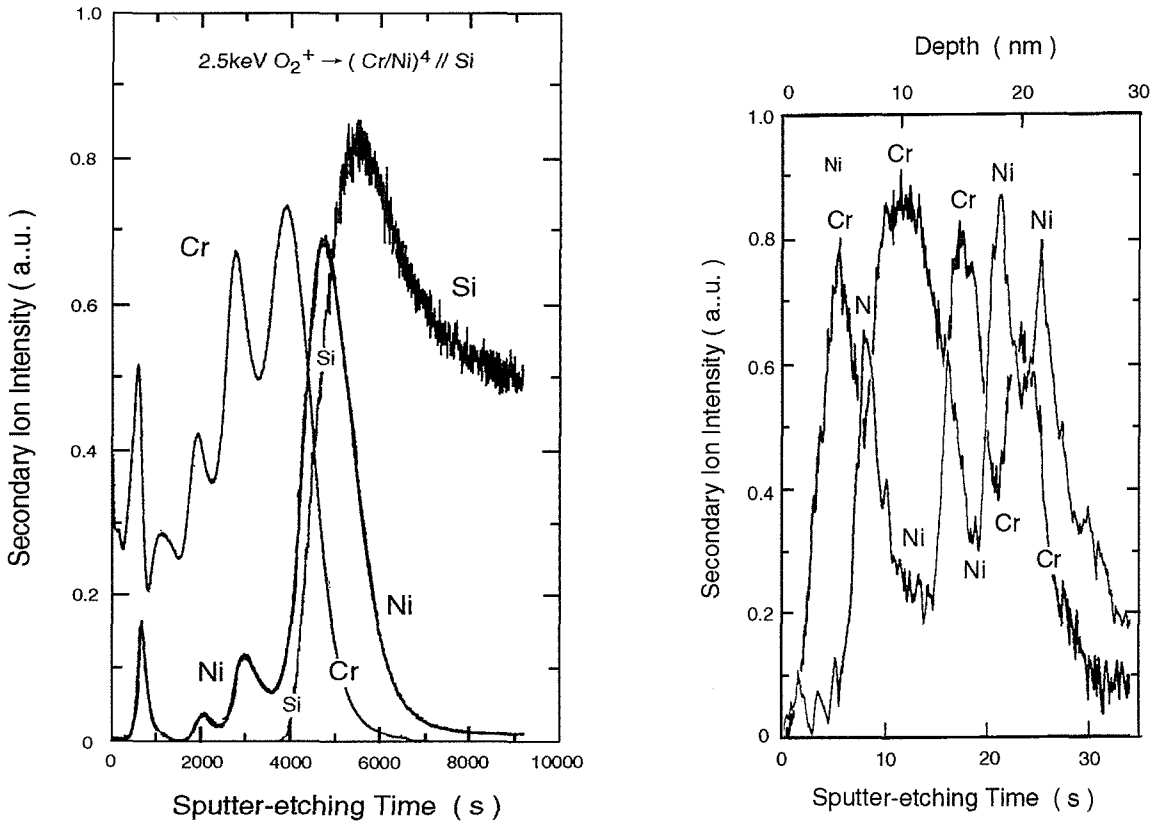

Fig. 2 Depth profiles of a multilayered Cr-Ni film (total thickness of 24 nm) on Si (100) obtained by SIMS (a) and SNART (b).

at a particular time before reaching substrate. It results that the atomic composition of Cr and/or Ni was found constant across the sputtered surface.

To assess the capability of SNART as a tool for quantitative analysis, it is necessary to determine the reproducibility from run to run in element sensitivity over the entire mass range and measure the variability in relative sensitivity of trace elements for different matrix types. The analysis of standard insulating and conducting samples (the trace element concentrations vary by three orders of magnitude for the sample types) allows us to evaluate the machine response of SNART. We define an elemental sensitivity factor D^0_M and a measurable relative sensitivity factor (r.s.f.), D^0_M/D^0_R which encompasses all machine sensitivities as follows:

$$\text{r.s.f.} = D^0_M/D^0_R = I^0_M \bullet C_R / I^0_R \bullet C_M$$

where I^0_M is the detected trace element ion current, C_R is the known concentration of the reference element (at%), I^0_R is the detected ion current of the reference element and C_M is the known trace element concentration (at%). For cross-sample comparison, Fe for conductors ($C_R=C_{Fe}$) and Si for insulators ($C_R=C_{Si}$) were usually chosen. The r.s.f.'s (averaged over 3 to 6 run) were determined at constant conditions for both conducting and insulating standard samples and showed excellent reproducibility from run to run (<5% spread for up to 6 repetitions). High-mass, low-melting-point elements such Pb and Sn and volatile low-mass elements such as P, however, show a large matrix dependency with generally very high r.s.f.. On the other hand, mid-range elements such as Ni, Co and Mo, show little matrix dependency and have r.s.f. values within one order of magnitude of unity. The neutral-to-

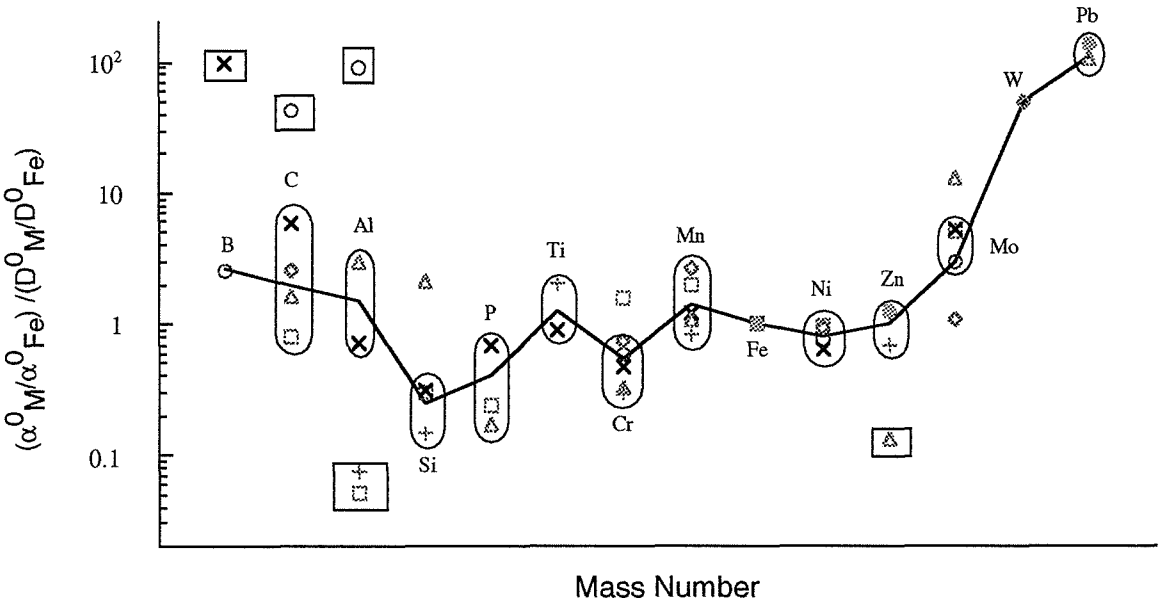

Fig. 3 A ratio of the calculated relative neutral-to-ion conversion factor, α^0_M/α^0_{Fe} to the machine measured relative sensitivity factor, D^0_M/D^0_{Fe}.

ion conversion factors (NICF) , α^0_M , which represent the probability of postionized particle detection independent of geometric and transmission effects, were theoretically determined for a selection of elements M in the ionizing volume of an E.B.E. plasma, using experimentally determined profiles for the radial beam-plasma parameters and a semi-empirical form for the electron impact ionization cross-section. A comparison between the relative NICF s, a^0_M/a^0_{Fe} and machine measured relative sensitivity factors D^0_M/D^0_{Fe} tests the validity of the model and demonstrates the influence of transmission and geometric factors on the measured ion signal. Deviations in the ratio $(\alpha^0_M/\alpha^0_{Fe})$ $/(D^0_M/D^0_{Fe})$ from unity can be used to investigate the functional dependency in instrumental and geometrical effects. The ratios obtained from the SNMS analysis of the 8 standard metal samples at normal operating conditions is shown in Fig. 3 and generally good agreement is found. For metallic elements in the intermediate mass range, the variation is smaller allowing semi-quantitative analysis (D^0_M/D^0_{Fe} varies by less than one order of magnitude over the samples). For increasing elemental mass (m/e>100), however, the ratio of the predicted current to the detected ion current increases . It may be accounted for by a strong mass dependency in the transmission of the mass spectrometer, however other effects not included in the model may be significant in these cases. These may include competing ionization mechanisms such as penning and charge exchange.

3. POSTIONIZATION BY SYNCHROTRON RADIATION

Postionization by photon as shown in Table 1 is one of the promising techniques for SNMS and has been intensively investigated over ten years. In this technique, schemes of resonant multiphoton ionization (RMPI) and nonresonant multiphoton ionization (NRMPI) by Laser are usually used. However, in order to obtain uniform r.s.f. for all elements one would have to get saturation of photoionization regardless of ionization potential for the elements in a well-defined ionization volume because slower spatial fall-off of cross section in a laser beam intensity leads more of unsaturated regime of ionization. On the other hand, synchrotron radiation (SR) makes atoms or molecules directly ionized in a scheme of single photon ionization because its photo energy exceed the ionization potential for every element in a whole cross

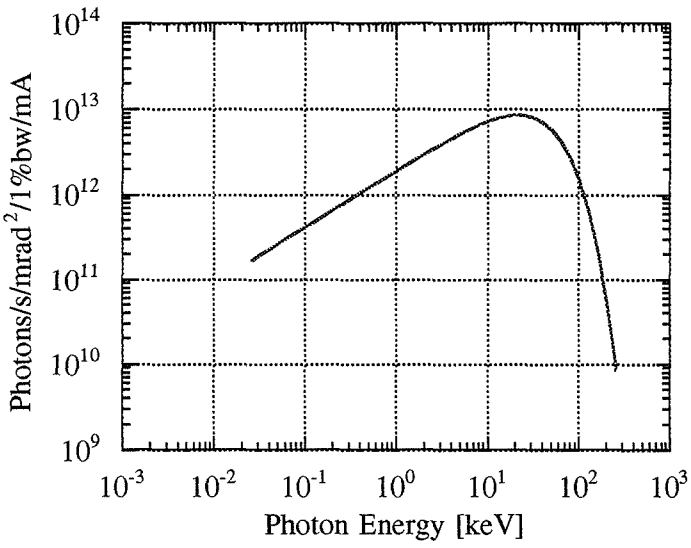

Fig. 4 Photon spectra of TRISTAN AR of KEK.

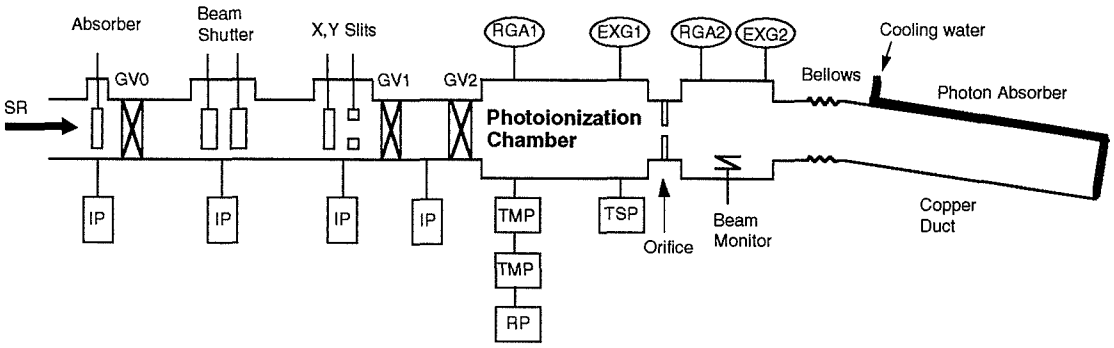

Fig. 5 A schematic of the beam line, NE#9 of TRISTAN AR.

section of its photon beam. Insertion devices like a wiggler and an undulator where structures with periodic arrays of magnets are used bring us a higher photon intensity by more than two orders of magnitude with continuous spectra and with a series of harmonics respectively in comparison with a conventional bending magnet. In addition SR offers a very high sampling frequency with an order of MHz at least depending on a number of electron or positron bunches in an accelerator although the sampling frequency of sputtered neural is limited by the repetition frequency of a laser which is usually in a range up to 100Hz for high power laser. No adoption of SR to postionization of sputtered neutrals has been, however, attempted since the first report was made by Oshima et al. [35] using a beam line of the Photon Factory in KEK. Considering those features use of SR from an e^- accelerator (6.5GeV, ~40mA) called TRISTAN AR which has photon spectra shown in Fig. 4 and has a critical energy of 26.3keV is being planned. A built beam line or NE#9 of TRISTAN AR shown in Fig. 5 mainly consists of photon absorbers, beam shutters, X - Y slits and a photoionization chamber. The chamber where a base pressure is in a range of 10^{-8} Pa is set at a distance of about 15 m from the SR source where a bending magnet is used for light source. A typical photon flux density given by the spectra in Fig. 4 was $6X10^{16}$ photons/cm^2s. A total cross section of whole electrons below 8 keV of binding energy are calculated to be $1X10^{-15}$ cm^2 for Si for example. A photon beam of which size is adjustable by X - Y slits without reducing the flux density shines sputtered neutrals above a sample to be analyzed.

4. SUMMARY

Effective sputtering of materials and efficient postionization of sputtered neutrals are achievable in SNART. Improvement in the ion optic system of a quadrupole mass spectrometer allowed the acquisition of conducting and insulating material mass spectra with a detection sensitivity of 40 ppb and 5 ppm at low sputtering energy (< 600eV and < I50eV), respectively. Run to run reproducibility in the observed concentrations is good (< 5%), and over most of the mass range for nonvolatiles, the r.s.f.'s (insulators and conductors) vary by less than one order of magnitude from matrix to matrix. The large variability in r.s.f.'s with matrix element observed for low-mass volatile and also high-mass low-melting-point ele-

ments poses a problem. A comparison between the calculated relative NICF and the measured r.s.f. was made showing generally good agreement. Postionization of sputtered neutrals by SR is being under investigation. SR especially gives photon energies over a photoionization energy range to access the entire periodic table system. The prepared beam line would be able to offer sufficient photon flux for the aim.

ACKNOWLEDGMENTS

All works introduced in this review were carried out in collaborations with M. Hamagaki, T. Hara, The Institute of Physical and Chemical Research, S. Hayashi, Nippon Steel Corporation and J. W. Bradley, University of Manchester) for SNART and with Y. Suetsugu and K. Kanazawa, KEK for the photon beam line. The author wish to thank the people. Thanks are also due to Y. Suetsugu and K. Kanazawa, National Laboratory for High Energy Physics for collaborations of photon beam line.

References

[1] H. A. Storms, K. F. Brown and J. D. Stein, Anal. Chem.49(1977)2023.[1] R.E. Honig, J. Appl. Phys. 29(1958)549.
[2] R.E. Honig, in Advances in Mass Spectrometry, J.C.Waldron, ed. (Pergamon Press, London, 1959), p.162.
[3] J.R. Woodyard and C.B. Cooper, J. Appl. Phys. 35(1964).
[4] H. Oechsner and W. Gerhard, Surf. Sci. 44(1974)480.
[5] N. Winograd, J.P. Baxter and F.M. Kimock, Chem. Phys. Lett. 88(1982) 581.
[6] C. H. Becker and K. T. Gillen, Anal. Chem. 56(1984)1671.
[7] A. Wucher, F. Novak and W. Reuter, J. Vac. Sic. Technol. A6(1988)2265.
[8] K.H. Mueller and H. Oechsner, Mikrochimica Acta[Wien], Suppl. 10(1983) 51.
[9] H. Oechsner, Pro. IX IVC-V ICSS, Madrid (1983).
[10] K.-H. Mueller, K. Seifert and M. Wilmers, J. Vac. Sci. Technol. A3(1985)1367.
[11] H. Gnaser, J. Fleichhauer and W. O. Hofer, Appl.Phys. A37(1985) 211.
[12] N.E. Sanderson, E. Hall, J. Clark, P. Charalambous and D. Hall, Mikrochimca. Acta [Wien], 1 (1987) 275.
[13] J. Tumpner, R. Wilsch and A. Benninghoven, J. Vac. Sci. Technol. A5 (1987) 1186.
[14] D. Lipinsky, R. Jede, O. Ganschow and A. Benninghoven, J. Vac. Sci. Technol. A3(1985)2007.
[15] M. Hamagaki, S. Hayashi and S. Kato, Vacuum 41(1990)1730.
[16] S. Kato and S. Hayashi, 1st Int. Workshop on Postionzation Techniques in Surf. Analysis, Kaiserslautern, W.Germany, Oct.(1989).
[17] S. Hayashi and S. Kato, ibid.
[18] Y. Hasiguchi, S. Hayashi, T. Ohtsubo, S. Kato, H. Hamagaki, T. Hara, K. Aoyagi and S. Namba, Surf. & Interf. Analysis 14(1989)595.
[19] S. Hayashi, Y. Hashiguchi, K. Suzuki, T. Ohtsubo and B.J. McIntosh, Surf. & Interf. Analysis 17(1991)773.
[20] H.N. Migeon and M. Schuhmacher, Proc. 1st RIKEN Symp. on Postion-ization Techniques of Sputtered Neutrals, Ed. S. Kato, Wako, Japan (1990)p.16.
[21] T. Shimamura, ibid.
[22] T. Ishitani, N. Sakudo, H. Tamura and I. Kanomata, Phys. Lett. 67A (1987) 375.
[23] G. Kampwerth, M Terhorst, E. Niehuis and A. Benninghoven, Proc. of SIMS VIII, 1991, p.563.
[24] J.E. Parks, D.W. Beekman, L.J. Moore, H.W. Schmitt, M.T. Spaar and E.H. Taylor, Inst. Phys. Conf. Ser. 84(1986)157.
[25] P. Gelin and J.L. Debrun, Nucl. Instrum. Methods in Phys. Res. B40/41(1989)190.
[26] C.H. Becker, Methods of Surface Characteerization, Vol. 2, Ionspetroscopy of Surfaces, Chapter 6, ed. A.W. Czanderna (Plenum Press), in press.
[27] N. Thonnard, J.E. Parks, R.D. Willis, L.J. Moore and H.F. Arlinghaus, Surface and Interface Analysis in printing.
[28] N. Thonnard, Presented at 1st RIKEN Symp. on Postionization Techniques of Sputtered Neutrals, Ed. S. Kato, Wako, Japan (1990).
[29] G. Blaise, Scanning Electron Microscopy I(1985)31.
[30] S. Kato, Ionics 10(1989)35.
[31] S. Kato, M. Hamagaki, T. Hara, K. Aoyagi and S. Namba, Nucl. Instr. & Meth. in Phys. Res B35(1988)550 .
[32] S. Kato, Proc. of 1st RIKEN Symp. on Postionization Techniques of Sputtered Neutrals, Ed. S. Kato, Wako, Japan (1990), p.14.
[33] W. Bradley and S. Kato, J. Vac. Soc. Jap 136 (1993)128.
[34] W. Bradley and S. Kato, ibid. to be submitted.
[35] M. Oshima, S. Maeyama, T. Kawamura, T. Maruo and K. Nagai, J. Vac. Sci. Technol. A8(1990)2570.

Quantitative Analysis of Micro-volume by Focused Ion Beam Secondary Ion Mass Spcetrometry (FIB-SIMS)

*Yoshimasa Nihei, Bunbunoshin Tomiysau, Tetsuo Sakamoto and Masanori Owari**
Institute of Industrial Science, University of Tokyo
*Environmental Science Center, University of Tokyo

1 Introduction

Secondary ion mass spectrometry (SIMS) is well established as one of the most sensitive methods for local analysis. Using O^+, O_2^+, O^-, or Cs^+ ions as a primary beam, many studies for quantitative analysis have been carried out. However, further improvements in spatial resolution and sensitivity are needed for the analysis of smaller volume of materials and far smaller amounts of atoms.

Recently, liquid-metal ion sources (LMIS) have been developed that can produce much higher current density beams with diameters < 0.1 μm that are much smaller than those of other widely used primary beams for SIMS. Levi-Setti *et al.* have used a gallium LMIS to construct an imaging SIMS by using a magnetic sector type mass analyzer [1]. Benninghoven *et al.* have developed the high resolution surface imaging system by combining TOF-SIMS, Laser-SNMS and Focused Ion Beam (FIB) [2].

We constructed a submicron SIMS with a parallel ion mass detection system by using a gallium primary beam extracted from a LMIS [3], and studied fundamental factors for quantitative analysis of small volumes and particles. Moreover, we devise the new type of three dimensional SIMS analysis by using FIB-SIMS.

2 Instrumentation of FIB-SIMS

In order to improve the spatial resolution of SIMS, the narrower and brighter ion beam such as FIB is needed. Because of the higher sputtering rate of FIB, however, the signal intensity of SIMS changes very rapidly. Therefore, in order to get quantitative and integrated intensity of secondary ions, and the ratio of them, the simultaneous detection of multiple elements would be required. This kind of detection system will bring us the another advantage such as higher efficient detection of secondary ions.

The schematics of the apparatus are shown in Fig. 1. The apparatus consists of a primary ion optical column, a secondary electron detector, secondary ion transfer optics including a total secondary ion detector, a plane-focusing mass analyzer equipped with multichannel ion detection system, and control electronics.

Field-emitted Ga^+ ions are accelerated to 35 kV and focused on the sample. The beam diameter on the sample is estimated to be < 0.1 μm for a 100 pA beam current; the primary beam density is estimated to be ~ 1 A/cm^2. Therefore, both high-spatial resolution and large sputtering rate are realized. Secondary electrons (SE) are detected with a SE detector in order to display a SE image of the sample surface. Secondary ions (SI) are accelerated by a sample

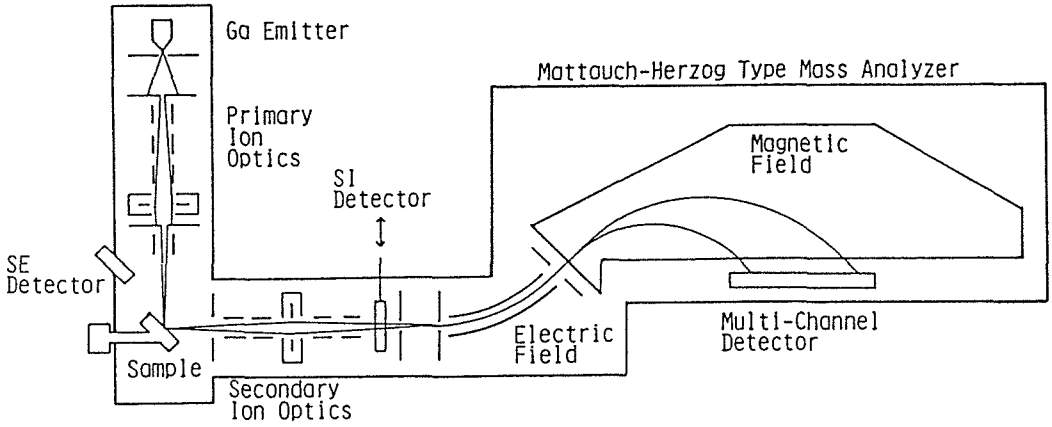

Figure 1: Schematic diagram of the multichannel detection submicron secondary ion mass spectrometer.

bias (7.5 - 10 kV) and transferred to the mass spectrometer. The SI detector can be inserted in the SI transfer optics in order to monitor total SI intensity without mass separation for obtaining a SI image. The Mattauch-Herzog type mass analyzer features plane focusing with the dispersion proportional to $(m/e)^{1/2}$ along the focal plane. Therefore, this type of mass spectrometer is suitable for multichannel detection by using a position sensitive detector. A multichannel parallel detector is placed on the focal plane, and covers 1 : 2 mass range with 120 independent channels. Therefore, all ions whose m/e are within 1 : 2 mass range (e.g, $m/e = 10 - 20, 20 - 40$), are detected simultaneously.

3 Quantitative Analysis

3.1 Shave-off Analysis and Relative Sensitivity Factor (RSF)

In general, secondary ion yield largely depends on the incident angle of the primary ion beam to the sample surface. When the sample is not a flat plane such as a particle, a difficult topographic effect is introduced. Therefore, for the quantitative analysis of fine particles by SIMS, special attention should be paid to maintain the incident angle constant. In order to circumvent the topographic effect, especially edge enhancement, we developed a new scanning mode, "Shave-off "mode [4]. Figure 2 illustrates the Shave-off analysis of a micro particle. In the Shave-off mode, a fast horizontal sweep of a FIB is combined with a very slow vertical sweep. The FIB shaves the particle off from an edge to another one completely. Therefore, after only one frame scan, the entire volume of the particle is sputtered out. In the conventional analysis, the primary ion beam is too broad to shave a particular section of a micro particle. Furthermore, the outer part is sputtered more quickly than the top part, because the sputtering rate depends on the incident angle. In this situation, the structural information on the particle can be no longer obtained. On the other hand, in the Shave-off mode, the edge of FIB always shaves the edge of a sample. Therefore, the incident angle of the FIB is kept constant. Thus, in the Shave-off mode, (i) edge effect is canceled and (ii) knock-on mixing and sputter deposit are negligible.

A method of quantitative analysis by SIMS is needed to use " Relative Sensitivity Factor (RSF) ". In the Shave-off mode, RSFs of 13 elements (Li, B, Na, Mg, Al, Si, K, Ca, Ti, Fe, Sr, Ba and Pb) in glass matrices were obtained [5]. RSF, S_r(A), of element A relative to

element R is defined by Eq. (1).

$$S_r(\mathrm{A}) = \frac{\text{impurity ion (A) intensity (counts/s)/impurity atom density (atoms/cm}^3\text{)}}{\text{reference ion (R) intensity (counts/s)/reference atom density (atoms/cm}^3\text{)}} \quad (1)$$

Determined RSFs for oxide glass matrix by Ga FIB are plotted in Fig. 3 as a function of the first ionization potential of each element, where ^{28}Si is adopted as a reference element. Electropositive elements such as alkali and alkali-earth metals gave large values of RSF. As the first ionization potential increases, RSF decreases logarithmically. In this plot, the slope is approximately 0.5 decade/eV.

The Ga FIB SIMS enables analysis of individual microparticles through the use of its high spatial resolution. Therefore, by utilizing the RSFs determined from the Shave-off analyses of oxide glass matrices, the quantitative analysis of fine particles is made possible.

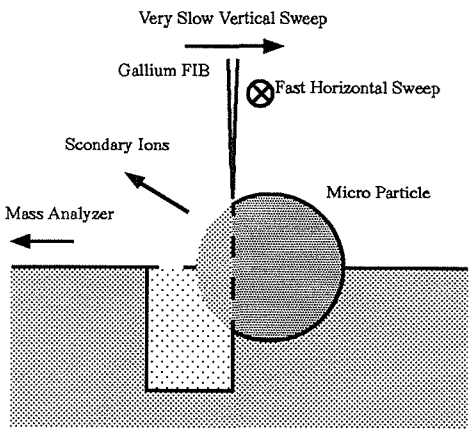

Figure 2: Shave-off analysis of a micro particle.

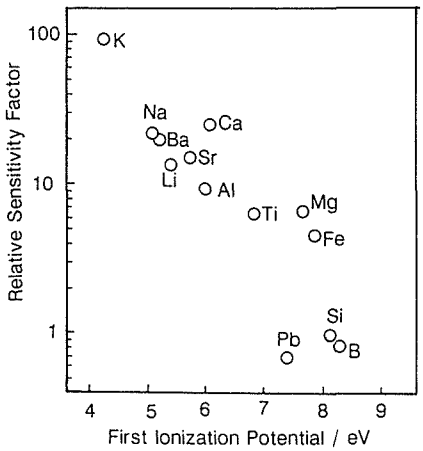

Figure 3: Relationship between relative sensitivity factor for gallium primary ion beam and first ionization potential of elements. (Reference : ^{28}Si)

3.2 Oxygen Matrix Effect

An important factor for quantitative analysis is matrix effect on secondary ion yield. Especially, the presence of oxygen on a surface or in a matrix enhances positive secondary ion yield, greatly. The oxygen matrix effect is thought to be useful for the improvement of detection limit.

In a Ga FIB SIMS, by introducing an oxygen gas into a specimen chamber the positive secondary ion intensity is enhanced by $1 \sim 2$ orders [6]. The amount of enhancement depends on oxygen partial pressure, FIB scanning condition and sample material. This enhancement effect by ambient oxygen is considered to be the result of implantation of adsorbed oxygen into atomic mixing layer. Under this assumption, we made a calculation model for oxygen matrix effect by ambient oxygen [7]. Experimental and calculated results on a Al sheet is shown in Fig. 4. The calculation well reproduced the experimental results, quantitatively. Furthermore, the calculation model tells us that the most important quantity is the equilibrium oxygen coverage during FIB bombardment. At a certain oxygen pressure, in order to obtain the best effect of oxygen, the coverage should be kept as much as possible by reducing the average current density or using a pulsed FIB.

Contrary to the advantage of the oxygen matrix effect, when the oxygen is distributed in a matrix inhomogeneously, much attention to the anomalous effect of oxygen is necessary for SIMS analysis. In Ga FIB SIMS, it is not an usual case where the secondary ion of implanted Ga is measured at a comparable intensity of matrix ion. This means that Ga primary ion is accumulated in the sample at a considerable concentration. Therefore, the behavior of Ga^+ secondary ion intensity to the oxygen matrix effect should be an interest. We measured both Cu^+ and Ga^+ secondary ion intensities at various oxygen partial pressures [8]. The sample was a polycrystalline Cu sheet with purity of 99.9 %. Prior to the experiment the native surface oxides were removed by ion bombardment for 30 minutes. According to the variation of Ga^+ during the presputtering, the accumulation of Ga had been in a steady state within 10 minutes. The beam conditions were 30 keV energy, 0.3 $\mu m\phi$, 230 pA current, 10° of incident angle to the surface normal and rastered area of 20 × 20 μm^2.

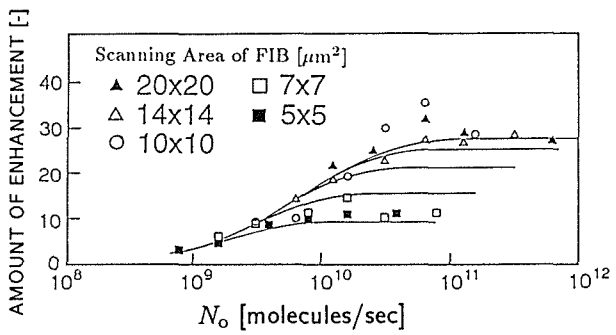

Figure 4: Dependence of Al^+ secondary ion intensity from a polycrystalline Al sheet on the number of oxygen molecules collide with scanning area per unit time and scanning area.

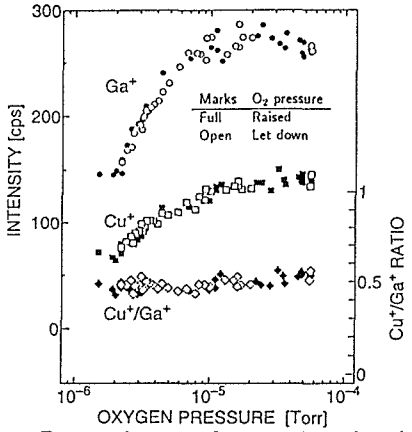

Figure 5: Dependence of secondary ion intensities of Cu^+ and Ga^+ from a Cu sheet on the oxygen partial pressure.

At first, the oxygen partial pressure was raised from the base pressure to 5 × 10^{-5} Torr within 150 seconds. The results are indicated by full marks in Fig. 5. As commonly observed, Cu^+ intensity increased non-linearly with the oxygen pressure. As for Ga^+ intensity, almost the same behavior was observed. As a result, the ratio of the two intensities remained constant. After that, the oxygen pressure was let down to the base one within 150 seconds. The results are open marks in Fig. 5. Although the pressure was reversely varied, each intensity showed a good coincidence at the same pressure. Thus, the behaviors of matrix and Ga^+ secondary ion are found to be quite similar under this experimental condition. This situation is expressed by Eq. (2),

$$\frac{I_{Cu^+}}{I_{Ga^+}} = \frac{C_{Cu} P_{Cu^+} G_{Cu^+}}{C_{Ga} P_{Ga^+} G_{Ga^+}} \simeq \text{constant}, \tag{2}$$

where C is the atomic concentration, P is the ionization probability and G is the instrumental factor. By introducing an oxygen gas, C_{Cu}, C_{Ga}, P_{Cu^+} and P_{Ga^+} should be changed largely compared with G. Under a condition where C_{Ga} is approximately constant, i.e. at low oxygen concentration, the exact variation of C_{Cu} can be obtained from the intensity ratio. Furthermore, if the product of the other factors in Eq. (2) is determined under various experimental conditions, the ratio of concentration can be obtained. Therefore, there is a possibility of using Ga as an internal standard in Ga FIB SIMS.

4 Application of FIB-SIMS

In SIMS analyses, as shown in Fig. 6 the conventional method of the three dimensional analysis is defined as the combination of a layer by layer sputter etching and an elemental mapping. However, the sputtering rate might change during ion bombardment. Such depth positioning, therefore, tends to be uncertain. On the other hand, by cross-sectioning using a Ga FIB, one can get any section in a sample directly. After that, using the Ga FIB as an analytical probe, the elemental maps of the cross-section are obtained. We defined this procedure as the novel three-dimensional analysis. This method has the advantages of (i) ability to analyze any section of a sample and (ii) highly accurate positioning under microscopic observation.

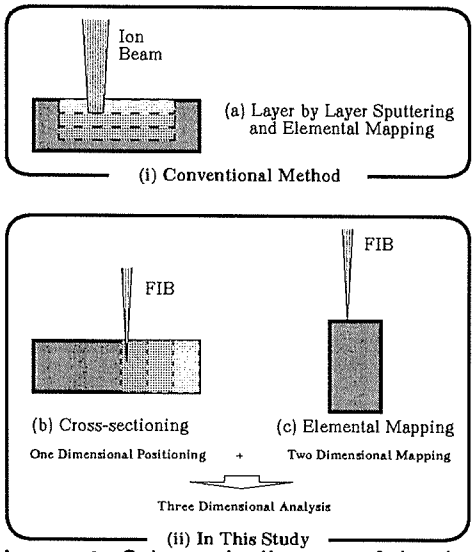

Figure 6: Schematic diagram of the three dimensional analysis.

We present the novel three-dimensional analysis and Shave-off analysis of (i) inorganic microcapsules [9] and (ii) non-metallic inclusion particles in steel by Ga FIB SIMS [8].

4.1 Inorganic Microcapsule

We measured inorganic microcapsules, with diameters from 2 to 3 μm. The condition of the primary ion beam was as follows : 35 kV acceleration, 70 pA current, and 0.2 μm diameter. The samples are inorganic microcapsules, which consist of a thin shell of silicon dioxide encapsulating the powder of titanium dioxide [10].

The procedure of the cross-sectioning of the capsule is as follows. At first, one of the capsule on an indium plate was selected. After that, the capsule was cross-sectioned by line scanning of FIB at oblique incidence. The exposed surface was observed and analyzed by FIB SIMS to obtain elemental maps. Figure 7 shows the elemental maps of ^{28}Si (a) and ^{48}Ti (b) of a microcapsule and the sketch of the microcapsule (c). The images (a) and (b) were obtained simultaneously from the same capsule. An internal vacancy of microcapsule was clearly observed. During these measurements, any charging of the capsule wall and the contents was not observed.

We performed Shave-off analyses for 42 particles on an indium plate. By observing the Shave-off profile of each particle, we estimated the volume of the internal vacancy of each microcapsule quantitatively. Figure 8 shows the observed and expected Shave-off profiles of a microcapsule; particle A as an example. The sweep velocity of the primary beam was 1/600 μm$\cdot$s^{-1} in the vertical direction. If there was no internal vacancy, the Shave-off profile should appear like the expected profile. The disagreement between the expected profile with no vacancy and the observed one indicates the existence of an internal vacancy. We fitted the expected profile to the observed one by using the diameter and thickness of each particle, and estimated the volume of the internal vacancy.

The results obtained from the profile of particle A and other 41 particles are shown in

Table 1. The volume of internal vacancy which were obtained from 42 particles are dispersed from 0 to 80 vol.% and the average value was 42 %. On the other hand, the volume of internal vacancy obtained from bulk chemical analysis was 40 vol.% [10]. Our experimental value for the volume of the internal vacancy agrees well with the bulk chemical analysis.

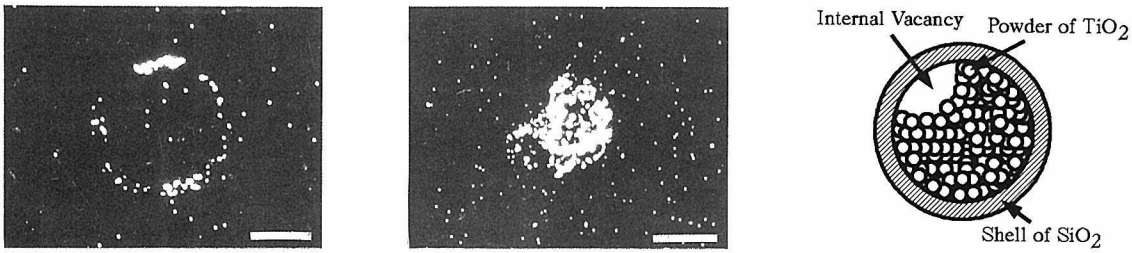

(a) $^{28}Si^+$ image (b) $^{48}Ti^+$ image (c) Sketch

Figure 7: The elemental maps of the cross-section of a microcapsule. (Scale bar : 1 μm)

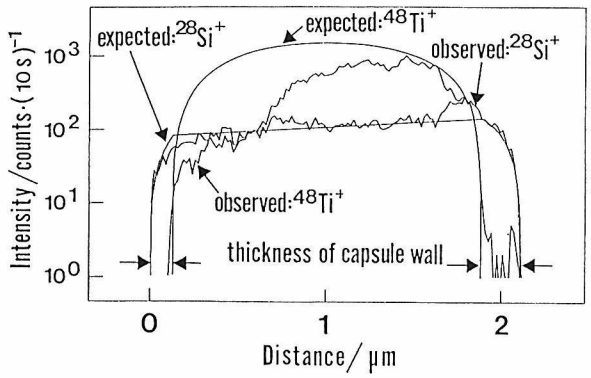

Figure 8: The observed and expected Shave-off profiles of single microcapsule; particle A.

Table 1: Results obtained in this study.

	Diameter of capsule (μm)	Thichness of thin shell (μm)	Volume of internal vacancy (vol.%)
Particle A	2.1	0.18	30
Range (min.-max.)	1.0-4.2	0.04-0.27	0-80
Average	2.2	0.13	42

4.2 Non-metallic Inclusion in Steel

We carried out the novel three dimensional analysis of non-metallic inclusion particles in steel. The inclusion particles were segregated onto the surface of the steel by electron bombardment heating. The beam condition of the primary Ga^+ ion beam was as follows : 35 kV acceleration, 250 pA current and 0.2 μm diameter.

Figure 9 shows the typical results. The total secondary ion image of the cross-section of the segregated inclusion onto the surface of the steel is shown in Fig. 9(a). The cross-section was very flat except for the lump on it. The secondary ion signals from the inclusion and the sputtered material during the cross-sectioning were also observed. By mass analyzing, the elemental maps of Al and Ca were obtained, respectively. Aluminum and Ca were distributed inhomogeneously over the cross-section.

In order to obtain the information about the origins of the inclusions, we carried out compositional analyses of the individual particles. 10 particles of the inclusion were analyzed by the Shave-off analysis. Figure 10 shows the typical Shave-off profiles of each inclusion particle. The signals were accumulated for every 8 seconds. From the Shave-off profiles, the diameters of the inclusion particles were estimated. Typical Shave-off profile of homogeneous particles is shown in Fig. 10 (a). There was only one particle (c), whose compositional distribution was heterogeneous. In the Shave-off profile (c), the profiles of $^{27}Al^+$ and $^{40}Ca^+$ were different from

that of $^{24}Mg^+$. The signal of molecular ion AlN^+ was observed from the particle (b).

The composition of each particle was obtained from these profile and the relative sensitivity factors by assuming that the inclusion consists of oxides. Using these data, the cluster analysis, which is a kind of multivariate analysis, was carried out. From the cluster analysis, the inclusions were classified into four kinds. The average composition of each cluster is listed in Table 2. These results bring us the information on the generation process of the inclusions.

Table 2: Results of the cluster analysis of the inclusions. (wt.%)

Cluster No.	Al_2O_3	CaO	MgO	SiO_2	Number of particle
1	77.7	22.0	0.3	0.0	6
2	76.1	0.7	23.3	0.0	2
3	73.4	3.9	8.7	13.9	1
4	25.4	73.7	1.9	0.0	1

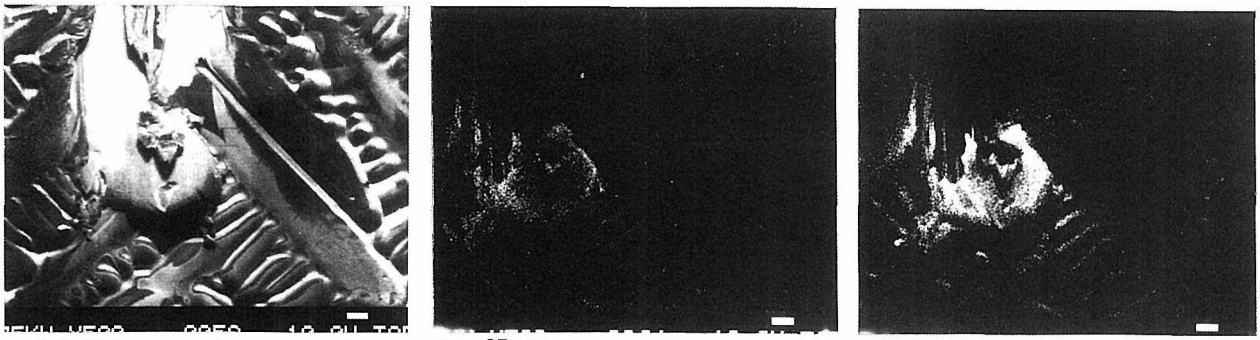

(a) SI image of cross-section (b) $^{27}Al^+$ image of cross-section (c) $^{40}Ca^+$ image of cross-section

Figure 9: Images of the cross-section of the particles. (Scale bar : 10 μm)

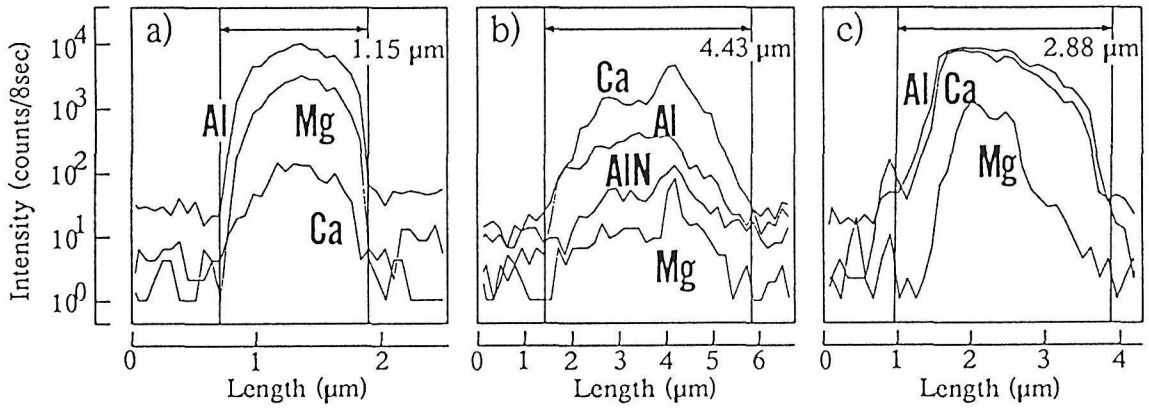

Figure 10: Shave-off profiles of single inclusion.

5 Summary

A submicron resolution SIMS apparatus was constructed by combining a Ga FIB and a multichannel parallel detection system. The Ga FIB SIMS has high spatial resolution and characteristic scanning mode; Shave-off mode. In the Shave-off analysis, edge effect is canceled, and knock-on mixing and sputter deposit are negligible. For quantitative analysis, RSFs for oxide glass matrix by the Shave-off mode of the Ga FIB are determined. By using the RSFs, we carried out Shave-off analyses of the inorganic microcapsules and the inclusion particles with diameter of around only a few μm. Through these analyses, the Ga FIB SIMS is recognized to be a very powerful tool for quantitative analysis of microparticles. For non-oxide particles, additional techniques such as utilization of the oxygen matrix effect will provide us further improvement on the detection limit. Moreover, *in situ* combination of micromachining and high resolution elemental mapping enables three-dimensional analysis of the microstructure of materials under microscopic observation.

References

[1] R. Levi-Setti, J. M. Chabala, K. Gavrilov, J. Li, K. K. Soni and R. Mogilevsky : *Secondary Ion Mass Spectrometry SIMS IX*, eds. A. Benninghoven, Y. Nihei, R. Shimizu and H. W. Werner, p.233, John Wiley & Sons (1994).

[2] J. Zehnpfenning, E. Niehuis, H-G. Cramer, T. Heller, R. Möllers, M. Terhorst, A. Schnieders, Zhiyuan Zhang and A. Benninghoven : *Secondary Ion Mass Spectrometry SIMS IX*, eds. A. Benninghoven, Y. Nihei, R. Shimizu and H. W. Werner, p.561, John Wiley & Sons (1994).

[3] Y. Nihei, H. Satoh, S. Tatsuzawa, M. Owari, M. Ataka, R. Aihara, K. Azuma and Y. Kammei : J. Vac. Sci. & Technol. **A5** (1987) 1254.

[4] H. Satoh, M. Owari and Y. Nihei : J. Vac. Sci. & Technol. B**6** (1988) 915.

[5] H. Satoh, M. Owari and Y. Nihei : Jpn. J. Appl. Phys. **32** (1993) 3616.

[6] T. Sakamoto, B. Tomiyasu, N. Mie, M. Owari and Y. Nihei : *Secondary Ion Mass Spectrometry SIMS IX*, eds. A. Benninghoven, Y. Nihei, R. Shimizu and H. W. Werner, p.53, John Wiley & Sons (1994).

[7] T. Sakamoto, B. Tomiyasu, M. Owari and Y. Nihei : Surf. Interface Anal., **22** (1994) 106.

[8] Y. Nihei, B. Tomiyasu, T. Sakamoto and M. Owari : Proceedings of Japan-China Joint Symposium, in press.

[9] B. Tomiyasu, N. Mie, M. Owari and Y. Nihei : *Secondary Ion Mass Spectrometry SIMS IX*, eds. A. Benninghoven, Y. Nihei, R. Shimizu, H. W. Werner, p.565, John Wiley & Sons (1994).

[10] Y. Nakahara, S. Tsubota, M. Mizuguti and F. Nakahara : Extended Abstracts of the 6th International Conference on Surface and Colloid Science, p.539 (1988), Hakone

Ultra Fine Feature Analysis Using Secondary Ion Emission

M. Schuhmacher and F. Hillion
Cameca, 103, bd Saint-Denis, B.P. 6, 92403 Courbevoie Cedex, France

INTRODUCTION

In recent years, progress in various fields of applied materials science has been a direct consequence of the ability to investigate the material microstructure at a continuously decreasing spatial scale. For instance, the development of VLSI technology for semiconductor devices requires the analysis of dopant distribution in sub-micron areas and the improvement of the chemical and mechanical properties of composite materials requires interface analyses.

For the future, analytical tools offering increasingly better ability for elemental chemical analysis at high lateral resolution will continue to be necessary to support the materials science progress.

The mass spectrometry of secondary ion emission, called as the SIMS technique, is widely used for trace element analysis at the ppm to ppb level in materials science, geology ,biology.... The important features of this technique are :

- Elemental, molecular and isotopic analysis. Elemental analysis from H to U,
- high sensitivity (ppm to ppb range),
- Sub-micron lateral resolution,
- In-depth distribution can be measured with a high depth resolution (5 to 100 nm range).

However, the instrumental limitations of the commercially available SIMS instruments lead to significant reduction of theoretical performance in the case of ultra fine features analysis.

The purpose of this paper is to outline the key instrumental parameters which control the performance for small area analysis and to introduce a new SIMS instrument generation optimized for such applications.

BASIC CONSIDERATIONS FOR SMALL AREA ANALYSIS

The SIMS technique is a destructive method. The sample to be analyzed is sputtered by a primary ion beam of 1-20 keV energy. Under this primary ion bombardment, the target atoms are ejected and ionized to produce a characteristic signal.

The secondary ion intensity measured for a given ion species M_i is given by the relationship :

$$I(M_i) = T \times Y_i \times d_b \times S \times S_y \times [M] \qquad (1)$$

where

T : is the overall transmission (including collection optics, mass spectrometer and detectors),
Y_i : is the ion yield of the species M_i (*i.e.* the ratio Number of emitted ions M_i / Number of sputtered atoms M),
d_b : is the primary beam intensity (in ion/s/μm^2),
S : is the sputtered area (in μm^2),
S_y : the sputter yield (*i.e.* the number of atoms ejected from the target per primary ion implanted),
[M] = the atomic fraction of the species M in the target.

The product $T \times Y_i$, called as the useful yield τ, is the ratio Number of detected M_i ions / Number of sputtered M atoms. The useful yield is a very important parameter because it includes both instrumental (transmission) and physical (ionization) characteristics. By definition, τ^{-1} is the mean number of atoms M which must be removed from the sample to detect one M_i ion. If a Poisson distribution is assumed for the secondary ions, it can be considered that at least N (= $10^4/A\%^2$) ions must be counted in order to measure a secondary ion intensity with an accuracy of A%. The sputtered microvolume *v* necessary to count these ions is given by the relationship :

$$v(\mu m^3) = \frac{N}{\rho \times \tau \times [M]} \qquad (2)$$

ρ : is the atomic density of the target (in at/μm^3).

As long as the collision cascades can be neglected, this volume sets the limit to the spatial resolution consistent with the detection of the species M at a given concentration level and accuracy, and on a given SIMS instrument. Let us consider numerical values in order to evaluate the limits of the technique : A% = 25, $\rho = 5.10^{22}$ at/cm^3, $\tau = 10^{-3}$ (a reasonable useful yield value). It gives a minimum detectable concentration [M] of 3.10^{-7} and 3.10^{-4} for a spatial resolution of 1 and 10^{-3} μm^3, respectively.

In practical cases, very often, we need to get information about the concentration level for several species. Thus, the minimum spatial resolution computed above must be multiply by the number of analyzed species in the case of a sequential detection mode.

We have computed from equation (2) what would be the *theoretical* spatial resolution at a given ion yield and mass spectrometer transmission. To evaluate a *practical* limit for both spatial resolution and detection limit, the signal/noise ratio and the acquisition time has to be also considered.

Actually, the measured secondary ion intensity must be higher than the background of the detection system D_{bkg}. From equation (1) it therefore comes the constraint on the primary density :

$$d_b \geq \frac{D_{bkg}}{T \times Y_i \times S \times S_y \times [M]} \qquad (3)$$

The background of an electron multiplier used in pulse counting mode to detect ions is in the range 10^{-1} c/s. For a spatial resolution of 10^{-3} μm^3, let us consider an ion probe size of 0.1 μm (which means that each intensity measurement will be sampled over a depth of 0.1 μm). Moreover let us assume a sputter yield S_y of 3, from equation (3). This gives a primary beam density d_b of at least $1.25\ 10^7$ ion/s/μm^2 (i.e. 0.2 mA/cm^2) in order to detect a concentration level of $3\ 10^{-4}$.

With such a primary beam density, a time of 133 sec. is required to sputter the microvolume of 10^{-3} μm^3. It means that if a sample area of 2×2 μm^2 must be investigated, at least 20×20 data points must be acquired for an acquisition time of 14.7 hours. This time must be multiplied by the number of species to be analyzed.

Such data acquisition times are prohibitive for the practical use of the SIMS technique for analyzing very small areas. The ways to reduce these acquisition times are : to increase the number of secondary ions collected per volume unit of sputtered sample and/or to increase the sputter rate. The former could be achieved by maximizing the ion yield of the ejected atoms and the transmission of the mass spectrometer ; note that these improvements are also necessary if a better spatial resolution is required. The latter could be obtained by increasing the probe density in the very small probe. Let us consider these different points in the following sections.

NATURE OF PRIMARY IONS

Equation (3) has allowed us to compute the minimum primary beam density required for practical applications whatever the nature of primary ions. But a second important consideration is the choice of the primary ion for a given application. By writing equation (3) with the following form :

$$d_b \times Y_i \times S_y \geq \frac{D_{bkg}}{T \times S \times [M]} \qquad (4)$$

it appears that the best primary ion choice is the one which maximizes the product $d_b \times Y_i \times S_y$.

We are going to consider only O_2^+, Ga^+ and Cs^+ which are the more common ion beams used on SIMS instruments.

The sputter yield S_y depends on the mass ratio of the primary and target atoms. For instance, it decreases by a factor of 2 from Cs^+ to Ga^+ in Si target. However, generaly speaking, for a given target, the variations of the sputter yield as a function of the primary ion type can be neglected compared to the variations of d_b and Y_i.

Ionization efficiency :

The ionization probability depends on the chemical state of the sample surface during the sputtering process. This chemical state results from the matrix composition itself, but also from the implantation of primary ions, the bombardment induced diffusion and the surface reaction with the vacuum gas phase. By bombarding the sample with reactive primary ions it is therefore possible to change the surface chemistry in a way which increases ion yields.

It is well known that the use of oxygen and cesium primary ions enhances the ion yield for the etched species with a low ionization potential and a high electron affinity, respectively. In a reverse way, the sputtering under rare gases or gallium bombardment leads to rather low ionization efficiency [1,2]. In *table 1* we have reported experimental values of useful yields measured for different species etched from different matrices under different primary ion bombardments. Useful yields are reported for positive secondary ions (M^+) in the case of oxygen and gallium primary ions and for negative secondary ions (M^-)for cesium.

Table 1 : Useful yields as a function of the species, the matrix and the primary ions (measured on a CAMECA IMS 5f instrument)

Matrix	Species	O_2^+	Cs^+	Ga^+
Silicon	Si	$5.1\ 10^{-3}$	$1.6\ 10^{-2}$	$6.0\ 10^{-5}$
	B	$3.1\ 10^{-3}$	$2.8\ 10^{-4}$	$6.4\ 10^{-6}$
	BSi		$2.8\ 10^{-3}$	
	P	$2.1\ 10^{-5}$	$7.1\ 10^{-4}$	$3.0\ 10^{-7}$
Silicon oxide	Si	$3.8\ 10^{-2}$	$4.9\ 10^{-3}$	$1.4\ 10^{-2}$
	B	$3.9\ 10^{-3}$	$5.6\ 10^{-4}$	$6.4\ 10^{-6}$
	P	$3.4\ 10^{-4}$	$1.3\ 10^{-3}$	$2.1\ 10^{-5}$
Steel	Ni	$7.9\ 10^{-4}$		$3.9\ 10^{-5}$
	Cr	$3.4\ 10^{-2}$		$2.5\ 10^{-4}$

The comparison of the data shows that in the non-oxide matrices the useful yield values for Ga^+ bombardment are 2 or 3 decades lower than under reactive primary ions. In the case of oxide

matrices, the high oxygen concentration in the sample reduces the differences for positive secondary ions between O_2^+ and Ga^+, but for negative secondary ions Cs^+ remains the best selection.

In terms of acquisition time and detection limit, the compensation of the much lower ion yield for non-reactive primary ions would require a higher ion beam density d_b by a factor of one or two decades. But in any case this compensation will be obtained at the expense of the spatial resolution because a larger volume of matter will be sputtered.

Primary ion probe density

The primary ion probe density mainly depends on the brightness and energy spread of the source, and the balance between the gaussian size of the demagnified image of the source and the aberrations brought by the probe forming system.

Oxygen beams are generally produced by a duoplasmatron source. This kind of source provides positive or negative oxygen ions. In the case of positive polarity, it works with a brightness of about 100 $A/cm^2/sr$.

Cesium beams can be produced either by thermal ionization sources [3] or liquid metal ion gun (LIMG) [4]. Thermal ionization sources provide a cesium beam with a brightness of 150 $A/cm^2/sr$ at 10 keV energy, an excellent emission stability (0.5 % over 10 mn), a small energy dispersion (< 1eV) and no manipulation of liquid cesium. Cs LMIG are much brighter (in the range of 10^5 $A/cm^2/sr$) but have a large energy dispersion, and due to the high reactivity of liquid cesium, such sources are not very stable and have a short life time. Thermal ionization sources will continue to be preferred until the actual performance of Cs LIMG is improved.

Gallium beams are produced with LMIG with a brightness of 10^5 $A/cm^2/sr$ and good stability and life time.

Note that due to the high energy dispersion of ions emitted from a field emission gun, the beam density of the probe focused onto the sample surface by the primary column is mainly limited the chromatic aberrations. In order to minimize them, LIMG works at high accelerating voltage (> 25 kV) which is a drawback in terms of depth resolution.

In the design of *conventional* SIMS instruments (*conventional* means commercially available today), the objective lens of the primary column works with a rather long working distance (several centimeters) due to the presence of the secondary ion extraction system in front and near the sample surface. A different design has been investigated by Slodzian et al. [5]. It consists of using the same optical system to co-axially focus and collect the primary ion probe and secondary ions, respectively. It is schematically represented in figure 1. Compared to the conventional configuration where the primary ion beam is non-coaxial with the collection system, this optical arrangement has the great advantage of considerably shortening the distance between the sample and the probe forming lens (few tenth millimeters). Thus the focal length and aberrations of the objective lens are minimized, which leads to a smaller probe diameter at a given ion current. A second advantage of this experimental setup is to sputter the target with a normal incidence of the primary beam with respect to the sample surface. This reduces the shadowing effects when sputtering non flat surface with an oblique incidence. Such shadowing effects may induce uneven sputter rate over the analyzed area and it results a distortion of the measured in-depth distribution.

At the exit of the objective column, the secondary ions travel through a set of parallel plates which act as an electrostatic separator for the primary and secondary beams provided that both ion types are of opposite signs and of equal energy. The constraint of opposite polarity is not a limitation of

such a design because we have seen that Cs^+ ion bombardment enhances negative ion emission whereas O_2^+ or O^- enhances positive ion emission. So that it is always possible to select a polarity combination consistent with high ion yields and the co-axial focusing system.

Figure 1 : Schematic representation of the conventional and co-axial probe forming systems.

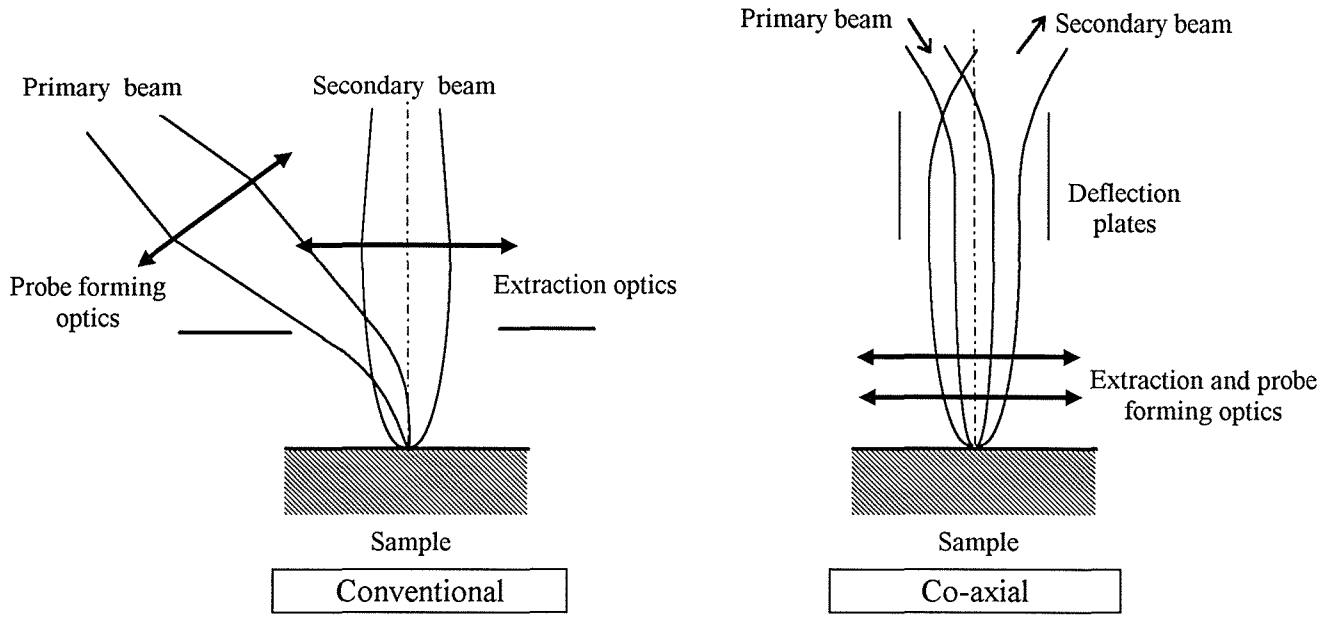

Practically, the use of a Cs^+ beam is very often preferred because its density is higher than for O^- probe and about one third of the elements of the periodic table have an electron affinity high enough to produce negative ions with good ion yields. Furthermore it is also possible to analyze electropositive elements under Cs^+ bombardment with a good sensitivity by measuring the signal for molecular ions. For instance, Al has a very low electron affinity (0.44 eV) but the molecular ions AlO have an affinity of 3.6 eV which is as high as, for instance, Cl (3.6 eV).

Slodzian et al [5] have developed a prototype instrument with a thermal ionization cesium source combined with a co-axial objective lens and collection optics. They demonstrated that a Cs^+ probe of 100 nm in diameter (68% of the intensity) carrying 5 pA can be routinely obtained, with an ultimate performance of 30 nm.

If we compare these values to the routine performance provided by a gallium source mounted in a conventional configuration on a SIMS instrument (about 60 nm carrying 25 pA [6]), we conclude that the product $Y_i \times d_b$ is maximized for a cesium beam formed by a co-axial system in spite of the beam density disadvantage. It is worthwhile mentioning that the product $Y_i \times d_b$ for Ga beam could be increased by chaining pre-implantation of the sample surface with either oxygen or cesium (according to the species type to be analyzed) and acquisition under Ga^+ bombardment. But such solution would require three ion guns on the same instrument and would be time consuming. Note that if the Cs LMIG technology improves in the future to reach the performance of Ga LMIG, it could become the best source choice for practical applications.

SECONDARY ION OPTICS

Acquisition times and detection limits depend direct on the useful yields (equations (2) and (3)). We have just seen that the useful yield is maximized by selecting the right primary ions. Another key parameter is the overall transmission T.

Collection optical system

Generally speaking, the collection optical system of a high transmission SIMS instrument consists of two different stages to collect secondary ions with the best efficiency. The first stage is a strong extraction field to reduce the broadening of the secondary ion beam due to the initial angular and energy distribution of secondary ions. The second stage is a matching section which is necessary to fit the secondary beam emittance with the angular acceptance of the mass spectrometer itself.

Mass spectrometer

The mass spectrometer must have high mass resolution capabilities because of the presence of a large number of clusters in the secondary emission which results in mass interferences (for instance, ^{31}P and $^{30}Si^{1}H$). Moreover, we have seen that the spatial resolution is inversely proportional to the number of analyzed species unless a parallel collection mode is used.

Taking into account these two considerations, quadrupole type mass spectrometers are not of interest because they work at low mass resolution only and in sequential acquisition mode, furthermore they cannot analyze secondary ions extracted in a field of several tens of kV/cm which is a necessary condition to reach a high collection efficiency. There are two kinds of mass spectrometer offering high mass resolution and parallel detection : the time of flight (TOF) mass spectrometer and the double focusing mass spectrometer with a Mattauch-Herzog layout.

The basic principle of the TOF mass spectrometer is to perform the mass separation of the different species as a function of their time of flight between the sample surface and the detector [7,8]. For such a mass separation all secondary ions must enter in the mass spectrometer within the shortest time interval. The shorter the time interval, the better the mass resolution. The only way to fulfill this condition is to pulse the primary beam in order to sputter the sample for a very short time compared to the time of flight. Then, when the last secondary ions emitted by the first primary pulse reaches the detector a second primary pulse is applied and so on. Typically, the pulse length ranges from 1 to 10 nanoseconds and the repetition rate is of 10 kHz.

The main advantage of the TOF mass spectrometer is to collect in a quasi-parallel mode secondary ions over a large mass range (from mass 1 to 1000 or even more depending of the repetition rate) for each primary pulse ; no secondary ions are lost. The drawback is the low duty cycle (10^{-5}, 10^{-4}) which greatly reduces the sputter rate compared to a mass spectrometer working with continuous sputtering. For instance, let us assume a measurement to be carried out over an area of $2 \times 2\ \mu m^2$ with a lateral resolution of 0.1 µm and a mass resolution of 4000 (10% definition). Such experimental conditions require a pulse width of 3 ns at the mass 56 (it would be still shorter at lower mass), which leads to 10 primary ions/pulse, i.e. 10^5 ions/s with a gallium source running at 10 kHz repetition rate [8]. From equations (2) we know that a minimum sputtered volume of $10^{-3}\ \mu m^3$ is necessary to achieve a detection limit of 3×10^{-4} . By using a TOF mass spectrometer, with a sputter yield of 3, the acquisition time would be $5\times10^{10}\times10^{-3}\times20^2/(3\times10^5)$ = 18 hours. It must be mentioned that, a new acquisition mode (the "burst mode" recently developed at Münster university [9]) allows one to increase the data rate by a factor of 2 to 10 according to the analyzed mass range. The smaller the mass range the higher the data rate. For instance if the above analysis example were iron analysis in silicon, the acquisition in time in the "burst mode" would be reduced to 3 hours.

A Mattauch-Herzog mass spectrometer consists of the combination of an electrostatic analyzer and a magnetic sector having a long final focal plane along which the different ion species are focused. Parallel detection is therefore possible provided that a detection system fitted along the focal plane has a sensitivity, a dynamic range and a spatial resolution good enough to collect different species independently. Two detection systems could be considered : a long channel plate covering the focal plane length or discrete detectors such as electron multipliers. The former would offer a parallel detection over the full mass range of the mass spectrometer but the high intensity signal to be measured would probably saturate microchannels. The latter offers a much higher dynamic range (from 0.1 up to 10^6 c/s) but only a limited number of species can be detected in the parallel mode.

A magnetic sector mass spectrometer working in parallel detection mode does not require a pulsed primary beam. Therefore, compared to a TOF system it provides considerably shorter acquisition times. For instance, for the same application as the one considered for the TOF system, the acquisition time would be $3\times3\times6/10^4$ hours, i.e. 278 times faster, but only a limited number of species (4 or 5) would have been analyzed.

From the above comparison of mass spectrometer types it appears that a TOF system is more suitable when a very small volume of material has to be sputtered (monolayer or sub-monolayer, static SIMS mode) because it works at low sputter rate, or when unknown contamination must be investigated because all collected ions are detected and therefore it is not required to presuppose the species to be analyzed. A magnetic sector working in multi-collection mode is more dedicated to very small analysis areas when the volume of matter to be sputtered (fixed by the available number of atoms per volume unit and the useful yield) represents several tenths of μm^3 (dynamic SIMS) because of high sputter rate, and when available information about the sample allows us to decide which species are of interest before starting the analysis.

MAGNETIC SECTOR SIMS FOR ULTRA FINE FEATURES ANALYSIS

The SIMS instrument developed by Slodzian et al [5] has been specially designed for very small area analysis in dynamic SIMS mode. Therefore it combines reactive primary ion bombardment to enhance ion emission, a co-axial objective lens and collection system to focus a high density probe and a magnetic sector mass spectrometer capable of working in multi-collection mode with 4 parallel detectors. A commercial version of this prototype now exists in the CAMECA SIMS product line : the "Nanosims 50" [10].

The general layout is schematically represented in figure 2.

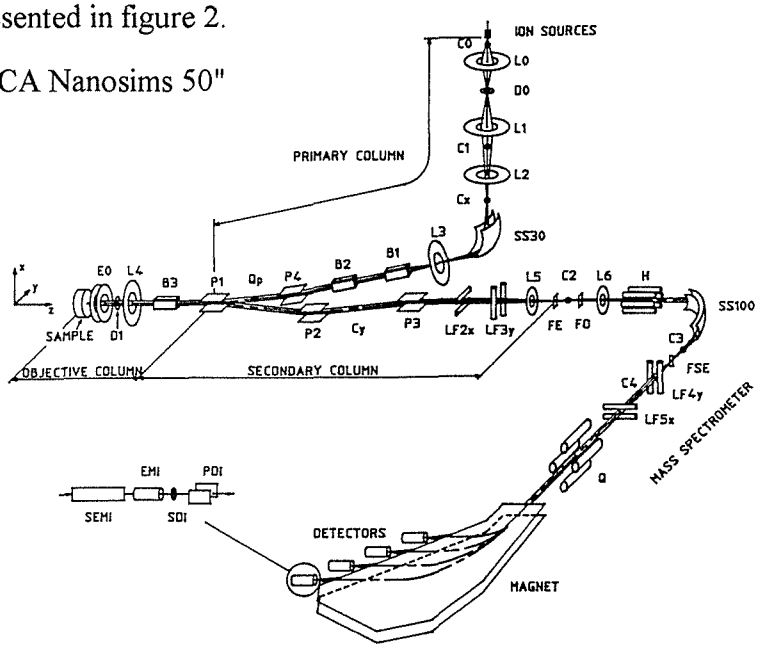

Figure 2 : General layout of the "CAMECA Nanosims 50"

The design of the mass spectrometer gives a transmission of 60% up to 4000 mass resolution. The magnetic sector provides a portion of mass spectrum along the focal plane corresponding to a mass range from M to 25M, where M is the mass of the species following the smaller radius trajectory. A maximum mass of 595 a.m.u is reached at the largest radius of 350 mm for secondary ions accelerated at 10 kV.

The detection system consists of four electron multipliers which can be moved on trolleys under vacuum along the focal plane. The acquisition system allows one to simultaneously acquire five images (4 scanning ion images and one scanning electron image induced by the primary ion bombardment).

The preliminary results obtained in different fields (materials science and biology) have demonstrated the high potential of such as instrument for trace element mapping with high lateral resolution [5, 11]. The reasonable sputter rates achievable even in small probe operations also offer very interesting capabilities for investigating trace element in-depth distribution in small areas. For instance, let us assume that the in-depth distribution of the three dopants B, P and As must be recorded within an area of 0.5×0.5 μm^2 in a semiconductor device. Typical experimental conditions would be a lateral resolution of 0.1 μm, a primary beam raster size of 3×3 μm^2 and a mass resolution of at least 4000 to eliminate the interference peak SiH on P. Thanks to the combination of the Cs^+ bombardment and the high transmission mass spectrometer the following useful yield values are targeted : $\tau(BSi^-) = 5.6 \times 10^{-3}$, $\tau(P^-) = 5.7 \times 10^{-3}$, $\tau(AsSi^-) = 1.4 \times 10^{-2}$. The signal of the three dopants plus a reference signal (Si for example) could be recorded in multi-collection mode. It would result an in-depth distribution of the three dopants measured with a sampling depth of 116 nm for each data point (i.e. 9 data points over 1 μm depth) and a detection limit of 20, 20 and 8 ppm for B, P and As respectively, measured with a statistical precision of 25 %. The total acquisition time would be 28 mn.

CONCLUSION

By its nature small features analysis means a limited volume of matter. A SIMS instrument dedicated to such applications must therefore be equipped with ion sources providing reactive ion beams to enhance the secondary emission. Furthermore, the mass spectrometer must be optimized to collect secondary ions with the best efficiency, and to have capabilities of high mass resolution and a parallel detection. Two kinds of mass spectrometers can be considered : time of flight and magnetic sector. The TOF system will be preferred for static SIMS applications and magnetic sector for dynamic SIMS applications. A SIMS instrument equipped with a cesium source, a probe forming system optimized for small beam operation and a high transmission mass spectrometer equipped with parallel detection system can be advantageously used to map and record in-depth profile of trace elements at a very small spatial scale. Typically, at a spatial resolution of 10^{-3} μm^3, trace elements in the 100 ppm range concentration can be detected.

References

1. Storm HA, Stein JD, Brown FK, ARL probe news Joint US/Japan seminar on SIMS technique Honolulu, (1976).
2. Schuhmacher M, Migeon HN, Rasser B, "Comparative useful yield measurements under oxygen, cesium and gallium bombardment", Proceedings 8th Int conf on SIMS, Amsterdam,(1992), p 49.
3. Slodzian G, Daigne B, Girard F, Boust F, Hillion F, "A thermal ionization source for a Cs^+ ion probe", Proceedings VIIIth Int conf on SIMS, Amsterdam, (1992) p 227.
4. Shichi H, Umemura K, Nomura S, " Microarea element analysis using Cs LMIS incorporating SEM/SIMS, Proceedings 8th Int conf on SIMS, Amsterdam, (1992), p 259.
5. Slodzian G, Daigne B, Girard F, Boust F, Hillion F, "Scanning secondary ion analytical microscopy with parallel detection., Bio cell (1992), 74, 43.
6. Hallégot P, Girod C, Le Beau MM, Levi-setti R, "High spatial resolution SIMS imaging of labelled, Human Chromosomes", Proceedings 7th Int conf on SIMS, Monterey, (1989), p 327.
7. Bennighoven A, "Chemical analysis of inorganic and organic surfaces and thin films by static TOF SIMS", Angew.Chem.Int.Ed.Eng. (1994), 33, 1023.
8. Schiewters J, Cramer HG, Heller T, Jurgens U, Niehius E, "High resolution surface imaging with a TOF-SIMS, J Vac Sci Technol, A (1991), 9, 2864
9. Cameca France, Technical note TN9403A, 1994.
10. Hillion F, Daigne B, Girard F, Slodzian G, Schuhmacher M, "A new performance instrument : the CAMECA NANOSIMS 50", Proceedings 9th Int conf on SIMS, Yohohama, (1993), to be edited.
11. Bou P, Vandelnbulcke L, Herbin R, Hillion F, "Diamond film nucleation and interface characterisation, J. Mater. Res. (1992), 8, 2151.

Oxygen Grain Boundary Diffusion in Zinc Oxide Ceramics

Hajime Haneda, Isao Sakaguchi, Akio Watanabe and Junzo Tanaka
National Institute for Research in Inorganic Materials, 1-1 Namiki, Tsukuba, Ibaraki 305, Japan

Metal-oxide varistors used in surge arresters are ZnO-based ceramic semiconductor devices with highly nonlinear current-voltage characteristics similar to back-to-back Zener diodes, but with much greater current-, voltage, and energy-handling capabilities(1-2). Such materials are characterized by non-uniform grain size, porosity, second phase distribution, impurity segregation and grain-grain misorientation. The electric properties of ZnO varistors are, furthermore, known to be greatly influenced by the defect chemistry of ceramics. In this paper, we focus our attention on attempts to investigate grain boundary diffusion of oxygen ions in various ZnO-based ceramics.

EXPERIMENTAL

ZnO based ceramics hot-isostatic-pressed were used for oxygen diffusion experiment. The oxygen self-diffusion was investigated by a gas-solid isotopic exchange technique using ^{18}O as the tracer. The polished specimens were diffusion-annealed in O_2 at $5.0x10^4$Pa with ^{18}O enrichment of 20 to 98% in a high-frequency induction furnace with Pt-Rh susceptor. The ^{18}O concentration of the gaseous phase was measured using a double focusing massspectrometer. The change of ^{18}O content in the gaseous phase could not be detected during diffusion annealing. The normal depth profile and the lateral distribution of oxygen isotopes were measured by a secondary massspectrometer(SIMS) with an electron multiplier as the detector. Cesium positive ions were used as the primary ions with the ion currents of 5 to 20nA. A normal induced electron gun was used for relieving the samples of the extra charge.

RESULTS and DISCUSSION

Figure 1 shows the depth profile of ^{18}O in a typical ZnO samples. The condition of the constant concentration at the surface for a semi-infinite medium was be used. The solid line in Fig.1 indicates the fitted value using date near surface(<1000nm) with a simple error function (3). Lattice diffusion coefficients were obtained, using this equation. The profile had a long tail at large depth. It is obvious that the long tail was not due to the lattice diffusion but might be caused by the diffusion along grain boundaries.

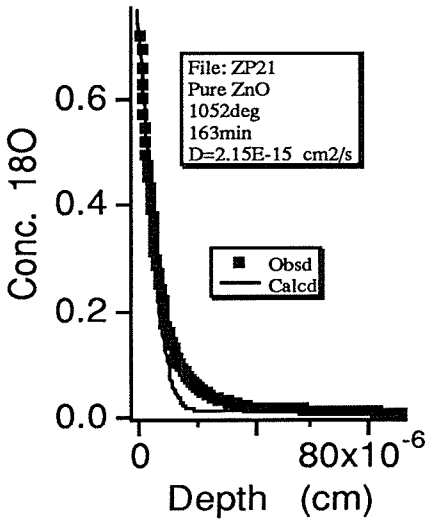

Fig.1. Depth profile of oxygen 18 in zinc oxide ceramics. Closed rectangular, the measured values and solid line, calculated values by a simple error function.

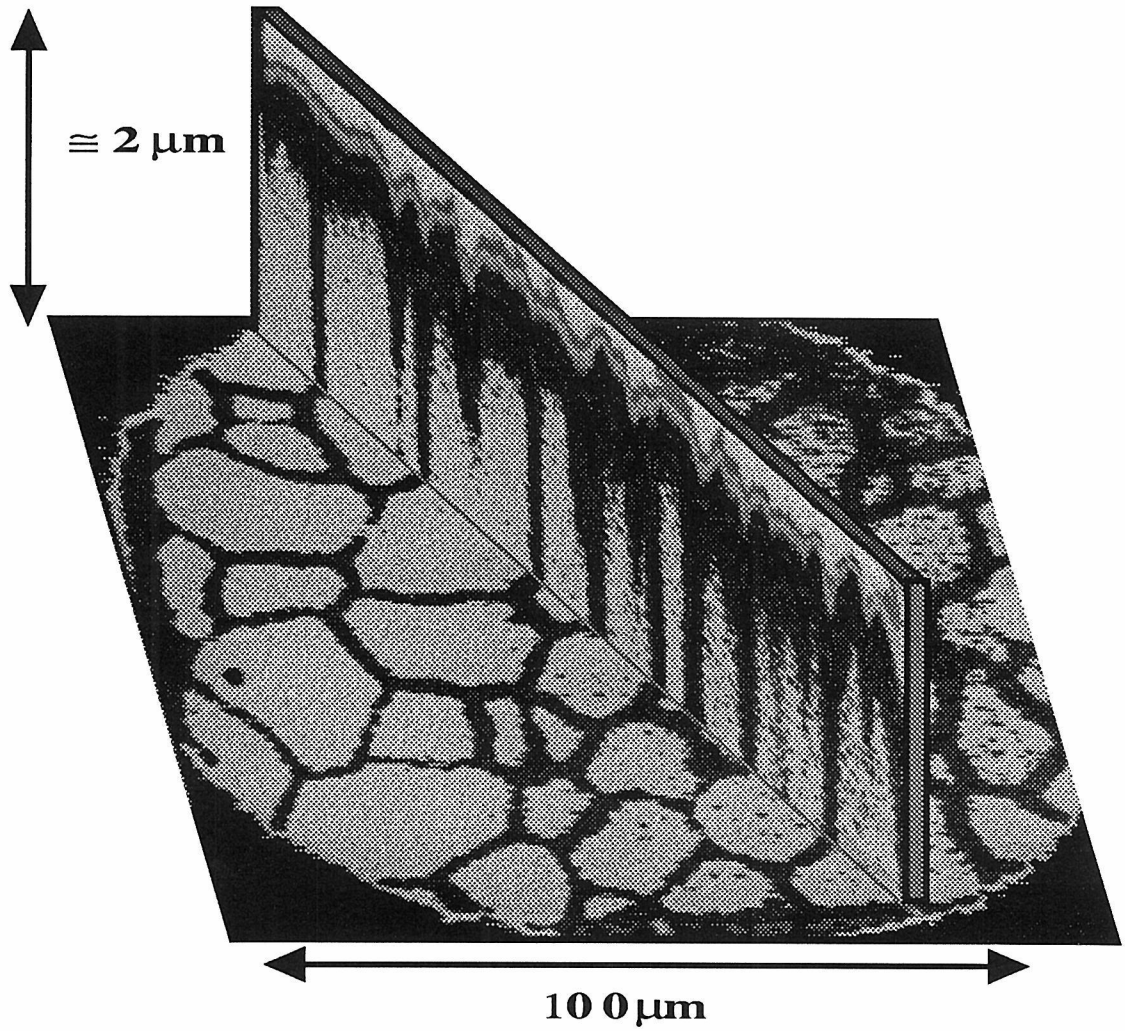

Fig.2 The 3D distribution of oxygen-18 in pure ZnO ceramics after diffusion-annealing.

As seen in figure 2 of ^{18}O ion image at 2mm depth, the grain boundary network could be observed in all samples. The lattice diffusion coefficients of oxygen ions depended on dopants. The values of the lattice diffusion coefficients with higher valence dopants compare with zinc ions are greater than lower valence dopant such as lithium ions. This fact indicates that the oxygen ions diffuse with an interstitialcy mechanism. Le Claire(4) have proposed the relation between the grain boundary diffusion coefficient and concentration at large depth, which is useful in present case. Using his equation, the values of grain boundary diffusion coefficients are estimated. The variation range of the grain boundary diffusion coefficients was narrower than that for the lattice diffusion, which indicates that the structure of grain boundaries and mechanism for grain boundary diffusion of oxygen ions little depend on the characteristics of the dopants.

REFERENCES

1. G.D.Mahan, L.M.Levinson, and H.R.Philipp, Appl.Phys.Lett., **33**, 80 (1978).
2. T.K.Gupta, J.Am.Cerm.Soc., **73**, 1817 (1990).
3. J. Crank, in "THE MATHEMATICS OF DIFFUSION,"(Oxford University Press, London, 1957)
   P.30.
4. A.D.Le Claire, Brit. J. Appl. Phys., **14**, 351-6 (1963).

Secondary Ion Mass Spectrometric Analysis of ^{18}O and ^{28}Si Distribution in Implanted Materials

Isao Sakaguchi, Shunichi Hishita and Hajime Haneda
National Institute for Research in Inorganic Materials
Namiki 1-1 Tsukuba, Ibaraki 305, Japan

Abstract

The change on oxygen diffusion profiles during silicon implantation into YAG ceramics were investigated with a secondary ion mass spectrometry. After Si implantation (projection range=140nm), the decrease of ^{18}O concentration and the annihilation of grain boundary diffusion were observed. The decrease of ^{18}O concentration is explained by resulting from the diffusion into bulk along grain boundaries with the excitation of YAG during implantation.

I. Introduction

Ion implantation is one of the most useful methods to modify the physicochemical properties of surface, because of the exact controllability of ion concentration and the easy controllability of the ion beam position. Numerous insulators have been implanted with various ions in large doses and energy ranges and investigated on the states in as-implanted crystals and on the precipitation process after the thermal treatment [1]. In the research on the complex oxide, garnets such as $Y_3Fe_5O_{12}$ (YIG), $Y_3Al_5O_{12}$ (YAG) and $Gd_3Ga_5O_{12}$ (GGG) have been studied [1]. However, there is no research on the behaviour of elements constituting lattice during the impurity implantation and on the polycrystalline form. The isotopic labelling is required to observe the behaviour of elements constituting lattice. YAG ceramics have been mentioned as potentially useful optical ceramics because this material has a transparent form [2]. Sinterability and creep characteristics are particularly affected by minor defects or impurities. From these reasons, Yttrium-Aluminium-Garnet ($Y_3Al_5O_{12}$, YAG) ceramics is used in this study and silicon is selected as the implanted impurity. The purpose of this study is to examine the behaviour of oxygen during the silicon implantation.

II. Experimental

Transparent YAG ceramics were synthesized using the powders with the urea method. The powder components were sintered at 1973K for 24hrs in vacuum. These samples were annealed at 1673K for 12hrs. The samples were cut into rectangular prisms of $5x5x1mm^3$ and mechanically polished. The sample was further cleaned off with dilute water, acetone and ethanol. The oxygen diffusion experiment was performed with the apparatus for isotope exchanges of oxygen at 1373K for 5hrs. Implantation of Si^+ (accelerating voltage 150KeV, implanted dose $1x10^{16}ions/cm^2$) was performed at 300K for 18hrs. After the ion implantation, the disappearance of thermal etch at grain boundary on sample surface was observed by the optical reflection microscope.

The profiles of ^{18}O and ^{28}Si were measured using a SIMS (CAMECA, IMS-4F) with $^{133}Cs^+$ as the primary ion, an accelerating voltage of 10 kV. To prevent charging at the specimen surface, the electron gun was employed. Intensities for the $^{16}O^-$ and $^{18}O^-$ were monitored. The concentration profile was calculated from the oxygen intensities as follows: $C=I(^{18}O)/[I(^{16}O)+I(^{18}O)]$, where $I(^{16}O)$ and $I(^{18}O)$ were the intensity of ^{16}O and ^{18}O. The depth of the sputtered craters was measured by using a Dektak 3030 to determine the sputter rate. The secondary ion images of ^{18}O, $^{16}O_2$ and ^{28}Si were measured by using RAE of SIMS.

III. Results and Discussion

Figure 1 shows the depth profiles of ^{18}O and ^{28}Si in the diffusion and the implantation samples. The profile A in Fig. 1 is the typical profile of ^{18}O diffusion in an annealed sample and consists of the volume and grain boundary contributions. This profile was analyzed by the

several equations [3,4]. The determined volume (Dv) and grain boundary diffusion coefficients (δDgb) were 7.4×10^{-21} m^2/s and 1.4×10^{-26} m^3/s and the results were in good agreement with previous results [5]. The profile B of ^{28}Si in as-implanted sample is shown in Fig. 1. The projection range and implanted depth of Si in as-implanted sample are observed at 140 and 280nm in depth, respectively. The Si rich layer near surface is found. The profile C in Fig. 1 is the ^{18}O profile in as-implanted sample and the decrease of ^{18}O concentration in the regions of volume and grain boundary diffusion is observed.

In order to investigate the change of ^{18}O profile during ion implantation, the ^{18}O profiles in annealed and as-implanted samples are compared. The ^{18}O concentration in as-implanted sample was low rather than that in annealed sample. Especially, the decrease of ^{18}O concentration in the implanted sample is remarkable in the regions of volume and grain boundary diffusion in the annealed sample. The decrease of ^{18}O concentration near 220nm in the implanted sample is very small. There is possibility that oxygen tends to diffuse both ways, i.e., towards the sample surface and into the bulk of the sample. It is considered that the effect of ^{18}O outerdiffusion in the as-implanted sample is very small, because the exchange reaction of oxygen at surface could be ignored under the condition of Si implantation. There is one explanation that the decrease of ^{18}O concentration results from the diffusion into bulk with the excitation of YAG during implantation. In this explanation, the grain boundary, which is the extended defect into bulk, plays as the most important path of ^{18}O transport from the implanted layer including the radiation damage to bulk. It is considered that the change of ^{18}O profile in as-implanted sample is explained by the above explanation.

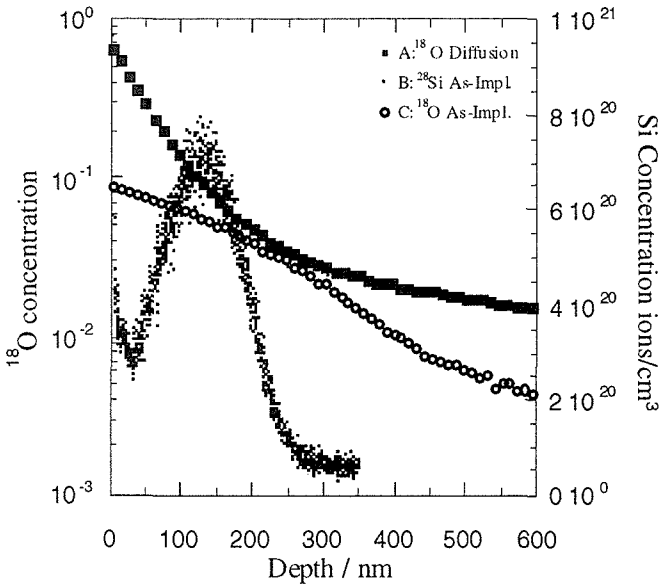

Fig. 1. Oxygen and silicon profiles in diffusion and as implanted samples.

References

[1] A. Perez and P. Thevenard, Defect creation in ion bombarded inorganic insulators, pp.156-94 in Ion beam modification of insulators, Edited by P. Mazzoldi and G.W. Arnold, Elsevier Science Publisher B. V., New York, 1987.

[2] G. De With, "Translucent $Y_3Al_5O_{12}$ Ceramics: Something Old, Something New"; pp. 2063-75 in High Tech. Ceramics, Edited by P. Vincenzini, Elsevier Science Publishe B. V., Amsterdam, 1987.

[3] J. Crank, The Mathematics of Diffusion; Ch.3.3. Oxford University Press, London, U.K., p.414 (1975).

[4] A.D. LeClaire, Br. J. Appl. Phys., 14, 351-56 (1963).

[5] I.Sakaguchi, H.Haneda, J. Tanaka, K. Yanagitani, submitted.

Application of FAB-SIMS for the Analysis of Fish Otolith

H. Seyama, J.S. Edmonds, M.J. Moran*, A. Tanaka, Y. Shibata, M. Soma and M. Morita*
National Institute for Environmental Studies, 16-2, Onogawa, Tsukuba, Ibaraki 305, Japan
*Western Australian Marine Research Laboratories, P.O. Box 20, North Beach, W.A. 6020, Australia

Abstract. Microstructure of an otolith (calcareous ear-stone) from a teleost fish was examined by fast atom bombardment - secondary ion mass spectrometry (FAB-SIMS). A section of the otolith has revealed seasonal periodicity in Sr, Na, and K concentrations that corresponded to visually observed annual banding. Strontium maxima corresponded to Na and K minima and vice versa. In addition an increase in Sr concentration from the core of otolith to the edge indicated that more Sr became incorporated into the otolith with growth of the fish.

INTRODUCTION

The major problem of SIMS analysis of poorly conducting materials is the charge build-up on sample surfaces due to bombardment by an ion beam. Application of fast atom bombardment (FAB) instead of primary ion bombardment is efficient to minimize the surface charging [1,2]. We have already demonstrated that O_2 FAB is suitable for the stable SIMS measurement of a heterogeneous insulating sample such as rock [2] and aerosol [3,4]. In this study, we will show the analysis of a fish otolith by use of FAB-SIMS. A part of this work has been already reported [5,6].

Fish otoliths are hard, stone-like, non-bony structures forming part of the organs, located in the inner ear, which sense position and motion in vertebrates [7]. In teleost fish, otoliths are formed of calcium carbonate in the aragonite crystal form [7,8] and become larger with the growth of fish by the addition of layers to outer surface. In sections through an otolith there is usually visible evidence of periodicity in the formation of concentric layers on daily, annual and sometimes intermediate time scales [9,10]. The elemental composition of otoliths, like that of other calcareous tissues of biological origin, such as corals [11], has potential use as an indicator of past environmental, climatological and oceanographic conditions [12]. In particular, the concentration of Sr has been shown to be negatively correlated with temperature for aragonitic carbonate in both non-biological [13] and biological systems [11].

EXPERIMENTAL

A thin section, 1mm thick, cut to include the nucleus (core), was obtained from an otolith (Fig. 1) taken from a red emperor (*Lutjanus sebae*) from Western Australian coastal waters. The age of the fish was estimated as 27 years by a count of the visual bands within the otolith. After polishing, the sample was cleaned by ultrasonication in water. The otolith was formed of calcium carbonate in the aragonite crystal form. Analysis by inductively coupled plasma atomic emission spectrometry (ICP) of whole otoliths from *Lutjanus sebae* (5 samples) gave the following elemental concentrations (mean and range): Ca, 38.6 %, 37.3-40.3; Na, 4582 mg kg^{-1}, 4344-4884; K, 731 mg kg^{-1}, 704-840; Sr, 1805 mg kg^{-1}, 1772-1916.

Calcium carbonate samples containing Sr were synthesized as standards for the quantification of Sr in the otolith. The calcium carbonate was precipitated from $Ca(NO_3)_2$ solution containing known amounts of $Sr(NO_3)_2$ by adding $(NH_4)_2CO_3$ solution. The dried powder of calcium carbonate was pressed into a pellet for FAB-SIMS measurement. The Sr concentration in the carbonate sample was determined by use of ICP.

Positive secondary ion spectra, line-scans and images were taken by a CAMECA IMS4f ion microscope with a FAB source. A 15 keV O_2 neutral beam was used to bombard the sample surface. The primary neutral O_2 beam used under FAB-SIMS measurement was produced by passing an O_2^+ ion beam (15 keV, 1 μA) through the neutralization chamber where O_2 gas was introduced. A copper grid (700 X 500 μm mesh) was placed between the sample and the inside face of the sample holder in order to reduce the sample charging. A detailed description of FAB-SIMS measurement has been reported elsewhere [2]. The resolution of the mass spec-

trometer was about 250. The secondary ion images were taken on a resistive anode encoder (RAE) image acquisition system.

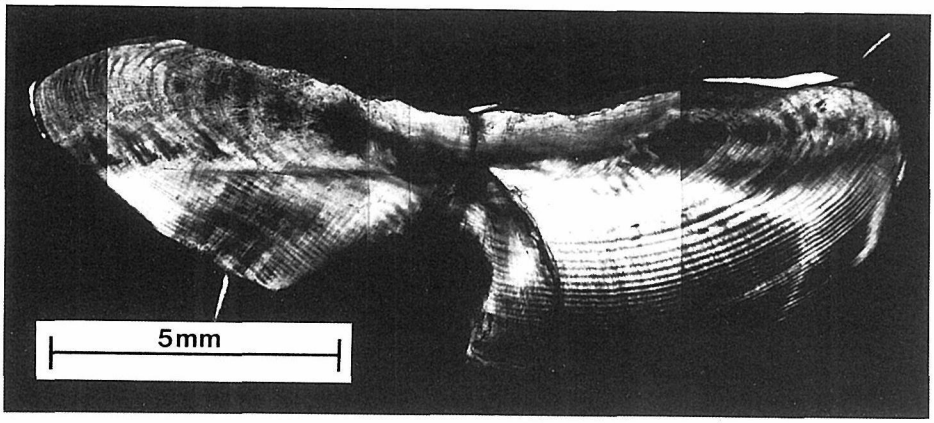

Figure 1.
Otolith cross-section.

RESULTS AND DISCUSSION

The otolith sample had a visually observed annual banding structure (Fig. 1). In the positive secondary ion mass spectrum of the otolith, Sr^+, Na^+ and K^+ ions were detected with main $Ca_lO_mH_n^+$ ions due to the calcium carbonate matrix. Line-scans of $^{23}Na^+$, $^{39}K^+$, $^{40}Ca^+$ and $^{88}Sr^+$ secondary ions were measured by 5 μm step scanning of the sample from the edge to the nucleus across the light and dark zones. The area analyzed at each step was of 8 μm diameter. To compensate the effect of sample charging on the detected secondary ion intensities, the intensity ratios of $^{23}Na^+$, $^{39}K^+$ and $^{88}Sr^+$ relative to $^{40}Ca^+$ (matrix element) were calculated and plotted against distance (Fig. 2). The charging effect for the relative $^{88}Sr^+$ intensity was successfully compensated. However, compensation of the charging effect was insufficient for the relative $^{23}Na^+$ and $^{39}K^+$ intensities. Consequently a lowering of relative intensities of these two ions was found in the vicinity of the copper grid. It can therefore be assumed that Ca and Sr are contained in the same phase, i.e. the aragonite lattice, and Na and K are contained in another phase, possibly another mineral phase. The total concentration of Na (about 0.45%) and protein (<1%) suggested that most Na was unlikely to be associated with protein.

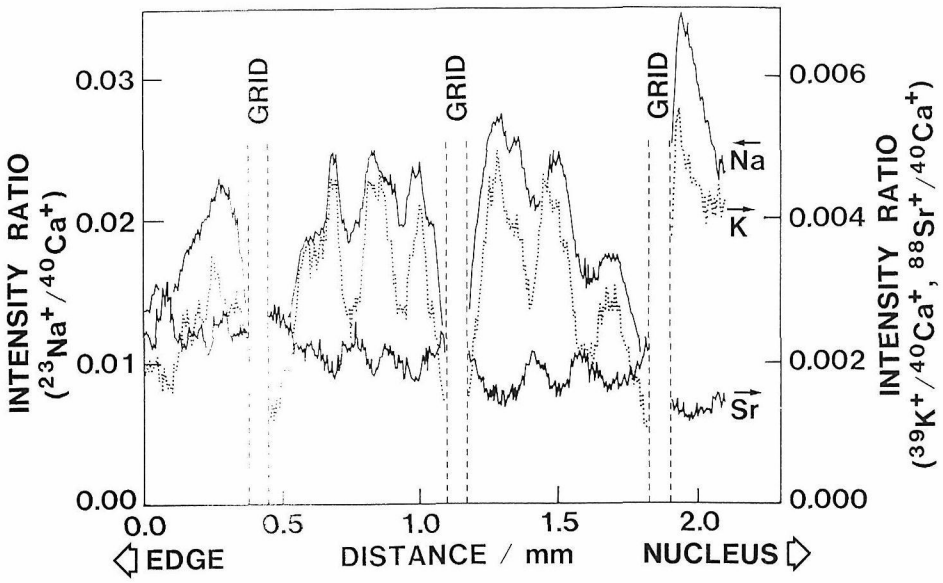

Figure 2.
Line-scans of $^{23}Na^+$, $^{39}K^+$ and $^{88}Sr^+$ across annual banding structure.
Intensity ratios of three ions to $^{40}Ca^+$ are plotted against distance from edge to nucleus.

Figure 2 shows the variation in the relative concentrations of Na, K and Sr in the sample. Oscillating patterns of relative intensities with a 100–200 μm repeat period, corresponding to the visual bands, were clearly observed. The patterns for Na and K were similar to each other. The repeat period near the edge of the otolith was shorter than that near the nucleus, and again this pattern was consistent with the pattern of annual banding observed in the sample. The relative intensities of the three elements showed fluctuations of ±10–30%. In addition it can be seen that the maximum Sr intensities corresponded to the minimum Na and K intensities and vice versa,

and that the Sr intensity decreased from edge to nucleus by about 45%. By using the copper grid as a reference marker it was possible to assign the high Sr, low Na, K zones to the dark bands (assumed to result from slower, winter growth [10]), and the low Sr, high Na, K zones to the light (summer) bands. Thus the deposition of Sr may well be temperature related.

The $^{88}Sr^{+}/^{40}Ca^{+}$ intensity ratio was converted into Sr concentration by use of a calibration line between $^{88}Sr^{+}/^{40}Ca^{+}$ and Sr concentration in calcium carbonate. Interferences may result from $^{40}Ca^{48}Ca^{+}$ and $^{44}Ca_2^{+}$ ions in the quantitative measurement of $^{88}Sr^{+}$ ion. The intensity of these interfering ions estimated from $^{40}Ca_2^{+}$ intensity was lower than 5% of the observed intensity at mass 88. Assuming homogeneous distribution of Sr in the synthesized carbonates, the calibration line is represented as $I(Sr/Ca) = 8.93 \times 10^{-7} \times C_{Sr}$ where I(Sr/Ca) is $^{88}Sr^{+}/^{40}Ca^{+}$ intensity ratio; C_{Sr} is Sr concentration (mg kg^{-1}). Figure 3 suggests the heterogeneous distribution of Sr in the otolith, whereas the average (2200 mg kg^{-1}) of Sr concentrations observed in the line-scan was comparable to the estimated mean Sr concentration (1800 mg kg^{-1}) in whole otoliths. An increase in Sr concentration from the core of otolith to the edge indicates that more Sr became incorporated into the otolith with growth of the fish. The seasonal fluctuation in Sr concentration was 300–800 mg kg^{-1}. An image of $^{88}Sr^{+}$ distribution is shown in Fig. 4. The heterogeneous Sr distribution, i.e. the microstructure of the otolith is clearly demonstrated.

Mean concentration for Sr of 2200 mg kg^{-1}, mean concentration for Ca in whole otoliths of 38.6%, mean fluctuation in Sr concentration of 600 mg kg^{-1} and an annual temperature range of 7°C (winter, 18°C; summer, 25°C) gave, assuming linearity, an approximate relationship of

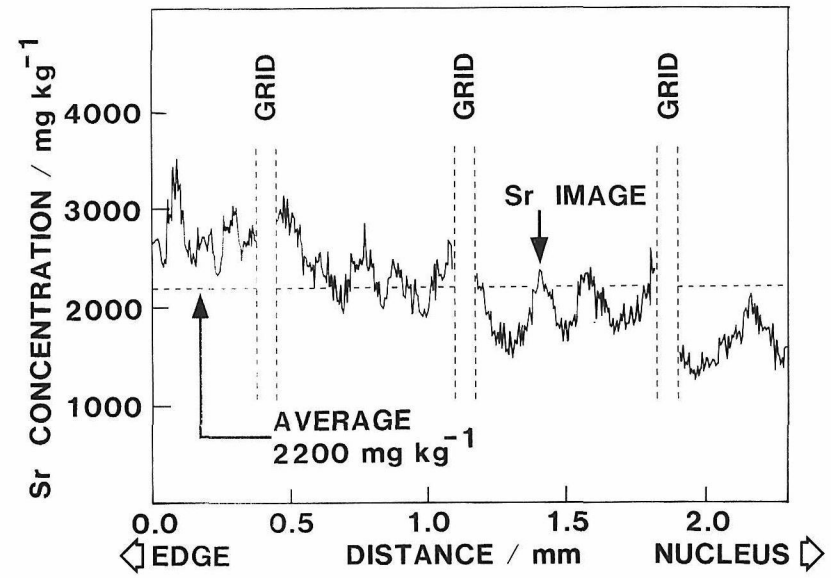

Figure 3.
Line-scan of Sr concentration across annual banding structure.

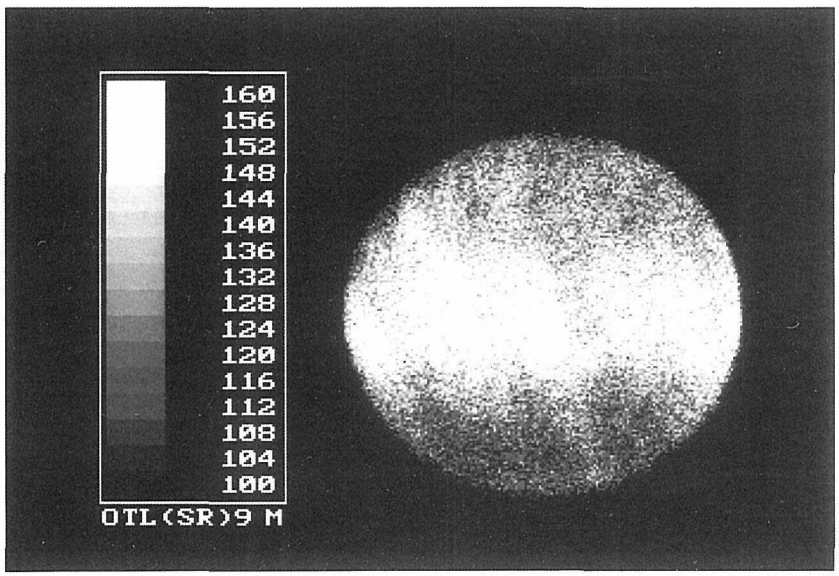

Figure 4.
$^{88}Sr^{+}$ secondary ion image (250 μm diameter) of area indicated in Fig. 3.
Acquisition time is 100 sec.
Unit of scale is counts of each pixel.

$$C_{Sr}/C_{Ca} \times 10^3 = 10.4 - 0.22T \quad (1)$$

where C_{Ca} is Ca concentration (mg kg^{-1}); T is temperature (°C). The similar equations have been already reported for fish otolith [12], coral [14] and inorganically precipitated aragonite [13] as follows:

$$C_{Sr}/C_{Ca} \times 10^3 = 16.37 - 0.22T \quad \text{for fish otolith (Radtke [12])} \quad (2)$$

$$C_{Sr}/C_{Ca} \times 10^3 = 24.75 - 0.18T \quad \text{for coral (Smith } et\ al. \text{ [14])} \quad (3)$$

$$C_{Sr}/C_{Ca} \times 10^3 = 23.5 - 0.086T \quad \text{for inorganic aragonite (Kinsman and Holland [13])} \quad (4)$$

Radtke reported a relationship (eq. (2)) obtained by analysis of whole otoliths from fish maintained in aquaria at a range of temperatures [12]. The temperature coefficient (0.22) in eq. (2) is same as our value, whereas the Sr concentration (about 5000 mg kg^{-1}) calculated from eq. (2) at 20°C is larger than the value in this work. On the other hand, the temperature coefficient of fish otolith is larger than those of coral [14] and inorganic aragonite [13]. In addition the Sr concentrations (8000–9000 mg kg^{-1}) of coral and inorganic aragonite at 20°C are larger than that of the fish otolith. This shows a greater variation of C_{Sr}/C_{Ca} with temperature in fish otolith than for aragonite in non-biological system or for aragonitic coral. It appears, therefore, that biological factors are of much greater importance than simple inorganic fractionation in determining the concentrations of Sr in otolith carbonate, but that these factors are themselves temperature dependent. However variations in Sr concentration across the otolith section suggest that caution should be exercised in attempting to derive temperature data from analysis of whole otoliths.

CONCLUSION

This work has shown the value of FAB–SIMS technique with high spatial resolution as a tool for the elemental analysis of intact mineral samples having microstructure. It has been clearly demonstrated by the FAB–SIMS analysis that fluctuations in the concentrations of Sr, Na and K in fish otoliths, which were likely to be temperature dependent and therefore related to season, corresponded to visual banding accepted as being formed on an annual basis. It has also been shown that biological factors, presumably related to fish physiology, may predominate over inorganic processes in determining trace element concentrations in otolith carbonate.

REFERENCES

1. F. Degréve and J. M. Lang, *Surf. Interface Anal.*, **7**, 177 (1985).
2. H. Seyama and M. Soma, *Surf. Interface Anal.*, **15**, 289 (1990).
3. H. Seyama, Y. Soma, M. Soma, S. Takao, T. Sakurai and S. Tagami, *Fresenius' J. Anal. Chem.*, **341**, 619 (1991).
4. H. Seyama and M. Soma, in *Secondary Ion Mass Spectrometry SIMS IX*, A. Benninghoven *et al.*, Eds., Wiley, Chichester, in press.
5. H. Seyama, J. S. Edmonds, M. J. Moran, Y. Shibata, M. Soma and M. Morita, *Experientia*, **47**, 1193 (1991).
6. H. Seyama, J. S. Edmonds, M. J. Moran, A. Tanaka, M. Soma, Y. Shibata and M. Morita, in *Secondary Ion Mass Spectrometry SIMS VIII*, A. Benninghoven, K. T. F. Janssen, J. Tumpner and H. W. Werner, Eds., Wiley, Chichester, 707 (1992).
7. D. Carlstrom, *Biol. Bull.*, **124**, 441 (1963).
8. E. T. Degens, W. G. Deuser and R. L. Haedrich, *Mar. Biol.*, **2**, 105 (1969).
9. S. E. Campana and J. D. Neilson, *Can. J. Fish. Aquat. Sci.*, **42**, 1014 (1985).
10. R. C. Summerfelt and G. E. Hall, Eds., *Age and Growth of fish*, Iowa State University Press, Ames (1987).
11. R. C. Schneider and S. V. Smith, *Mar. Biol.*, **66**, 121 (1982).
12. R. L. Radtke, *Comp. Biochem. Physiol.*, **92 A**, 189 (1989).
13. D. J. J. Kinsman and H. D. Holland, *Geochim. Cosmochim. Acta*, **33**, 1 (1969).
14. S. V. Smith, R. W. Buddemeier, R. C. Redalje and J. E. Houck, *Science*, **204**, 404 (1979).

Secondary Ion Mass Spectrometric Study of P-doped Homoepitaxially Grown Diamond

T. Ando, H. Haneda, M. Akaishi, Y. Sato and M. Kamo
National Institute for Research in Inorganic Materials
1-1 Namiki, Tsukuba, Ibaraki 305, Japan

We have investigated impurities at the interface between homoepitaxial diamond thin layers and diamond substrates as well as the diffusion of the impurities by using secondary ion mass spectrometry (SIMS). A significant amount of oxygen has been observed at the interface. The amount oxygen remaining at the interface between the grown layer and substrate diamond decreases with increasing deposition temperature. No oxygen is detected at the interface of the samples which are grown above the deposition temperature of 850 °C. No significant change of the impurities was observed after an annealing treatment under a high pressure and high temperature condition (7.7 GPa, 2350 °C), in which diamond is thermodynamically stable.

Introduction

The homoepitaxy of diamond via chemical vapor deposition is a process of considerable scientific and technological importance. For the application of semiconducting diamond, another important process is controlling the distribution of impurities in the crystal (e.g. doping and diffusion of hetero-elements). Synthesis and characterization of boron-doped homoepitaxially grown diamond films have been carried out by many researchers.[1] The introduction of phosphorous as an n-type dopant during CVD growth of diamond has also been investigated by several groups.[2,3] We have previously reported SIMS analysis of boron-doped and phosphorous-doped epitaxial diamond films.[4] In order to obtain higher quality epitaxial diamond layers, it becomes more important to analyze the interface between grown diamond layers and substrate diamond. In this paper, we report SIMS analysis of impurities of the epitaxially grown diamond and the interface as well as the thermal diffusion of the impurities.

Experimental

High-pressure synthesized single crystals, which were polished to within 4° of the direction of (110) face, were used for substrates. After polishing, the samples were treated in boiling mixtures of sulfuric acid (H_2SO_4, 90%) and nitric acid (HNO_3, 10%) for 1 hour to remove impurities, then thoroughly washed in distilled water. A diamond epitaxial layer was grown on the diamond substrate by microwave-assisted plasma chemical vapor deposition (CVD) in the temperature range from 720°C to 900°C. The apparatus for the synthesis of diamond was the same as that reported in previous papers.[4,5] A gaseous mixture of methane (1.0 vol%) and hydrogen was fed at the rate of 50 ml min^{-1} and the pressure was kept at 40 Torr. Phosphine (PH_3) gases diluted with hydrogen were used for the doping of phosphorous. The deposition temperature was controlled by adjusting the microwave power, and was measured by a radiation pyrometer equipped with a silicon detector. Before deposition, the diamond substrates were treated in a hydrogen plasma at the same temperature as that for the deposition for 30 minutes.

Two samples of P-doped diamond were prepared simultaneously in the same CVD batch, and one of the pair was treated under very high pessure and high temperature (HP-HT) conditions. The HP-HT treatment was performed in a modified belt type high pressure apparatus with a bore of 32 mm.[6] The phosphorous-doped homoepitaxially grown diamond

with substrate diamond was input into a capsule made of graphite as shown Fig. 1. The treatment pressure was 7.7 Gpa and the temperature was 2350 °C, a condition in which diamond is thermodynamically stable.[7] Pressure was calibrated at room temperature by means of the known pressure induced phase transitions of Bi, Tl, and Ba. Temperature was estimated from the relations between the input power and temperature, which we had obtained in advance by measuring the temperature with a W5%Re-W26%Re thermocouple. The annealing condition was kept constant for approximately 1 hour.

SIMS measurements were performed using a CAMECA IMS-4F ion micro-analyzer. The primary ion was 10 KeV Cs^+. Negative secondary ions were analyzed. The depth was not calibrated by the subsequent use of a profilometer, and the data is therefore plotted versus the number of scan cycles.

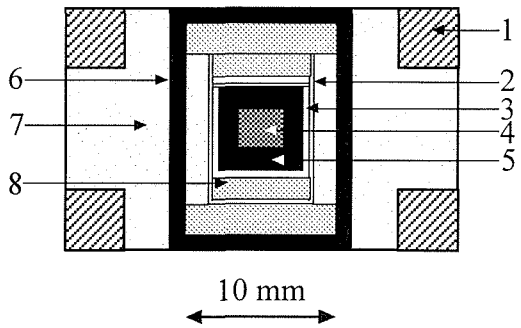

Figure 1 Schematic drawing the sample assembly for the HP-HT annealing treatment.
1: Steel Ring, 2: Ta Foil, 3: Ta Capsule,
4: CVD Diamond Sample, 5: Graphite Capsule,
6: Graphite Heater, 7: NaCl-10wt% ZrO_2,
8: NaCl-20wt% ZrO_2.

Results and Discussion

Inpurities at the interface

Figure 2 shows depth profiles of SIMS of the epitaxial diamond film which was grown at 720 °C. Before deposition, the substrate was treated in a hydrogen-plasma at 720 °C for 30 minutes in the same reactor. Masses 13, 16, and 31 indicate carbon-13, oxygen and phosphorous, respectively. The ^{13}C signal was used as a reference for the diamond matrix, because the intensity of the ^{12}C signal was too high. This result indicates that a significant amount of oxygen exists at the interface between the

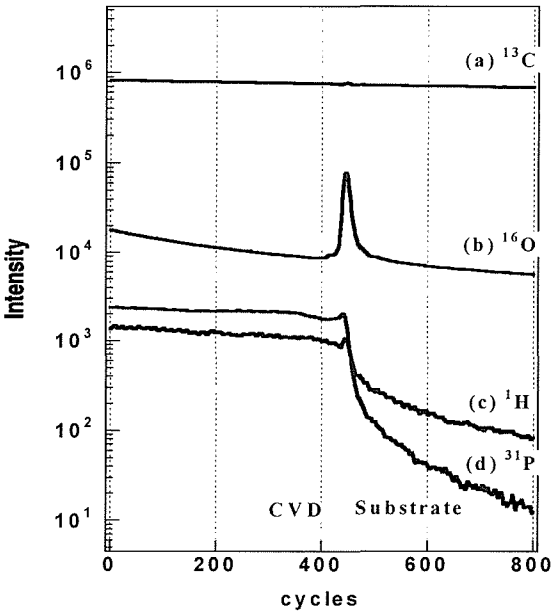

Figure 2 Depth profiles from SIMS analysis of ^{1}H, ^{13}C, ^{16}O and ^{31}P of the interface region of P-doped diamond grown at 720°C on the (110) plane of undoped HP-HT diamond.
(without the HP-HT annealing treatment).

epitaxial diamond thin layer and the diamond substrate. In order to clarify the interface, phosphorous was doped in the epitaxial diamond layer during plasma CVD using PH_3. Little difference was observed on the remaining oxygen at the interface either P-doped or undoped sample was used. Phosphorous and hydrogen were observed in the epitaxial layer when PH_3 was added in the reactant gaseous mixture. The mass intensity of oxygen in the epitaxial diamond layer is as high as that in the substrate diamond. This level of oxygen can be attributed to the background level of the instrument. This result suggests that the content of oxygen in the epitaxial growth layer may be negligible. The intensity of oxygen increases at the only interface layer. It is difficult to estimate quantitatively the concentration of the remaining oxygen, because the matrix effect on the secondary ion yield is provable changed at the interface. This result indicates that a significant amount of oxygen exists at the grown-diamond / substrate-diamond interface at the low-temperature growth of diamond. This remanent oxygen at the interface may cause defects of the epitaxial layer.

Several researchers have reported that oxygen can adsorb on diamond surfaces. We have also

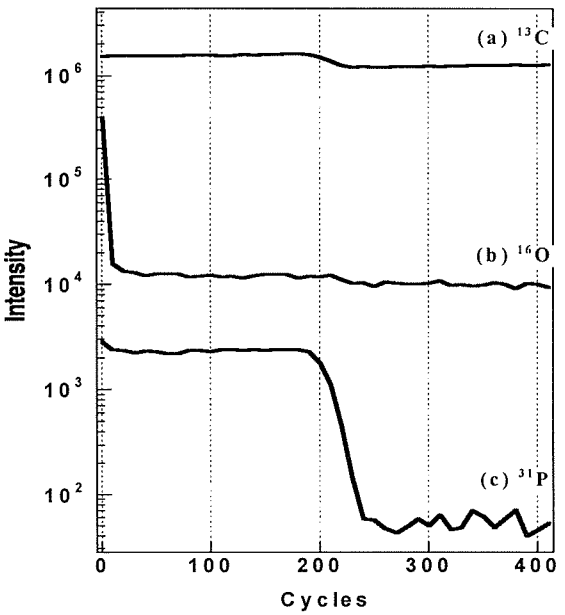

Figure 3 Depth profiles from SIMS analysis of ^{1}H, ^{13}C and ^{31}P of the interface region of P-doped diamond grown at 850°C on the (110) plane of undoped HP-HT diamond.

reported that the diamond surface is oxygenated by the acid cleaning treatments.[8] CO_2 and CO are desorbed from the oxidized diamond surface by raising the surface temperature.[8] Before the homoepitaxial growth of diamond, the substrate diamond surface is usually oxygenated. During growth, the oxygen on the substrate surface remains at the interface between the epitaxial layer and the substrate. As no oxygen is detected in the epitaxial layer, oxygen must not be incorporated into the diamond during the CVD process.

Figure 3 shows depth profiles of SIMS of the epitaxial diamond film which was grown at 850 °C after the substrate was treated in hydrogen-plasma at 850 °C. In contrast with the growth at 720 °C, no increase of oxygen was detected at the interface between the epitaxial layer and the substrate. In addition, no increase of hydrogen was observed at the interface. As oxygen chemisorbed on the substrate diamond surface had desorbed at 850 °C, and the surface had changed to a hydrogen terminated surface before the deposition, no oxygen remained at the interface.

Figure 4 shows that the relative mass intensity of the remaining oxygen (O / ^{13}C) at the interface decreases with increasing deposition temperature. This result suggests that diamond substrates need the H-plasma treatment above 850 °C to remove oxygen impurities at the interface. Previous temperature-programmed desorption (TPD) studies have revealed desorption features of CO and CO_2 from the diamond surface and is not contradictory with the present results. The TPD study of oxidized diamond powder has indicated that CO_2 desorbed from 285 to 715 °C and CO desorbed from 500 to 840 °C in 1% hydrogen.[8] The present SIMS analysis indicates that all oxygen chemisorbed on the diamond surface can not be removed below 820 °C, even under hydrogen-plasma conditions. This result agrees with the TPD study. In the previous study on the plasma-hydrogenation of oxidized diamond surface, the treatment temperature is the most dominant condition of changing the oxidized diamond to hydrogen-termination. The control of the surface temperature is important for the elimination of oxygen. In the case of the microwave-assisted plasma CVD of diamond below 850°C, diamond can be grown epitaxially on the diamond substrate, however, a small amount of oxygen atoms are remained at the substrate diamond surface during the growth of diamond. These oxygen atoms may interrupt the formation of C-C bond between the epitaxial diamond and the substrate diamond, and may cause the defects of diamond crystal. Hydrogen was not observed at the interface after the hydrogen-plasma treatment above 850 °C. This indicates that hydrogen chemisorption cannot interrupt the formation of C-C bond between epitaxial diamond and substrate diamond in the microwave-plasma CVD system.

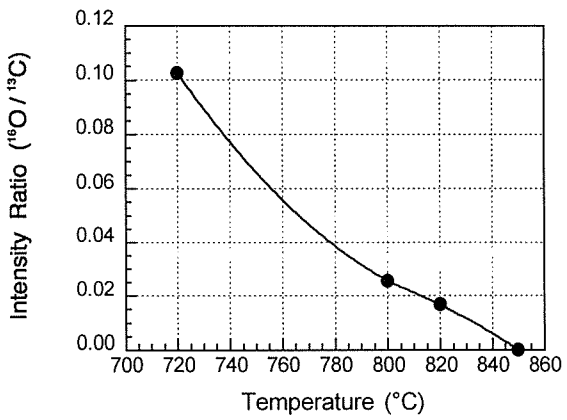

Figure 4 Change of the intensity ratio of O remained at the CVD / substrate interface with deposition temperature.

The diffusion of the impurities

The high temperature annealing treatment of diamond crystals has not been conducted to measure the diffusivity of impurities in diamond because diamond is easily transformed into the graphite phase. We have attempted the annealing temperature of 2350 °C under high pressure condition of 7.7 GPa to inhibit the phase transition. Figure 5 shows the result of the HP-HT treatment as compared to Fig 2. The depth profiles of SIMS indicate that there was very little change of the impurities in CVD diamond before and after the HP-HT treatment of 7.7 GPa, 2350 °C for 1 hour. This result suggests that the temperature of 2350 °C is too low for phosphorous to diffuse in the diamond crystal lattice. The diffusivity of phosphorous in diamond is considered to be extremely low owing to the very high atomic density and the tight binding of the diamond crystal lattice below 2350 °C. No change of electrical conductivity was observed after the HP-HT treatment. In the case of Li implanted diamond, some reports seem to indicate that Li ion implantation followed by suitable annealing actually yields n-type conduction.[9-11] Our data indicates that no motion of the phosphorous and oxygen could be confirmed in the homoepitaxially grown diamond up to the highest temperature investigated (2350 °C).

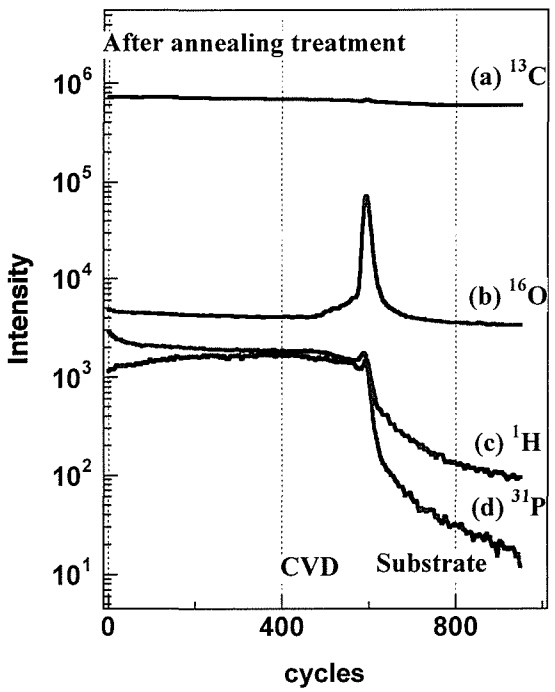

Figure 5 Depth profiles from SIMS analysis of ^{1}H, ^{13}C, ^{16}O and ^{31}P of the interface region of P-doped diamond grown at 720°C on the (110) plane of undoped HP-HT diamond.
(after the HP-HT annealing treatment at 2350 °C and 7.7 GPa).

Summary

This SIMS analysis reveals that oxygen atoms exist at the interface between epitaxial diamond and substrate diamond when the epitaxial diamond layer is grown at the relative low temperature. In order to remove the oxygen, it is necessary to elevate the surface temperature above 850 °C before the deposition.

No thermal diffusion of phosphorous and oxygen was observed below 2350 °C in this study.

Acknowlegements

The authors would like to thank Dr. S. Koizumi, and Dr. P. A. Dennig (National Institute for Research in Inorganic Materials) for many useful discussions and Ms. M. N. Gamo (Toppan Printing Co. Ltd.) for reading the manuscript.

References

1. *Advances in New Diamond Science and Technology*, S. Saito et al. ed. MYU, Tokyo, (1994)
2. K. Okano, H. Kiyota, T. Kurosu, and M. Iida, *Diamond & Relat. Mater.*, **2**, 35 (1993)
3. J. R. Flemish, S. N. Schauer, R. Wittstruck, M. I. Landstrass, and M. A. Plano, *Diamond & Relat. Mater.*, **3**, 672 (1993)
4. M. Kamo, H. Yurimoto, T. Ando and Y. Sato, *Proc. 2nd Int. Conf. New Diamond Sci. and Tech.* R. Messier et al. ed., p. 637 (1991)
5. M. Kamo, Y. Sato, S. Matsumoto, and N. Setaka, *J. Cryst. Growth*, **62**, 642 (1983)
6. S. Yamaoka et al., *J. High Pressure Inst. Jpn.*, **30**, 15 (1992)
7. *The Properties of Diamond*, J. E. Field ed., Academic Press, London, p. 473 (1979)
8. T. Ando, M. Ishii, M. Kamo, and Y. Sato, *J. Chem Soc. Faraday Trans.*, **89**, 1783 (1993)
9. C. Cytermann, R. Brener, and R. Kalish, *Diamond & Relat. Mater.*, **3**, 677 (1994)
10. I. M. Buckley-Golder, R. Bullough, R. M. Hayns, R. J. Willis, R. C. Piller, N. G. Blamire, G. Gard, and J. Stephen, *Diamond & Relat. Mater.*, **1**, 43 (1991)
11. S. Prawer, C. Uzan-Saguy, G. Braunstein, and R. Kalish, *Appl. Phys. Lett.*, **63**, 2502 (1993)

Chemical Bonding in Tellurite Glasses

Shigeru Suehara, Kazuo Yamamoto, Shunichi Hishita, Takashi Aizawa and Akihiko Nukui
National Institute for Research in Inorganic Materials
1-1 Namiki, Tsukuba, Ibaraki 305, Japan

Tellurite glasses are of technical interest because of their high refractive indices, dielectric constants, good infra-red transmissions and high thermal expansion coefficients.[1,2] Structural units (SUs) of them are reported to be TeOx (x=3~6) polyhedra, depending on modifier atoms.[3-8] It is in contrast with the SU of silicate glasses (a SiO_4 tetrahedron) which is not affected by modifier atoms. Usually, modifier atoms are added to enhance glass formation, as a result of network breaking (breaking the chains of SUs) and increment of entropy (decreasing liquidus temperature). In tellurite glasses, however, the modifier atoms play one more important role: causing the variation of the SU. We have investigated the bonding nature in tellurite glasses with use of first-principles molecular orbital calculations. Our calculations show that the variation of the SU is due to the charge transfer from modifier atoms to the TeO_6 octahedron.

In the random network model, glasses have the SUs similar to the short range order in the analogous crystalline compounds. On the analogy of crystalline tellurite compounds (M-Te-O; M=metal modifier atoms such as Cu, W, Li, Ba, Zn, etc.), the SUs should be TeOx (x=3~6) polyhedra as derived forms of the TeO_6 octahedron. Since the electronegativity of M is smaller than those of Te and O (0.8~1.9, 2.1, and 3.5 for M, Te, and O on the Pauling scale, respectively)[9], the charge transfer from M to TeO_6 should occur. In accordance with the transferred charge, the electronic structure of neutral (n=0) and negatively-charged (n=1~8) $(TeO_6)^{n-}$ clusters are calculated by using the self-consistent-charge discrete variational Xα (SCC-DV-Xα) method.[10] This method has been successfully applied to the interpretation of X-ray photoemission spectra for crystalline paratellurite.[11] In this method, the Hartree-Fock-Slater (HFS) equation for a cluster is self-consistently solved with use of a localized exchange potential (Xα potential). The exchange parameter α was taken to be 0.7 as usual. Numerical tellurium 1s~5p and oxygen 1s~2p atomic orbitals, obtained as solutions of the atomic HFS equations, were used for basis sets. The $(TeO_6)^{n-}$ cluster is made of one central Te atom and three kinds of octahedral O atoms; axial type O_I, equatorial types O_{II} and O_{III} as shown in Fig. 1. The calculations on this cluster were performed with C_2 point-group symmetry.

Results for Mulliken overlap populations, which scale bond order in simple meaning, versus net charge n for the $(TeO_6)^{n-}$ clusters are shown in Fig. 2. While the overlap population of Te-O_{II} bond increases slightly as n increases, those of bonds Te-O_I and Te-O_{III} decrease drastically to negative values at n=8 and 7, respectively. As no bonding is expected in the regions of the negative overlap population, the bonds Te-O_I and Te-O_{III} should be break and the coordination number of Te reduces from 6 via 4 to 2 as n increases. This is consistent with the variation of the SU (TeOx; x=3~6)[8], while odd oxygen coordination numbers do not appear essentially in our present calculations because of C_2 point-group symmetry.

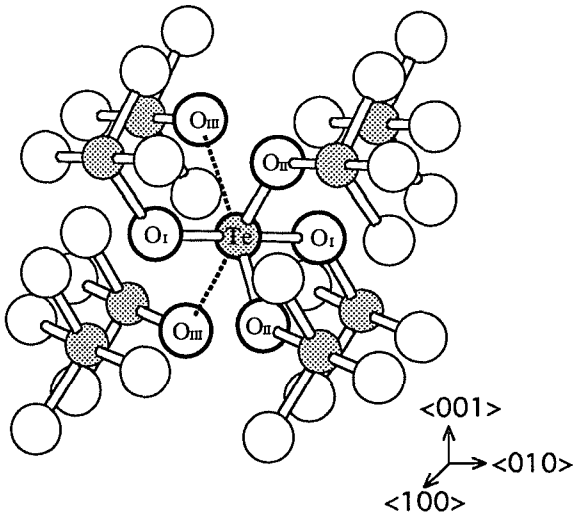

FIG. 1 Schematic illustration of a TeO_6 cluster in paratellurite. The TeO_6 cluster is made of one central Te atom and six octahedral O atoms which can be divided into following three types: The first is axial type (O_I) found at a distance of 3.84 a.u. from the central Te atom; The second is equatorial type (O_{II}) at a distance of 3.84 a.u.; The third is also equatorial type (O_{III}) found at a distance of 5.05 a.u..[15]

In order to understand the bond breaking due to the charge transfer, each orbital overlap population (OOP) in the neutral $(TeO_6)^{0-}$ cluster is shown in Fig. 3 with the energy level structure. Positive (negative) OOP means bonding (antibonding) feature of that orbital; The integral of the OOP below the highest occupied molecular orbital (HOMO) gives the Mulliken overlap population.[12] In the rigid band scheme, levels marked 1, 2, 3 and 4 is occupied in order by the transferred electrons. Each level can contain 2 electrons. The occupation of the levels 1, 2 and 3 hardly contribute to the Te-O bonding because of the small OOPs. These levels are of O 2p character and merely make lone pairs. Therefore, the bonding nature does not change up to n=6. When n exceeds 7, electrons occupy the marked 4 level and then the overlap populations of each bond are expected to decrease because of the large antibonding character of this level. In this case, Te-O_I bond is most weakened. However, Te-O_{III} bond is first broken since Te-O_{III} bond has smaller overlap population than Te-O_I from

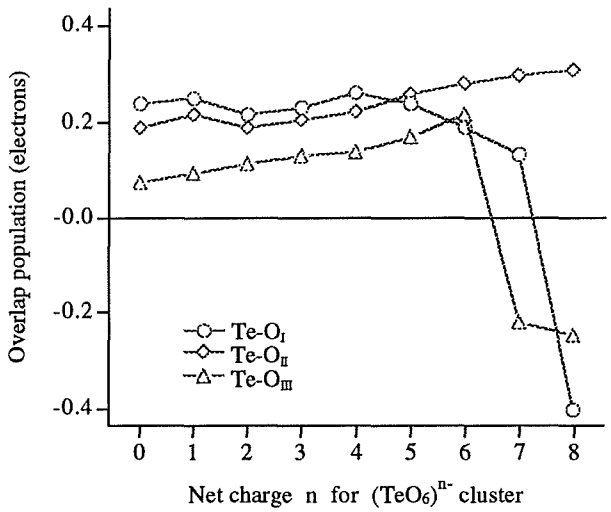

FIG. 2 Mulliken overlap populations for bonds Te-O_I, Te-O_{II} and Te-O_{III} versus net charge n for the $(TeO_6)^{n-}$ cluster.

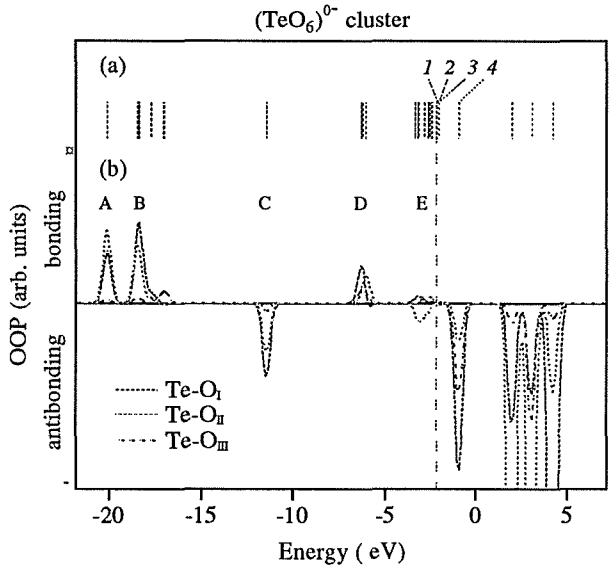

FIG. 3 a, Energy level structure of $(TeO_6)^{0-}$ cluster. Solid and dotted lines show occupied and unoccupied levels, respectively. Levels marked 1, 2 and 3 are of O 2p character and marked 4 level is of Te 5s and 5p, and O 2p characters.

b, Orbital overlap populations (OOPs) for bonds Te-O_I, Te-O_{II} and Te-O_{III} in the $(TeO_6)^{0-}$ cluster. The OOP curves are obtained by convolution of the OOP and a Gaussian function with 0.5 eV full width at half maximum. The vertical dashed line separates the occupied states in the left-hand side from the unoccupied states in the right-hand side. There are five well-separated 'bands' in the occupied state region. The bands A and B are mainly composed of O 2s with small amount of Te 5s and 5p bonding characters, respectively. The band C is made up of the Te 5s orbital admixed with O 2s antibonding states. The band D is bonding orbitals between Te 5p and O 2p containing a small amount of the O 2s antibonding character. The band E originates from the O 2p states.[11]

the beginning. The OOP at the marked 4 level for Te-O_{II} bond is the smallest antibonding character, and therefore, this bond remains in bonding state. Fig. 4 shows the contour map of the marked 4 level for the $(TeO_6)^{0-}$ cluster drawn for the equatorial plane, including atoms Te, O_{II} and O_{III}. The corresponding orbital for the $(TeO_6)^{8-}$ cluster, which refers to the HOMO, remains almost the same in spatial distribution. The lobe consisting of Te 5s and 5p orbital components can be clearly seen to point away from Te atom along the arrow, showing antibonding characteristic against O 2p orbital components. From the contour map, electrons at this orbital seem to contribute to the formation of the lone pair on Te which has been suggested by works on some tellurite compounds.[4,13,14]

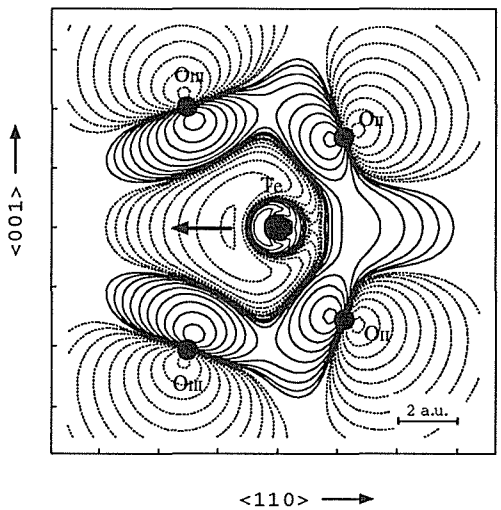

FIG. 4 Contour map of the marked 4 level in Fig. 3 for the $(TeO_6)^{0-}$ cluster. The contour are drawn for the equatorial plane including atoms Te, O_{II} and O_{III} in Fig. 1. The lobe of Te 5s and 5p orbital components can be clearly seen to point away from Te along the arrow, showing antibonding characteristic against O 2p orbitals.

In summary, we have shown that the variation of the structural unit of tellurite glasses is due to the charge transfer from modifier atoms to the TeO_6 octahedron with use of SCC-DV-Xα calculations on $(TeO_6)^{n-}$ (n=0~8) clusters. The OOP analysis reveal that the transferred electrons to the Te-O antibonding orbital cause breaking Te-O bonds and lead to reducing the coordination number of Te.

We thank Prof. H. Adachi (Kyoto Univ.) for use of the DV-Xα calculation program.

References

1. Stanworth, J. E. *Nature* **169**, 581 (1952).
2. Congshan, Z., Xiaojuan, L. & Zuyi, Z. *J. non-cryst. Solids* **144**, 89 (1992).
3. Lindqvist, O. *Acta Chem. Scand.* **22**,977 (1968).
4. Brown, I. D. *J. Solid St. Chem.* **11** 214 (1974).
5. Brady, G. W. *J. Chem. Phys.* **27**, 300 (1957).
6. Arnaudov, M. et al. *Mater. Res. Bull.* **17**, 112 (1982).
7. Adams, R. V. *Phys. Chem. Glasses* **2**, 10, (1961).
8. Mochida, N. et al. *Yogyo-Kyokai-Shi* **86**, 317 (1978).
9. Pauling, L *The Nature of the Chemical Bond* (Cornell Univ. Press, 1960).
10. Adachi, H., Tsukada, M. & Satoko, C. *J. Phys. Soc. Jpn.* **45**, 875 (1978).
11. Suehara, S., Yamamoto, K., Hishita, S. & Nukui, A. *Phys. Rev. B* **50**, 7981 (1994).
12. Hoffmann, R. *Rev. Mod. Phys.* **60**, 601 (1988).
13. Kozhukharov, V., Neov, S., Gerasimova, I. & Mikura, P. *J. Mater. Sci.* **21**,1707 (1986).
14. Galy, J., Meunier, G., Andersson, S. & Åström, A. *J. Solid St. Chem.* **13**, 142 (1975).
15. Wyckoff, R. W. G. *Crystal Structures*, 2nd edn (Interscience, New York, 1963).

Lattice Defects and Inclusions in Natural and Synthetic Diamond

A.R. Lang
H.H. Wills Physics Laboratory, University of Bristol
Tyndall Avenue, Bristol BS8 1TL, U.K.

Abstract. Defects imaged on a millimetre to nanometre scale by optical microscopy, X-ray and CL topography, and TEM are described. They include grown-in and glide dislocations, dislocation polygonisation and climb, the {100} platelets in natural diamonds, and voidites, the {111}-faceted bodies associated with degraded platelets. Crystallographic identifications among sub-μm size inclusions include apatite, biotite and species of carbonates and silicates.

1. Introduction. It is safe to assume that natural diamonds crystallised under the pressure and temperature conditions applying within the field of thermodynamic stability of diamond in the carbon phase diagram. This means that they were formed not less than about 150 km below the Earth's surface. The large synthetic diamonds discussed in this paper similarly crystallised in the diamond stability field, practical P and T conditions being typically 5.5 GPa and 1400°C. The dominant impurity element in diamond is nitrogen. Its concentration in natural diamond can be as high as 3,000 parts per million atomic (ppm), and in conventionally-grown synthetics up to about 300 ppm. Standard texts on diamond [1-4] devote many chapters to the effects of concentration and states of aggregation of N impurity on diamond properties. The accepted classification of diamonds, used in the following Sections, is based on their nitrogen-impurity-dependent optical absorptions. The broadest classification is into type I, the impure majority (~98% of natural crystals) that absorb UV below 330 nm and IR between 7 and 10 μm, and the purer type II (1-2% of naturals) that contain less than about 10 ppm N, transmit UV down to ~225 nm and negligibly absorb between 7 and 10 μm. Specimens containing significant N impurity are subdivided into type Ia, in which nitrogen is aggregated into non-paramagnetic defects, and type Ib in which N atoms remain singly substituting for C atoms, giving a characteristic EPR signal. Nitrogen - containing natural diamonds fall into class type Ia, with very rare exceptions. Conventionally-grown synthetics are type Ib. Among purer diamonds there is subdivision into type IIa, in which the few ppm present still dominate the electrical properties, and the p-type semiconducting type IIb, very rare in Nature, which contain typically <1 ppm boron and even less nitrogen. The chief N aggregates in type Ia diamonds are the A-defects, understood to be a pair of N atoms substitutionally occupying adjacent C sites in the diamond structure, and the B-defects, plausibly 4 N atoms tetrahedrally surrounding a vacancy. (A and B defects contribute characteristic components to the IR absorption spectrum.) Though neither A nor B defects have been directly imaged, the B/A ratio is of interest here because it is in relatively B-rich regions of natural diamonds that are discovered the remarkable 'partial platelets' and 'voidites' illustrated in Section 3.

2. Dislocations.

2.1. Plastic deformation in natural crystals. Type 1A diamonds of good optical quality and free from inclusions may contain very few grown-in dislocations; all, or almost all those present have been generated at a central nucleating point from which

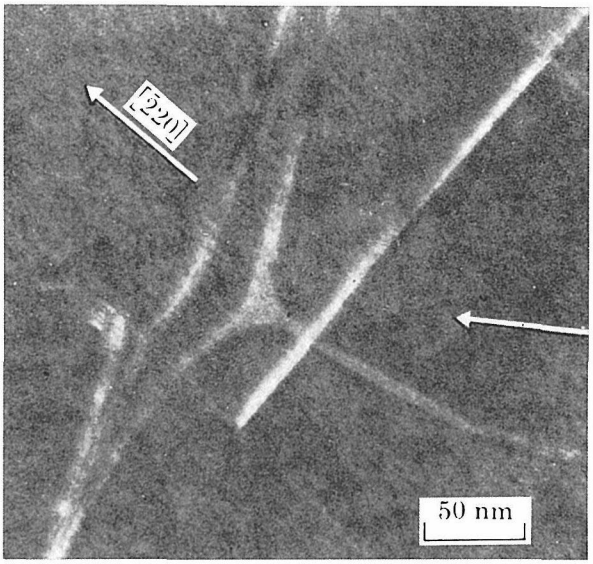

Fig. 1. Extended node in Type IIa diamond. WBDF image, g = $1\bar{1}\bar{1}$ (arrowed)

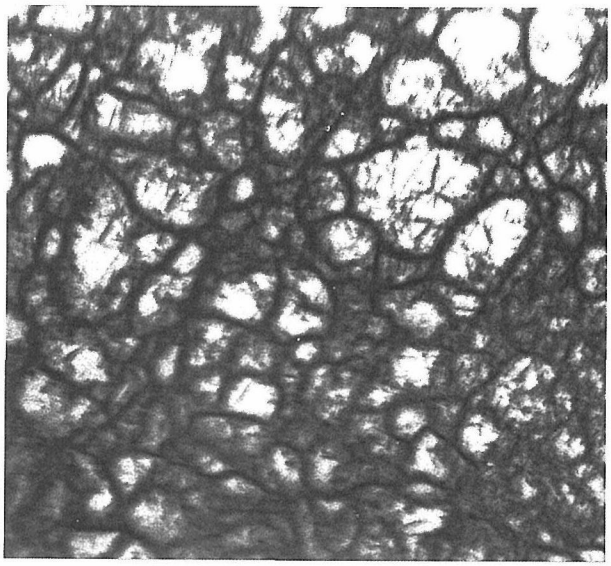

Fig.2.Dislocations in Type IIb diamond. CL image. Field width 330 μm

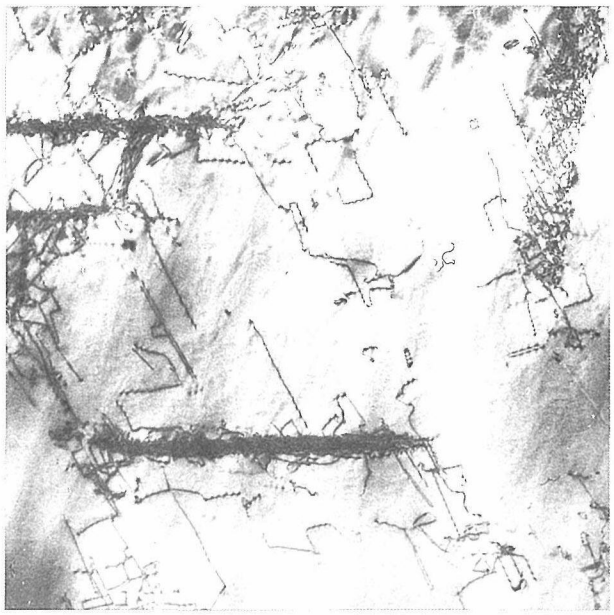

Fig. 3. Localised dislocation tangles on {111} in deformed diamond. Field width 5 μm.

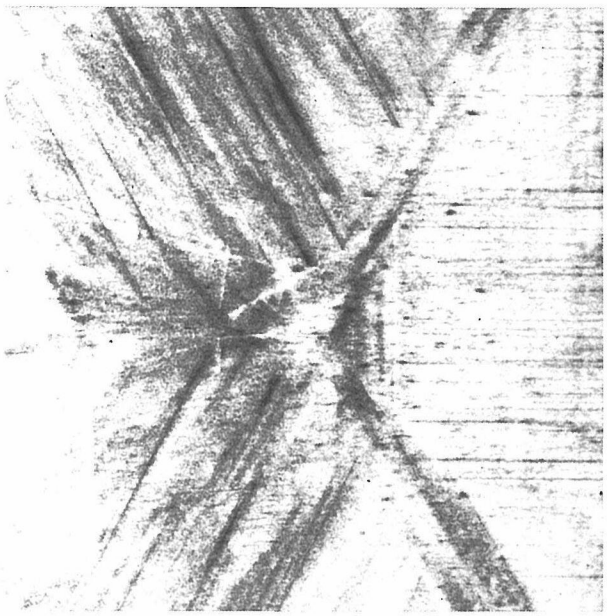

Fig.4. Grown-in dislocations in synthetic diamond. [111} view.Field width 1 mm.

they take fairly straight trajectories outwards to the external surfaces. In larger crystals dislocation-free volumes of mm^3 size may result. Topographic techniques [5-7] often reveal narrow growth zones of type IIa nature incorporated in crystals that are overall type Ia. Coherency stresses at type Ia/type IIa interfaces do not necessarily generate dislocations, so that these type IIa zones may also have low dislocation densities. However, in the author's experience, crystals that are entirely type IIa or type IIb are always dislocation-rich, having suffered strong plastic deformation in their history. In type IIa specimens the dislocation density is usually everywhere too high for individual dislocations to be resolved by cathodoluminescence (CL) topography. TEM usually shows more than one {111}<110> slip system active in a given specimen volume [8]. Configurations similar to those in Si and Ge deformed at relatively high T are observed. The much higher stacking-fault energy in diamond compared with Si and Ge makes

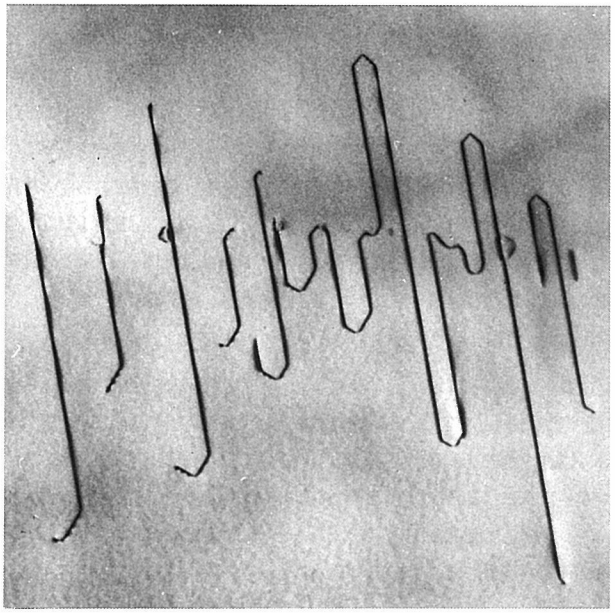

Fig. 5. Large <110>-segmented helix within cuboid growth sector. Field width 4.8 μm.

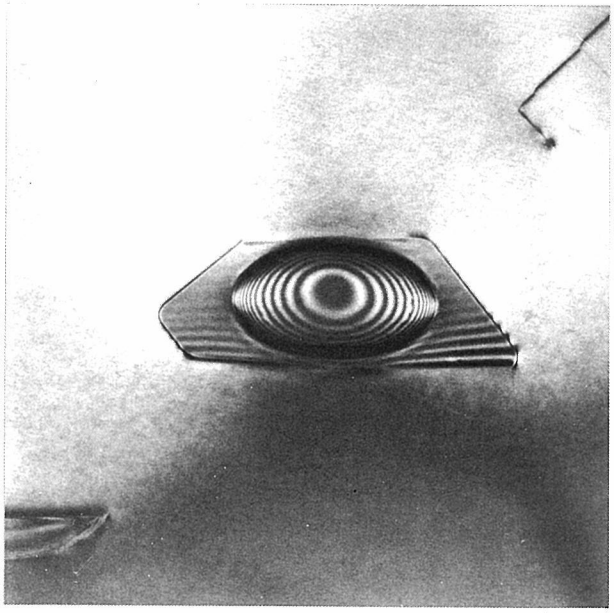

Fig. 6. Lenticular vesicle on stacking fault in cuboid growth sector. Field width 3μm.

difficult the measurement of this energy from dislocation dissociation observations in weak-beam dark-field (WBDF) images, e.g. Fig. 1, but this has been achieved, yielding ~280 mJm^{-2} [9].

A very different dislocation configuration has been found typical in natural type IIb diamonds. Their dislocations are fully polygonised, as shown by X-ray and CL topography, suggesting thorough annealing after plastic deformation [6, 10]. Fig. 2 is a direct print from a CL colour transparency. Hence the bright blue CL dislocation images appear as black lines, simulating dislocation diffraction contrast images as seen in X-ray topographs and bright-field TEM prints. Dense unresolved dislocation networks forming mosaic cell walls appear fully black in Fig. 2. A few individually-resolved dislocations show up as black lines within some almost dislocation-free cells, which have diameters up to 60 μm in this specimen.

Australian (Argyle Mine) diamonds fall in the type Ia category, but have generally low average N impurity, with type IIa and type Ia zones alternating. Plastic deformation is much in evidence. Fig. 3 (TEM courtesy of J. W. Steeds) shows localised dislocation tangles on the several {111} slip planes active. The (001)-orientation specimen foil, approx. 0.7 μm thick, was tilted to bring [110] close to the beam direction, and edge-on images of tangles on $(1\bar{1}1)$ are horizontal in Fig. 3. The tangles are probably centred on non-glissile Lomer-reaction dislocations, which have been observed in other diamonds [8].

2.2. Large synthetic diamonds. These diamonds are grown by the reconstitution method [11]. They exhibit {100} and {111} as major growth forms, with {110} and {113} in minor development. The configuration of grown-in dislocations depends on the seed orientation relative to the intended principal axis of growth on the seed. When that axis is [001], say, so that a single cube growth sector, corresponding to growth on (001), fills most of the total volume grown, X-ray topography shows that all, or nearly all, dislocations are 'inherited' from the seed crystal itself, or from imperfect epitaxy on the seed [12]. On the other hand, crystals whose principal growth axis is [111] have dislocation configurations like that in Fig. 4, which is an X-ray topograph of the central

area of a slice parallel to (111) in such a crystal. Three cube growth sectors are symmetrically disposed about a small central (111) sector. Separating the cube growth sectors are narrow, sheet-like {110} growth sectors, which contain only about 1 ppm N compared with 100-250 ppm N in the adjacent cube growth sectors. Consequently, this {110} growth has a lattice parameter up to 3×10^{-5} smaller than the surrounding cube-growth material [13]. It appears that the dislocations seen radiating outwards in the three cube growth sectors are generated at or close to the interfaces with the sheets of {110} growth. However, the density of dislocations is only about 300 lines mm^{-2}.

2.3. Dislocations and vesicles in natural diamond 'cuboid' growth. A not negligible fraction of natural diamonds have had at least some epochs during their growth when normal growth on flat octahedral facets was accompanied by non-faceted growth on hummocky surfaces whose orientation approximated to {100} in the mean, and this is termed 'cuboid' growth [2, 3, 14]. (Cuboid growth and natural diamond 'coat', to be discussed in Section 4, have some features in common in their IR absorption spectra.) The dislocation density in cuboid growth sectors is variable. Some can be nearly dislocation-free, as shown by X-ray topography. In other cases the dislocation density is high enough to be studied conveniently by TEM. In one of the latter class, configurations exhibiting extreme operation of dislocation climb processes were observed [15]. Fig. 5 shows one such configuration, which has no rivals known to the author among dislocations in other diamond-structure crystals. The image contains remaining segments of a single helix, much flattened in the (001) plane of the specimen, which was also the local mean growth surface orientation. Segments missing have been lost above and below the foil. Taking the Burgers vector direction as [110], lying roughly horizontally in the figure and perpendicular to the long, near-vertical, pure edge $[1\bar{1}0]$ segments, the mean helix axis is close to [110] and is marked by a line of vesicles having diameters from 20 nm to 130 nm.

In another region of the same specimen, where dislocation density was lower, much larger vesicles were found, some sitting on stacking faults (as in Fig. 6), or surrounded by dislocation loops [16]. In Fig. 6 the specimen foil, thickness 0.9 μm, is parallel to (001), $\mathbf{g} = 220$ points upwards. The stacking fault on (111) is intersected by top and bottom foil surfaces, but the circular lenticular vesicle is just contained within the foil. The mean diameter of 94 lenticles measured was 1.2 μm. Lenticles totally enclosed displayed concentric moiré fringes like those seen in Fig. 6. Internal pressures within lenticles deduced from moiré fringe counts were in the range 1.5 to 1.8 GPa.

3. Platelets and voidites. Pioneer TEM studies by Evans and Phaal [17] revealed platelets on {100} in type Ia diamond that accounted for the <100> 'spike' diffuse X-ray reflections exhibited by type Ia but not by low-N-impurity type IIa diamonds. Association with N impurity prompted a simple platelet model containing 4N per diamond a_0^2 that gave the then believed correct expansion of $\frac{1}{3}\, a_0$ normal to the platelet plane [18]. Platelets vary greatly in size. 'Giant' platelets, diameters from 1 to some tens of μm, can be seen individually by their visible and near-IR CL [6, 19]. Lath-like platelets, highly elongated parallel to one or other of the <110> directions in the platelet plane, were found by Woods up to 5 μm long in 1MeV TEM [20]. Fig. 7 (N. Sumida, unpublished) shows large platelets in a specimen 0.25 μm thick. The long lath-like platelets that intersect both top and bottom surfaces exceed 0.5 μm in length. Fig. 8, taken under similar WBDF conditions as Fig. 6(a) in Sumida & Lang [21] shows small platelets, diameters in the 10-20 nm range. Platelets of all sizes studied by TEM appear

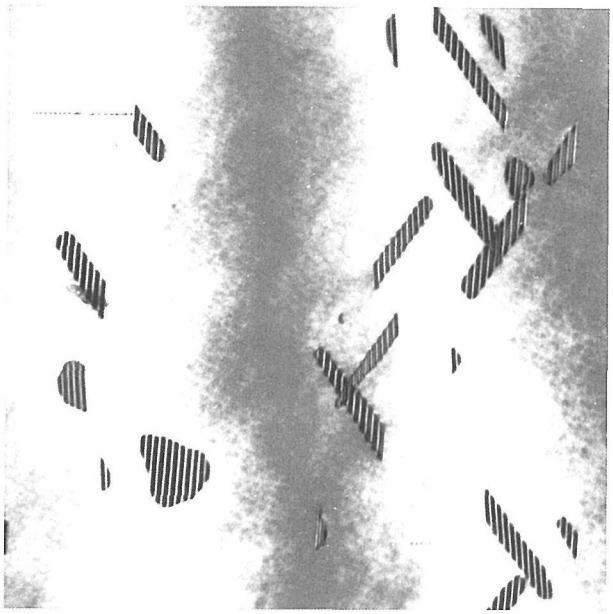

Fig. 7. Large {100} platelets. [110] zone axis image. Field width 2 μm.

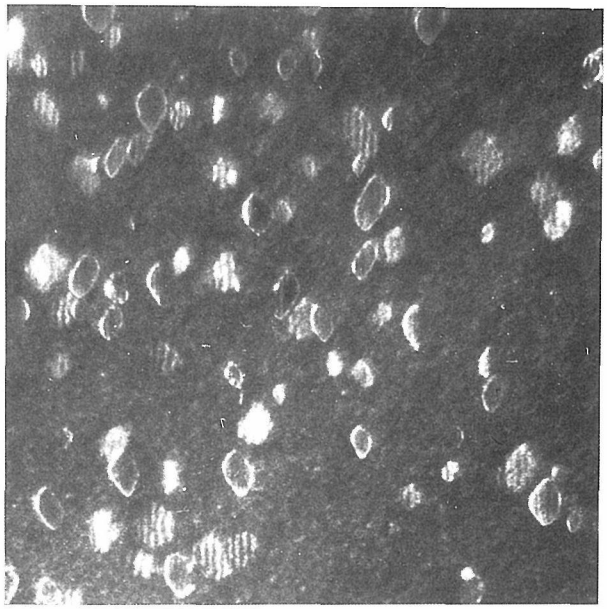

Fig. 8. Small {100} platelets, WBDF image. Field width 400 nm

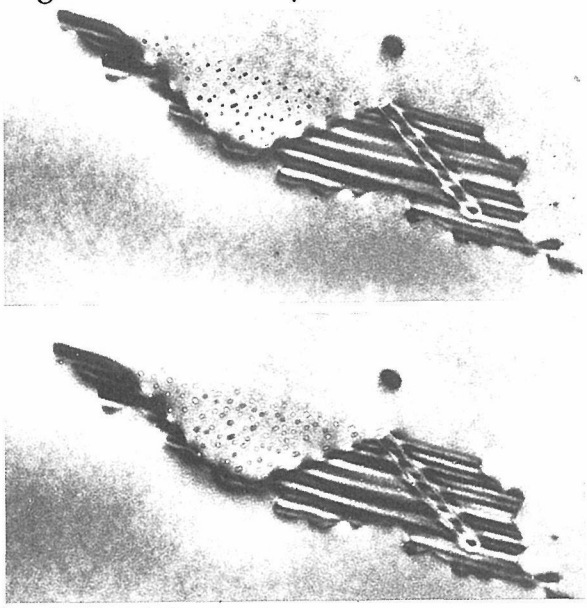

Fig. 9. Partial platelet and voidites. (Two focal conditions). Field width 0.9 μm

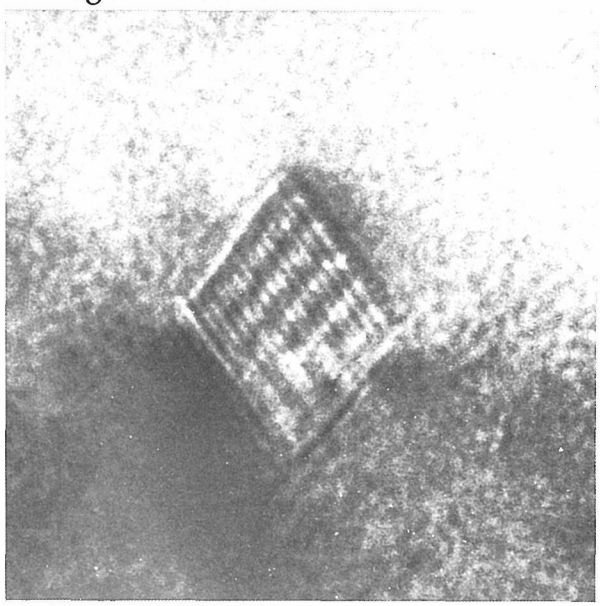

Fig. 10. Voidite showing both moiré and lattice fringes. Field width 15 nm.

to have the same structure, and to produce the same diamond matrix displacement normal to the platelet, which moiré fringe measurements give as between $0.35a_0$ and $0.362\,a_0$ [22]. This displacement, larger than $\frac{1}{3}\,a_0$, plus other evidence, including quantitatively relating total platelet area per unit volume to the nitrogen impurity concentration assessed by IR absorption [21], has led to abandonment of the 4N per a_0^2 model. Direct measurement of N in platelets by EELS and PEELS gives a variety of results [23, 24], but none greater than about 0.5 N per a_0^2 . All evidence, including lattice imaging of platelets viewed edge-on, e.g. [24, 25], suggests a uniform, ordered structure in platelets, but its details are unsolved.

The discovery of platelets apparently transformed into a sheet of small objects 5 - 10 nm in diameter surrounded by a perfect dislocation loop [26], and of 'partial platelets' in which some part of the fault-fringe-producing area was similarly replaced

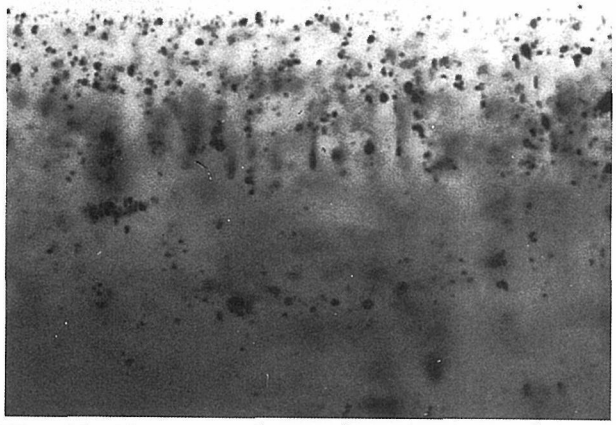

Fig. 11 Core-coat boundary in natural diamond. Field width 80 μm.

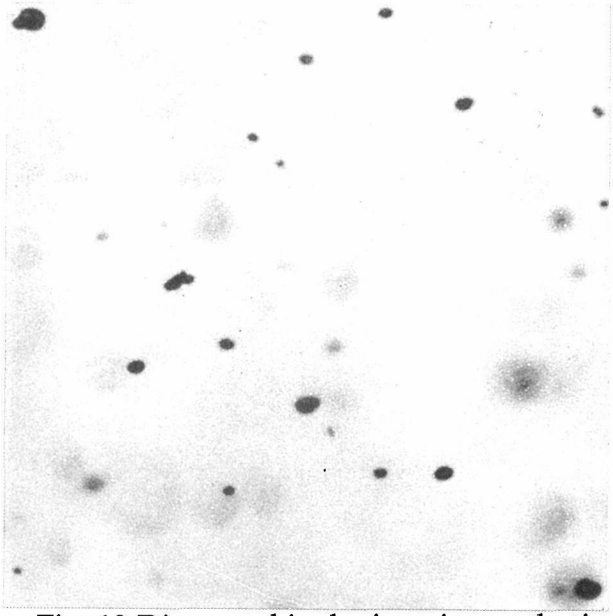

Fig. 12 Dispersed inclusions in synthetic diamond. Field width 80 μm.

[27], led to intensive high-resolution study of these defects [27, 28]. The small objects were called 'voidites' because they were visible by phase contrast, like voids would be, apparently having electron density roughly half that of diamond. Voidites are {111}-faceted bodies, ranging in shape from regular to highly elongated octahedra. Voidites in isolation can have diameters up to ~40 nm [29]; elongated voidites may be up to 100 nm long with, typically, 3 nm as minor diameter [27]. Fig. 9 shows a large partial platelet with voidites, average diameter ~5 nm, replacing fault-fringe contrast in its upper left area. The top image, in optimum focus, shows these most sharply. The bottom image is defocussed to reveal better a few small voidites on the right hand area that still shows apparently normal platelet fault-fringe contrast. (A dislocation dipole lies on, or very close to, this area.) Voidites are filled with crystalline substance, a f.c.c. structure in parallel orientation with the diamond matrix [30], and containing nitrogen [30, 31]. Fig. 10 (micrograph by N. Sumida), taken near diamond [110] zone axis diffraction conditions at 200 kV, shows a voidite whose mean diameter between its {111} faces seen edge-on is 4.3 nm. Running upper right to lower left are moiré fringes between diamond 111 and 'voidite-crystal' 111 spacings, whereas those running upper left to lower right are voidite-crystal 111 lattice fringes. The latter give 0.48 nm and the former 0.49 nm for the voidite-crystal a_0.

4. Inclusions in diamonds. Crystalline inclusions large enough for study by conventional optical and X-ray crystallographic methods have a well-established place in studies into the origin of natural diamonds [2,3]. Discussed here are the much smaller inclusions, suitable for study by TEM, that are found in the outermost growth zones of 'coated' diamonds. Such diamonds consist typically of a clear core enveloped by a green or grey coat, translucent but not transparent, densely populated by particles whose diameters are generally <1 μm. Transition from clear core to particle-filled coat is usually sharp, occurring over a distance similar to the average particle size, as shown in Fig. 11. This optical micrograph views in transmission a 1 mm thick plate polished parallel to (001). The core-coat boundary, parallel to an octahedral growth surface, intersects the near surface of the specimen along a horizontal trace. The growth direction is downwards and outwards towards the observer. Hence the coat thickness

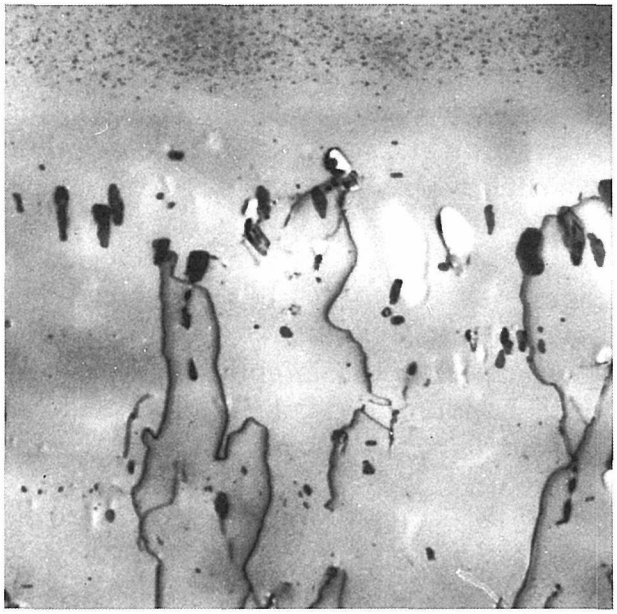

Fig. 13 TEM of core-coat boundary, orientation like Fig. 11. Field width 5 μm

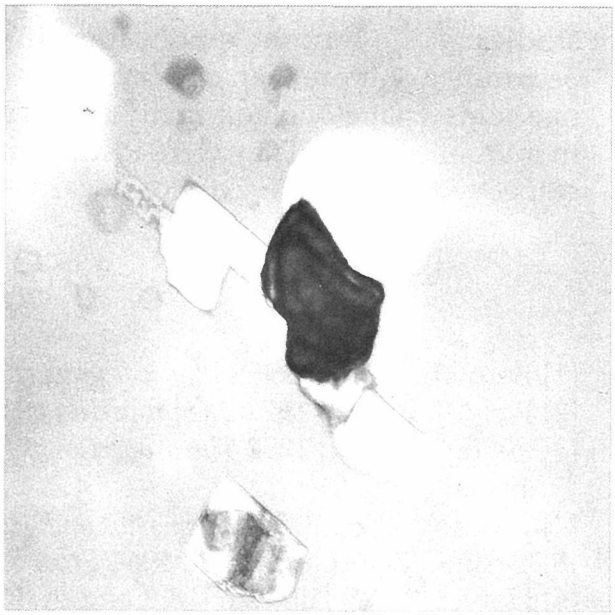

Fig. 14. Ankerite inclusion within diamond coat. Field width 0.8 μm.

penetrated increases towards the bottom edge of the micrograph,where the specimen becomes relatively opaque. This coated diamond has unusually large particles in its coat, but the particle density is typical. Contrast such particle density with that observed by similar methods in a synthetic crystal, displayed at the same magnification in Fig. 12. This volume was selected for its exceptionally high particle density, but particle sparseness compared with that in natural diamond coat shows that capturing individual particles for TEM study is not easy in synthetic crystals.

The low-magnification TEM of the core-coat boundary in a natural diamond, Fig. 13, provides an insight into conditions there. Specimen orientations in Figs. 11 and 13 are similar. Normal core is imaged in the top band in Fig. 13, and is filled with normal {100} platelets (seen merely as dots at this low magnification). Inclusions retained in the 0.5 μm thick specimen (and not lost in the ion-beam-thinning process to leave cavities behind) span a range of sizes from ~5 nm upwards. All but a few per cent of inclusions are incorporated in diamond matrix without generating dislocations, but the resulting columns of dislocation parallel to the growth direction account for the 'fibrous' texture of diamond coat recorded by X-ray topography [32]. Microanalytical EM techniques applied to diamond coat particles have identified apatite [33], biotite [34] and a variety of carbonates [35]. For example, the small coat particle retained in a cavity, seen in the centre of Fig. 14, was identified as ankerite, a Mg, Fe, Ca carbonate having the dolomite structure. It appears dark relative to diamond matrix because it is in diffraction orientation, showing quite good extinction contours, whereas the diamond matrix is non-diffracting. The overall diamond thickness in Fig. 14 is 0.7 μm. Cavities in the diamond show absorption contrast; those now empty appear light, those filled with non-diamond material show darker than their surrounds. Frequently observed are more than one crystal species residing together in a single cavity, a complicating factor in their study.

Returning to Fig. 12, note the irregular shape of a number of inclusions, suggesting that, as in natural diamond coat, multiple particle occupancy of a cavity can occur. Microradiography of this synthetic material using crystal-monochromatised CuKα radiation, and achieving 1 μm resolution, demonstrated that transition-metal-containing phases were a minority component in the inclusion population. TEM

studies (R. J. Vincent, publication in preparation) have indeed demonstrated the occurrence of more than one crystal species together in a single cavity. For example, in one somewhat elongated cavity three crystallites, each <1 μm in diameter, were found in mutual contact. They were identified by diffraction and X-ray spectroscopy as being respectively a b.c.c. Fe-Co alloy, a garnet and a clinopyroxene.

References

[1] Berman, R. (ed.) 1965 *Physical properties of diamond.* Oxford:Clarendon Press.
[2] Field, J. E. (ed.) 1979 *The properties of diamond.* London:Academic Press.
[3] Field, J. E. (ed.) 1992 *The properties of natural and synthetic diamond.* London:Academic Press
[4] Davies, G. (ed.) 1994 *Properties and growth of diamond.* London:INSPEC, I.E.E.
[5] Takagi, M. & Lang, A. R. 1964 *Proc. R.Soc.Lond.* A**281**, 310-322.
[6] Hanley, P. L., Kiflawi, I. & Lang, A. R. 1977 *Phil.Trans.R.Soc.Lond.* A**284**, 329-368.
[7] Lang, A. R. 1993 *Diamond and related materials* **2**, 106-114.
[8] Sumida, N. & Lang, A. R. 1981 *Inst.Phys.Conf.Ser. No. 60*, 319-324.
[9] Pirouz, P., Cockayne, D. J. H., Sumida, N., Hirsch, P. & Lang, A. R. 1983 *Proc.R.Soc. Lond.* A**386**, 241-249.
[10] Sumida, N. & Lang, A. R. 1981 *Phil.Mag.* A**43**, 1277-1287.
[11] Wentorf, R. H., Jr. 1971 *J.Phys.Chem.* **75**, 1833-1837.
[12] Lang, A. R. 1994 *J.Appl.Cryst.* **27**, 988-1001.
[13] Lang, A. R., Moore, M., Makepeace, A. P. W., Wierzchowski, W. & Welbourn, C. M. 1991 *Phil.Trans.R.Soc.Lond.* A**337**, 497-520.
[14] Lang, A. R. 1974 *Proc.R.Soc.Lond.* A **340**, 233-248.
[15] Walmsley, J. C. & Lang, A. R. 1992 *Phil.Mag.Lett.* **65**, 159-165.
[16] Walmsley, J. C., Lang, A. R., Rooney, M.-L.T. & Welbourn, C. M. 1987 *Phil.Mag.Lett.* **55**, 209-213.
[17] Evans, T. & Phaal, C. 1962 *Proc.R.Soc.Lond.* A**270**, 538-552.
[18] Lang, A. R. 1964 *Proc.Phys.Soc.* **84**, 871-876.
[19] Kiflawi, I. & Lang, A. R. 1977 *Nature, Lond.* **267**, 36-37.
[20] Woods, G. S. 1976 *Phil. Mag.* **34**, 993-1012.
[21] Sumida, N. & Lang, A. R. 1988 *Proc.R.Soc.Lond.A.* **419**, 235-257.
[22] Bursill, L. A., Hutchison, J. L., Sumida, N. & Lang, A. R. 1981 *Nature, Lond.* **292**, 518-520.
[23] Bruley, J. 1992 *Phil.Mag.Lett.* **66**, 47-56.
[24] Fallon, P. J., Brown, L. M., Barry, J. C. & Bruley, J. 1995 *Phil.Mag.* A**71**, in press.
[25] Barry, J. C. 1991 *Phil.Mag.* A**64**, 111-135.
[26] Stephenson, R. F. 1977 Ph.D. Thesis, University of Reading.
[27] Barry, J. C., Bursill, L. A., Hutchison, J. L., Lang, A. R., Rackham, G. M. & Sumida, N. 1987 *Phil.Trans.R.Soc. Lond..* A**321**, 361-401.
[28] Hirsch, P. B., Pirouz, P. & Barry, J. C. 1986 *Proc.R.Soc.Lond.* A**407**, 239-258.
[29] Van Tenderloo, G., Luyten, W. & Woods, G. S. 1990 *Phil.Mag.Lett.* **61**, 343-348.
[30] Hirsch, P. B., Hutchison, J. L. & Titchmarsh, J. 1986 *Phil.Mag.* A**54**, L49-L54.
[31] Bruley, J. & Brown, L. M. 1989 *Phil.Mag.* A**59**, 247-261.
[32] Kamiya, Y. & Lang, A. R. 1965 *Phil.Mag.* **11**, 347-356.
[33] Lang, A. R. & Walmsley, J. C. 1983 *Phys.Chem.Minerals* **9**, 6-8.
[34] Walmsley, J. C. & Lang, A. R. 1992 *Mineral.Mag.* **56**, 108-111.
[35] Walmsley, J. C. & Lang, A. R. 1992 *Mineral. Mag.* **56**, 533-543.

Characterization of Defect Structures of Homoepitaxial Diamond by Cross-sectional TEM

M. Tarutani, Y. Takai, R. Shimizu, T. Ando, M. Kamo* and Y. Bando**
Department of Applied Physics, Osaka University, Japan
*National Institute for Research in Inorganic Materials, Ibaraki, Japan

Abstract

A homoepitaxially grown CVD diamond film has been studied by cross-sectional TEM. Several kinds of defects are observed in the film and at the film/substrate interface. The interfacial defects localized on the (001) interface show strong diffraction contrast, and the inner defects aggregate nearly in line along <001> and <111> directions. They are found to be composed of interstitial-type dislocation loops. A little amount of Fe and Si impurities is detected at the interface by analytical electron microscopy, suggesting that the presence of the impurities is one of origins of the defects.

Introduction

Recent progress of heteroepitaxial diamond films grown by Chemical Vapor Deposition (CVD) is very attractive for a synthesis of large scale single-crystalline diamond films. For this purpose, detail characterization as well as further improvement of the growth techniques are indispensable. For the characterization, Scanning Tunneling Microscopy (STM) and Transmission Electron Microscopy (TEM) allow us to observe the atomic-scale structure which is of great help for more comprehensive understanding of the growth process.

Cross-sectional TEM (XTEM) has widely been applied to the studies on nucleation and growth mechanism of the CVD diamond on various substrates such as Si[1-3] and SiC[4,5]. However, a systematic investigation has hardly been performed mainly by the reason that preparation of TEM specimens is generally very difficult due to the extremely different properties of the diamond from those of the substrates, in hardness and resistivity for ion etching. The studies on homoepitaxial diamond reported[6-8] so far are also very few in spite of great interest in basic research.

In this paper, we describe our recent studies on homoepitaxial diamond by XTEM and Analytical Electron Microscopy (AEM)[9]. TEM observation of unique defect structures and newly developed experimental techniques for the TEM specimen preparation will be presented.

Experimental

The present homoepitaxial diamond film was synthesized by microwave plasma-assisted CVD on a single-crystalline high pressure synthetic diamond (001) substrate. The substrate surface was polished and then treated alternately by oxygen- and hydrogen-plasma to remove initial defects and contaminants as well as to make the surface smooth beforehand. The growth conditions are as follows; reaction gas was 1 % CH_4/H_2, gas pressure was 40 Torr and substrate temperature was kept at ~ 850 °C. The substrate size was 1x1.5x0.5 mm^3. A Si wafer was used in the CVD chamber as a substrate table. Temperature was measured by an optical pyrometer through the Si wafer.

A Focused Ion Beam (FIB) micromachining apparatus[10,11] was used to prepare a specimen for XTEM observation. This apparatus provides a finely focused Ga^+ ion probe of ~ 50

nm in diameter at 25 kV of accelerating voltage. A 360° rotation-tilt-type high precision sample holder and a scanning ion microscope image enable the specimen to be machined under stress-free condition at a precisely selected region.

A procedure of the specimen preparation is shown in Fig. 1. The sample was mounted by silver paste on a Cu disk, which is suitable for both FIB machining and TEM observation. A thin wedge-shaped section of ~ 5 - 10 μm long parallel to the (110) plane was curved out at a corner of the sample by the FIB machining, followed by 3 keV Ar^+ ion thinning to reduce the damaged surface layer caused by the FIB etching. The specimen thus prepared now allows us to observe cross-sectional structure of the diamond under a high-resolution TEM as shown later.

For XTEM experiment a JEM-200CX TEM was used by operating at 200 kV. For AEM experiment of Energy Dispersive X-ray Spectrometry (EDS) and Electron Energy-Loss Spectrometry (EELS), a JEM-3000F TEM equipped with a tungsten thermal field emitter was used by operating at 300 kV.

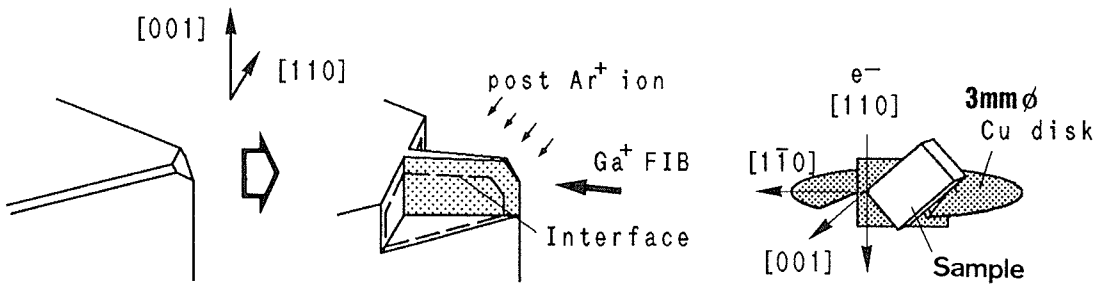

Figure 1. Scheme of the procedure of TEM specimen preparation. A thin wedge-shaped cross-section is curved out at a corner of the sample. TEM observation is performed in ~ [110] direction. A Cu disk can be set in a conventional TEM holder.

Results and Discussion

Figure 2 shows a bright field image of whole cross-section of the specimen observed in [110] direction. A dark horizontal line contrast is observed at the homoepitaxial diamond/substrate (001) interface, as indicated by an arrow. The contrast comes from diffraction effect due to the strain field around defects. Several kinds of defects are also observed in the homoepitaxially grown diamond film itself. It should be noted that the defects were neither induced nor removed from the initial position during the repeating experiment of specimen preparation and TEM observation. This suggests that they were certainly produced during the CVD process. Other broad black and white contours are due to thickness fringes, appearing every 27 nm thickness change.

Figure 3(a) shows an enlarged image of the interfacial region, indicating that the dark contrast is formed by many small defects of ~ 10 - 20 nm in diameter. They sometimes show characteristic contrast of a bright line on {111} plane surrounded by two dark side-areas as indicated by an arrow, which seems to be due to the dislocation loops[12]. Some of them are located apart from the interfacial line, which is supposed to be due to the initial roughness of the substrate generated by oxygen-plasma treatment. Figure 3(b) is a high-resolution electron microscope (HREM) image of an isolated loop, showing that an extra atomic plane on (1$\bar{1}$1) is inserted. Hence the defects at the interface are understood as the interstitial-type dislocation loops.

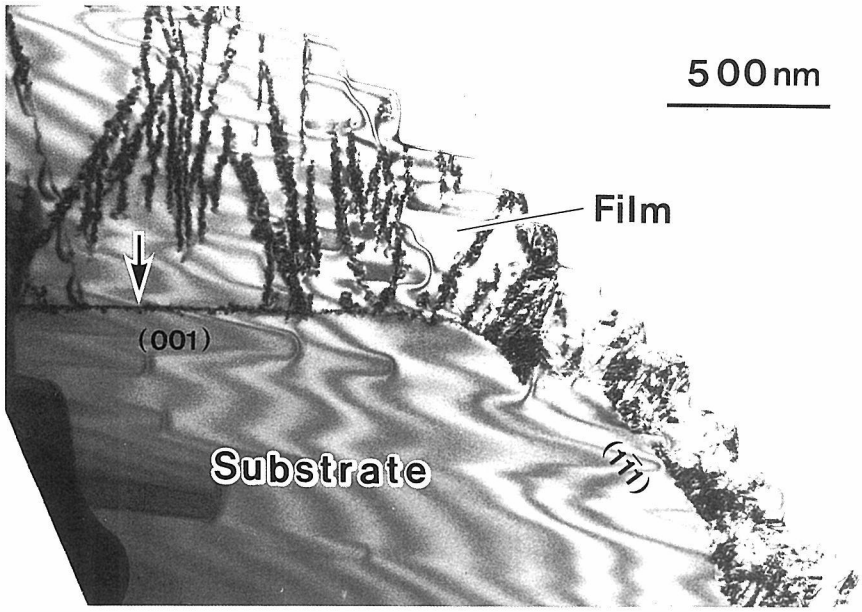

Figure 2. Whole view of the cross-sectioned specimen. Upper right part is eroded by the FIB machining. The (001) interface show marked diffraction contrast.

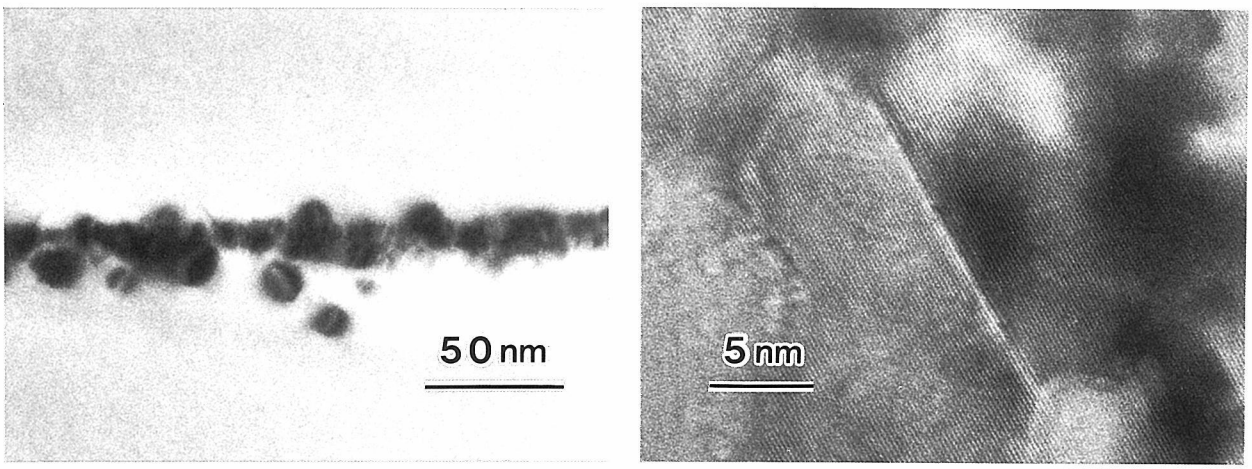

(a) (b)

Figure 3. (001) interfacial defects (a) enlarged image representing typical diffraction contrast of dislocation loop, (b) HREM image of an isolated one. The defect has an extra atomic plane on $(1\bar{1}1)$, showing that the defects are of interstitial-type.

The defect structure in the grown film varies depending on indices of substrate face. As shown in Fig. 4(a), the film on the $(1\bar{1}1)$ face has the defects which have been commonly observed in the CVD diamond, that is, stacking faults and twins. In the corresponding diffraction pattern, many extra spots and streaks can be seen. On the (001) face, however, several rope-shaped defects rising from the (001) interface are observed in Fig. 4(b) for the first time, which do not represent such characteristic diffraction pattern. The diamond growth on the {100} surface is well-known to proceed quite orderly because the surface is reconstructed to have 2x1 dimer rows[13] during the CVD process. Hence, this difference of the defect structure is supposed to be related to the growth mechanism.

As can be seen in Fig. 4(b), there are two types of contrast in the rope-shaped defects, one looks like series of sharp needles of ~ 50 nm long along the [001] direction, and the other has oval loop-shape contrast lying in rows along the <111> directions. They are considered to be present in the configuration of a scheme in Fig. 5, and notably the dislocation loops are arranged

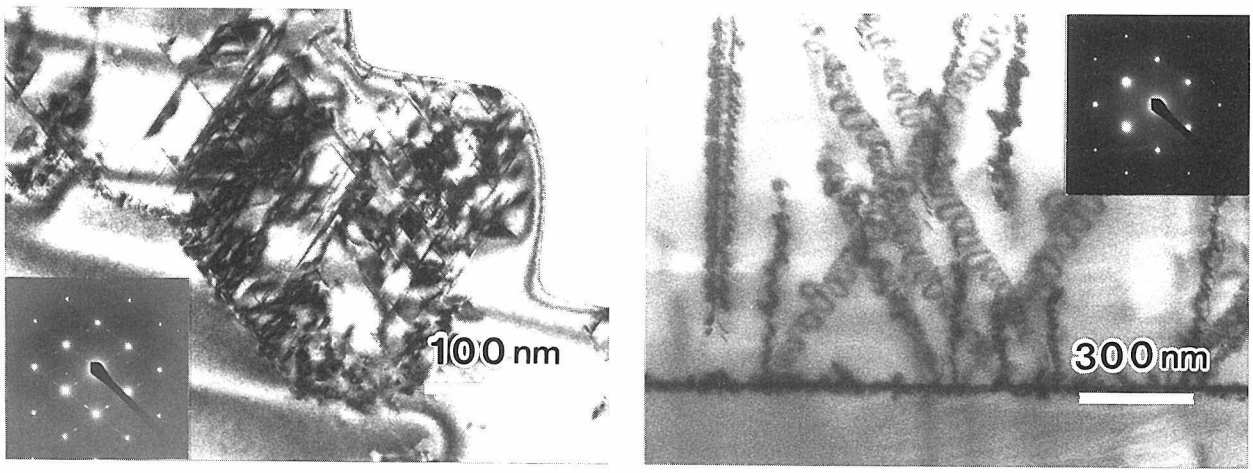

(a) (b)

Figure 4. Inner defects of the grown film (a) on the $(1\bar{1}1)$ face containing many stacking fault and twins, (b) rope-shaped defects on the (001) face.

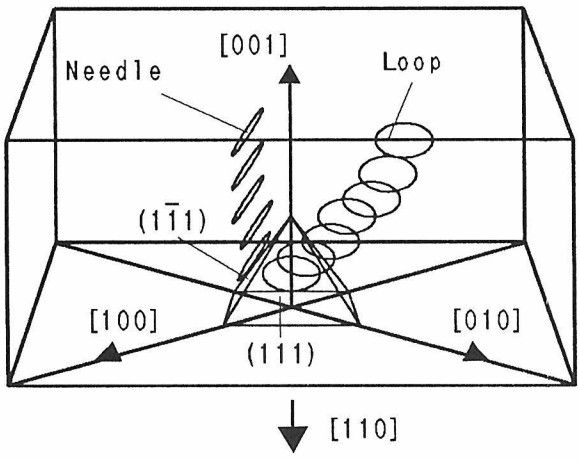

Figure 5. Scheme of the configuration of the rope-shaped defects. The defects parallel to the electron beam direction show needle-shape contrast, and the other oval loop-shape contrast.

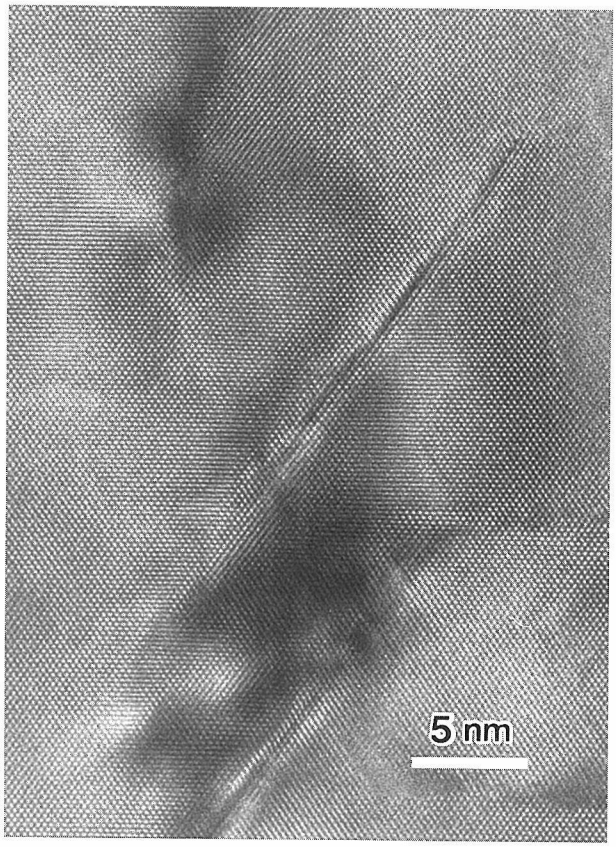

Figure 6. HREM image of the defect of needle-shape. The defect has double extra atomic plane.

on series of {111} planes of nearly same indices. Therefore both the contrasts are decided to be due to the same kind of dislocation loop. An HREM image of the defects is shown in Fig 6, in which doubly faulted loops having two extra atomic planes are observed in one defect. The defect planes extend irregularly and a lower end is rather ambiguous due to the strain of a neighbor defect. It is found that they are also the interstitial-type dislocation loops.

It is valuable for the researchers involved in the diamond synthesis to investigate the properties of these defects and to identify those origins. Since it is difficult to identify these imperfections only by the structural information, characterization by AEM was attempted.

Figure 7 shows an EELS spectrum of the CVD diamond film. No light element except carbon is detected. But the presence of some impurities was suggested through the EDS measurements. Figure 8 shows an EDS spectrum at the interface taken by a ~ 50 nm electron probe. Fe Kα (6.4 keV) and Si Kα (1.74 keV) X-rays were detected only at the interface region and not at the inner region, suggesting that the interfacial defects were induced by these impurities. The Fe impurity is probably attributed to the substrate inclusion segregated to the surface. The Si is more likely to be contaminant from the substrate table[14] generated at the early stage of the CVD process.

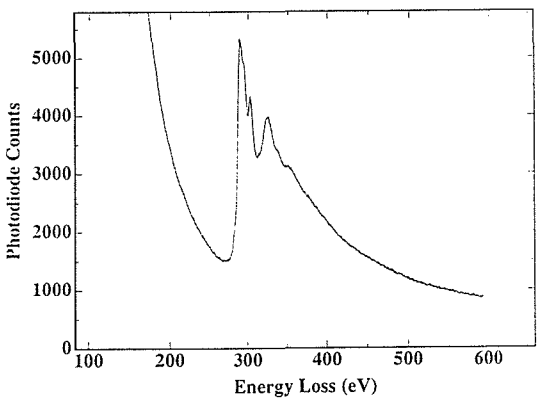

Figure 7. EELS spectrum of the grown diamond.

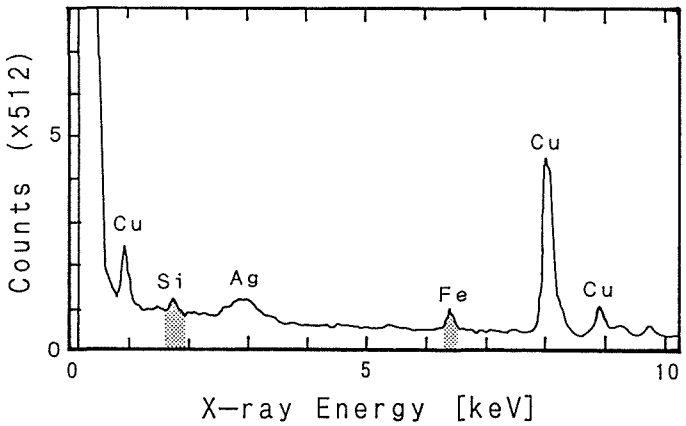

Figure 8. EDS spectrum of the interfacial defects. Si and Fe was detected only at the interface.

Conclusion

The defect microstructure of the homoepitaxial diamond has been investigated. In the present research, the FIB technique has contributed greatly to the XTEM works. The AEM analysis has shown the presence of the impurities at the interface which are suggested as in part the origin of the defects.

Acknowledgment

We would like to thank Mr. K. Kurashima and Dr. H. Suematsu for the helpful AEM experiment. One of the authors (M. Tarutani) greatly acknowledges financial support by a JSPS scholarship.

References

[1] B.E.Williams, J.T.Glass, R.F.Davis and K.Kobashi: J.Crystal Growth, **99** (1990) 1168.
[2] M.Tarutani, Y.Takai and R. Shimizu: Jpn.J.Appl.Phys., **31** (1992)L1305.
[3] C.J.Chen, T.S.Lin, L.Chang and F.R.Chen: Proc. 13th Int. Congr. Electron Microscopy, Paris, (1994) p.581.
[4] L.Chang, T.S.Lin, J.L.Chen and F.R.Chen: Appl.Phys.Lett.,**62** (1993) 3444.
[5] W.Zhu, X.H.Wang, B.R.Stoner, G.H.M.Ma, H.S.Kong, M.W.H.Braun and J.T.Glass: Phys.Rev., **B47** (1993) 6529.
[6] S.Iijima, Y.Aikawa and K.Baba: Appl.Phys.Lett., **57** (1990) 2646.
[7] W.Luyten, G.V.Tendeloo, S.Amelinckx and J.L.Collins: Phil.Mag., **A66** (1992) 899.
[8] M.Tarutani, T.Ando, Y.Takai, M.Kamo and R.Shimizu: Proc. 4th Int.Congr.New Diamond Sci.Technol.,Kobe,Japan, (1994) p.247.
[9] Y.Bando, Y.Kitami, K.Kurashima, T.Tomita, T.Honda and Y.Ishida: Microbeam Analysis, **3** (1994) 279.
[10] E.C.G.Kirk, D.A.Williams and H.Ahmed: Inst.Phys.Conf.Ser., **100** (1989) 501.
[11] M.Tarutani, Y.Takai, R.Shimizu, K.Uda and H.Takahashi: Technol.Repts.Osaka Univ., **43** (1993) 167.
[12] P.B.Hirsch, A.Howie, R.B.Nicholson, D.W.Pashley and M.J.Whelan: "Electron Microscopy of Thin Crystals", Butterworths, London (1965) p.178.
[13] T.Tsuno, T.Imai, Y.Nishibayashi, K.Hamada and N.Fujimori: Jpn.J.Appl.Phys., **30** (1991) 1063.
[14] M.Kamo, H.Yurimoto and Y.Sato: Appl.Surf.Sci., **33** (1988) 553.

Electronic States of Monolayer Hexagonal BN

Ayato Nagashima, Norihiko Tejima, Yasuo Gamou, Takanao Kawai and Chuhei Oshima
Department of Applied Physics, Waseda University, 3-4-1 Okubo, Shinjuku-ku, Tokyo 169, Japan

Angle-resolved ultraviolet photoelectron spectrospopy and angle- resolved secondary electron emission spectroscopy have been carried out for a film of single-crystalline monolayer hexagonal boron nitride (*h*-BN) formed on the Ni(111) surface to investigate both the valence- and conduction-band structures. The observed electronic dispersion relations were compared with some theoretical ones reported for bulk *h*-BN. Among these theoretical calculations, the one by A. Catellani *et al.* (Ref. [7]) is in the best agreement with the present results. We have discussesd the strength of the interfacial bond and the influence of this bond upon the electronic states of the monolayer *h*-BN film on the basis of the observed band structures for the BN film and a film of monolayer graphite formed on Ni(111).

I. INTRODUCTION

In recent years, much attention has been devoted to boron nitride (BN) in relation to its technological applications. From a fundamental scientific point of view, hexagonal BN (*h*-BN) is an attractive highly anisotropic insulating material isostructural to semimetallic graphite. While there is good agreement between the various theoretical band calculations and experimental results for graphite, such consensus has not been achieved for *h*-BN in spite of the structural similarity. As for the widths of the π bands, which are important for the electronic and optical properties, for instance, various different calculated values have been presented, ranging from 1.2 eV to 9.3 eV[1-7]. The reason why such a large discrepancy has arisen is mainly ascribed to the lack of precise experimental data concerning the band structure, with which the theoretical results can be evaluated. Although some papers have reported the experimental density of states for the valence electrons[8-10], as far as we know, no experimental dispersion relations of the energy bands in *h*-BN have been presented to date. This was due to the nonavailability of single-crystalline samples large enough for angle-resolved electron spectroscopy measurements.

In this experiment, we have observed both the valence- and conduction-band structures of a film of single-crystalline BN on the Ni(111) surface by using angle-resolved ultraviolet photoelectron spectroscopy (ARUPS) and angle-resolved secondary electron emission spectroscopy (ARSEES). The thickness of the film prepared by thermal decomposition of borazine ($B_3N_3H_6$) was 1 ML. The present results are compared with some theoretical band structures available at present and possible reasons for the agreement and disagreement among them are discussed. We have also discussed the strength of the interfacial bond and influence of this bond upon the electronic states of the monolayer *h*-BN film on the basis of the observed band structures for the BN film and a film of single-crystalline monolayer graphite (MG) formed on Ni(111).

II. RESULTS AND DISCUSSION

A. Dispersion curves of valence-band structure

The apparatus used in this experiment and the precise conditions for the preparation of the monolayer films of graphite and *h*-BN were described elsewhere[11,12]. Both the films are commensurate with the Ni(111) surface. In Fig. 1, we plotted the binding energies of the observed photoemission peaks in the ARUPS spectra of the monolayer *h*-BN/Ni(111) system versus the wave vector parallel to the surface. Open and solid circles represent the data obtained with He I and He II resonance lines, respectively. The theoretical energy band structure of the bulk *h*-BN[7] is also indicated by broken curves for comparison, where the theoretical valence-band maximum (VM) is placed at the binding energy of 4.0 eV to fit the theoretical band structure to the experimental one. The shaded bands represent the dispersion curves of the d bands observed for the clean Ni(111) surface with the photon energy of 21.2 eV. Almost all the branches near E_F observed for the BN-covered Ni(111) surface agree well with those for the clean surface. In Fig. 1, along the $\overline{\Gamma}\,\overline{M}$ direction, there is a branch at $\sim$ 1 eV, of which the corresponding one for the clean surface is not depicted. This is due to the strongly steep Fermi cutoff in the ARUPS spectra for the clean surface, of which the tail has obscured the existing structure at around 1 eV and made it impossible to assign the precise energy of this structure.

In Table I, we tabulate the observed values of the widths of the valence bands and the difference in energy between the maxima of the π and σ bands. σ_1 and σ_2 denote the higher and lower σ bands, respectively. In Table I, these experimental results are compared with the five band calculations presented by Nakhmanson *et al.*[2], Zupan[4], Zunger *et al.*[5], Robertson[6], and Catellani *et al.*[7]. Since all of these calculations except the one by Zunger *et al.* were performed for the bulk *h*-BN, some of the energy bands are split due to the interlayer interaction. Therefore, some of the spaces in Table I show double values.

Table 1: Experimental and theoretical values (in eV) for the widths of the valence bands and for the difference between the maxima of the π and σ bands. σ_1 and σ_2 denote the higher and lower σ bands, respectively.

	Width of π band	Width of σ_1 band	Width of σ_2 band	$\pi - \sigma$ energy difference
Experimental	5.8	6.5	8.2	0.9
Nakhmanson *et al.*(Ref. [2])	7.5, 9.3	8.7	9.2, 10	4.9, 5.8
Zupan (Ref. [4])	3.2, 3.5	4.5	6.3	0.7
Zunger *et al.*[a] (Ref. [5])	4.6	3.1	4.2	2.1
Robertson (Ref. [6])	4.9, 6.0	6.2	9.0	3.0
Catellani *et al.* (Ref. [7])	4.3, 6.7	6.2	7.4	1.7, 2.1

[a]Calculated with modified iterated extended Hückel method.

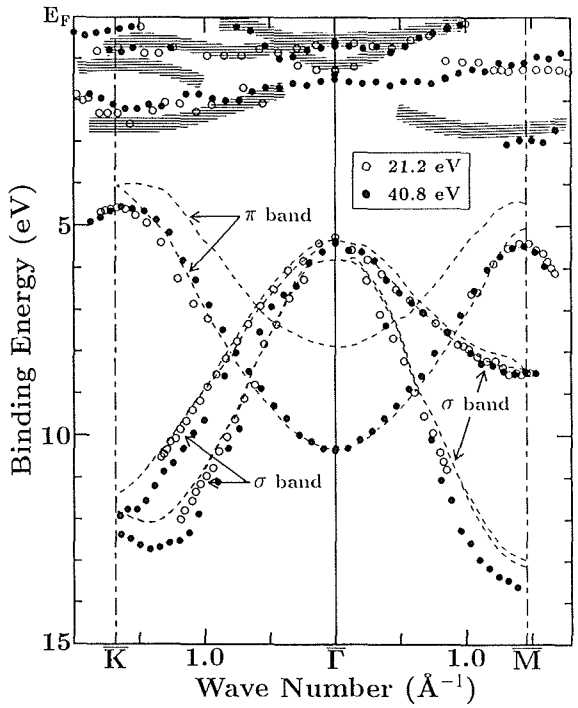

FIG. 1: Experimental valence-band structure of the monolayer *h*-BN/Ni(111).

In Ref. [5], the energy bands of the isolated monolayer *h*-BN film were calculated with three different methods, among which the modified iterated extended Hückel method gave relatively good agreement with the present results.

It is clearly seen from Table I that the results of Nakhmanson *et al.* with the orthogonalized-plane-wave (OPW) method do not agree well with the present results. For instance, the calculated widths of the π bands are 7.5 and 9.3 eV, of which the average is larger than the present experimental value by 2.4 eV. In addition, the difference in energy between the maxima of the π and σ bands (4.9 eV) is much larger than the present value (0.9 eV). Such a large value is also inconsistent with the experimental density of states for transitions from the π and σ bands to the B 1s core hole measured by K emission spectroscopy[8]. Next, we examine the results of Refs. [4-6] which were calculated with a tight-binding (TB) approximation. While the calculated band widths by Robertson agree well with the experimental ones, the works by Zupan and Zunger *et al.* have underestimated these values in spite of using the same calculation method. This contrast could be ascribed to the choice of the more realistic TB parameters in the Robertson's work[6], although it shows rather poor agreement with the experiments concerning the energy difference between the π and σ bands.

Among five calculations listed in Table I, the one by Catellani *et al.*[7] shows the best agreement with the experimental band structure. The agreement concerning both the band widths and the energy difference is good in comparison with the other calculations. In addition to this, it is only the band calculation in Ref. [7] that reproduces the observed feature described below; as shown in Fig. 1, the downward dispersion of the lower σ band along the $\overline{\Gamma}\,\overline{K}$ direction changes to the upward one at the point where the wave vector is about 1.4 Å^{-1}. In view of the fact that the first four calculations were done with non-self-consistent potentials and small basis sets, such as 16 atomic orbitals and 73 OPW's, the good agreement between the experiment and the latest calculation demonstrates that the all-electron full-potential self-consistent calculations with large basis sets (e.g. about 250 augmented plane waves used in Ref. [7]) are desirable for describing the band structure of the *h*-BN precisely, even for the description of the valence-band structure.

Despite the fairly good agreement, at the same time, there are some discrepancies between the results of Ref. [7] and the present work. First, the theoretical widths of all the bands are slightly smaller than the experimental values. This might stem from the underestimation of the theory about the inplane bond, although we could not completely rule out the possibility that the small contraction of the lattice constant of the BN film for matching with the periodicity of the Ni(111) surface widens the width of the valence bands. Second, if the value for the gap between the bonding π and anti-bonding π^* bands in the film is similar to the calculated one for the bulk BN (3.9 eV), the part of the π^* band could be observed under E_F since the experimental VM has the binding energy of 4.6 eV. However, we have not detected such a metallic band in the BN film. In fact, the authors of Ref. [7] mentioned that the use of the local-density approximation underestimates the values of energy gaps. Furthermore, the

experimental values for the energy gap in the bulk BN measured by several methods well exceeded the calculated value[5,13-15]. Therefore, we conclude that the monolayer *h*-BN film on the Ni(111) surface is an insulating material with a band gap energy over 4.6 eV.

B. Dispersion curves of conduction-band structure

In Fig. 2, we plotted the energy positions of the observed secondary-electron peaks in the ARUPS spectra measured with the photon energy of 21.2 eV and the ARSEES spectra versus the wave vector parallel to the surface. Open and solid circles represent the data acquired from the ARUPS and ARSEES measurements, respectively. The theoretical conduction-band structure for the bulk *h*-BN is also indicated by shaded bands, where the broken curves represent the interlayer states[7]. Because of the monolayer thickness of the film, such interlayer states have not been observed, of course, in the present study. Note that among the band calculations listed in Table I, only the one of Ref. [7] is available for comparison with the experimental band structure over the wide energy range from the vacuum level to 22 eV above E_F. As shown in Fig. 2, the theoretical band structure corresponds well with the experimental data. Especially, the observed lowest branch is excellently reproduced by the calculation and, with the help of the theoretical work, the observed splitting of this branch for the $\overline{\Gamma}\,\overline{M}$ direction is explained as the σ-π splitting of the bands.

In Fig. 2, whole the theoretical conduction bands were shifted in order to make a good fit with the experimental data, namely, the theoretical conduction-band minimum was placed at the energy of 2.7 eV above E_F. Accordingly, the band gap in the monolayer *h*-BN film is roughly estimated to be $\sim$ 7 eV, since the experimental VM was found at the binding energy of 4.6 eV. Compared to the experimental values for the band gap in the bulk BN measured by several methods[5,13-15], which were in the range of 5-6 eV, the above estimated value seems to be somewhat large. This discrepancy might be due to the final-state effect in the ARUPS measurement; because a hole left after photoemission is not fully screened by conduction electrons in the insulating film, the binding energies of the valence bands tend to be overestimated. A similar mechanism has been employed to explain the difference in the value for the HOMO-LUMO separation of solid C_{60} between the band calculation and the experiments performed by using photoemission and inverse photoemission spectroscopy[16]. Therefore, we infer that the band gap in the monolayer BN film (E_G in eV) is $4.6 < E_G \lesssim 7$.

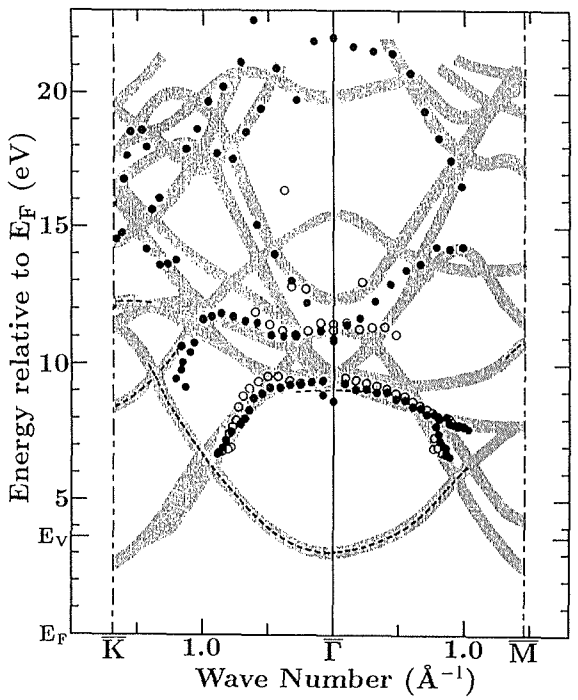

FIG. 2: Experimental conduction-band structure of the monolayer *h*-BN/Ni(111).

C. Comparison with monolayer graphite film

The present results on both the valence and conduction bands suggest that the electronic structure of the monolayer BN film is very similar to that of the bulk BN, implying the weak interaction between the film and the metal substrate. In fact, as shown in Fig. 1, the binding energies of the valence bands of the BN film are deeper than those of the d bands of the substrate by, at least, 2 eV. Because of this difference in energy, mixing of the electronic states of the overlayer with those of the substrate seems unfavorable. To gain a better understanding of the interfacial bonding between the overlayer and the metal surface, a comparison between the band structures of the monolayer BN/Ni(111) system and the MG/Ni(111) system is of great value.

Figure 3 shows the experimental band structure of the MG/Ni(111) system. A branch due to the emission of the secondary electrons[17] is indicated by the shaded band with vertical lines. The broken curves indicate the corresponding experimental band structure of bulk graphite[18]. The observed band structure of the MG is different from the bulk one for the following two features. First, while the σ bands of the MG agree fairly well with those of the bulk graphite, the π band of the MG lies at a much higher binding energy than the bulk one does. Second, as for the isolated monolayer graphite film, the unoccupied anti-bonding π^* band is connected with the π band at the $\overline{K}$ point[19]. Consequently, it may well be supposed that in the MG on the Ni(111) surface, the partially filled π^* band could be observed since the π band has the binding energy of 2.8 eV at the $\overline{K}$ point as shown in Fig. 3. However, such a connection of the conduction band with the π band at the $\overline{K}$ point has not been observed for MG/Ni(111). Instead, in the second Brillouin zone, we have detected one branch connected with the π

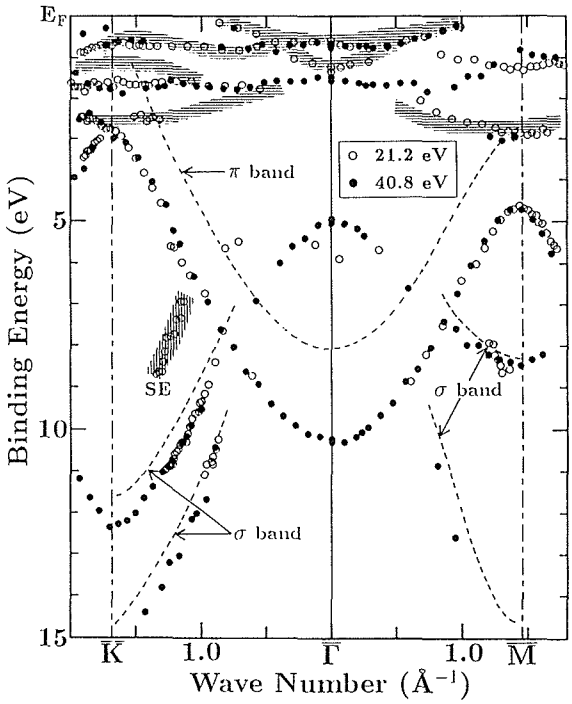

FIG. 3: Experimental band structure of the MG/Ni(111).

band at the $\overline{K}$ point, which could be a vestige of the severely deformed π^* band. Indeed, from the recent band-structure calculations of MG formed on the Ti-terminated TiC(111) surface, Kobayashi *et al.* have pointed out that the π^* band is drastically deformed by hybridization with the substrate[20]. Therefore, it is concluded that the π states, especially those with the energies near E_F, are hybridized with the d states of the substrate, which leads to the formation of the covalent bond between the overlayer and the metal substrate.

This hybridization has also changed the dispersion of the energy bands of the substrate. In Fig. 3, the shaded bands with horizontal lines represent the dispersion of the clean Ni(111) surface observed with a photon energy of 21.2 eV. Although some branches of clean Ni(111) agree with those of MG-covered Ni(111), the one along $\overline{\Gamma}\,\overline{K}$ at the energy of ~ 2 eV has disappeared upon the formation of the graphite overlayer and an almost flat branch has appeared instead. This is additional evidence that the mixing of the states with similar energies has taken place between the MG and the metal surface. Compared to this result, the difference in the band structure near E_F between the clean and BN-covered Ni(111) surfaces is small as shown in Fig. 1. Therefore, together with the fact that the observed band structure of the monolayer BN corresponds well with the theoretical one for bulk crystalline BN, we conclude that the bond between the BN film and the Ni(111) surface is weak compared to that between the MG and the same substrate.

III. SUMMARY

By using ARUPS and ARSEES, we have investigated the electronic dispersion relations of single-crystalline monolayer BN formed on the Ni(111) surface. Of the five theoretical band structures[2,4-7], the one calculated by Catellani *et al.* has shown the best agreement with the present experimental band structure. This result demonstrates that the self-consistent band calculation with a sufficiently large basis set is necessary for describing precisely the electronic properties of the BN. The band gap in the BN film (E_G in eV) has been estimated to be $4.6 < E_G \lesssim 7$, which is comparable with the experimental values for the band gap in bulk BN reported so far. While the band structure of the MG has been deformed strongly from that of the bulk graphite by the mixing of the π states with the d states of the substrate, such substantial mixing has not taken place in the BN/Ni(111) system, which is ascribed to the absence of electronic states in the BN film with energies near E_F. Therefore, it is concluded that the bond between the BN film and the Ni(111) surface is weak compared to that between the MG and the same substrate.

References

[1] E. Doni and G. Pastori Parravicini, Nuovo Cimento B **64**, 117 (1969).

[2] M. S. Nakhmanson and V. P. Smirnov, Fiz. Tverd. Tela (Leningrad) **13**, 3288 (1971) [Sov. Phys. –Solid State **13**, 2763 (1972)].

[3] R. Dovesi, C. Pisani, and C. Roetti, Int. J. Quantum Chem. **17**, 517 (1980).

[4] J. Zupan, Phys. Rev. B**6**, 2477 (1972).

[5] A. Zunger, A. Katzir, and A. Halperin, Phys. Rev. B **13**, 5560 (1976).

[6] J. Robertson, Phys. Rev. B **29**, 2131 (1984).

[7] A. Catellani *et al.*, Phys. Rev. B **36**, 6105 (1987).

[8] A. Mansour and S. E. Schnatterly, Phys. Rev. B **36**, 9234 (1987).

[9] E. Tegeler *et al.*, Phys. Stat. Sol. (b) **91**, 223 (1979).

[10] J. Barth, C. Kunz, and T. M. Zimkina, Solid State Commun. **36**, 453 (1980).

[11] A. Nagashima, N. Tejima, and C. Oshima, Phys. Rev. B**50** (to be published).

[12] A. Nagashima *et al.*, Phys. Rev. B**51** (to be published).

[13] U. Büchner, Phys. Status Solidi B **81**, 227 (1977); C. Tarrio and S. E. Schnatterly, Phys. Rev. B **40**, 7852 (1989).

[14] W. Baronian, Mater. Res. Bull. **7**, 119 (1977).

[15] M. R. Vilanove, C. R. Acad. Sci. Ser. B **272**, 1066 (1972); D. M. Hoffman, G. L. Doll, and P. C. Eklund, Phys. Rev. B **30**, 6051 (1984).

[16] T. R. Ohno *et al.*, Phys. Rev. B **44**, 13747 (1991); T. Takahashi *et al.*, Phys. Rev. Lett. **68**, 1232 (1992).

[17] A. Nagashima *et al.*, Phys. Rev. B **50**, 4756 (1994).

[18] T. Takahashi, H. Tokailin, and T. Sagawa, Phys. Rev. B **32**, 8317 (1985).

[19] G. S. Painter and D. E. Ellis, Phys. Rev. B **1**, 4747 (1970).

[20] K. Kobayashi and M. Tsukada, Phys. Rev. B**49**, 7660 (1994).

HRTEM of Grain Boundaries in the Diamond Thin Film

*Yaogang Zhang, Hideki Ichinose, Yoichi Ishida and Megumi Nakanose**
Department of Material Science, University of Tokyo, Tokyo, Japan
*Aerospace Division, Nissan Motor Co., Tokyo, Japan

Abstract

Σ 9 tilt boundaries in diamond thin film were investigated by HRTEM. {114} Σ 9 boundaries were more frequently observed than {221} and {115}/{111} Σ 9 boundaries. The latter two often appeared to be joint sections. Both equilibrium grain boundary energy and the local growth geometry determine the characteristic atomic structures of diamond grain boundaries.

INTRODUCTION

Although the grain boundaries in Si and Ge have been well studied[1], the knowledge of that in diamond is still far from complete. Some HRTEM observations have revealed the predominance of twin boundaries in diamond which is similar to that in Si and Ge[2, 3]. The quite different features were also observed[4]. In the present paper we will report some results of observation on Σ 9 tilt boundaries in diamond thin films by HRTEM and discuss their stability in relation not only to the equilibrium grain boundary energy but also to the local growth geometric condition.

EXPERIMENTAL

Diamond thin films are grown on the polished silicon substrates kept at high temperature by chemical vapor deposition. Crystal surface of the silicon substrates are chosen to be (110).

Obtained thin film is polycrystalline several micro meter in thickness. Silicon substrate is chemically dissolved to remove the film. the removed film is fixed on the stainless steel ring of 50 micro meter in thickness and 3 mm in diameter and then thinned by ion milling down to 10nm in thickness.

JEM-4000EX (Cs=1.0mm, Cc=0.7mm) high resolution electron microscope is employed for high resolution lattice imaging. High resolution observation is done at the condition of $\triangle E/E=2\times10^{-6}$ and mainly $\triangle F$=-48nm corresponding to the Schertzer focus condition.

RESULTS AND DISCUSSION

Figure 1 and Figure 2 show different kinds of Σ 9 CLS boundaries observed in diamond thin films. The geometrical atomic structure models are also showed in the respect figures.

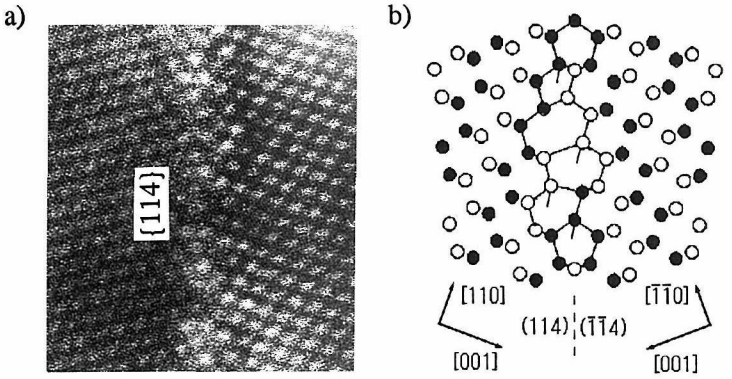

Figure 1. a) The lattice image of {114} Σ 9 grain boundary observed in diamond thin film and, b) its atomic structural model. The structural units consist of five-, six-, and seven-membered rings which contain at least one unbonded sp^3 orbital which is shown as broken bar.

In Figure 1 the symmetrical Σ 9 boundary (relative rotation angle θ =141.1°) is parallel to {114} plane. The structural units consist of five-, six-, and seven-membered rings which contain at least one unbonded sp^3 orbital respectively. Figure 2 has two sections of Σ 9 boundaries (θ =38.9°). One is

symmetric and parallel to {221} plane. Its structural units consist of 5- and 7- membered rings without unbonded sp^3 orbital as proposed by J.Hornstra for silicon[5]. The other, however, is asymmetrical and parallel to the {111} plane in the grain of one side and {115} in the other side. Its structural units consist of 5-, 6-, and 7-membered rings containing at least one unbonded sp^3 orbital in each ring which is similar to the case in {114} Σ 9 boundary.

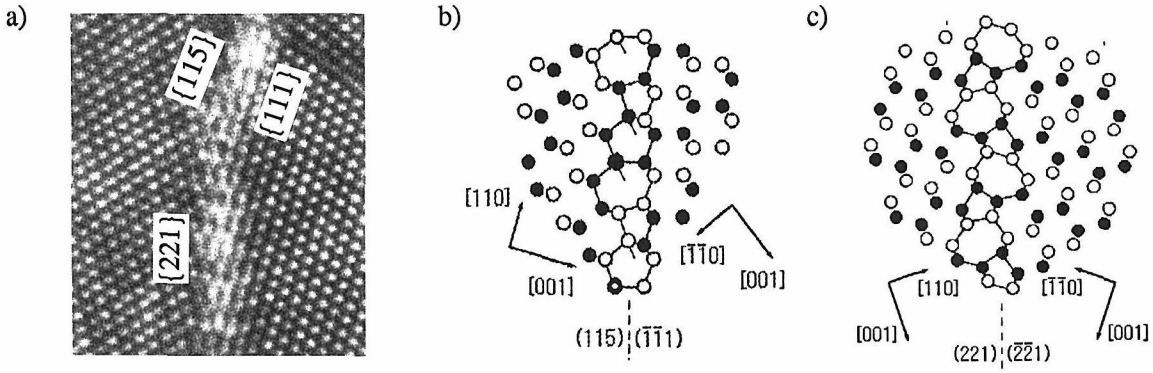

Figure 2. a) Lattice images of {115}/{111} and {221} Σ 9 grain boundaries observed in diamond thin film. b) Atomic structure models of {115}/{111} Σ 9 grain boundary. c) Atomic structure models of {115}/{111} Σ 9 grain boundary. The detail was described in text.

There are two points to be noted. One is that {114} Σ 9 grain boundaries are more frequently found than {221} Σ 9 grain boundaries in diamond thin films. The other is that symmetrical {221} Σ 9 boundary is connected with asymmetrical {111}/{115} Σ 9 boundary even though their structural units are totally different. Both of these features cannot be explained by the "least dangling bonds rule".

There are several possibilities that can be account for the above observed features. One is that all the dangling bonds are reconstructed[6] in {114} and {111}/{115} Σ 9 grain boundaries and give equivalent energy with that of {221} Σ 9 boundary which contains no gangling bond. The second is that some carbon atoms would take three sp^2 and one p_z orbital instead of four sp^3 to avoid dangling bond by forming π bonding which would lower the boundary energy greatly. And more likely, the above two mechanisms may work together to make the boundary energy lower.

In addition to the usual consideration of equilibrium boundary energy, the local growth geometric condition of grain boundary is worth to be taken into account.

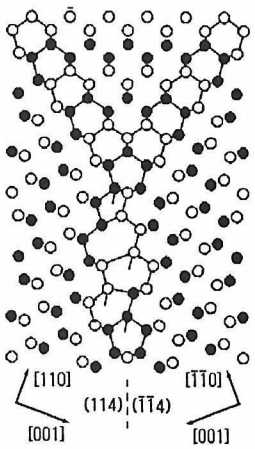

Figure 3. Local growth geometry of {114} Σ 9 boundary formed by meeting of two {111} Σ 3 twin boundaries.

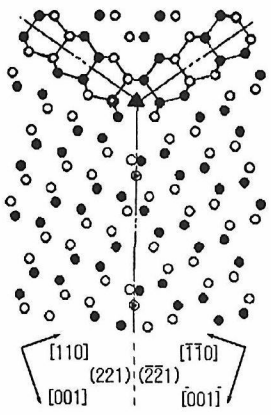

Figure 4. Local geometry of two {111} Σ 3 twin boundaries met by an angle of 109.5° . Asymmetrical 6-membered ring produced at meeting point implies asymmetrical structure of Σ 9 boundary.

As shown in Figure 3, two {111} Σ 3 twin boundaries meeting by 70.5° form a {114} Σ 9 boundary (θ =141.1°) readily. But in Figure 4, asymmetrical atomic arrangement is produced by meeting of two

{111} Σ 3 twin boundaries with an angle of 109.5° . The bisecting plane is not a mirror plane and {221} grain boundary cannot form on it unless rigid translation along <110> or <114> occurs which would introduce dislocations at triple point or distortions on Σ 3 twin boundary and both would increase energy greatly for diamond.

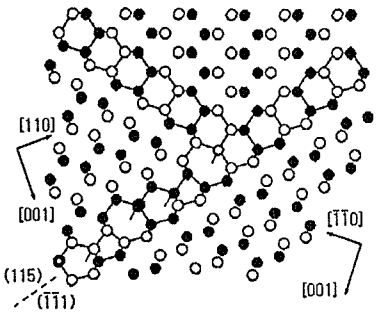

Figure 5. Local growth geometry of {115}/{111} Σ 9 boundary.

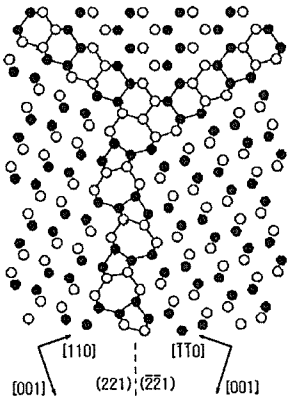

Figure 6. Local growth geometry of {221} Σ 9 boundary.

A more smooth way to produce a {221} Σ 9 boundary we proposed is as follow. Supposing another boat-shaped 6-membered ring is formed at triple point which will introduce an dangling bond, as shown in Figure 5, an asymmetric {111}/{115} Σ 9 boundary can be formed readily succeeding this 6-membered ring. While keeping the first unit of 5- and 7-membered rings same, we can construct a boundary parallel to {221} plane as shown in Figure 6. It should be noted that the {221} Σ 9 grain boundary is asymmetric in atomic arrangement from its starting point and the dangling bond problem also involved at its formation stage. This local growth condition should be another factor responsible for the observed features of Σ 9 grain boundaries.

ACKNOWLEDGMENT

The present research are supported by the Foundation for Promotion of Material Science and Technology of Japan.

REFERENCES

1. J.Thibault, J.L.Rouviere and A.Bourret, in Materials Science and Technology, edited by R.W.Cahn, P.Hassen and E.J.Kramer (VCH, Weinheim, 1991), Vol.4, p.321.
2. J.Narayan and A.S.Nandedkar, Phi. Mag. B63, 1181(1991).
3. D.Shechtman, J.L.Hutchison, L.H.Robins, E.N.Farabaugh and A.Feldman, J. Mater. Res., Vol.8, No.3, 473(1993).
4. H.Ichinose, M.Nakanose, K.Itoh and Y.Ishida, to be published in the proceedings of the 3rd IUMRS International Conference on Advanced Materials, Tokyo, Japan, 1993.
5. J.Hornstra, Physica 25, 409(1959).
6. M.Kohyama, R.Yamamoto and M.Doyama, Phis. Stat. Sol. (b) 138, 387(1986).

HVEM Study on Microstructures of Polycrystalline Cubic Boron Nitride

Lian-Long He, Minoru Akaishi and Shigeo Horiuchi*

National Institute for Research in Inorganic Materials, Namiki 1-1, Tsukuba, Ibaraki 305, Japan

*On leave from Laboratory of Atomic Imaging of Solids, Institute of Metal Research
Chinese Academy of Sciences, Wenhua Road 72, Shenyang 110015, P.R. China

Abstract: The microstructure of the translucent polycrystalline c-BN prepared at high pressure and temperature was investigated using a high voltage electron microscope. Grain size of the c-BN is less than 0.5 μm. It increases slightly with the treating temperature. A large number of nano-twins might be formed during the phase transformation from h-BN to c-BN. Secondary twins are formed in the growth stage.

INTRODUCTION

Cubic boron nitride (c-BN) is the second hardest materials with zinc blende-type structure and can be synthesized from hexagonal boron nitride (h-BN) under the extremely high pressure and temperature [1,2]. Although the polycrystalline c-BN was already synthesized in the later 1950s' the mechanism of phase transformation has not yet been clear. At present, there are some different methods to synthesize c-BN from ambient pressure phase of BN such as pyrolytic BN [3] and rhombohedral BN [4]. The microstructures of c-BN have never been reported, although the investigation of the microstructures is necessary to understand superior physical properties of the polycrystalline c-BN and the mechanism of the phase transformation. In this paper, the microstructures of the c-BN phase, which was synthesized directly from h-BN without any addition, was studied using high voltage electron microscope (HVEM).

EXPERIMENTAL

The polycrystalline c-BN was synthesized using h-BN at high pressure of 7.7 GPa and high temperature of 1800-2150 °C for 20-30 min. According to X-ray diffraction the product was mostly c-BN [5]. In order to investigate by HVEM, discs with thickness of 0.2 mm were cut out with a diameter of about 3 mm and then lapped mechanically to less than 100 μm. These foils were further thinned to 20 μm by a dimpling machine and finally by an ion-milling machine. The foils were observed by a HVEM (model H-1500) at an accelerating voltage of 1000 kV with a resolution power of about 0.12 nm.

RESULTS AND DISCUSSION

Fig.1 shows a typical morphology of the c-BN synthesized at 2000 °C. Grain size is less than about 0.5 μm. Each grain is divided into several subgrains. The electron diffraction (ED) pattern (the insert) implies that this c-BN phase has weak texture. Fig.2 is an image and a corresponding ED pattern, demonstrating that there are a large number of thin twins formed during the phase transformation from h-BN to c-BN. Fig.3 is a high resolution (HR) image taken with the electron beam parallel to the [110] direction of c-BN. Each twin slice contains only several atomic planes, i.e. the appearing frequency is very high. The ED spots in Fig.2(b) also confirm the twinning. The diffraction streaks are excited along $\langle 111 \rangle^*$, due to the effect of the twinning. These nano-twins must have occurred during the starting stage of the phase transformation. This characteristic twin structure reveals that the twin formation plays an important role in the phase transformation from h-BN to c-BN. Details will be discussed elsewhere [6]. Fig.4 is a (110) HR image which shows a stacking fault left in c-BN (indicated by arrows).

Fig.5 shows a typical structure of the c-BN grain prepared at relatively high temperature (2000 °C). There are some thick twins, which mutually cross to each other. They must have been formed during the growth stage (indicated by single arrows). Fig.6 shows a structure image of these secondary twins. In the crossing region, some disorder state can be found.

CONCLUSIONS

(1). Grain size of the c-BN phase is less than about 0.5 μm. The grains are composed of subgrains. The grain size increases slightly with the heating temperature.
(2). A large number of nano-twins may be formed during the starting stage of the phase transformation.
(3). Secondary twins are formed in the growth stage.

ACKNOWLEDGMENT

We would like to express our thanks to Dr. S. Yamaoka for his advise.

REFERENCES:

[1]. R.H. Wentorf, Jr., J. Chem. Phys. **26**(1957), 956 .
[2]. F.P. Bundy and R.H. Wentorf, Jr., J. Chem. Phys. **38**(1963), 1144.
[3]. F.R. Corrigan & F.P. Bundy, J. Chem. Phys. **63**(1975), 3812.
[4]. A. Onodera, K. Ichinose, H. Yoshihara, H. Nakae, T. Matsuda & T. Hirai, J. Mater. Sci. **25**(1990), 4279.
[5]. M. Akaishi, T. Saton, M. Ishii, T. Taniguchi, S. Yamaoka, J. Mater. Sci. Let. **12** (1993), 1883.
[6]. S. Horiuchi, L.L. He and M. Akaishi. in preparation.

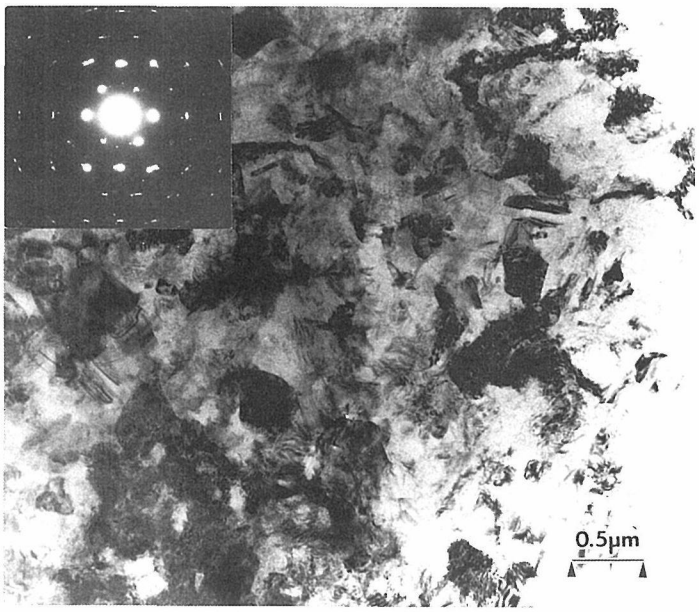

Fig.1 Typical morphology of the c-BN and the corresponding ED pattern.

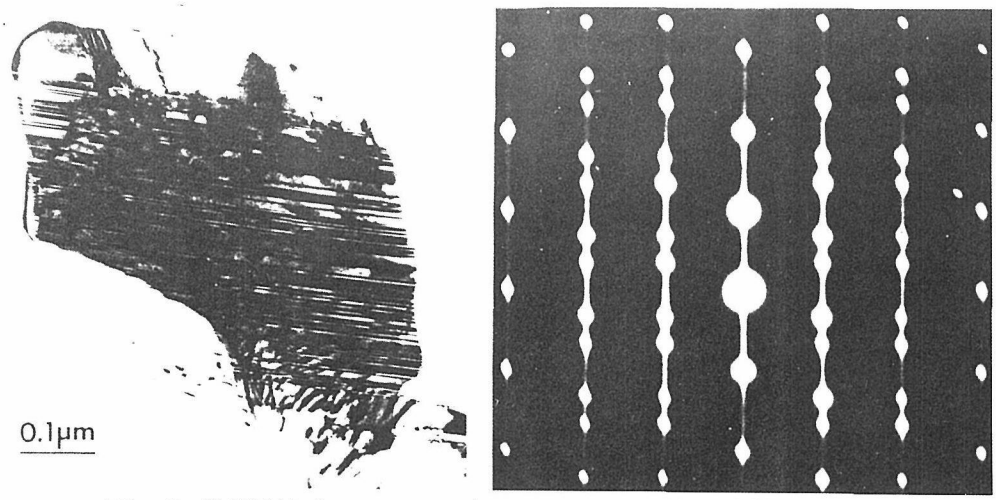

Fig.2 HVEM image and corresponding ED pattern, demonstrating a large number of thin twins.

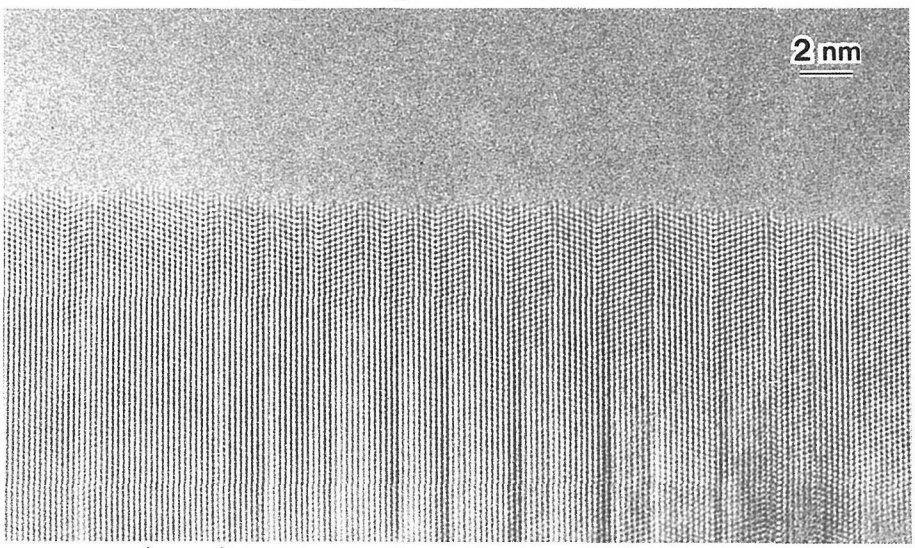

Fig.3 (110) HR image of c-BN showing nano-twins with thickness of several atomic planes.

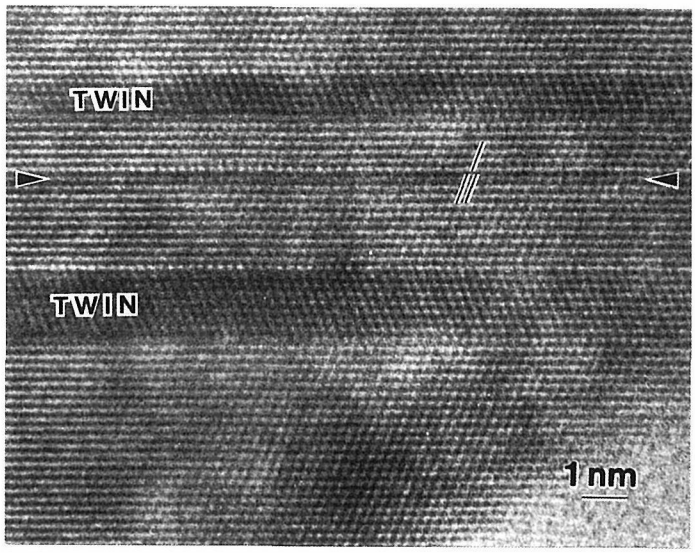

Fig.4 (110) HR image showing a stacking fault left in the c-BN.

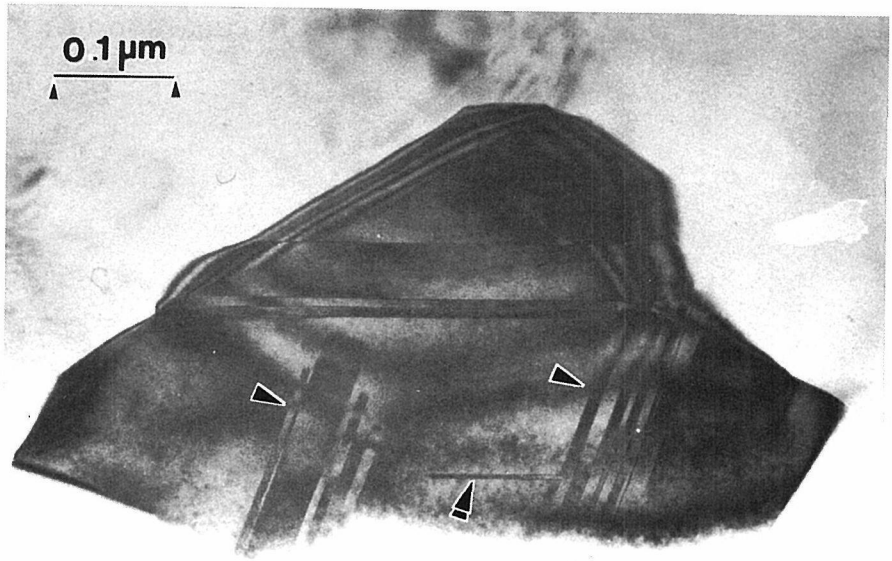

Fig.5 Typical structure of the c-BN grain with thick twins.

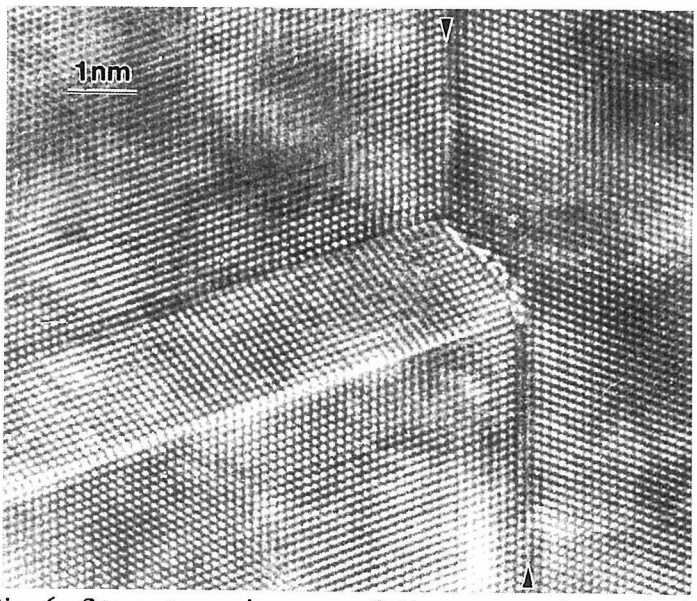

Fig.6 Structure image of the secondary twin.

HREELS of Diamond Oxidation Chemistry

Pehr E. Pehrsson and James E. Butler
Gas/Surface Dynamics Section, Code 6174
Naval Research Laboratory, Washington, DC 20375, U.S.A.

Abstract:

High resolution electron energy loss spectroscopy (HREELS) was used to obtain vibrational spectra from single crystal (100) diamond surfaces after oxidation, hydrogenation, and heating in ultrahigh vacuum (UHV). Complementary information was obtained with electron loss spectroscopy (ELS), low energy electron diffraction (LEED) and Auger electron spectroscopy (AES). The diamonds were hydrogenated in a microwave hydrogen plasma at 800°C, to produce a smooth, uniform, monohydrided surface. Activated oxygen generated with a heated Ir filament introduced carbonyl, ether (bridge-bonded) and hydroxyl groups onto both hydrogenated and reconstructed C(100) surfaces. The C=O stretch frequency increased with prolonged oxidation, possibly due to surface roughening and formation of higher oxidation states, e.g. carboxylic acid or carboxylic anhydride. Heating reduced the carbonyl and hydroxyl intensities more rapidly than the total oxygen concentration, suggesting that these groups desorbed first.

Introduction:

The chemistry between the diamond surface and hydrogen or oxygen has a profound influence on CVD diamond growth, and technologically significant properties such as electron emission[1], electrical conductivity[2], and metal contacts[3]. While progress has been made in understanding this chemistry, there is only limited data available on well-prepared and characterized low-index, single crystal surfaces. Such surfaces are critical in order to distinguish the chemistry of the low-index face from that of high-energy sites such as steps, ledges and defects. TPD and IR studies have been performed on diamond powders[4,5,6] and single crystal (100) faces[7,8]. Electron-based surface vibrational studies (HREELS) on single crystals by several workers[9,10,11,12,13,14] have primarily focussed on the hydrogen, and to a lesser extent, the oxygen chemistry. In this work, we prepared smooth, uniformly-terminated C(100) surfaces and examined their interactions with both molecular and filament-activated oxygen.

Experimental:

The four diamonds studied were semiconducting, type IIB natural diamonds, cut in the form of 4 x 4 x 0.25 mm plates polished to within 2° of the (100) face. The as-received samples were boiled for 15 minutes in 3 HCl: 1 HNO_3 and 15 minutes in 3 H_2SO_4: 2 HNO_3 and then immersed in 1:1:1 HF/HNO_3/acetic acid followed by a DI water rinse, in order to remove non-diamond, metal and Si/SiO_2 contaminants; the latter was a common contaminant on as-received diamonds. Auger electron spectroscopy (AES) and energy loss spectroscopy (ELS) verified that the acid oxidized the diamond surfaces and removed any non-diamond (sp^2 bonded) carbon and other contaminants. Heated crystals were allowed to cool to $T < 50°C$ before analysis began.

The diamond crystals were exposed to a hydrogen plasma in an microwave plasma reactor (Astex) operating at 600 W in 10 Torr of H_2, and T_{sub}=800°C for periods ranging from 30-120 minutes. This procedure has been shown to produce smooth, well-ordered, hydrogenated C(100)[13b].

At the end of the plasma treatment, substrate heating was discontinued, followed by the plasma when T_{sub}<600°C, and finally the hydrogen at T_{sub} <45°C. The samples were then inserted into the analysis chamber, usually within 30 minutes. One sample was treated in a D_2 plasma to test for exchange with hydrogen or oxygen in the air and pickup of hydrocarbon contaminants.

All experiments were performed in a stainless steel ultra-high vacuum (UHV) chamber (base pressure $<2 \times 10^{-10}$ Torr). The diamonds were held on a comparatively large Ta stud by spotwelding Ta wires across opposing corners of the crystal. The Ta stud was heated from the back by an electron beam heater. The diamond could thus be heated while it was dosed with oxygen or hydrogen, or to desorb surface species. The temperature of the stud was measured by optical pyrometry and by a thermocouple spot-welded to it. The 2 techniques generally agreed to within 20°, but both measured the temperature of the Ta stud, not the diamond.

Excited oxygen (hydrogen) was created by leaking 2×10^{-6} Torr of molecular oxygen (hydrogen) into the chamber via a leak valve while pumping the chamber with only a turbomolecular pump. The sample face was then rotated in front of and positioned 1cm from an Ir (W) wire resistively heated to 1050-1100°C (1400-1800 °C), as measured by optical pyrometry. There were no other line-of-sight hot filaments or other potential sources of activated species. The flux of atomic species emitted from the filament and striking the sample was unknown, but was assumed to be proportional to the molecular species flux measured in Langmuirs (L), where 1 L = 10^{-6} Torr-sec. In this paper, we describe exposures in the presence of a hot filament as O (H) exposures and exposures without a hot filament as O_2 (H_2) exposures. Absolute inter-apparatus exposure comparisons are impossible due to dosing geometry and filament temperature effects. However, exposures within a given experiment were directly comparable since the dosing geometry and filament temperature were unchanged. At the end of a dose, the sample heater was first turned off, then when the sample temperature had dropped below 200°C, the filament current was turned off, then finally the gas flow into the chamber. Samples heated without dosing were held at the desired temperature for 3 minutes.

Recent work[15] concludes that atomic oxygen creation on a hot Ir filament occurs only at temperatures high enough to simultaneously evaporate metal from the filament. Ir contamination did occur in some of our early experiments, so the filament temperature was subsequently reduced. In-situ AES and subsequent ex-situ XPS revealed no Ir conatmination at the lower filament temperatures, although activation of the oxygen continued, as evidenced by the heightened reactivity of the oxygen after exposure to the filament compared to unexcited molecular oxygen.

The HREEL spectra were acquired with a 127° cylindrical monochromator and analyzer (LK Instruments, Model LK2000). The incident electron beam had an energy between 10 and 12 eV and a direction 60° from the surface normal. All of the spectra discussed in this paper were acquired in both the specular scattering mode, and so are are governed by dipole selection rules[16], although the spectrometer analyzer is rotatable, and off-specular data were acquired. The chamber was also equipped with Auger electron spectroscopy (AES), secondary electron emission spectroscopy (SEES), electron loss spectroscopy (ELS) and low energy electron diffraction (LEED).

Results:

The hydrogen plasma-treated (100) surfaces exhibited a sharp,low-background two domain 2x1 LEED pattern with spots visible at incident electron energies as low as 14 eV, indicative of a smooth, well ordered surface[13b]. HREELS on these surfaces revealed intense features at 1225 ± 5 and 2920 ± 5 cm^{-1}, and broader features at 2440 ± 10 and 3660 ± 10 cm^{-1}, as shown in Figure 1. The LEED pattern from the plasma deuterated crystal was identical to that from the plasma

hydrogenated samples. However, the HREELS spectra had strong features at 698, 1157, 1332 and 2184 cm^{-1}, and weaker features at 837 and 1072 cm^{-1}. The 1225 and 2920 cm^{-1} modes observed on the plasma-hydrogenated surface were virtually absent (Figure 1). The Auger C-KLL lineshape and the ELS spectra of all of the plasma-treated crystals were characteristic of diamond[17]. The ELS spectra did not exhibit the feature at 6-7 eV from the main peak, which is attributed to a $\pi\pi^*$ transition accompanying formation of double bonds or aromaticity during graphitization or reconstruction.

Heating the hydrogenated crystals to 1100 °C weakened or eliminated the HREELS modes at 1225 and 2920 cm^{-1}, and generated a new mode at 725±20 cm^{-1}. The 698, 837, 1072, 1157 and 2184 cm^{-1} modes on the deuterated sample weakened or disappeared after annealing to $920<T_{sub}<1004$°C (figure 1). A large feature at 738±5 cm^{-1} emerged to dominate the spectrum, along with small features at 970±10cm^{-1}, 1157 and 1332 cm^{-1}. The 2x1 LEED pattern persisted on both the hydrogenated and deuterated samples, and the $\pi\pi^*$ mode in the ELS spectrum emerged.

Hydrogenated samples exposed to molecular oxygen exhibited no new HREELS modes nor AES O-KLL intensity at room temperature, but developed new HREELS features at 1460±10 and 1750±10 cm^{-1} when $T_{sub}\geq 500$°C. The temperature at which T_{sub} first causes these changes has not yet been determined. Based on the AES O-KLL/C-KLL ratio, the coverage attained on this surface after a 480 L exposure was roughly 0.1 ML[18].

Exposure to activated oxygen at $T_{sub}\geq 24$°C altered the HREELS spectra of the plasma-hydrogenated surfaces, both before and after heating to desorb surface hydrogen, by generating new features at 1720±10 and 3540±20 cm^{-1} and additional intensity from 800-1150 cm^{-1} . Individual modes in the latter region were difficult to distinguish from the other modes near 1225 cm^{-1} (figure 2). The 1720 cm^{-1} mode was distinct and shifted to higher frequency with continued oxidation, attaining a maximum value of about 1795 cm^{-1}. The modes at 1225 and 2920 cm^{-1} simultaneously diminished, and the frequency of the 2920 cm^{-1} mode increased to a maximum of 3030±10 cm^{-1}. The LEED pattern transformed to a 1x1 pattern as the 2nd order spots disappeared, while the minimum primary beam energy at which spots were visible increased to 45-60 eV, suggesting smaller surface domains and possible roughening. The AES O-KLL/C-KLL peak-to-peak height ratio saturated at 0.15 after doses totaling 1.7×10^4 L, corresponding to roughly 0.25 ML of oxygen[18]. The ELS spectrum was unchanged during the oxidation, with no strengthening of the $\pi\pi^*$feature.

Different hydrogenated crystals were exposed to O doses totalling 1.2×10^5 L at substrate temperatures ranging from 24°C to 500°C, as seen in figure 3. The HREELS spectra from the sample oxidized at 500°C had more intensity from 800-1150 cm^{-1} and less from 1720-1800 cm^{-1} than the sample oxidized at 24°C. The O-KLL/C-KLL ptp height ratios ranged from 0.12-0.15, or oxygen coverages of 0.2-0.25 ML[18].

Heating the oxidized crystals reduced and then eliminated the HREELS features at 800-1150, 1720, and 3540 cm^{-1}, although the intensity at 1720 and 800-1150 cm^{-1} sometimes persisted to T_{sub} > 975°C (figure 4). AES revealed that oxygen desorption occurred at $250<T_{sub}<975$°C. The intensity of the 1720 cm^{-1} mode diminished more rapidly upon heating than the O-KLL/C-KLL ratio for $350°C\leq T_{sub}\leq 550°$, but they diminished at approximately the same rate at $T_{sub}\geq$550-600°C. The peaks at 1225 and 2920 cm^{-1} reintensified as the modes associated with the oxygen exposure diminished. A feature at 715 cm^{-1} mode emerged as the 2920 cm^{-1} mode disappeared ($T_{sub}>920$°C). The LEED pattern returned to 2x1, but the 2nd order spots were usually not as bright as on the plasma-treated surface. The puck temperature sometimes exceeded 1100°C, yet the 2920 cm^{-1} mode persisted, while on other samples it disappeared entirely at $920<T_{sub}<1000$°C.

Discussion:

We believe the discrepancy between the desorption temperatures for deuterated and hydogenated surfaces, and the unexpectedly high oxygen desorption temperatures reflects inadequate

and irreproducible thermal contact between the sample and the Ta puck on which it sits. The absolute temperatures obtained are probably inaccurate, and should be used only to identify trends. More accurate temperatures may require insertion of a thermocouple into a hole bored directly in the crystal.

We assign the modes at 1225 and 2920 (940 and 2184) cm^{-1} to the C-H (D) bend and stretch, respectively, and the broad modes at 2440 and 3660 to the 1st and 2nd overtones of a lattice mode at 1220 cm^{-1}, in agreement with other workers[6,12,13]. The weak but persistent 1225 cm^{-1} feature on the deuterated surface heated to 1004°C is not attributable to the C-H bend and may be the abovementioned surface phonon. The C-H (C-D) stretch is symmetric, and composed of only one peak. If the (100) surface had dihydride moieties, or a significant density of edge sites, other peaks would appear[6]. Therefore, we conclude that the plasma hydrogenated (deuterated) surface is primarily the monohydride, i.e. one H atom per surface C atom[11,13c]. The large intensity ratio between the elastic peak and inelastic loss modes suggests that the surface is relatively smooth[13], consistent with the low minimum beam energy for LEED spots, and direct AFM evidence[19]. The lack of C-H or C-O modes on plasma deuterated crystals exposed to air confirms that the deuterated (and presumably the hydrogenated) (100) surface is stable to exchange with oxygen and hydrogen. The plasma-treated surface is smooth and uniformly terminated; a good platform for further chemistry, e.g. annealing or oxygen dosing.

The appearance of the 720 and 738 cm^{-1} modes upon heating of the hydrogenated or deuterated diamond surfaces to high temperatures coincided with the reduction or loss of the C-H and C-D HREELS modes and increased intensity in the $\pi\pi^*$ mode in the ELS spectra. Thus we attribute both the 720 and 738 cm^{-1} features to a surface phonon, probably associated with surface reconstruction and/or graphitization. The reason for the difference in their frequencies is unknown. The observed 2x1 LEED patterns accompanying these changes is consistent with surface reconstruction into π-bonded dimer rows following desorption of the hydrogen[13c].

Our AES-based estimates of 0.2-0.25 ML oxygen surface coverage at saturation are lower than the 0.5 ML values previously obtained by XPS this author and others, but this may reflect the fact that the AES ratios all come from samples oxidized in-situ, rather than exposed to air[20]. The authors have observed that samples exposed to air during or after oxidation adsorb water and other contaminants.

The 800-1150, 1720, and 3540 cm^{-1} HREELS features which develop after exposure to molecular oxygen at T_{sub}=500°C or activated oxygen at $T_{sub}\geq$24°C appear only when AES confirms the presence of surface oxygen, and are attributed to oxygen-containing surface moieties.. Based on general ranges for IR frequencies, molecular analogs, and frequencies calculated for diamond by other workers[7], we attribute the 800-1150, 1720, and 3540 cm^{-1} features to the ether-bonded stretch and/or the hydroxyl C-OH stretch, the carbonyl C=O stretch, and the hydroxyl O-H stretch, respectively. The 800-1150 cm^{-1} modes seem more likely to be associated with the ether-bonded oxygen, since O exposure at 500°C (figure 3) generates a surface with strong intensity in that range, but little intensity in the O-H stretch region (3540 cm^{-1}).

The increased C=O stretch frequency accompanying higher surface oxygen coverage was previously observed during DRIFTS experiments on diamond powders, and explained as the formation of more highly oxygenated carbon groups such as lactones, carboxylic acids and carboxylic anhydrides. Likewise, the frequency decrease during heating correlates with a lower oxygen concentration. The divergence in intensity of the HREELS 1720 cm^{-1} feature and the O-KLL/C-KLL ratio indicates preferential desorption of C=O groups (or possibly conversion to other groups) at T_{sub}<550°C, and confirms other observations during TPD[4] and DRIFTS[6] experiments on oxidized diamond powders. The numbers and energies of bond-breaking necessary for desorption also suggest that C=O groups desorb more readily than ether-bonded oxygen[7]. As discussed above, it is unlikely that the T_{sub}> 975°C apparently needed to eliminate all of the C=O HREELS intensity are

accurate.

The reappearance of hydrogen on the surface following the loss of oxygen may occur because oxygen desorbs as CO or CO_2[4], leaving highly reactive carbon groups on the surface which adsorb background gas in the chamber. Although the base pressure is $<2x10^{-10}$ Torr, the pressure rises into the 10^{-9} Torr range during high-temperature anneals; enough time to readsorb surface hydrogen during the 20-30 minute cooldown prior to acquisition of the HREELS spectra. We note that when the deuterated surface was annealed to 1004°C, removing all of the surface deuterium, the surface did not rehydrogenate for a period of days. Thus, heating an oxidized sample to temperatures high enough to desorb much of the oxygen but not the hydrogen generates a surface more reactive to hydrogen than either the hydrogenated surface or the hydrogenated surface after heating above the hydrogen desorption temperature.

The diminished sharpness of the LEED pattern after repeated oxidation and annealing or rehydrogenation cycles suggests gradual oxygen-induced surface roughening. The appearance of a mixture of different groups, (carbonyl, hydroxyl and ether-bonded oxygen) is consistent, and has been suggested previously by TPD data taken on single crystal (100) diamond[7].

Summary:

Plasma-hydrogenation smooths and uniformly terminates the C(100) surface with monohydride groups, creating a good surface for subsequent chemistry. Temperature measurement on such samples is still problematic and the absolute values obtained are probably unreliable. The hydrogenated surface is unreactive to molecular oxygen at 24°C, but does react at T_{sub}=500°C. Both the oxidized and hydrogenated surfaces react at $T_{sub}\geq$24°C and above with oxygen activated by a hot Ir filament. The oxidized C(100) surface contains a mixture of hydroxyl and/or ether-bonded, and various carbonyl-containing groups. Some of the C=O species preferentially desorb at T_{sub}<550°C, but some of both the carbonyl and ether-bonded groups persist to higher temperatures. The surface at least partially rehydrogenates after oxygen desorption, until T_{sub} exceeds the hydrogen desorption temperature, probably between 925 and 1000°C.

Acknowledgements: The authors thank J. Russell, B. Thoms, B. Mackey, and M. Owens for technical help and scientific discussions.

Figures:

Figure 1) HREELS of C(100) surfaces; a) plasma-hydrogenated (x0.33); b) plasma-deuterated; and c) heated to 1004°C (x0.33).

Figure 2) HREELS spectra of plasma-hydrogenated C(100) heated to 1100°C and then exposed to activated oxygen at T_{sub}=300°C; a) plasma hydrogenated; b) heated to 1100°C (x2); c) $2x10^3$ L (x0.2); d) $1.7x10^4$ L (x0.4); and e) $2.8x10^4$ L (x0.4).

Figure 3) HREELS spectra of C(100) oxidized with activated oxygen at a) plasma-hydrogenated (x3); b) 24°C (x0.8); c) 300°C (x2); and d) 500°C (x0.5). Total dose in each case was≈ $1.2x10^5$ L.

Figure 4) HREELS spectra of C(100); a) oxidized with activated oxygen and then; b) heated to 550°C; c) 750°C (x0.6); d) 975°C (x1.5); and e) 1100°C (x2).

References:

1. P.E. Pehrsson, J.P. Long, J.E. Butler, M. Marchywka, submitted to Appl. Phys. Lett.
2. Y. Mori, H. Kawarada, A. Hiraki, Appl. Phys. Lett., 58(9), 940 (1991)

3. S.A. Grot, G.S. Gildenblatt, C.W. Hatfield, C.R. Wronski, A.R. Badzian, T. Badzian, R. Messier, IEEE Elect. Dev. Lett., 11(2), 100 (1990)
4. a) S. Matsumoto, H. Kanda, Y. Sato, N. Setaka, Carbon, 15, 299 (1977)
b) S. Matsumoto, N. Setaka, Carbon, 17, 485 (1979)
c) S. Matsumoto, Y. Sato, N. Setaka, Carbon, 19, 232 (1981)
5. R. Sappok, H.P. Boehm, Carbon, 6, 573 (1968)
6. a) T. Ando, M. Ishii, M. Kamo, Y. Sato, J. Chem. Soc., Far. Trans., 89(11), 1783 (1993)
b) T. Ando, K. Yamamoto, M. Ishii, M. Kamo, Y. Sato, J. Chem. Soc., Far. Trans., 89(19), 3635 (1993)
7. Thomas, Rudder and Markunas, J. Vac. Sci. Technol. A, 10(4), 2451 (1992)
8. L. M. Struck, M.P. D'Evelyn, J. Vac. Sci. Technol. A, 11(4), 1992 (1993)
9. B.J. Waclawski, D.T. Pierce,N. Swanson, R.J. Celotta, J.Vac. Sci.Tech., 21 (2), 368 (1982)
10. B. Sun, X. Zhang, Z. Lin, Phys. Rev. B, 47(15), 9816 (1993)
11. T. Aizawa, T. Ando, M. Kamo, Y. Sato, Phys. Rev. B, 48(24) (1993)
12. S. T. Lee, G. Apai, Phys. Rev. B, 48(4) (1993)
13. a) B.D. Thoms, J.E. Butler, Phys. Rev. B, 50(230, 17450 (1994)
b) B.D. Thoms, M.S. Owens, J.E. Butler, C. Spiro, Appl. Phys. Lett., 65(23), 2957 (1994)
c) B.D. Thoms, J.E. Butler, Surf. Sci., in press
14. M.N. McGonigal, J.N. Russell, Jr., P.E. Pehrsson, H.G. Maguire, J.E. Butler, J. Appl. Phys., in press
15. V.S. Smentkowski, J.T. Yates, Jr., J. Vac. Sci. Technol. A, 12(1), 219 (1994)
16. H. Ibach, D.L. Mills, "Electron Energy Loss Spectroscopy and Surface Vibrations", Academic Press, New York, (1982)
17. P.G. Lurie, J.M. Wilson, Surf. Sci., 65, 453 (1977)
18. B.B. Pate, Surf. Sci., 165, 83 (1986)
19. A. Joshi, K.V. Ravi, Proc. 3rd Intl. Mtg. on Dia. Mater., Honolulu, Ha, (ed. J.P. Dismukes, K.V. Ravi) V93-17, 613 (1993)
20. J.O. Hansen, T.E. Derry, P.E. Harris, J.P.F. Sellschop, R.G. Copperthwaite, "Ultrahard Materials Applied Technology" V4, (ed. C. Barrett), DeBeers Ind. Diamond Div., London, (1988)

Figure 1)

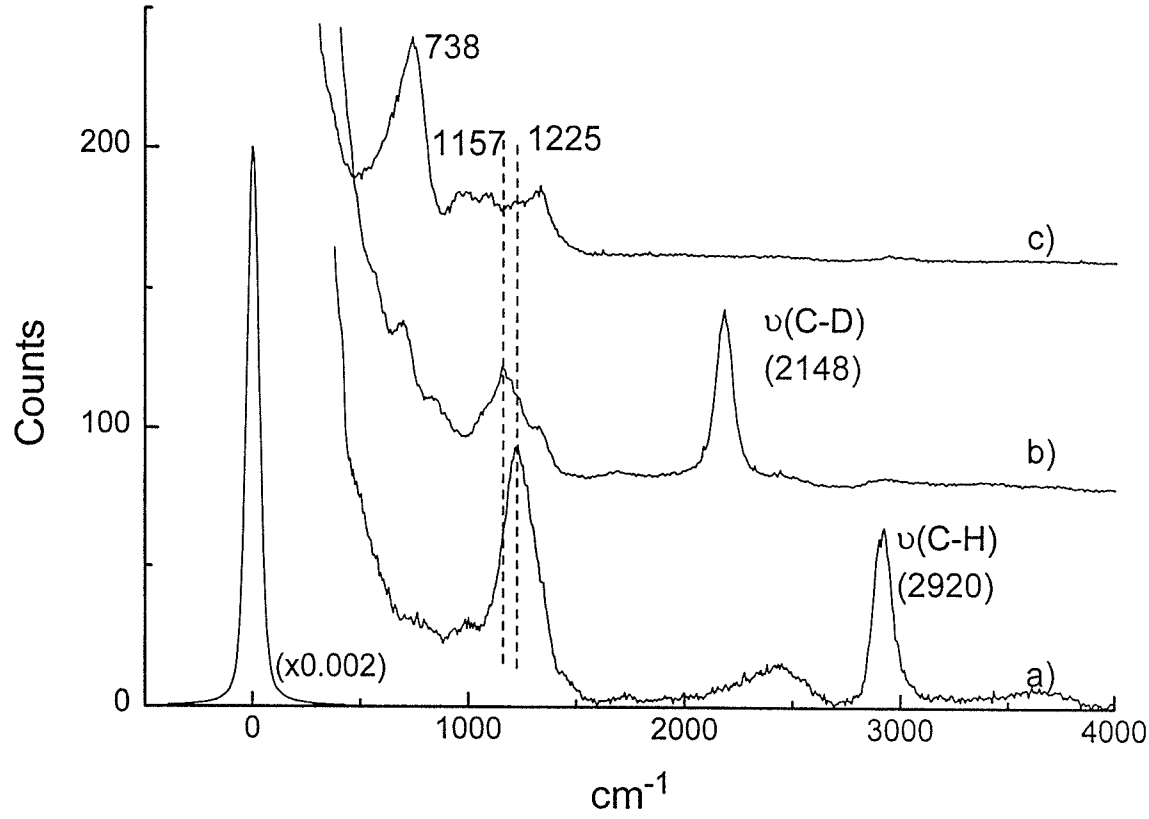

Figure 2)

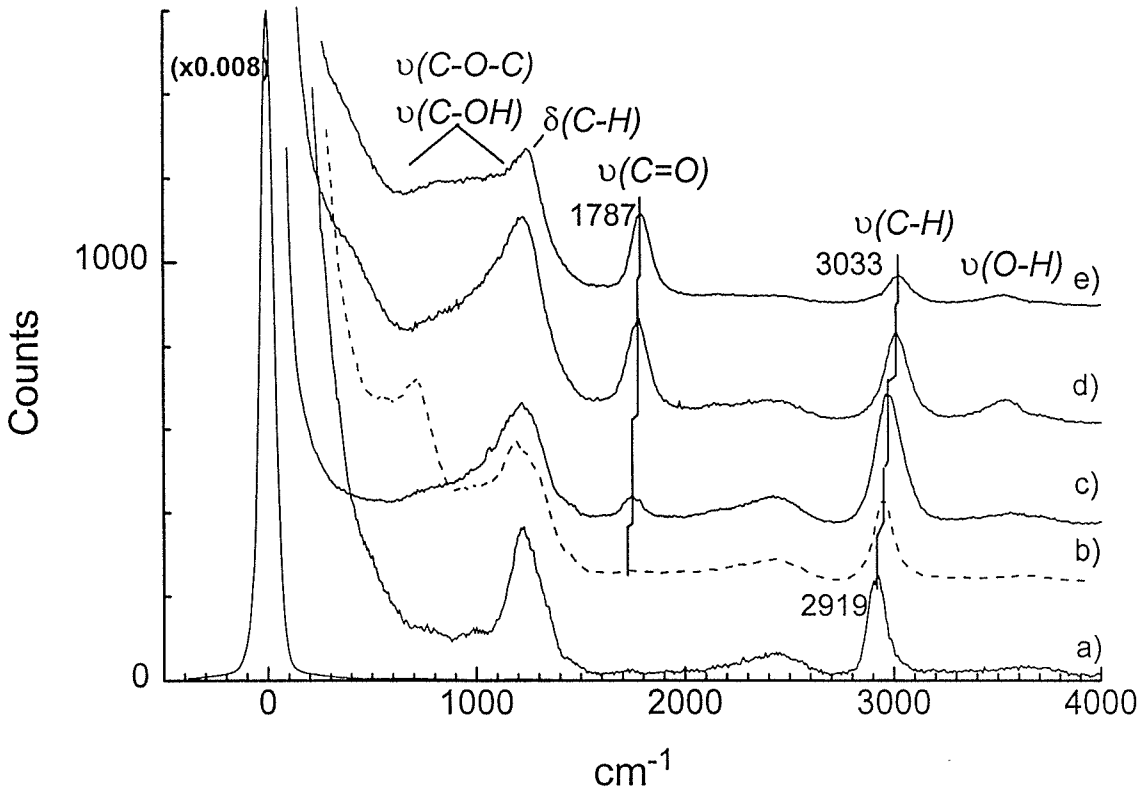

Figure 3)

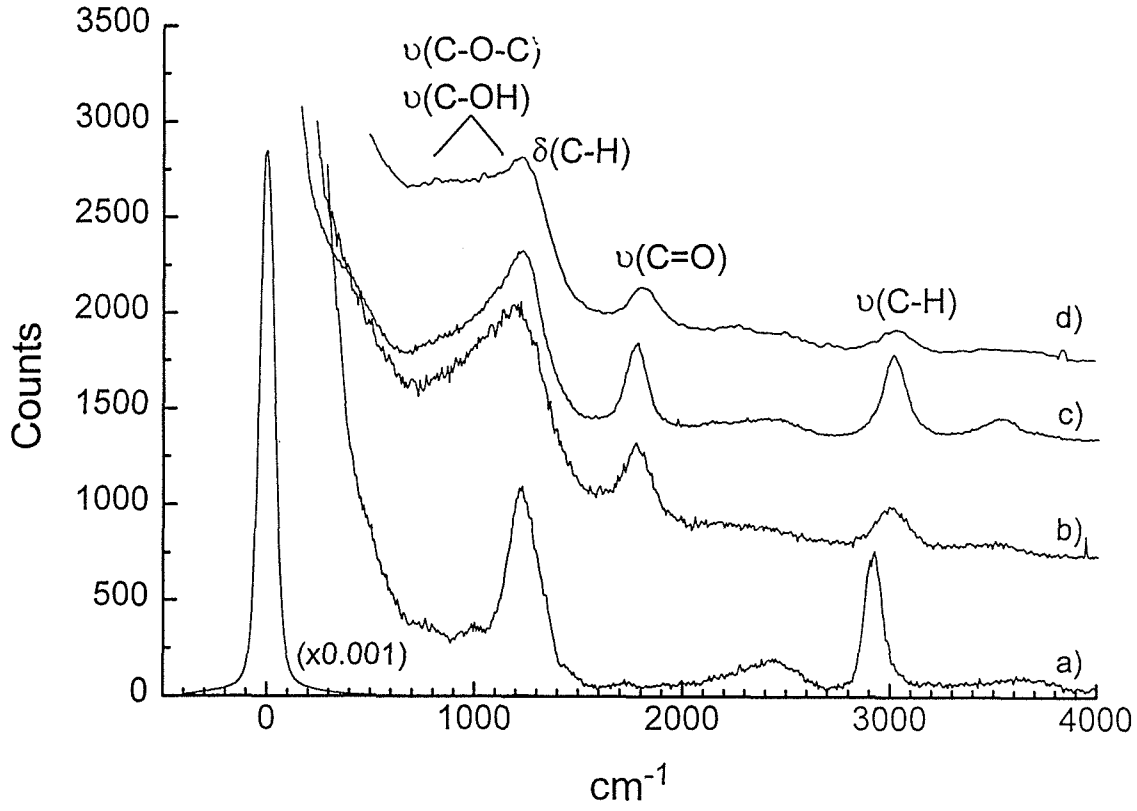

Figure 4)

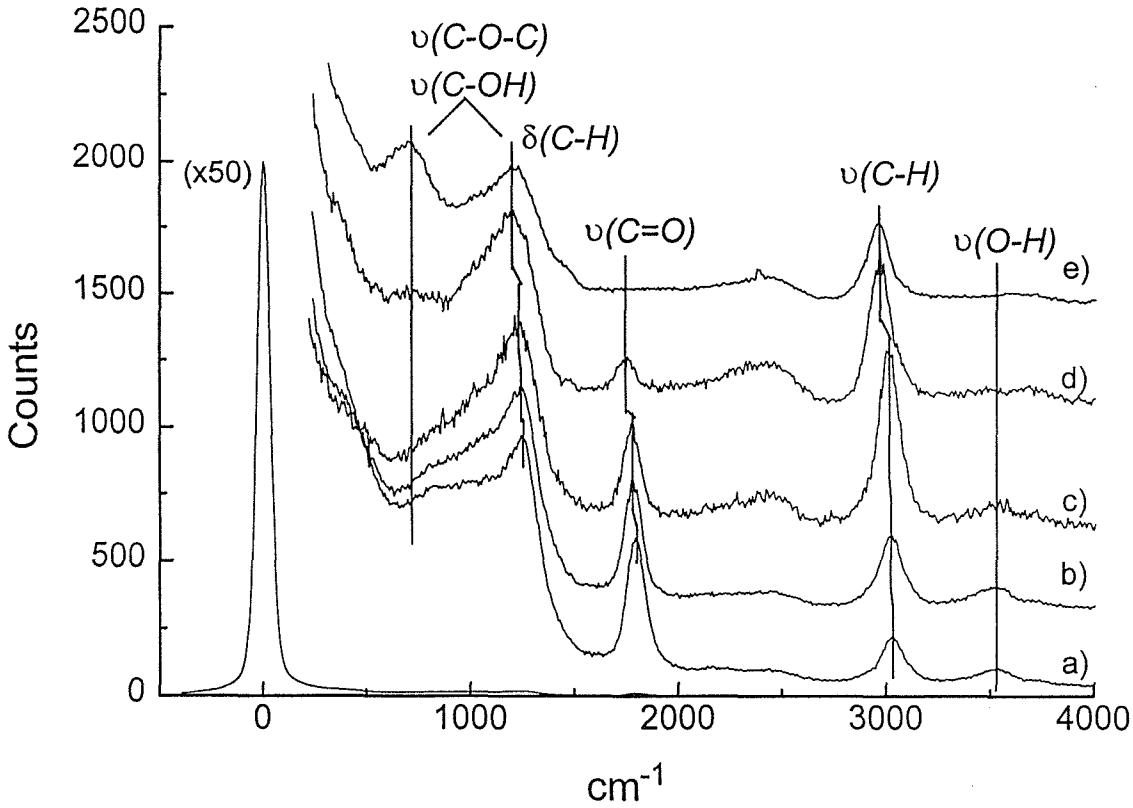

Growth Property of Diamond Epitaxial Films

Takashi Tsuno and Naoji Fujimori
Itami Research Laboratories, Sumitomo Electric Industries
1-1-1 Koyakita, Itami, Hyogo 664, Japan

Abstract

The surface observation using scanning tunneling microsopy (STM) and electron diffraction was carried out for the diamond epitaxial film grown (001), (111), (110) substrates and misoriented (001) substrates. The images with atomic order resolution were obtained by STM. The growth properties of these epitaxial films and the effect of methane concentration during growth were considered from these observations.

1. INTRODUCTION

For the further understanding of the diamond growth by chemical vapor deposition (CVD)[1-3] , the observation of the growth surface can give essential information. The observation with atomic scale resolution are desirable in order to know the growth characteristic and the factors important for the growth, because the crystal growth does take place via incorporation of atoms. Scanning tunneling microscopy (STM) is thought to be one of the most successful methods for surface analysis because of its atomic resolution and it has been applied for diamond in many cases.[4-10] In this paper, we report on the surface observation and the suggested growth properties of (001), (111) and (110) epitaxial films.

2. EXPERIMENTAL

The substrates for epitaxial growth were type Ib synthesized diamond with an area of 2mm x 1.5mm or 2mm x 5mm and 0.3mm thick. The growth was carried out by micro-wave plasma assisted CVD[3] with NIRIM-type reactor. Methane and hydrogen were introduced into the reactor and diborane was also add for the B-doped films.

After the growth, the samples were taken out from the reactor into the normal atmosphere and moved to the characterization system. The surface observation was carried out using low energy electron diffraction (LEED) and STM, both in air and in ultra high vacuum (UHV). Even the un-doped epitaxial films are conductive in air and the STM observation was possible. The specimens for UHV-STM were the B-doped films and the sample annealing was carried out by direct current through the epitaxial layer.

The growth rate was estimated by the observation of the cleaved section and its dependence on the substrate off-angle and methane concentration was investigated.

3. RESULTS AND DISCUSSION

3-1. Surface structure

Figures 1(a) and (b) shows STM images of epitaxially grown diamond(001) surface. Many rows are seen along two directions that are perpendicular to each other. The distance between the adjacent rows is 0.5nm corresponding to 2x1 structure. The atomic configuration of the 2x1 structure is considered to be a dimer-type reconstruction with hydrogen adsorption as shown in Fig. 2. This surface structure reduces dangling bonds by bonding of adjacent dangling bonds and hydrogen adsorption. In Fig. 1(a), significant extension of dimer rows is seen. Only single dimer row extends onto the lower terraces. There exist two types of mono-atomic steps on diamond(001), S_A steps and S_B steps.[11] S_A steps are straight, while S_B steps are rugged due to the extension of the dimer rows as observed in Fig.1(b).

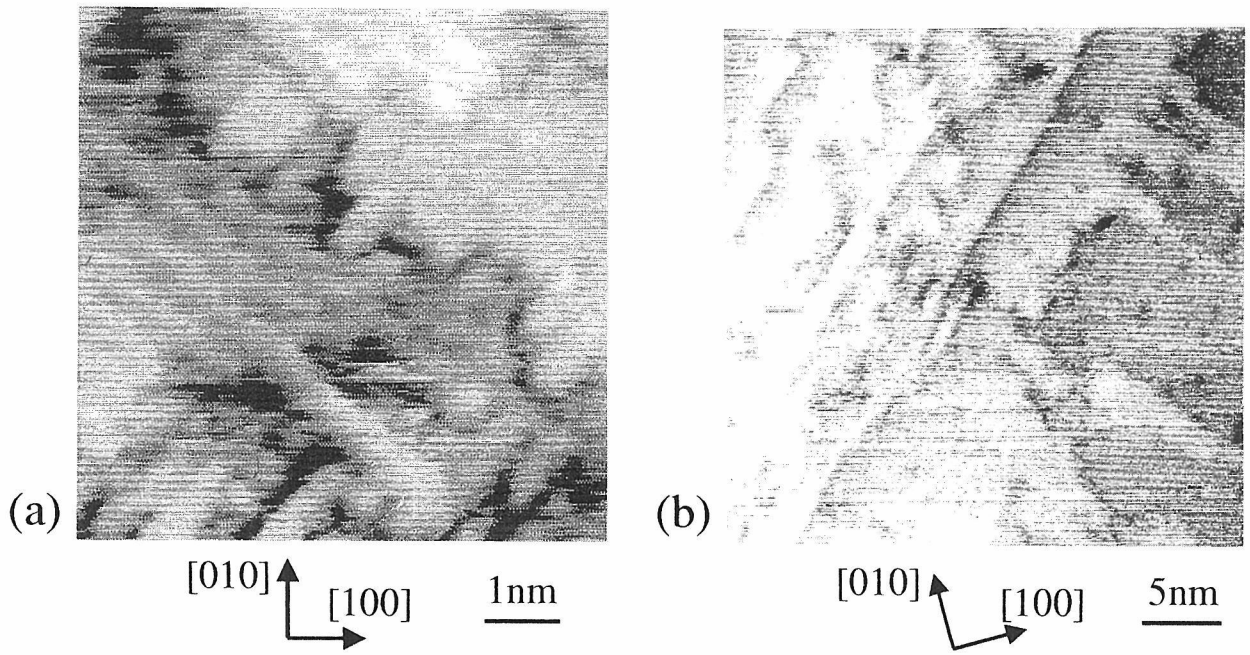

Fig. 1 STM image of diamond(001) epitaxial film.

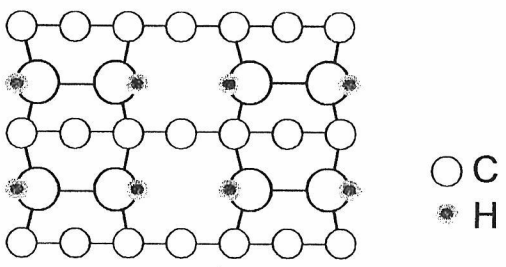

Fig. 2 Structure of diamond(001) 2x1-H

The 2x1 reconstruction was confirmed by UHV-STM observation too. Fig. 3(a) and (b) show images of the B-doped homo-epitaxial film after the sample was degassed at 400°C. These images show straight S_A steps and rugged S_B steps again. In Fig.3(a), it is found that the length of dimer rows differ mainly by even number of dimers, showing two dimers form the gorwth unit.

The images obtained after annealing at 900°C and 1000°C is shown in Fig. 4(a) and (b). Though Fig. 4(a) shows 2x1 reconstruction, the tunneling spectra for this images are quite different from those for Fig. 3(a) and (b). We consider that Figs. 3 represents the hydrogen-terminated dimer structures as same with as-grown surface. On the other hand, Fig. 4(a) shows the dimer without hydrogen adsorption. After annealed at 1000°C , we could not observe STM image with atomic resolution (Fig. 4(b)) and LEED did not showed clear pattern.

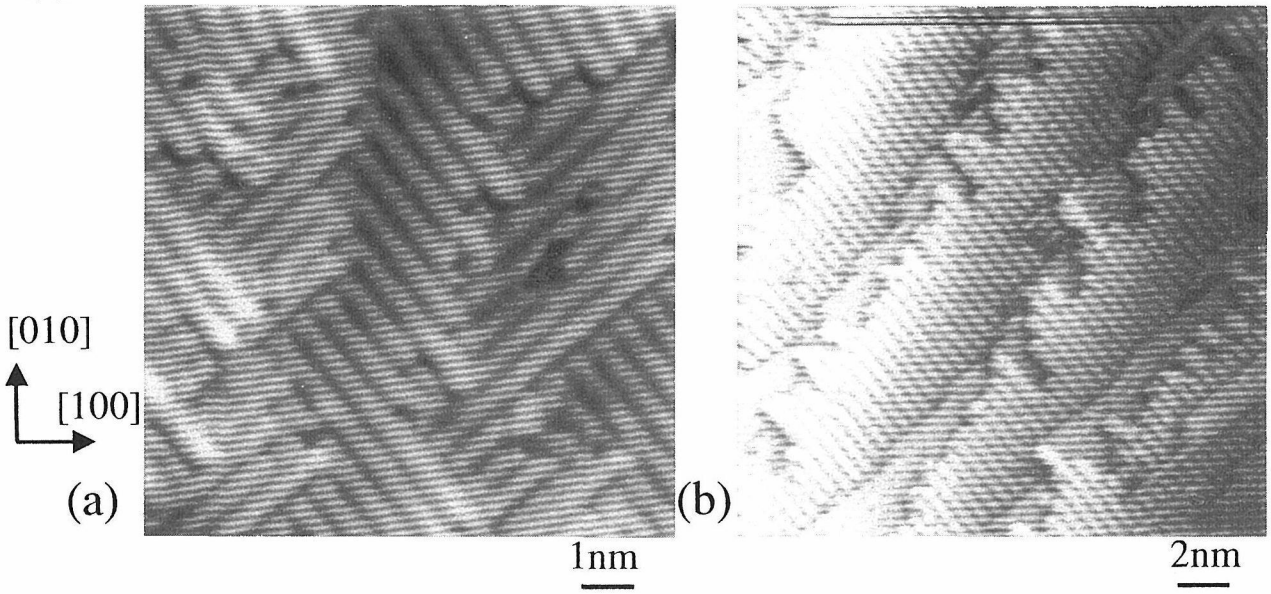

Fig. 3 STM image of diamond(001) epitaxial film.

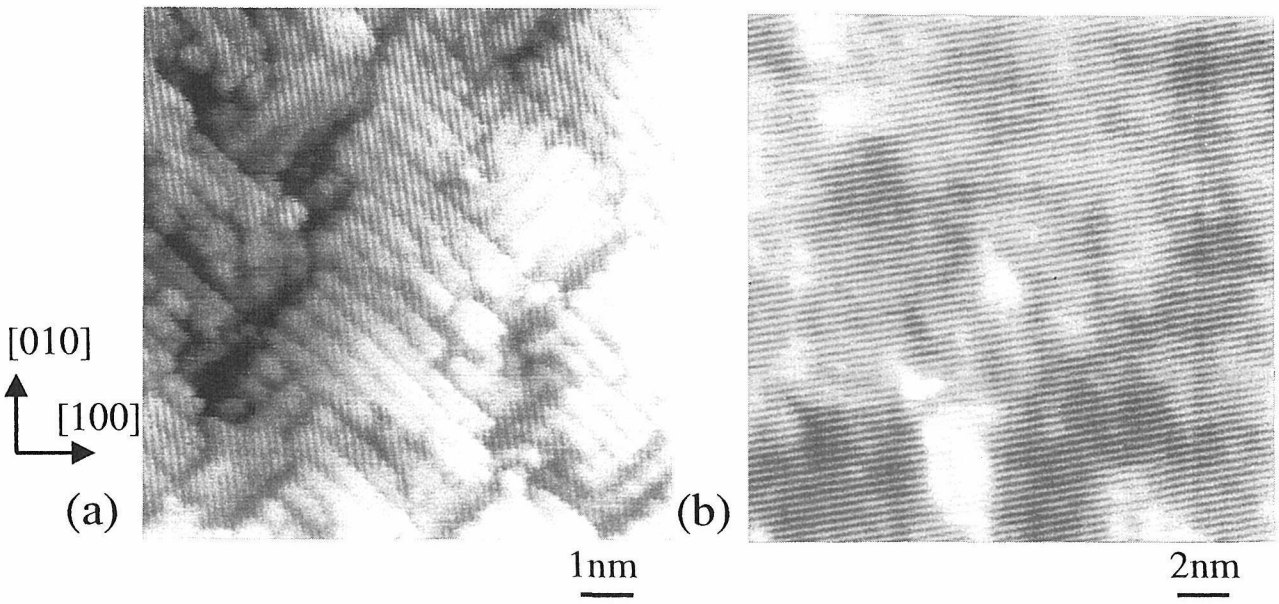

Fig. 4 STM image of diamond(001) epitaxial film after annealed at (a) 900 C and (b) 1000 C.

Figures 5(a) and (b) are STM images of the (111) epitaxial film, which showed 1x1 LEED pattern. The surface was macroscopically much rougher than the (001) and triangular structures were observed as shown in Fig. 5(a). However, flat terraces were observed on the top of the triangular structure and 1x1 priodicity was confirmed. (Fig. 5(b)) The majority of the observed steps were bi-layer steps in the <112> direction. These steps showed very straight on atomic scale and kinks of 1x1 units were observed at intervals of more than several 1nm. These results suggest that the steps are very stable and that bi-layer kink growth takes place at the step.

The (110) face is not observed in diamond particles grown by CVD. It was reported that the (110) epitaxial films were very rough after the observation by Nomarski microscopy and reflection high energy electron diffraction. This STM study also showed the very rough surface for the (110) epitaxial films. Almost no areas of flat (110) faces are observed in Fig.6, but narrow islands were found to extend in the [110] direction. The inclination of the face of these islands was found to be in the range from 30° to 40° away from the substrate, which coincides with the angle formed by {110} and {111}, 35°. This indicates that the growth on (110) substrate makes two inclined {111} surface.

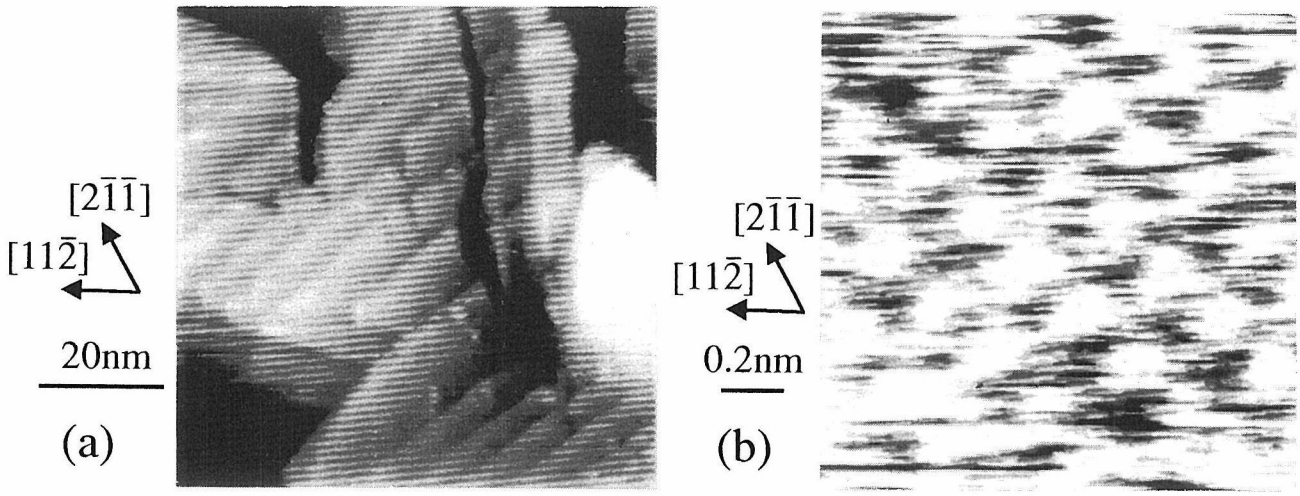

Fig. 5 STM image of diamond(111) epitaxial film.

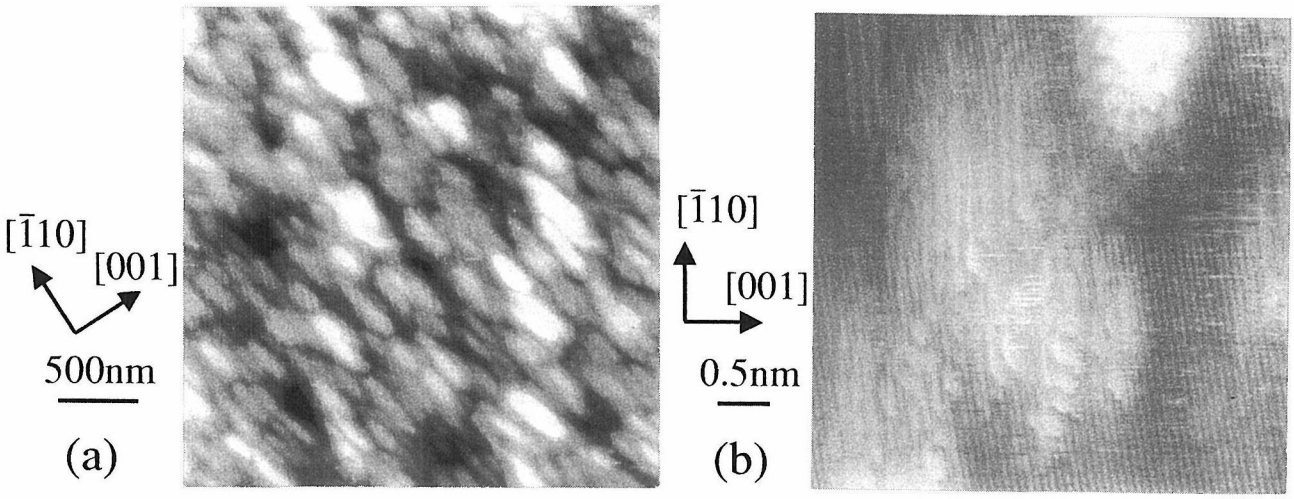

Fig. 6 STM image of diamond(110) epitaxial film.

3-2 Growth on misoriented substrate

Single-domain 2x1 surface of MBE-grown Si(001) is well known to be formed on vicinal surface.[13] We carried out the epitaxial growth on misoriented diamond (001) substrates. The LEED pattern of the sample grown on 4.3° misoriented substrate with the methane concentration of 2.0 % is shown in Fig. 7. The superstructure spots from one domain are far brighter than those from another domain, suggesting a nearly perfect single-domain 2x1 surface. The STMimage in Fig 8 showed that the bi-atomic height steps are formed all over the image.

It is considered that the step-flow causes the single-domain surface, because the step-flow rate of S_B is higher than that of S_A. On the other hand, growing with 6% methane concentration on the substrates with the very same misorientation, the double-domain and rougher surface was observed by STM. These results is explained by assuming the higher 2-dim. nucleation rate during the growth with the higher methane concentration.

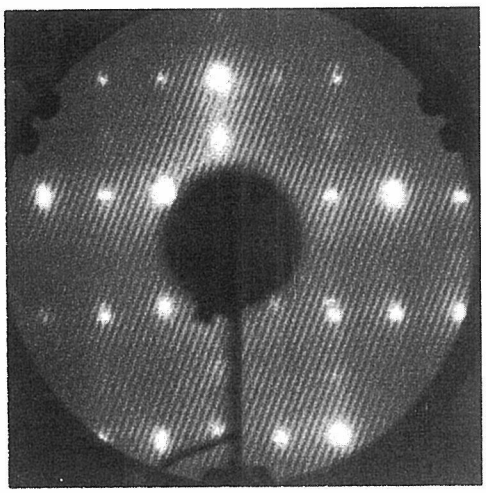

Fig. 7 LEED pattern of diamond(001) single-domain 2x1 surfcae.

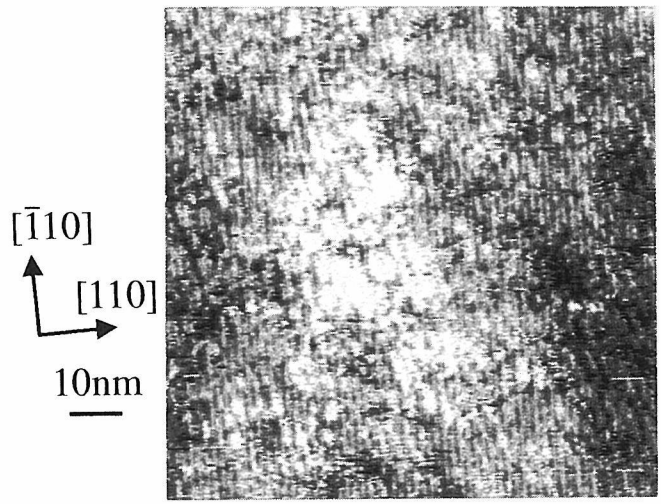

Fig. 8 STM image of diamond epitaxial film grown on misoriented (001) substrate.

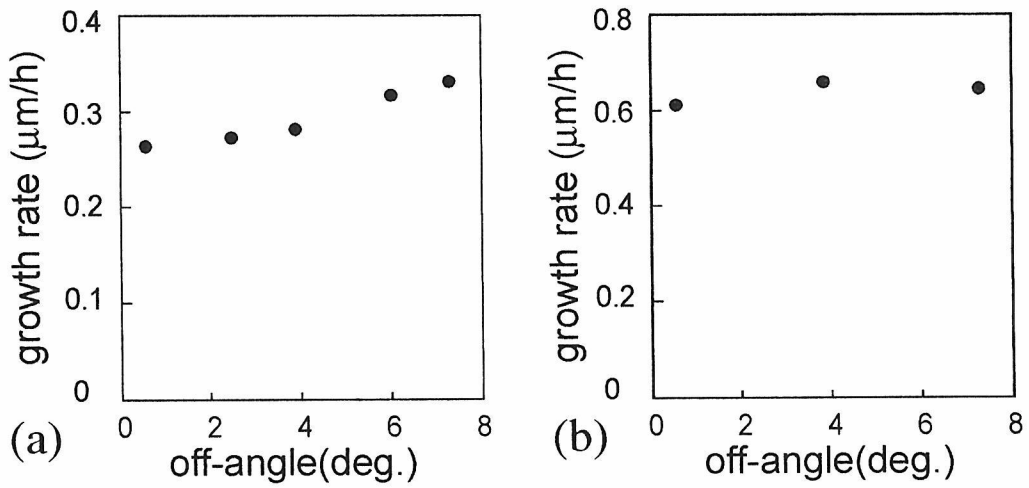

Fig. 9 Dependence of epitaxial growth rate on off-angle from (001). Misorientation was toward [110]. Methane concentration during growth rate was (a) 1% and (b) 6%.

Figure 9(a) and (b) show the dependence of growth rate on off-angle for the methane concentration of 1% and 6% , respectively. The growth with 1% methane concentration showed the higher growth rate with the increase of off-angle, while off-angle had smaller effect for the higher methane concentration growth. These result also support the higher rate of 2-dim. nucleation for the higher mehtne growth.

4. CONCLUSION

The surface observation and the growth simulation were carried out for diamond epitaxial films. The results obtained are summarized as follow,
1) In the (001) growth, the dimer row extension from S_B steps is dominant.
2) The ratio of 2-dim. nucleation rates to step-flow becomes the higher with the increase of the methane concentration.
3) The (111) growth takes place via incorporation of carbon atoms at the kinks.
4) The (110) growth surface shows prolonged islands with (111) and $(11\bar{1})$, indicating substantially growth on {111} facets.

5. REFERENCES

1) P. V. Deryaguin, B. V. Spitsyn, A. E. Gorodetsky, A. P. Zakahrov, L. L. Bouilov and A. E. Aleksenko: J. Cryst. Growth **31** (1975) 44.
2) S. Matsumoto, Y. Sato, M. Kamo and N. Setaka: Jpn. J. Appl. Phys. **21** (1982) 483.
3) M. Kamo, Y. Sato, S. Matsumoto and N. Setaka: J. Cryst. Growth **62** (1983) 642.
4) T. Tsuno, T. Imai, Y. Nishibayashi, K. Hamada and N. Fujimori: Jpn. J. Appl. Phys. **30** (1991) 1063.
5) T. Tsuno, T. Tomikawa, S. Shikata, T. Imai and N. Fujimori: Appl. Phys. Lett. **64** (1994) 572.
6) T. Tsuno, T. Tomikawa, S. Shikata and N. Fujimori: J. Appl. Phys. **75** (1994) 1526.
7) H. G. Busmann, H. Sprang, J. V. Hertel, W. Zimmermenn-Edling and H. J. Gü nterodt: Appl. Phys. Lett 59 (1991) 295.
8) H. G. Busman, W. Zimmermenn-Edling, H. Sprang, H. J. Günterodt and J. V. Hertel: Diamond Relat. Mater. **1** (1992) 979.
9) H. G. Maguire, M. Kamo, H. P. Lang, E. Meyer K. Weissendanger and H. J. Güntherodt: Diamond Relat. Mater. **1** (1992) 634.
10) H. Sasaki and H. Kawarada :Jpn. J. Appl. Phys. **32** (1993) L1771.
11) D. J. Chadi: Phys. Rev. Lett. **59** (1987) 1691.
12) H. Shiomi, K. Tanabe, Y. Nishibayashi and N. Fujimori: Jpn. J. Appl. Phys. **29** (1990) 34.
13) N. Aizaki and T. Tatsumi: Surf. Sci. **174** (1986) 658.

Surface Phonon Dispersion of CVD Grown Diamond

Takashi Aizawa
National Institute for Research in Inorganic Materials
1-1 Namiki, Tsukuba, Ibaraki 305, Japan

By using high-resolution electron energy loss spectroscopy (HREELS), surface phonon dispersion was investigated on hydrogen- and deuterium-terminated diamond (111) surfaces homoepitaxially grown by chemical vapor deposition (CVD) method. The as-grown surface is terminated by hydrogen and the surface carbon atoms are in the sp^3 hybridized state judging from the C–H stretching frequency. The off-specular HREELS shows two C–H stretching modes and two C–H bending modes, which is consistent with the CH_3 termination. The dispersionless C–H modes indicates weak direct interaction between each adsorbed species. An acoustic surface phonon is observed and shows a small isotope shift, which can be explained by either CH_3-termination or H-(monohydride) termination model.

1. Introduction

Although diamond is one of materials attracting wide interest, the number of available information about its surfaces is very small compared with Si. There are some difficulties in the diamond surface research: One is in preparing the surface. As diamond is the hardest material, it is difficult to polish an atomically smooth surface. Moreover, as diamond is metastable in low pressure, it is difficult to get well-ordered surface by usual cleaning techniques in vacuum: heating and ion-bombardment. Another difficulty is that diamond is an insulator. Charging up makes electronic spectroscopies difficult.

Recently, chemical vapor deposition (CVD) technique enables homoepitaxial growth of single-crystalline semiconducting diamond films on natural diamond surfaces. Surfaces of similar quality can be reproduced by fine controlling the CVD conditions. Our previous low energy electron diffraction (LEED) and high-resolution electron energy loss spectroscopy (HREELS) study revealed that the as-grown surface is a well-ordered hydrogen terminated surface [1,2]. Charging up does not occur on this semiconducting film surface. Thus the difficulties of diamond surface can be solved by using the CVD grown films.

Hydrogen plays an important role for the CVD process [3-6]. Investigation about hydrogen reaction on diamond surfaces is therefore important to understand the diamond CVD growth mechanism. Vibrational method is a powerful technique to detect surface hydrogen. A lot of optical studies using infrared absorption [7-9] and infrared-visible sum frequency generation spectroscopies [10] have been published. On the other hand, HREELS has not been so popular in diamond studies. HREELS has advantages over the optical methods: high surface sensitivity, which enables us to use a single-crystal well-ordered surface as a sample, and a different selection rule from the optical methods, which makes it possible to detect dipole-inactive modes and to determine the surface phonon dispersion [11].

In this paper, I demonstrate HREELS results of hydrogen- and deuterium-terminated diamond (111) surfaces and determine the surface phonon dispersion. The results are compared with calculational results using a valence force model in a slab configuration, and the surface structure is discussed.

2. Experimental

Samples were B-doped semiconducting homoepitaxial single-crystal films grown by plasma assisted chemical vapor deposition (CVD) [12]. Natural diamond single-crystal (111) substrates (about 4 mm × 4 mm × 2 mm) were polished with accuracy of ±4°. After cleaning procedures, the homoepitaxial layer was grown in the following conditions: Gaseous mixtures of methane (1.0 %), diborane (2 ppm) and hydrogen were fed at the rate of 50 ml/min and the pressure was kept at 40 Torr. Applied microwave power was about 300 W. The reaction temperature of the diamond surface was kept at 770–780°C, which was measured by an optical pyrometer. A film about 500 nm thick was deposited after 3–4 h of the growth.

HREELS experiments were performed in an ultra-high vacuum (UHV) chamber equipped with facilities of HREELS, LEED and AES. The chamber was evacuated by oil diffusion and Ti-sublimation pumps, achieving the base pressure of 2–4 × 10^{-8} Pa. The HREELS spectrometer consisted of a double-pass electrostatic cylindrical-deflector-type monochromator and the same type of analyzer. Energy resolution of the spectrometer is 4–6 meV [13].

The sample was transferred from the CVD apparatus to the HREELS chamber in air. It was clipped by a small Ta plate, which was suspended by Ta wires. The sample was heated in a vacuum by passing a current through the wires or by electron bombardment (EB) from a filament placed behind the sample. The sample temperature was measured by an infrared (λ = 2.0 μm) optical pyrometer (emissivity was set to 0.3).

All HREELS were taken at room temperature. In the HREELS measurement, the electron incident and detection angles were each 72° to the surface normal in the specular reflection mode. The incident angle θ_{in} was changed in the off-specular spectra. The phonon energy (frequency) is directly determined from the loss energy. Simultaneously, the phonon wave vector parallel to the surface ($k_{||}$) is determined using the momentum conservation law.

In H-D exchange experiments, research-grade D_2 gas was leaked to the pressure of 5 × 10^{-3} – 1 × 10^{-2} Pa. Heating the sample by EB above 600°C in the D_2 gas resulted in complete exchange of the surface hydrogen to deuterium.

3. Results and discussion

Figure 1 shows off-specular HREELS spectra of H-plasma-grown surface followed by mild (~ 400°C) annealing. The measurements were done along [1 $\bar{1}$ 0] azimuth that corresponds with the $\bar{\Gamma}$ – $\bar{K}$ axis of the surface Brillouin zone (SBZ). The C–H stretching vibration is divided into two peaks at 352 and 361 meV, which are assignable to

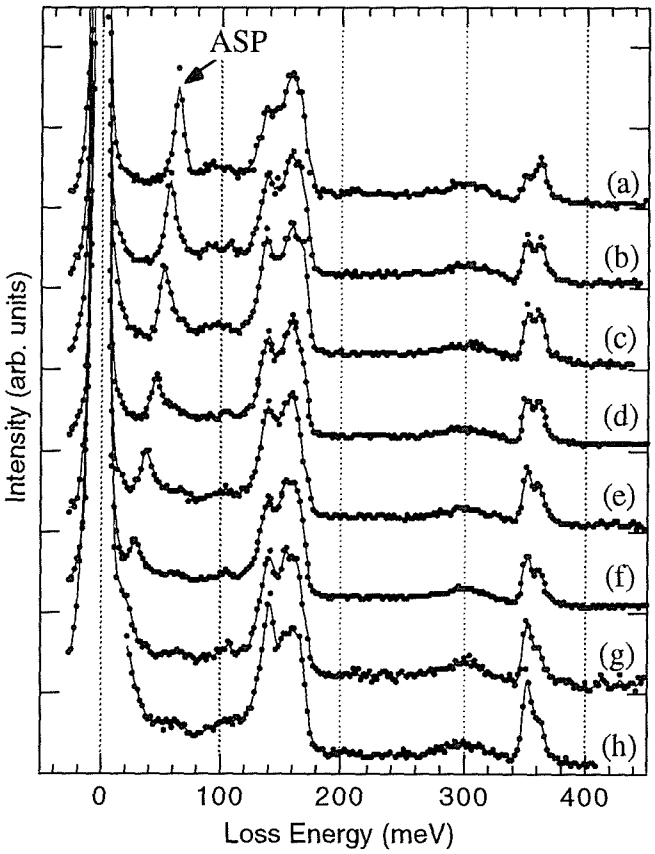

Fig. 1. Off-specular HREELS spectra of H-terminated diamond (111). The detection angle is fixed at 72° to the surface normal. The incidence angles are (a) 21°, (b) 27°, (c) 30.5°, (d) 36°, (e) 42°, (f) 48°, (g) 54°, and (h) 61°. Azimuth is [1-10] and primary electron energy is 15.0 eV.

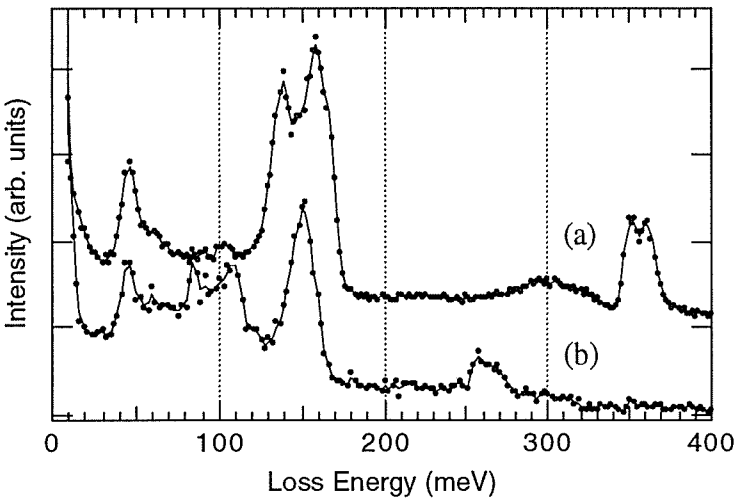

Fig. 2. Off-specular (θ_{in}=54°) HREELS spectrum of diamond (111) (a) before and (b) after the H–D exchange process.

symmetric and asymmetric stretching modes of CH_3 species, respectively. With the H–D exchange procedure, the spectrum changed as shown in Fig. 2. For the D-terminated surface, the C–D stretching mode consists of two components at 263 and 270 meV as shown in Fig. 2 (b). The energy ratio of this isotope shift is 1.34, which is very close to a square root of the reduced mass ratio ($\sqrt{2\times 13/14}$ = 1.363). The two modes around 138 meV and 165 meV on the H-terminated surface shift to 88 meV and 108 meV on the D-terminated surface. Judging from the isotope shift, these are

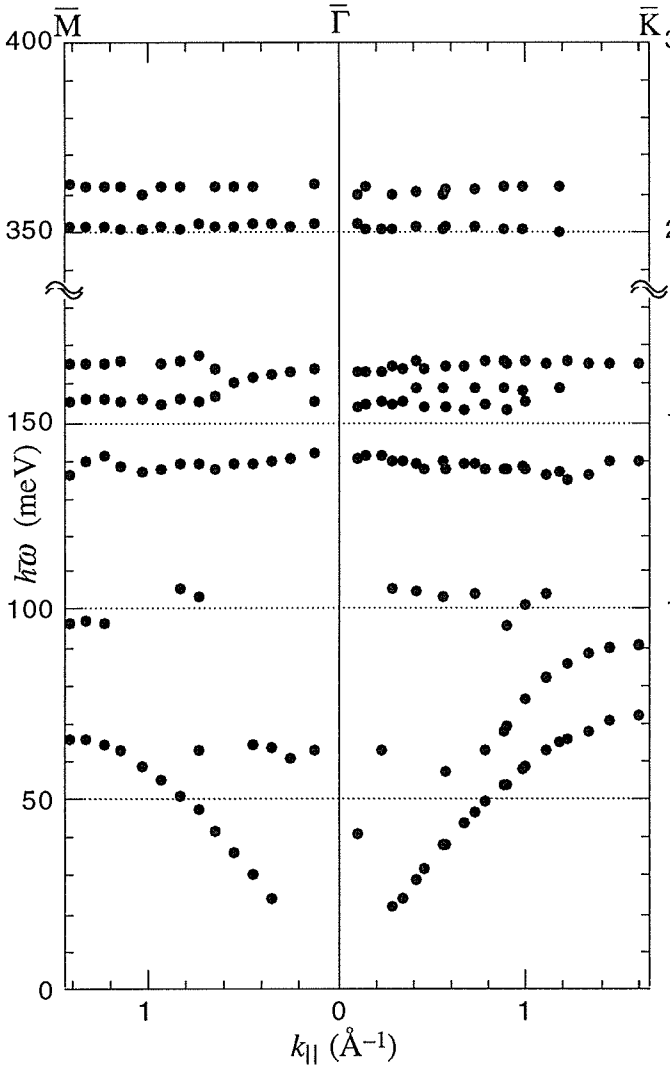

Fig. 3. Measured phonon dispersion of H-terminated diamond (111) surface.

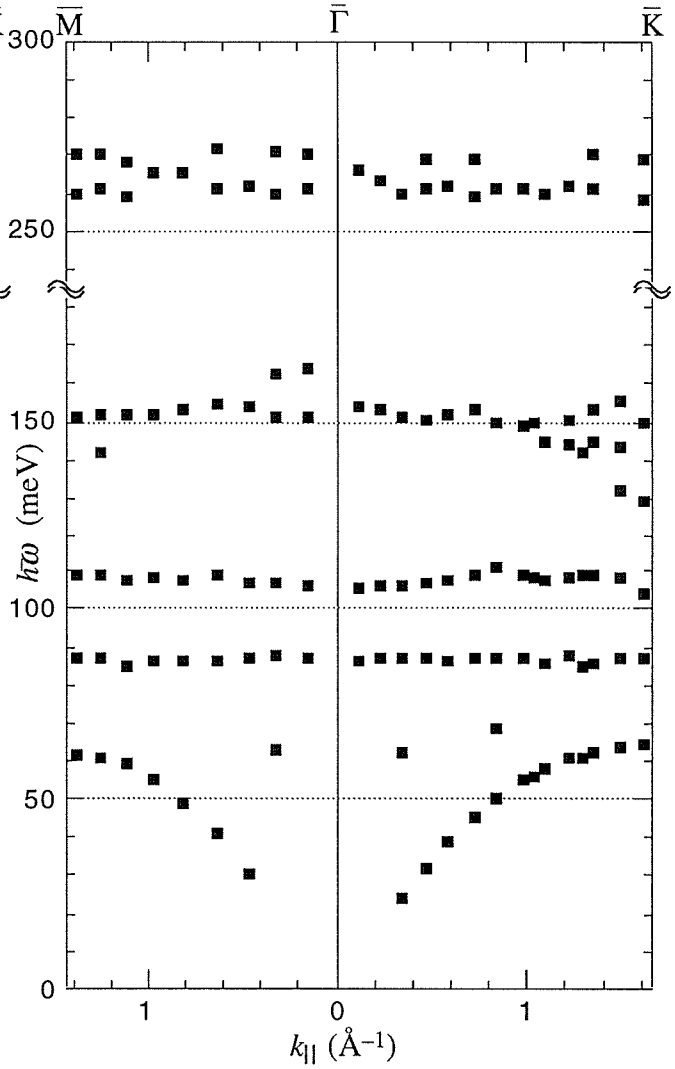

Fig. 4. Measured phonon dispersion of D-terminated diamond (111) surface.

assigned to C–H (C–D) bending modes. However, the frequency ratio is much larger than expected from the mass ratio. This is probably because a C–C stretching bulk mode interacts with the C–H bending modes. This bulk mode remains around 150 meV in Fig. 2 (b). In the low energy region, an acoustic surface phonon (labeled "ASP" in Fig. 1) appears, which largely shifts with the incidence angle. The surface should be fairly smooth and well ordered, for the ASP mode was clearly observed up to the SBZ edge.

In Fig. 3 and 4, the phonon dispersion relations of H- and D-terminated diamond (111) surfaces are shown, respectively. The C–H and C–D stretching and bending modes are almost dispersionless, meaning that direct interaction between the surface species is small. The acoustic mode shows a little isotope shift in the SBZ edge region: At the $\overline{K}$ point, this mode appears at 72 meV on the H-terminated surface while appears at 64 meV on the D-terminated surface. As this mode is an acoustic mode, surface carbon atoms should mainly vibrate. Adsorbed H or D atoms should vibrate together with the C atoms to which they are bound, because

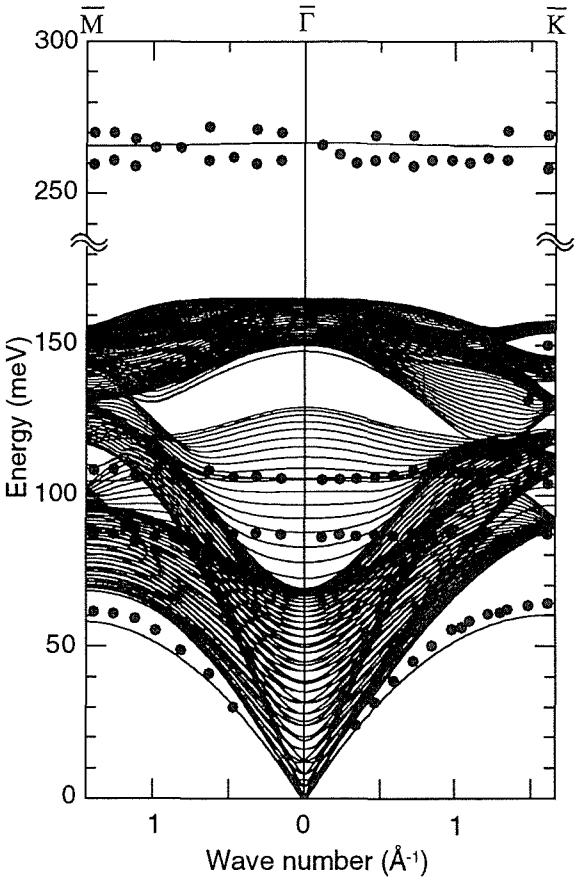

Fig. 6. Calculated phonon dispersion for D-terminated model.

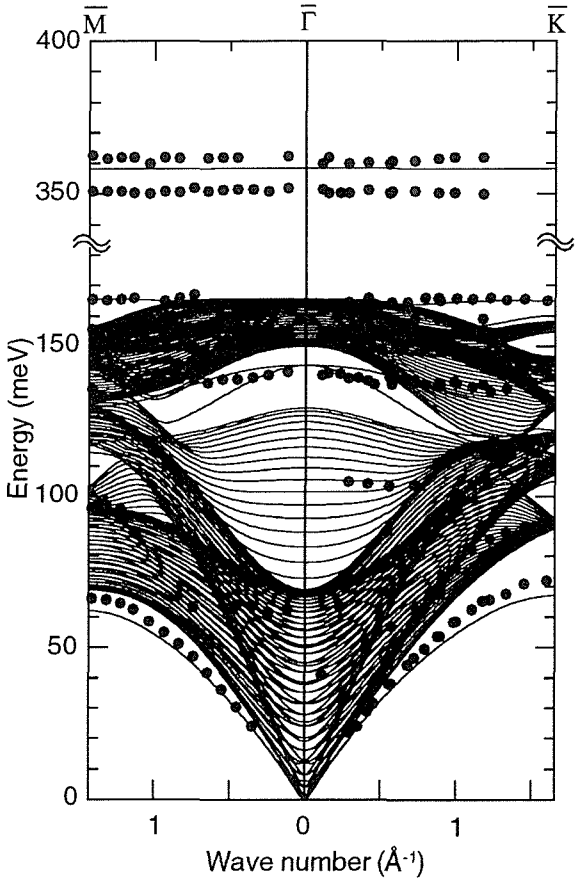

Fig. 5. Calculated phonon dispersion for monohydride (–H) terminated model. Experimental data are also plotted.

their mass is much lighter than C. In the edge region of the SBZ, the phonon wavelength is comparable to the interatomic distance, and the vibrational amplitude is usually localized to the outermost layer even in an acoustic surface mode. In a simplest model, the vibrational frequency is defined as $\omega = \sqrt{k/m}$, where k is a force constant and m is mass of the vibrating atomic group. When H is exchanged to D, no change is expected in k, so that the frequency ratio is given as a square root of the mass ratio. In the case of monohydride (CH) group, the frequency ratio becomes $\sqrt{14/13} = 1.038$, while in the methyl (CH_3) group, the ratio is $\sqrt{18/15} = 1.095$. The experimental value (72/64 = 1.13) is more consistent with the methyl group.

We performed a lattice-dynamical calculation using a valence force model in a slab configuration. The valence force constants, which well reproduce the bulk phonon dispersion of diamond [14] and the vibrational modes of propane molecule [15], are adopted and the dynamical matrix is calculated in the 30

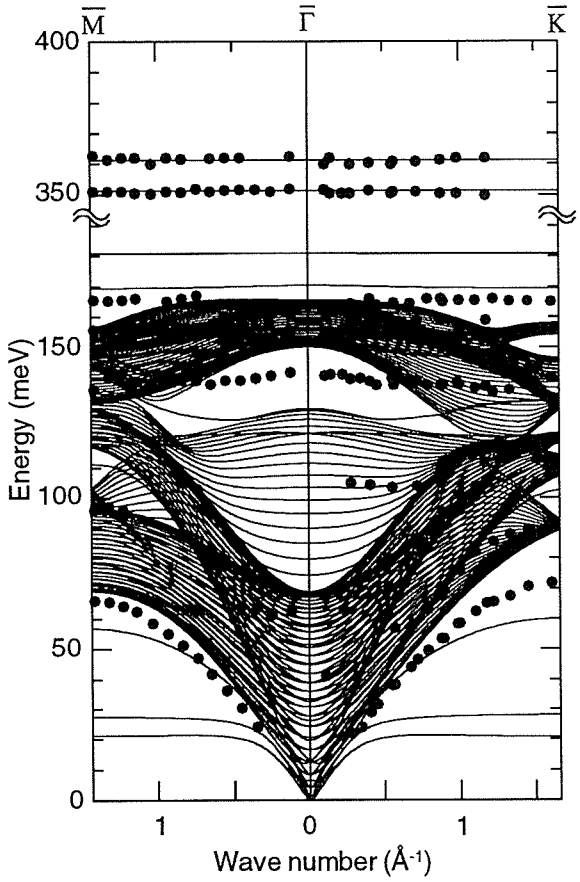

Fig. 7. Calculated phonon dispersion for methyl (–CH3) terminated model.

Although the shift of the acoustic mode can be explained better by the H-terminated model than the CH_3 terminated model, separation of the C–H (C–D) stretching mode is impossible in the uniform H termination. Recently, local $\sqrt{3} \times \sqrt{3}$ reconstruction was found on a CVD grown diamond (111) face by STM [16,17]. If the split of C–H stretching mode is caused by some kinds of defects like the local reconstruction or step edges, the comparable intensity of the two stretching modes means high density of the defects, which seems inconsistent with the clear appearance of one acoustic surface mode. Anyway, correlation of the C–H mode separation with the surface uniformity should be investigated by combining other methods like STM.

4. Summary

In summary, the surface-phonon dispersion relations have been determined by HREELS on the H and D covered (111) 1 × 1 surfaces. Two C–H (C–D) stretching modes and two C–H (C–D) bending modes were observed in the off-specular spectra. They are double layers slab. Figures 5–8 shows the results. Contrary to the above expectation, the monohydride terminated model also reproduces the observed isotope shift of the acoustic mode. In this case, the surface carbon atoms vibrate parallel to the surface in this mode, and the H or D has more amplitude than C. The C–H bending modes are better reproduced in this model. But the separation of C–H stretching mode is never explained by the monohydride model. In the case of methyl termination, the corresponding ASP mode is reproduced in the calculation as a vertically vibrating mode. The ratio of the isotope shift is consistent with the experimental data, but agreement of the absolute value is less satisfactory. Moreover, horizontally vibrating modes appear in low energy region because no interaction is taken into account between the adjacent methyl groups. The total agreement with the experimental data is worse than the monohydride terminated model, except that the C–H stretching separation is reproduced. Further improvement is necessary to obtain a valid CH_3 terminated model in the calculation.

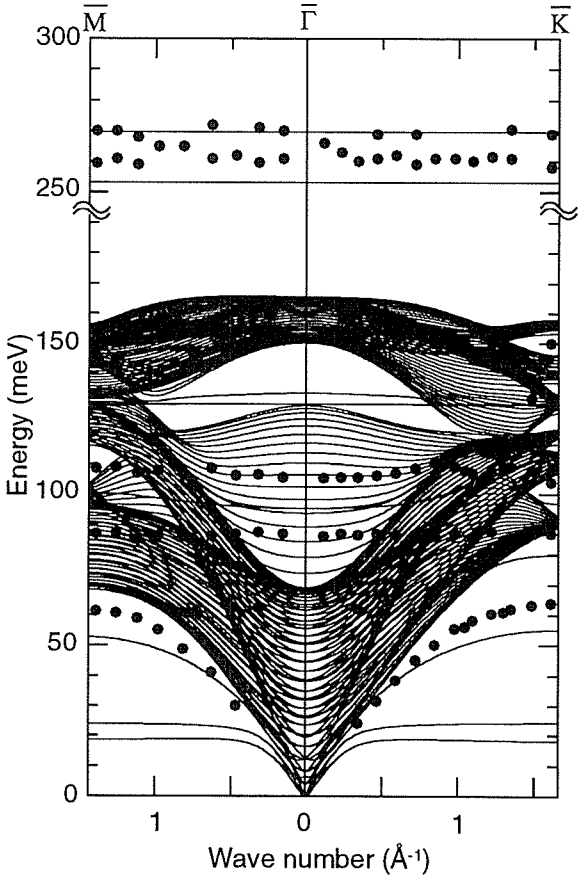

Fig. 8. Calculated phonon dispersion for CD3-terminated model.

almost dispersionless, which shows little interaction between the adsorbed surface hydrocarbon species. Additionally, one surface acoustic phonon and one bulk mode were observed. The isotope shift of the stretching mode is reasonable while that of the bending mode is larger, probably because of some mixing effect with the bulk phonon. A little isotope shift was observed in the acoustic surface phonon at the edge region of the SBZ. If the (111) surface is terminated by methyl species, the two stretching modes and the shift of the acoustic mode sound well explained. However, the realistic force constant model of such a surface is not yet obtained without direct interaction between the adjacent methyl species. The monohydride termination model can reproduce the shift of the acoustic mode better, but appearance of the two C–H stretching modes cannot be explained by this model assuming an uniform surface. The off-specular HREELS measurement, combined with the isotope shift, thus gives clear mode assignments and fruitful information about the surface structure.

References

1 T. Aizawa, T. Ando, M. Kamo and Y. Sato, *Phys. Rev. B,* ***48*** (1993) 18348.
2 T. Ando, T. Aizawa, K. Yamamoto, Y. Sato and M. Kamo, *Diamond Relat. Mater.,* ***3*** (1994) 975.
3 R. C. DeVries, *Annu. Rev. Mater. Sci.,* ***17*** (1987) 161.
4 J. C. Angus and C. C. Hayman, *Surface,* ***241*** (1988) 913.
5 S. Matsumoto, M. Hino and T. Kobayashi, *Appl. Phys. Lett.,* ***51*** (1988) 737.
6 P. K. Bachmann and W. van Enckevort, *Diamond Relat. Mater.,* ***1*** (1992) 1021.
7 R. Sappok and H. P. Boehm, *Carbon,* ***6*** (1968) 283.
8 R. Sappok and H. P. Boehm, *Carbon,* ***6*** (1968) 573.
9 T. Ando, M. Ishii, M. Kamo and Y. Sato, *J. Chem. Soc., Faraday Trans.,* ***89*** (1993) 1783.
10 R. P. Chin, J. Y. Huang, Y. R. Shen, Y. J. Chuang, H. Seki and M. Buck, *Phys. Rev. B,* ***45*** (1992) 1522.
11 H. Ibach and D. L. Mills, *Electron Energy Loss Spectroscopy and Surface Vibrations,* Academic Press, New York, 1982.
12 M. Kamo, T. Ando, Y. Sato, K. Bando and J. Ishikawa, *Diamond Relat. Mater.,* ***1*** (1992) 104.
13 C. Oshima, R. Souda, M. Aono and Y. Ishizawa, *Rev. Sci. Instrum.,* ***56*** (1985) 227.
14 H. L. McMurry, A. W. Solbrig, Jr., J. K. Boyter and C. Noble, *J. Phys. Chem. Solids,* ***28*** (1967) 2359.
15 H. L. McMurry, *Spectrochimica Acta,* ***21*** (1965) 2091.
16 H. -G. Busmann, S. Lauer, I. V. Hertel, W. Zimmermann-Edling, H. -J. Güntherodt, Th. Frauenheim, P. Blaudeck and D. Porezag, *Surf. Sci.,* ***295*** (1993) 340.
17 H. Sasaki and H. Kawarada, *Jpa. J. Appl. Phys.,* ***32*** (1993) L1771.

Author Index